

**Carnegie Mellon University**  
**MELLON COLLEGE OF SCIENCE**

**THESIS**

SUBMITTED IN PARTIAL FULFILLMENT OF THE REQUIREMENTS  
FOR THE DEGREE OF

**DOCTOR OF PHILOSOPHY IN THE FIELD OF PHYSICS**

TITLE: "CP Fraction Measurement of  $\pi^+\pi^-\pi^0$  and  $K^+K^-\pi^0$ "

PRESENTED BY: Onur Albayrak

ACCEPTED BY THE DEPARTMENT OF PHYSICS

Roy Briere	5/26/16
ROY BRIERE, CHAIR PROFESSOR	DATE

Stephen Garoff	5/26/16
STEPHEN GAROFF, DEPT HEAD	DATE

APPROVED BY THE COLLEGE COUNCIL

Fred Gilman	5/26/16
FRED GILMAN, DEAN	DATE

# Measurement of the $CP$ -even Fraction in the decays $D^0 \rightarrow \pi^+\pi^-\pi^0$ and $K^+K^-\pi^0$

Submitted in partial fulfillment of the requirements for  
the degree of

Doctor of Philosophy  
in  
Physics

Onur Albayrak

B.S., Physics, Bogazici University  
M.S., Physics, Carnegie Mellon University

Carnegie Mellon University  
Pittsburgh, PA  
May, 2016

# Abstract

Measurement of the  $CP$ -even Fraction in the decays  $D^0 \rightarrow \pi^+\pi^-\pi^0$  and  $K^+K^-\pi^0$

Onur Albayrak  
Doctor of Philosophy  
Department of Physics  
Carnegie Mellon University  
2016

The  $e^+e^-$  collision data sample collected with the BESIII detector at  $\sqrt{s} = 3.773$  GeV is used to investigate quantum-correlated  $\psi(3770) \rightarrow D^0\bar{D}^0$  decays. The fractional  $CP$ -even content,  $F_+$ , for the decays  $D^0 \rightarrow \pi^+\pi^-\pi^0$  and  $D^0 \rightarrow K^+K^-\pi^0$  is determined with improved precision compared to previous measurements. Values of  $F_+ = 0.968 \pm 0.006(\text{stat}) \pm 0.009(\text{syst})$  and  $0.782 \pm 0.035(\text{stat}) \pm 0.008(\text{syst})$  are obtained for the final states  $\pi^+\pi^-\pi^0$  and  $K^+K^-\pi^0$ , respectively. The large  $CP$ -even content makes these final states good candidates for the measurements of unitarity triangle angle  $\gamma$  using  $B^\pm \rightarrow DK^\mp$  decays at  $B$  factories.

## Acknowledgments

It was almost six years ago when I first passed through the Fort Pitt Tunnel and arrived at this amazing city full of amazing people. Since then it became a place I can call home, where I worked hard, jumped through many hoops to finally arrive to the point where one writes the acknowledgment section for his PhD thesis.

Many, many people have helped, influenced, and been with me during and before my time at CMU and I would like to mention some of them here.

To start off, I would not be here without the support of my family: Gonul the mom, Akif the dad, and Oznur the sister. They made me who I am today and for that I am grateful. They were the ones that were calming me during my time at college and through the grad school applications. I hope they will forgive me for the time periods when I did not call them as frequent as they would have wanted. Thank you for everything, I do not know how one can thank his family enough. I should also mention Gokhan, my brother-in-law, for his support as a brother. He is the one that put my mind at ease knowing that my sister is happy even I have not talked to her for a while.

I am quite sure that CMU Physics department is one of the few departments in the nation where one would feel as a part of the family. For that I am grateful and thank everyone from the staff, to the faculty and the hard working fellow grad students. I was lucky enough to be a part of the amazing class starting grad school in 2010. They were the opposite of one imagines as a “physics grad student”. I salute my first year office mates Sam and Marilia for their amazing friendship during the tough first year of grad school. Sam, being a Pittsburgh native, helped us get around in Pittsburgh and learn to love it. I am sorry for whistling too much in the dungeon. I should also mention Stephan and Patrick, with our great conversations about anything and teaching me all about the America and American people. I am quite sure that they are the reason that new people that I meet are amazed with my generic knowledge about American culture. I will miss our luncheons greatly.

First two years of the grad school is very tough due to getting used to the new environment with all the classes and workload. At that time, Batu, my first roommate ever, was the reason why I did not have any issues getting used to a totally new place and living away from my family for the first time. I did not speak much at the time, with all the stress, but we had good times together. Then, I started sharing an apartment with Gunay, the best roommate in the observable universe. He has been an amazing comrade all these years, and for that I am grateful. I was and am his humble padawan in the kitchen, mediocre video game companion, and unhelpful wingman at the bars/nightclubs. I thank him for not giving up on me with all my bitter comments about everything. During my last two years in Pittsburgh, I had the privilege to be roommates with Sercan. He educated me about humanities and social sciences as I started from nothing. We had amazing time with politically incorrect comments, watching all the TV shows, and playing late night FIFA. I should also mention my roommate Mert for one brief summer. I never knew the guy that I met on a camping trip would end up CMU, and we would share an apartment. He taught me all about the left-wing politics and dealt with all my politically incorrect comments about everything. All these people I mentioned made the life easier in Pittsburgh and they are the reasons why I can call Pittsburgh, home.

I should also mention the following people and thank them. Emre Can, with all his bitter comments about me. Emre Can, again with his bitter comments but big heart and a person that you know will be there for you when you need him. Yigit and Duygu, for their great hearts and friendship all these years. Ekin, Berkin, Meric, Beril, for their amazing friendship and all the conversations we had. Ugur, for being the amazing person he is with his big heart. Volkan Cirik, whom I am sorry that I get to know so late but sure to keep in touch. Also all the other great people of Pittsburgh: Recep, Irem, Tugce, Bekir, Erva, Nurcan, Ayse, Cagri, Lindsay, and Engin Burak. All the members of our FizikVeSpam mail group especially Levent, Alp, Mali, Bugra, Volkan, Ahmet, and Tuna. I do not know how I would have gone through grad school application process and the first two years without all emails we exchanged. Dr Taylan Akdogan and Dr Alpar Sevgen for their help and influence over me to follow my dreams to come to grad school.

I am also grateful for the amazing group that I had in the department, starting from Dr. Chunlei Liu. Without him, I am quite sure that my PhD would have been at least a year longer. He is a man of few words but taught me well to get around in the BESIII software and also in Beijing. I also thank Dr. Jake Bennett for all the helpful conversations that we had during the last two years. I should also mention Bai-Cian Ke my fellow group mate, and thank him for the stuff that he needed to do as I try to finish up my thesis. I also thank Dr. Hajime Muramatsu for all the nice conversations we had during my time in China and I will miss working with him deeply. Finally, the boss himself, Professor Roy Briere, without him this PhD will not become a reality. He was an amazing teacher, always willing to talk about anything, anytime. I truly believe that if other advisors were similar to him in terms of guiding the students, the grad school experience would be very different for a lot of people. I thank him for this great opportunity that he gave me. He helped me build my confidence and I thank him for all the respect I received in our collaboration in BESIII.

I also thank all the people I met during my trips to China where I spent a total of six amazing months.

One can not finish the acknowledgments of a CMU Physics degree without mentioning the great Professor Manfred Paulini. Thanks to him, this department becomes the “home” for all the students across the planet. He was of great help and mentor for all my years in CMU and I can not thank him enough.

Finally, I want to thank my soon-to-be wife, Melike. Without her, I do not know when I would have been writing this, or where. Her love and patience got me through the tough final stretch to finish my studies. She was the one calming me down, as I could get worried about anything, anytime and she was the one taking care of me when I needed to work on my thesis long hours. I also apologize for not participating in any sort of planning for anything claiming that I am working on my thesis. I know that we will build an amazing family together of which she will be the main architect.

# Contents

<b>1</b>	<b>Motivation</b>	<b>1</b>
1.1	The $CP$ Fraction Measurement . . . . .	2
<b>2</b>	<b>Experimental Apparatus</b>	<b>4</b>
2.1	BEPCII Accelerator . . . . .	4
2.2	BESIII Detector . . . . .	4
<b>3</b>	<b>Samples and Event Selection</b>	<b>8</b>
3.1	Samples . . . . .	8
3.2	Event Selection . . . . .	9
3.3	$\Delta E$ Distributions . . . . .	12
3.4	$K_s$ Selection . . . . .	17
3.5	Intermediate Resonances in the Tag Modes . . . . .	19
<b>4</b>	<b>Single Tags</b>	<b>21</b>
4.1	Mass Sideband Subtraction . . . . .	29
4.1.1	Mass Sideband Subtraction for $K_s\eta'(\rho\gamma)$ . . . . .	29
4.1.2	Mass Sideband Subtraction for $K_s\omega$ . . . . .	33
<b>5</b>	<b>Double Tags</b>	<b>37</b>
5.1	$\pi^+\pi^-\pi^0$ vs. tag modes . . . . .	41
5.2	$K^+K^-\pi^0$ vs. tag modes . . . . .	45
5.3	Mass Sideband Subtraction for Double Tags . . . . .	49
5.3.1	$\pi^+\pi^-\pi^0$ vs. tag modes . . . . .	49
5.3.2	$K^+K^-\pi^0$ vs. tag modes . . . . .	52
<b>6</b>	<b>Peaking Background</b>	<b>54</b>
6.1	Peaking-background Study for $CP$ Single Tags . . . . .	54
6.1.1	Peaking Background for Combined $CP$ Tags . . . . .	60
6.1.2	Peaking Background for $K_s\pi^0\pi^0$ . . . . .	62
6.1.3	Peaking Background for $K_s\eta'(\pi^+\pi^-\eta)$ . . . . .	64
6.1.4	Peaking Background for $K_s\eta'(\rho\gamma)$ . . . . .	66
6.1.5	Peaking Background Study of $K_s\omega$ . . . . .	68
6.1.6	Mass Sideband Study of $K_s$ for the Tag Modes . . . . .	70
6.2	Peaking Background Study for $\pi^+\pi^-\pi^0$ . . . . .	77
6.2.1	Single-tag Candidate . . . . .	77
6.2.1.1	Peaking-background Yields for Single-tag $\pi^+\pi^-\pi^0$ . . . . .	79
6.2.1.2	$K_s\pi^0$ Background in $\pi^+\pi^-\pi^0$ . . . . .	83
6.2.2	Peaking Background for Double Tags . . . . .	85
6.3	Peaking Background for $K^+K^-\pi^0$ . . . . .	88
6.3.1	Single-tag Candidates . . . . .	88
6.3.2	Double-tag Peaking Background for $K^+K^-\pi^0$ . . . . .	90
<b>7</b>	<b>Efficiency calculations</b>	<b>92</b>
7.1	Efficiency of single-tag yields . . . . .	92
7.2	Double-tag efficiency . . . . .	93

<b>8</b>	<b>Systematic Uncertainties</b>	<b>96</b>
8.1	Sensitivity of $F^+$ to Changes in $N^+, N^-$	96
8.2	Tag-side Efficiency Systematic Uncertainties	96
8.3	Signal-side Efficiency Systematic Uncertainties	97
8.3.1	Momentum spectrum of particles	98
8.4	Single-tag peaking backgrounds	101
8.5	Double tag peaking backgrounds	101
8.6	$K_s$ veto of $\pi^+\pi^-\pi^0$	102
8.7	Yield Systematic Uncertainties	102
8.8	Summary of Uncertainties	103
8.9	MC in/out Test	103
<b>9</b>	<b><math>F_+</math> Measurement and Implications</b>	<b>105</b>
9.1	Data Measurement	105
9.2	Implications	105
<b>A</b>	<b>Determining the Efficiencies over the Dalitz Plot for Signal Single-tag Modes</b>	<b>107</b>
<b>B</b>	<b>Double Tag Dalitz Plots</b>	<b>114</b>
B.1	$\pi^+\pi^-\pi^0$ Double Tag Dalitz Plots	114
B.2	$K^+K^-\pi^0$ Double Tag Dalitz Plots	116
B.3	Dalitz Plot of $CP$ contribution to the signal modes	118
<b>C</b>	<b>Peaking Background Box Plots</b>	<b>119</b>
C.1	$\pi^+\pi^-\pi^0$ vs. $CP$ Tag 2D $M_{BC}$ Distributions	120
C.2	$K^+K^-\pi^0$ vs. $CP$ Tag 2D $M_{BC}$ Distributions	124

## List of Figures

1	Schema of the BEPCII . . . . .	4
2	The BESIII detector. . . . .	6
3	The BESIII detector cross section. . . . .	7
4	$\Delta E$ distributions of the tag modes for the MC simulation. Blue dashed line is used for the signal shape, green for the background, and red for the whole fit. . . . .	13
5	$\Delta E$ distributions of the tag and the signal modes for the MC simulation. Blue dashed line is used for the signal shape, green for the background, and red for the whole fit. . . . .	14
6	$\Delta E$ distribution of the tag modes for the data. Blue dashed line is used for the signal shape, green for the background, and red for the whole fit. . . . .	15
7	$\Delta E$ distribution of the tag and the signal modes for the data. Blue dashed line is used for the signal shape, green for the background, and red for the whole fit. . . . .	16
8	The $K_s$ variables for the $CP$ tags, mass and flight significance, $L/\sigma$ from the MC sample. . . . .	17
9	Tag side $K_s$ variables, vertex $\chi^2$ of the MC sample. . . . .	18
10	The $K_s$ variables for the $CP$ tags from the MC sample . . . . .	18
11	Reconstructed intermediate $\eta'$ resonance masses for $\pi^+\pi^-\eta$ and $\rho\gamma$ decays from the MC sample of the $CP$ tag mode candidates. . . . .	19
12	The reconstructed $\omega(\pi^+\pi^-\pi^0)$ invariant mass distribution for the MC sample of the $CP$ tag mode candidates. . . . .	20
13	$M_{BC}$ fits to the $CP$ tags of the MC sample. . . . .	23
14	$M_{BC}$ fits to the $CP$ tags of the MC sample. . . . .	24
15	$M_{BC}$ fits to the $CP$ tags of the data sample. . . . .	25
16	$M_{BC}$ fits to the $CP$ tags of the data sample. . . . .	26
17	$M_{BC}$ fits to the $CP$ tags of the MC fake data sample. . . . .	27
18	$M_{BC}$ fits to the $CP$ tags of the MC fake data sample. . . . .	28
19	The $\eta' \rightarrow \rho\gamma$ mass distribution for the $K_s\eta'(\rho\gamma)$ decay using the MC sample. In the left plot, green is the signal region, red denotes the sideband regions. On the right, signal events and background are shown. . . . .	30
20	Fit to the $M_{BC}$ distribution for the $K_s\eta'(\rho\gamma)$ signal region of the MC sample. . . . .	30
21	Fit to the $M_{BC}$ distribution for the $K_s\eta'(\rho\gamma)$ sideband regions in the $\eta' \rightarrow \rho\gamma$ mass distribution for the MC sample. . . . .	31
22	The $\eta' \rightarrow \rho\gamma$ mass distribution for the $K_s\eta'(\rho\gamma)$ decay using data sample. In the left plot green is the signal region, red denotes the sideband regions. On the right, signal events and background is shown for the data sample. . . . .	31
23	Fit to the $M_{BC}$ distribution for the $K_s\eta'(\rho\gamma)$ signal region in the $\eta'$ mass distribution of the data sample. . . . .	32
24	Fit to the $M_{BC}$ distribution for the $K_s\eta'(\rho\gamma)$ sideband regions in the $\eta'$ mass distribution of the data sample. . . . .	32
25	The $\omega \rightarrow \pi^+\pi^-\pi^0$ mass distribution for the $K_s\omega$ decay using the MC sample. In the left plot green is the signal region, red denotes the sideband regions. On the right, signal events and background is shown. . . . .	33
26	Fit to the $M_{BC}$ distribution for the $K_s\omega$ signal region in the $\omega \rightarrow \pi^+\pi^-\pi^0$ mass distribution of the MC sample. . . . .	34
27	Fit to the $M_{BC}$ distribution for the $K_s\omega$ sideband regions in the $\omega \rightarrow \pi^+\pi^-\pi^0$ mass distribution of the MC sample. . . . .	34



28	The $\omega \rightarrow \pi^+\pi^-\pi^0$ mass distribution for the $K_s\omega$ decay using the data sample. In the left plot green is the signal region, red denotes the sideband regions. On the right, signal events and background is shown for the data sample. . . . .	35
29	Fit to the $M_{BC}$ distribution for the $K_s\omega$ signal region in the $\omega$ mass distribution of the data sample. . . . .	35
30	Fit to the $M_{BC}$ distribution for the $K_s\omega$ sideband regions in the $\omega \rightarrow \pi^+\pi^-\pi^0$ mass distribution of the data sample. . . . .	36
31	Regions in the $M_{BC}$ distribution. . . . .	38
32	Two dimensional $M_{BC}$ distributions for $\pi^+\pi^-\pi^0$ DT candidates for the MC. Red for the signal region, and green for four side band regions. . . . .	41
33	Two dimensional $M_{BC}$ distributions for $\pi^+\pi^-\pi^0$ DT candidates for the MC. Red for the signal region, and green for four side band regions. . . . .	41
34	Two dimensional $M_{BC}$ distributions for $\pi^+\pi^-\pi^0$ DT candidates for the MC. Red for the signal region, and green for four side band regions. . . . .	42
35	Two dimensional $M_{BC}$ distributions for $\pi^+\pi^-\pi^0$ DT candidates for the MC. Red for the signal region, and green for four side band regions. . . . .	42
36	Two dimensional $M_{BC}$ distributions for $\pi^+\pi^-\pi^0$ DT candidates for the data sample. Red for the signal region, and green for four side band regions. . . . .	43
37	Two dimensional $M_{BC}$ distributions for $\pi^+\pi^-\pi^0$ DT candidates for the data sample. Red for the signal region, and green for four side band regions. . . . .	43
38	Two dimensional $M_{BC}$ distributions for $\pi^+\pi^-\pi^0$ DT candidates for the data sample. Red for the signal region, and green for four side band regions. . . . .	44
39	Two dimensional $M_{BC}$ distributions for $\pi^+\pi^-\pi^0$ DT candidates for the data sample. Red for the signal region, and green for four side band regions. . . . .	44
40	Two dimensional $M_{BC}$ distributions for $K^+K^-\pi^0$ DT candidates for the MC. Red for the signal region, and green for four side band regions. . . . .	45
41	Two dimensional $M_{BC}$ distributions for $K^+K^-\pi^0$ DT candidates for the MC. Red for the signal region, and green for four side band regions. . . . .	45
42	Two dimensional $M_{BC}$ distributions for $K^+K^-\pi^0$ DT candidates for the MC. Red for the signal region, and green for four side band regions. . . . .	46
43	Two dimensional $M_{BC}$ distributions for $K^+K^-\pi^0$ DT candidates for the MC. Red for the signal region, and green for four side band regions. . . . .	46
44	Two dimensional $M_{BC}$ distributions for $K^+K^-\pi^0$ DT candidates for the data sample. Red for the signal region, and green for four side band regions. . . . .	47
45	Two dimensional $M_{BC}$ distributions for $K^+K^-\pi^0$ DT candidates for the data sample. Red for the signal region, and green for four side band regions. . . . .	47
46	Two dimensional $M_{BC}$ distributions for $K^+K^-\pi^0$ DT candidates for the data sample. Red for the signal region, and green for four side band regions. . . . .	48
47	Two dimensional $M_{BC}$ distributions for $K^+K^-\pi^0$ DT candidates for the data sample. Red for the signal region, and green for four side band regions. . . . .	48
48	The $\pi^+\pi^-\pi^0$ invariant mass distribution in $K_s\omega$ vs. $\pi^+\pi^-\pi^0$ DT events from the MC on the left. The $\eta'$ mass distribution in $K_s\eta'$ vs. $\pi^+\pi^-\pi^0$ DT events from the MC on the right. Magenta is used for background and cyan for the signal. . . . .	49

49	The $\pi^+\pi^-\pi^0$ invariant mass distribution in $K_s\omega$ vs. $\pi^+\pi^-\pi^0$ DT events from the data on the left. The $\eta'$ mass distribution in $K_s\eta'$ vs. $\pi^+\pi^-\pi^0$ DT events for the data on the right. Magenta is used for background and cyan for the signal. . . . .	50
50	The $\pi^+\pi^-\pi^0$ invariant mass distribution in $K_s\omega$ vs. $K^+K^-\pi^0$ DT events from the MC on the left. The $\eta'$ mass distribution in $K_s\eta'$ vs. $K^+K^-\pi^0$ DT events from the MC on the right. Magenta is used for background and cyan for the signal. . . . .	52
51	The $\pi^+\pi^-\pi^0$ invariant mass distribution in $K_s\omega$ vs. $K^+K^-\pi^0$ DT events for the data on the left. The $\eta'$ mass distribution in $K_s\eta'$ vs. $K^+K^-\pi^0$ DT events for the data on the right. Magenta is used for background and cyan for the signal. . . . .	53
52	ST candidate, signal only, and peaking background fits of $CP$ tags. . . . .	56
53	ST candidate, signal only, and peaking background fits of $CP$ tags. . . . .	57
54	ST candidate, signal only, and peaking background fits of $CP$ tags. . . . .	58
55	ST candidate, signal only, and peaking background fits of $CP$ tags. . . . .	59
56	ST candidate, signal only, and the peaking background fits to the $CP$ combined tags. . . . .	61
57	$M_{BC}$ fit to the peaking background of $K_s\pi^0\pi^0$ with various contributions removed. . . . .	62
58	$M_{BC}$ fit to the peaking background of $K_s\pi^0\pi^0$ with various contributions removed. . . . .	63
59	Left: the $\eta'$ mass distribution for the $K_s\eta'(\pi^+\pi^-\eta)$ candidates. Green is the signal region, red denotes the sideband regions. Right: signal events (red) and background (green), and total (blue). . . . .	64
60	$M_{BC}$ fit to the $K_s\eta'(\pi^+\pi^-\eta)$ signal region in the $\eta'$ mass distribution. . . . .	64
61	$M_{BC}$ fit to the $K_s\eta'(\pi^+\pi^-\eta)$ sideband regions in the $\eta'$ mass distribution. . . . .	65
62	$M_{BC}$ vs $M_{\eta'}$ distribution of $K_s\eta'(\pi^+\pi^-\eta)$ . . . . .	65
63	Fit to the $M_{BC}$ distribution for peaking background of $K_s\eta'(\rho\gamma)$ with various contributions removed. . . . .	66
64	$M_{BC}$ fit to the $K_s\eta'(\rho\gamma)$ with signal, $K_s\pi^-\pi^+\pi^0$ , $K_s\omega$ , and $K_s\eta$ removed. . . . .	67
65	$M_{BC}$ fit to the peaking background of $K_s\omega$ with various contributions removed. . . . .	68
66	$M_{BC}$ fit to the $K_s\omega$ with signal with $K_s\pi^-\pi^+\pi^0$ and $K_sK_s\pi^0$ removed. . . . .	69
67	Side band and the signal region yield fits for the $K_s$ study for the MC. . . . .	71
68	Side band and the signal region yield fits for the $K_s$ study for the MC. . . . .	72
69	Side band and the signal region yield fits for the $K_s$ study for the MC. . . . .	73
70	Side band and the signal region yield fits for the $K_s$ study for the data sample. . . . .	74
71	Side band and the signal region yield fits for the $K_s$ study for the data sample. . . . .	75
72	Side band and the signal region yield fits for the $K_s$ study for the data sample. . . . .	76
73	The $\Delta E$ distribution of the ST $\pi^+\pi^-\pi^0$ candidates from the MC for the signal (left) and peaking background (right). . . . .	77
74	Dalitz plot of $\pi^+\pi^-\pi^0$ using all the MC sample with using various $K_s$ veto. . . . .	78
75	$\pi^+\pi^-\pi^0$ yield fits with different $K_s$ vetoes using the MC sample. . . . .	80
76	Peaking background for $\pi^+\pi^-\pi^0$ using the MC sample, with different $K_s$ vetoes. . . . .	81
77	Peaking background for $\pi^+\pi^-\pi^0$ using the MC sample, with $K_s\pi^0$ removed using truth information, showing the remaining backgrounds. . . . .	82
78	Dalitz plot of $\pi^+\pi^-\pi^0$ candidates, without any $K_s$ veto, that are generated as $K_s\pi^0$ decays. . . . .	83
79	$K_s\pi^0$ events in DP of $\pi^+\pi^-\pi^0$ . . . . .	84
80	Wide $K_s$ veto. . . . .	84
81	Double tag candidates with $CP+$ vs. $\pi^+\pi^-\pi^0$ candidates and peaking background distribution using all the MC sample. . . . .	86

82	Double tag candidates with $CP-$ vs. $\pi^+\pi^-\pi^0$ candidates and peaking background distribution using all the MC sample. . . . .	86
83	$\Delta E$ distributions of the ST $K^+K^-\pi^0$ events (left and peaking background (right) . . .	88
84	Single-tag candidates for $K^+K^-\pi^0$ decay . . . . .	89
85	Signal only and the peaking background distribution for the $K^+K^-\pi^0$ candidates . .	89
86	Double-tag candidates of $CP+$ vs $K^+K^-\pi^0$ using the MC sample. . . . .	91
87	Double-tag candidates of $CP-$ vs $K^+K^-\pi^0$ using the MC sample. . . . .	91
88	Data and MC overlays of charged pion momentum distributions of $\pi^+\pi^-\pi^0$ events. .	99
89	Data and MC overlays of $\pi^0$ momentum distributions of $\pi^+\pi^-\pi^0$ events. . . . .	99
90	Data and MC overlays of charged kaon momentum distributions of $K^+K^-\pi^0$ events. .	100
91	Data and MC overlays of $\pi^0$ momentum distributions of $K^+K^-\pi^0$ events. . . . .	100
92	DP efficiency for single tag $\pi^+\pi^-\pi^0$ events . . . . .	108
93	DP efficiency for single tag $K^+K^-\pi^0$ events . . . . .	109
94	Dalitz Plot distributions that are used in the calculation of the DP efficiency for $\pi^+\pi^-\pi^0$ mode. . . . .	110
95	Dalitz Plot projections that are used in the calculation of the DP efficiency for $\pi^+\pi^-\pi^0$ mode. . . . .	111
96	Dalitz Plot distributions that are used in the calculation of the DP efficiency for the $K^+K^-\pi^0$ mode. . . . .	112
97	Dalitz Plot projections that are used in the calculation of the DP efficiency for $K^+K^-\pi^0$ mode. . . . .	113
98	$\pi^+\pi^-\pi^0$ vs. $CP+$ events the data sample . . . . .	114
99	$\pi^+\pi^-\pi^0$ vs. $CP-$ events for the data sample . . . . .	115
100	$K^+K^-\pi^0$ vs. $CP+$ events for the data sample . . . . .	116
101	$K^+K^-\pi^0$ vs. $CP-$ events for the data sample . . . . .	117
102	Dalitz Plot distributions of the signal modes separated by $CP$ content for $\pi^+\pi^-\pi^0$ and $K^+K^-\pi^0$ . . . . .	118
103	$CP$ tag vs. $\pi^+\pi^-\pi^0$ peaking background study plots for MC sample. . . . .	120
104	$CP$ tag vs. $\pi^+\pi^-\pi^0$ peaking background study plots for MC sample. . . . .	121
105	$CP$ tag vs. $\pi^+\pi^-\pi^0$ peaking background study plots for MC sample. . . . .	122
106	$CP$ tag vs. $\pi^+\pi^-\pi^0$ peaking background study plots for MC sample. . . . .	123
107	$CP$ tag vs. $K^+K^-\pi^0$ peaking background study plots for MC sample. . . . .	124
108	$CP$ tag vs. $K^+K^-\pi^0$ peaking background study plots for MC sample. . . . .	125
109	$CP$ tag vs. $K^+K^-\pi^0$ peaking background study plots for MC sample. . . . .	126
110	$CP$ tag vs. $K^+K^-\pi^0$ peaking background study plots for MC sample. . . . .	127

## List of Tables

1	Decays contributing to the $\pi^+\pi^-\pi^0$ decay in the BESIII decay tables. . . . .	10
2	$CP$ tag modes used and branching fractions in percent, with resonance decay rates and MC reweighting included for the BES MC. The PDG branching ratios do not include the daughter decay branching ratios. . . . .	10
3	Branching fractions of intermediate resonances in %. The PDG branching ratios do not include the daughter decay branching ratios. . . . .	10
4	Decays contributing to the $K^+K^-\pi^0$ decay in the BESIII decay tables. . . . .	11
5	DTag Candidate Requirements. . . . .	11
6	$\Delta E$ Requirements . . . . .	12
7	Requirements for resonances. . . . .	19
8	Single Tag Yields. . . . .	22
9	Sideband subtraction numbers of $K_s\eta'(\rho\gamma)$ for the MC sample. . . . .	29
10	Sideband subtraction numbers of $K_s\eta'(\rho\gamma)$ for the data sample. . . . .	30
11	Sideband subtraction numbers of $K_s\omega$ for the MC sample. . . . .	33
12	Sideband subtraction numbers of $K_s\omega$ for the data sample. . . . .	34
13	Double-tag Sideband Regions . . . . .	38
14	Double-tag counts for signal and sideband regions. For $\pi^+\pi^-\pi^0$ vs. tag modes for the MC sample. . . . .	38
15	Double Tag counts for signal and sideband regions. For $K^+K^-\pi^0$ vs. tag modes for the MC sample. . . . .	39
16	Double Tag counts for signal and sideband regions. For $\pi^+\pi^-\pi^0$ vs. tag modes for the data sample. . . . .	39
17	Double Tag counts for signal and sideband regions. For $K^+K^-\pi^0$ vs. tag modes for the data sample. . . . .	39
18	Double Tag yields for $\pi^+\pi^-\pi^0$ vs. tag modes, before the mass side band subtraction for $K_s\eta'(\rho\gamma)$ and $K_s\omega$ . . . . .	40
19	Double Tag yields for $K^+K^-\pi^0$ vs. tag modes, before the mass side band subtraction for $K_s\eta'(\rho\gamma)$ and $K_s\omega$ . . . . .	40
20	Sideband subtraction numbers for $K_s\eta'$ vs. $\pi^+\pi^-\pi^0$ from the MC. . . . .	50
21	Sideband subtraction numbers for $K_s\eta'$ vs. $\pi^+\pi^-\pi^0$ for the data sample. . . . .	50
22	Sideband subtraction numbers for $K_s\omega$ vs. $\pi^+\pi^-\pi^0$ from the MC. . . . .	50
23	Sideband subtraction numbers for $K_s\omega$ vs. $\pi^+\pi^-\pi^0$ for the data sample. . . . .	51
24	Sideband subtraction numbers for $K_s\eta'(\rho\gamma)$ vs. $K^+K^-\pi^0$ from the MC. . . . .	52
25	Sideband subtraction numbers for $K_s\eta'(\rho\gamma)$ vs. $K^+K^-\pi^0$ for the data sample. . . . .	53
26	Sideband subtraction numbers for $K_s\omega$ vs. $K^+K^-\pi^0$ from the MC. . . . .	53
27	Sideband subtraction numbers for $K_s\omega$ vs. $K^+K^-\pi^0$ for the data sample. . . . .	53
28	$M_{BC}$ yields and the resulting peaking background ( $pBG$ ) ratios for $CP$ tags. . . . .	55
29	Individual contribution of the tags to the total background and the ST yield. $pBG'$ is the peaking background calculated using the formula $(S + pBG) - S$ . . . . .	55
30	Yields from the fits and the resulting peaking-background fractions for the combined $CP+$ and $CP-$ tags. . . . .	60
31	Peaking-background study yields for the $K_s\pi^0\pi^0$ mode. . . . .	62
32	Peaking background fractions for $K_s\pi^0\pi^0$ mode. . . . .	62
33	Yields for the peaking-background study yields for the $K_s\eta'(\rho\gamma)$ mode. . . . .	66
34	Peaking background fractions for the $K_s\eta'(\rho\gamma)$ mode. . . . .	66

35	Yields from the peaking-background study yield for the $K_S\omega$ mode. . . . .	68
36	Peaking background fractions for the $K_S\eta'(\rho\gamma)$ mode. . . . .	68
37	Yields from the three mass regions of the $\pi^+\pi^-$ distributions and their resulting peaking-background fractions from the MC. . . . .	70
38	Yields from the three mass regions of the $\pi^+\pi^-$ distributions and their resulting peaking-background fractions from the data sample. . . . .	70
39	$K_S$ vetoes for $\pi^+\pi^-\pi^0$ . $M_{K_SPDG}$ is taken to be $0.4976 \text{ GeV}/c^2$ . . . . .	78
40	Single-tag peaking-background study of $\pi^+\pi^-\pi^0$ from the MC. . . . .	79
41	Yields of the DT peaking-background study and the fractions for $\pi^+\pi^-\pi^0$ vs. com- bined $CP$ tags. . . . .	85
42	Yields of the DT peaking-background study and the fractions for $\pi^+\pi^-\pi^0$ vs. indi- vidual $CP$ tags. . . . .	85
43	Numbers of the events in the five regions of 2D $M_{BC}$ distribution for all $\pi^+\pi^-\pi^0$ vs. $CP$ tags. . . . .	85
44	Region counts for the 2D $M_{BC}$ distribution for the signal only $\pi^+\pi^-\pi^0$ vs. $CP$ tags events. . . . .	87
45	Region counts for the 2D $M_{BC}$ distribution for the peaking background events for $\pi^+\pi^-\pi^0$ vs. $CP$ tags. . . . .	87
46	Single-tag peaking-background study of $K^+K^-\pi^0$ . . . . .	88
47	Yields from the DT peaking-background study yields and the fractions for $K^+K^-\pi^0$ vs. individual $CP$ tags. . . . .	90
48	Region counts in the 2D $M_{BC}$ distribution for all $K^+K^-\pi^0$ vs. $CP$ tags. . . . .	90
49	Region counts in the 2D $M_{BC}$ distribution for signal only $K^+K^-\pi^0$ vs. $CP$ tags. . . . .	90
50	Region counts in the 2D $M_{BC}$ distribution for peaking background $K^+K^-\pi^0$ vs. $CP$ tags. . . . .	90
51	DT peaking background study yields and fractions for $K^+K^-\pi^0$ vs. combined $CP$ tags. . . . .	91
52	The detection efficiencies of single-tags modes from the MC, after sideband subtrac- tion. . . . .	92
53	Corrected single-tag yields. . . . .	92
54	Double-tag efficiency of tag modes vs. $\pi^+\pi^-\pi^0$ for MC, including the scaling factor $x_{\pm}$ . . . . .	94
55	Double-tag efficiency of tag modes vs. $K^+K^-\pi^0$ for MC, including the scaling factor $x_{\pm}$ . . . . .	94
56	Double-tag corrected yields of tag modes vs. $\pi^+\pi^-\pi^0$ . . . . .	94
57	Double-tag corrected yields of tag modes vs. $K^+K^-\pi^0$ . . . . .	95
58	Average number of tracks, $\pi^0$ , $K_S$ , and $\gamma$ per event for $CP+$ and $CP-$ single-tags, weighted by the reconstructed yields. . . . .	97
59	Results of systematic studies varying $CP+$ tags. . . . .	101
60	Results with altered $K_S$ veto . . . . .	102
61	Results with altered C region scale factor. . . . .	103
62	Summary of the contributions to the systematic uncertainty in %, for the measured $F_+$ for each of the two signal modes, and the total uncertainty. Systematic uncer- tainties on the yields are still to be determined. . . . .	103
63	Results of the in/out test from the MC, and $F_+$ values for the $\pi^+\pi^-\pi^0$ and $K^+K^-\pi^0$ final states and the number of standard deviations ( $\sigma$ ) the input and output values differ. . . . .	104

64	$F_+$ values for the $\pi^+\pi^-\pi^0$ and $K^+K^-\pi^0$ final states for this analysis and for an earlier experiment. . . . .	105
----	--	-----

## 1 Motivation

Determinations of the Cabibbo-Kobayashi-Maskawa (CKM) [1, 2] matrix elements provide valuable information on the consistency of the Standard Model and an insight in to the search for new physics. Measurement of all the angles  $\beta$ ,  $\alpha$ , and  $\gamma$ <sup>1</sup> of the unitarity triangle in decays of  $B$  mesons is a way of checking the consistency of the CKM matrix. The angle  $\beta$  is measured with high precision at the two B factories, with the BaBar and Belle detectors [3]. The measurement of the angle  $\alpha$  is more difficult than that of  $\beta$  due to theoretical uncertainties. Only time-dependent  $CP$  asymmetries in  $b \rightarrow u\bar{u}d$  decays can be used in the measurement of  $\alpha$ , compared to many different transitions that can be utilized for  $\beta$ . The final angle  $\gamma$  does not depend on the CKM elements that involve the top quark. Therefore, it can be measured using the tree-level decays of the  $B$  meson. The interference of  $B^- \rightarrow D^0 K^-$  ( $b \rightarrow c\bar{u}s$ ) and  $B^- \rightarrow \bar{D}^0 K^-$  ( $b \rightarrow u\bar{c}s$ ) transitions, where  $D^0$  and  $\bar{D}^0$  both decay to the same final state, is instrumental for the  $\gamma$  measurement.

Various methods have been used to measure  $\gamma$ , exploiting different types of  $D$  decays, where  $D$  denotes a neutral  $D$  meson. The GLW [4, 5] method uses  $D$  decays to the  $CP$  eigenstates such as  $D \rightarrow \pi^+\pi^-$  or  $D \rightarrow K^+K^-$ . This method lacks high precision due to the relative rate difference in the  $B \rightarrow D$  decays. The ADS [6, 7] method tries to remove the rate difference problem by using  $D$  final states where Cabibbo-allowed  $\bar{D}^0$  and doubly-Cabibbo-suppressed  $D^0$  decays interfere. Examples of these final states include  $D^0 \rightarrow K^-\pi^+$  and  $D^0 \rightarrow K^-\pi^+\pi^0$ . Various measurements that use the CLEO-c results [8] on the average strong phase differences for these  $D$  decays, have been carried out by LHCb [9]. Another method considers three-body final states where both the  $D^0$  and  $\bar{D}^0$  have large branching fractions, such as  $K_s\pi^+\pi^-$  and  $K_sK^+K^-$ . These decays can be used in the  $\gamma$  measurement by optimizing the analysis to use well-chosen bins across the Dalitz plot to avoid cancellation of the interference. This method, GGSZ [10], provides a precise measurement of  $\gamma$ ; however, it includes uncertainty due to the  $D$  decay modeling.

All the methods for measuring  $\gamma$  that are mentioned above take advantage of the quantum-correlated production of  $D\bar{D}$  mesons in  $e^+e^-$  collisions at an energy corresponding to the  $\psi(3770)$  resonance. The quantum correlation of the  $D$  meson pair implies that when a  $D$  meson is detected in a certain  $CP$  eigenstate, the other  $D$  meson must be a  $CP$  eigenstate with the opposite eigenvalue. This enables the charm factories to look for final states that have a certain  $CP$  eigenstate, being assured then that the other  $D$  meson must have the opposite  $CP$  eigenvalue. Current best measurements of  $\gamma$  combine the different methods and are summarized in Ref. [3]. BABAR [11] uses results from the GLW, ADS and GGSZ analyses to measure  $\gamma = 69^{+17}_{-16}$ , Belle [12] gets,  $\gamma = 68^{+15}_{-13}$ , and LHCb [13]  $\gamma = 70.9^{+7.1}_{-8.5}$ , using the same analyses.

A large branching ratio final state common to  $D^0$  and  $\bar{D}^0$  is a valuable candidate for the  $\gamma$  measurement. The decay  $D^0 \rightarrow \pi^+\pi^-\pi^0$ , with a branching ratio of  $(1.470 \pm 0.090)\%$  [14] is a good example of such a final state has attracted interest recently [15, 16]. The  $\pi^+\pi^-\pi^0$  final state has a lot of potential because of its symmetric Dalitz plot distribution, which is a sign that the decay is dominated by a single  $CP$  eigenstate. An isospin analysis of  $D^0 \rightarrow \pi^+\pi^-\pi^0$  [17] shows that the final state is almost exclusively  $I = 0$  and, given that the parity and the G-parity are  $-1$ , and  $G = (-1)^J C$ ,

<sup>1</sup>Also denoted as  $\phi_1$ ,  $\phi_2$ , and  $\phi_3$ , respectively

then  $C$  is expected to be  $-1$ , resulting in a  $CP$  even decay. A similar decay  $D^0 \rightarrow K^+ K^- \pi^0$  is also studied [18, 19]; it has a lower branching ratio of  $(3.29 \pm 0.14) \times 10^{-3}$  and is found to be less  $CP$  pure. These two final states are considered in the  $\gamma$  measurement using the so-called the quasi-GLW method, in which the fraction of the  $CP$ -even fraction in the final state would be an external input.

Improving the  $CP$  fraction measurements of these multibody self-conjugate final states will pave the way for a better determination of the  $\gamma$ . Taking advantage of the largest data sample taken at the  $\psi(3770)$  resonance, we aim to improve the current measurements of the  $CP$  fraction in the decays  $D^0 \rightarrow \pi^+ \pi^- \pi^0$  and  $K^+ K^- \pi^0$ . Details of the measurements are given in the next section.

## 1.1 The $CP$ Fraction Measurement

93% of the decays are  $D\bar{D}$  pairs for the data collected at 3.773 GeV.  $D$  tagging (DTag) is used for selecting  $D$  meson decays. A single-tag (ST), is when only one of the  $D$  meson decays are reconstructed. A double-tag (DT) event is when the partner  $D$  decay is also reconstructed. In this analysis both of the  $D$  decays are hadronic decays. In a DT event, since all the particles are reconstructed, energy and momentum conservation can be used for further studying the events.

We also take advantage of how the  $\psi(3770)$  is produced at the threshold, where it enables us to retrieve the  $CP$  content of one  $D$  decay depending on the opposite  $D$  decay. The center of mass energy being at the threshold for producing  $\psi(3770)$  ensures that no additional particles are produced. The  $\psi(3770)$  is produced quantum-correlated where quantum numbers are  $J^{PC} = 1^{--}$ . If one rewrites the  $\psi(3770) = (D^0 \bar{D}^0 - \bar{D}^0 D^0) / \sqrt{2}$ , using the  $CP$  eigenstates  $D_{\pm}^0 \equiv (D^0 \pm \bar{D}^0) / \sqrt{2}$ , one can arrive at  $\psi(3770) = (D_+ D_- - D_- D_+) / \sqrt{2}$ . This will ensure if one  $D$  decays in a  $CP$  even state, other  $D$  meson will decay in an odd  $CP$  state.

Measurement of the  $CP$  fraction is done using the ratio of the yields of double- and single-tag candidates. A single-tag (ST) candidate is where only one of the neutral  $D$  candidates is reconstructed without a requirement on the other  $D$ , and a double-tag (DT) candidate is where both  $D$  mesons are reconstructed through hadronic decays.

The tagging and the use of ratios cancels the need to know how many  $D$  mesons are produced in the  $e^+e^-$  collisions. The number of single-tags are given by  $S = 2N_{D\bar{D}}B_TB_T\epsilon_T$  where  $N_{D\bar{D}}$  is the number of  $D\bar{D}$  pairs produced,  $B_T$  is the branching ratio of the tag mode, and  $\epsilon_T$  is the reconstruction efficiency of the tag candidate. Similarly number of double-tag events are given by  $2(2)N_{D\bar{D}}B_TB_S\epsilon_{TS}$ , where  $B_S$  is the branching ratio of the signal mode,  $\epsilon_{TS}$  is the reconstruction efficiency of the double tag candidate, and (2) is due to the enhancement of the quantum-coherence of  $CP+$  vs  $CP-$  decays. Using the DT/ST ratio,  $N_{D\bar{D}}$  is canceled  $\frac{D}{S} = 2B_S \frac{\epsilon_{TS}}{\epsilon_T}$ , where  $\epsilon_{TS} \approx \epsilon_T \epsilon_S$ .

he details of the reconstruction are given in the following sections, but the formulation is explained here.



The formula for the  $CP$  fraction,  $F_+$ , in a particular signal decay is given below.

$$F_+ = \frac{N^+}{N^+ + N^-} \quad (1)$$

$$N_{\pm} = \frac{M^{\pm}}{S^{\pm}} \quad (2)$$

$$S_{\pm} = \frac{S_{meas}^{\pm}}{(1 - \eta_{\pm} y_D)}, \quad (3)$$

where  $F_+$  is the fraction of the  $CP+$  content for the signal mode,  $M^{\pm}$  is the number of double-tag events for a signal channel versus  $CP\mp$  tags, and  $S_{\pm}$  is the number of single-tag events for  $CP\mp$  decay modes. Finally,  $\eta$  is the  $CP$  eigenvalue mode and  $y_D$  is the mixing parameter. The value for the mixing parameter is taken from the latest average from the HFAG group [3];  $(0.62 \pm 0.08) \%$ , and it is set to zero for the Monte Carlo (MC) simulation sample. All the yields above are efficiency corrected. Therefore, determination of the number of double and single tags are required, together with the measurement of the reconstruction efficiencies.

## 2 Experimental Apparatus

### 2.1 BEPCII Accelerator

The Beijing Electron Positron Collider II (BEPCII) is an electron-positron accelerator located on the campus of the Institute of High Energy Physics (IHEP) in Beijing, China. This two-ring collider has a design luminosity of  $1 \times 10^{33} \text{cm}^{-2}\text{s}^{-1}$  at a center-of-mass energy of 3.78 GeV. It can run at energies between 2.0 – 4.6 GeV, with two symmetric beams. The layout of the accelerator with the interaction point is shown in Figure 1.

The two storage rings are 237.5 m in circumference. Electrons and positrons collide at the interaction point (IP) with a horizontal crossing angle of 11 mrad. The BEPCII accelerator is operated in multi-bunch mode with 93 bunches in each ring. Bunches are separated by 2.4 m or 8 ns. The single-beam current can be as high as 910 mA.

The accelerator is also used for synchrotron radiation, at a beam energy of 2.5 GeV.

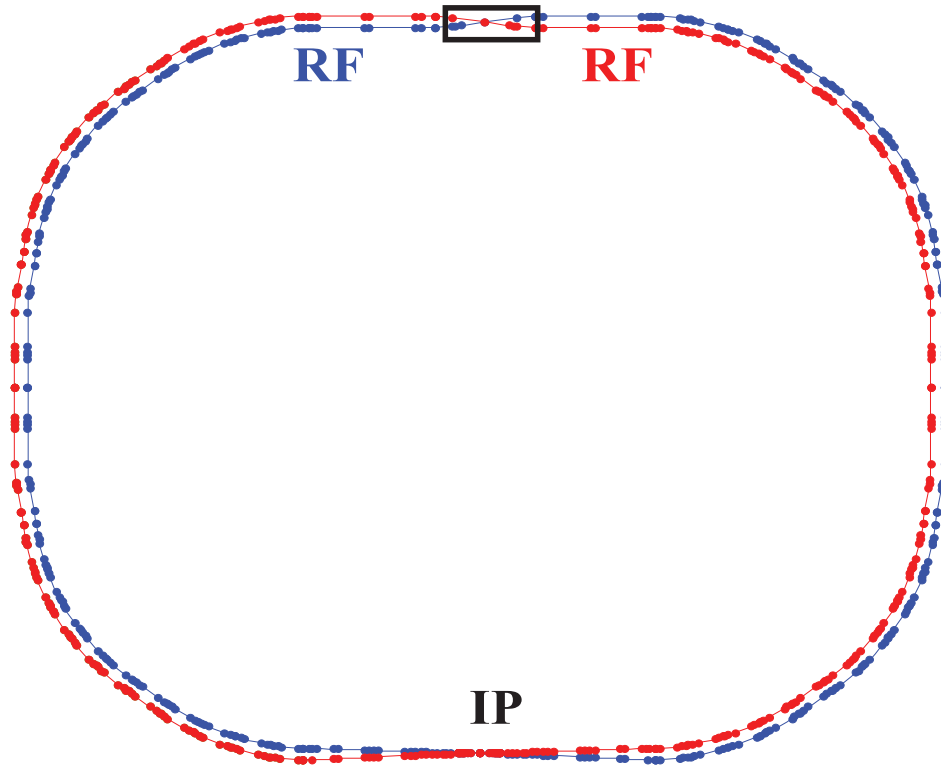


*Figure 1: Schema of the BEPCII*

### 2.2 BESIII Detector

The Beijing Spectrometer III (BESIII) is a general purpose detector located at the interaction point of the BEPCII accelerator. The BESIII detector consists of a multilayer drift chamber (MDC), plastic scintillator Time-Of-Flight counters (TOF), a CSI(Tl) crystal electromagnetic calorimeter (EMC),

a superconducting solenoid magnet (SSM), and a muon system (MUC). A schema of the BESIII detector is given in Figures 2 and 3 and details can be found elsewhere [20].

The superconducting solenoid magnet (SSM) operates at a field of 1 T, which is optimized for precise momentum measurements in the charm energy region, while not creating too many multiple-pass “curler” tracks at lower momenta. The magnet has a length of 3.52 m with a mean radius of 1.482 m. The SSM runs at a nominal current of 3369 A.

The main drift chamber (MDC) is used for charged particle tracking. The MDC uses a helium-based gas mixture,  $He - C_3H_8$ . A ratio of 60:40 is chosen for this mixture to reduce the effect of multiple scattering, while sustaining the  $dE/dx$  resolution. The chamber is 2.58 m in length and has an inner radius of 0.059 m and outer radius of 0.81 m, with a total of 43 layers. The polar angle coverage of the detector is  $|\cos(\theta)| \leq 0.83$  for a track that passes through all layers, and 0.93 for a track that passes through 20 layers. The cells of the chamber are approximately square with a half-width of about 6 mm in the inner portion and 8.1 mm in the outer portion of the drift chamber. The momentum resolution of the MDC is around 0.5% at 1 GeV/c, while the  $dE/dx$  resolution for minimum ionizing pions is 6%.

The time-of-flight detector surrounds the MDC and is used for particle identification. The TOF is based on plastic scintillators and consists of a barrel and two end cap regions. The TOF has a timing resolution of 90 ps (120 ps) in the barrel (end cap) region. The barrel part of the TOF has a solid angle coverage of  $|\cos(\theta)| < 0.83$  and the end cap regions cover  $0.85 < |\cos(\theta)| < 0.95$ .

The energies of photons and electrons are measured using the electromagnetic calorimeter (EMC). The EMC cluster-finding algorithm requires a minimum cluster energy of 20 MeV. It has good  $e/\pi$  separation for momentum higher than 200 MeV/c. A total of 6240 CsI(Tl) crystals are used in the calorimeter, and the whole system is placed outside the TOF system. These crystals cover 93% of  $4\pi$  and are located in one barrel and two end cap sections. The EMC has an energy resolution of 2.5% (5%) at 1 GeV, with a position resolution of 6 mm (9 mm) in the barrel (end cap).

Particles that escape all the inner layers of the BESIII detector and the SSM travel through the muon chamber (MUC) system. The muon chambers consist of resistive plate counters that are layered within the steel plates of the magnetic flux return yoke of the SSM. The MUC is used for particle identification, which is achieved based on the penetration depth. The MUC system provides 2 cm position resolution for muons, with 89% coverage of the full solid angle. The efficiency of the detector is measured to be 90% for muons that have momenta larger than 0.5 GeV/c and drops to 10% for pions at 0.5 GeV/c.

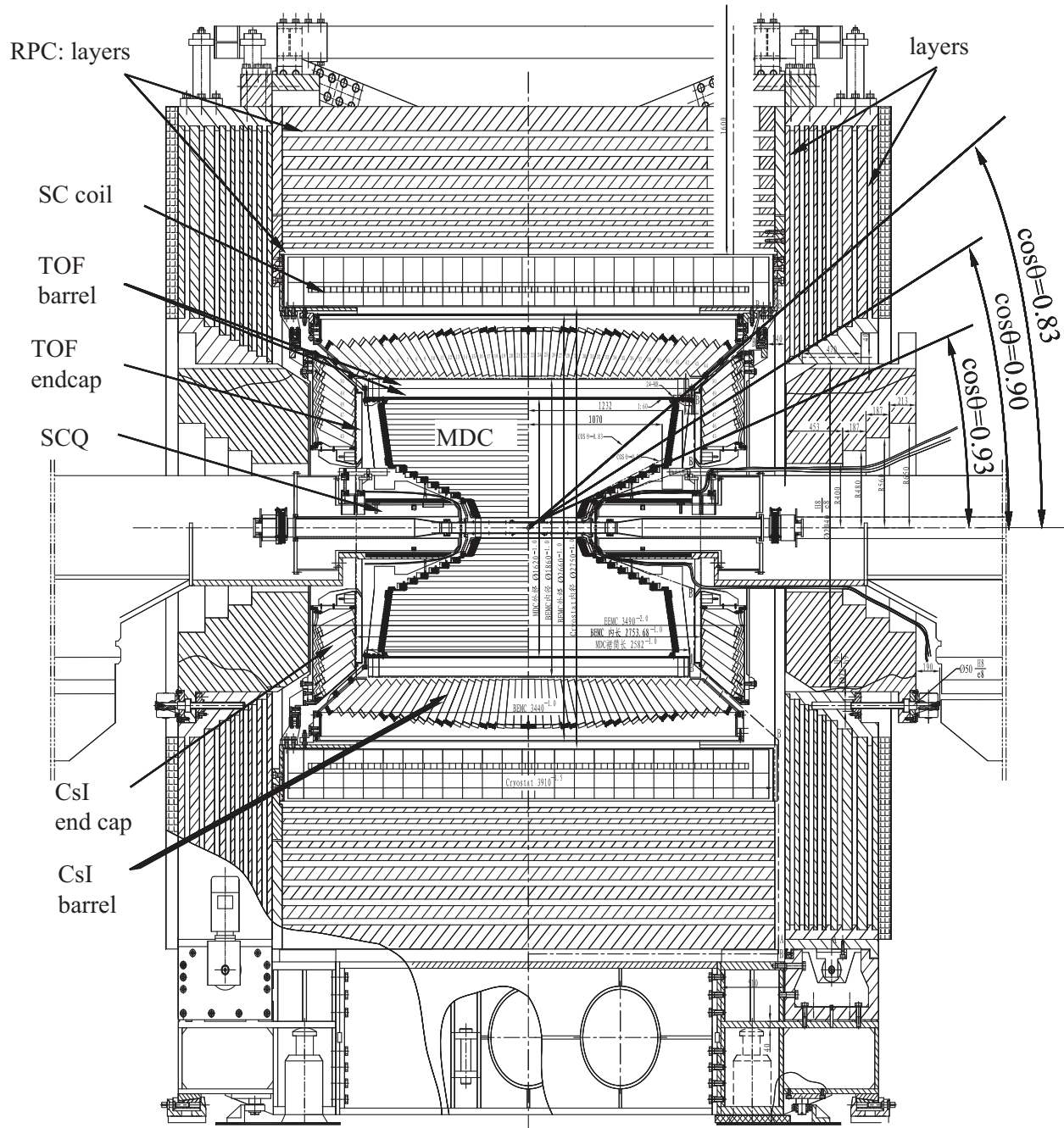
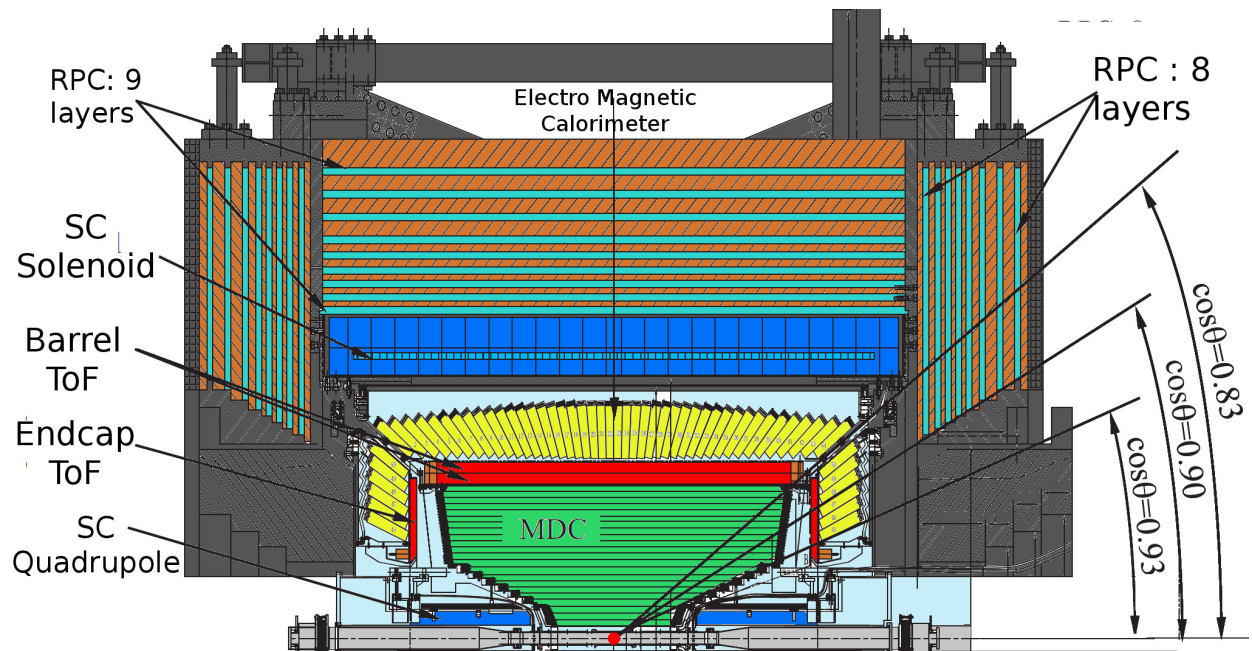


Figure 2: The BESIII detector.



*Figure 3: The BESIII detector cross section.*

### 3 Samples and Event Selection

#### 3.1 Samples

The analysis uses the  $\psi(3770)$  data taken in 2010 and 2011 with a luminosity of  $2.93 \text{ fb}^{-1}$  [21, 22]. This data sample is currently the largest available at the  $\psi(3770)$  resonance and can be used in many quantum-correlation analyses, improving previous measurements of CLEO-c with about 3.5 times the integrated luminosity (CLEO-c had  $818 \text{ pb}^{-1}$ ). The BESIII detector, described in Section 2.2, provided us with very good particle resolution, together with a clean event environment to perform this analysis.

Monte Carlo samples that are used for this analysis are listed below.

- 2010 and 2011  $D^+D^-$ , 10.8 times the data
- 2010 and 2011 QCMC MC  $D^0\bar{D}^0$ , 10.8 times the data
- 2010 and 2011  $q\bar{q}$ , 7.4 times the data
- 2010 and 2011 *non* $DD$ , 10.2 times the data

BESIII uses a decay table for  $D$  mesons that is derived from the PDG [14]. Most of the three-body decays are generated with non-interfering contributions of various possible resonant intermediate states and a non-resonant term. Dalitz decay models are also used for some well-known particle decays such as the  $\omega \rightarrow \pi^+\pi^-\pi^0$ .

Some of the two-body decays that contribute to other final states do not have the correct branching fraction in the BESIII decay table. The  $\pi^+\pi^-\pi^0$  and  $K^+K^-\pi^0$  final states are studied for such problems and excess contributions are removed to match the PDG levels. Two examples for such decays are  $D^0 \rightarrow f_0\pi^0$  and  $D^0 \rightarrow \rho(2S)^-\pi^+$ , where the contribution was in excess of the PDG values. The decay  $D^0 \rightarrow f_0\pi^0$  was listed as having a branching fraction of 0.0032, therefore, 98% of the events are discarded for the  $\pi^+\pi^-\pi^0$  final state. Similarly, the decay  $D^0 \rightarrow \rho(2S)^-\pi^+$  was listed with a branching ratio of 0.0065, 90% of the candidates are discarded for  $\pi^+\pi^-\pi^0$  final state. Resulting branching ratio values are given in Table 1.

In the standard BESIII  $\psi(3770)$  MC, each  $D$  decay is independent of how the other  $D$  decays. For a single-tag event this gives an accurate representation of the data. However, differences between MC and data arise from having each  $D$  decay independently for double-tag events. A filtration is performed to randomly filter out events from the standard MC based on the likelihood of each  $D^0$  and  $\bar{D}^0$  final-state combination. Particles in the final states are categorized, and events are weighted based on these categories to double, stay unchanged, or reduced to zero (in a slightly simplified picture), due to quantum correlations. The filter makes sure the decay of opposite  $CP$  eigenstates are enhanced, whereas same-sign  $CP$  decays are forbidden. This quantum-correlated MC sample (QCMC) enables us to study the  $CP$  fraction measurement in a more realistic decay environment where some decays are enhanced and some decays are forbidden.

### 3.2 Event Selection

We use the BESIII Offline Software System (BOSS) to process the data. The BOSS 6.6.4.p02 version of this software package is used for this analysis. Other sub-packages that are used with their version numbers are listed below.

- DTagAlg (v56), together with DTagTool (v11), is for reconstructing  $D$  meson candidates through hadronic decay channels with loose requirements on the candidates for future investigation.
- SimplePIDSvc (v11) is a particle identification (PID) software package developed by the CMU group that combines the information gathered from EMC, MDC and TOF to help the user identify particles.
- Pi0EtaToGGRAlg (v10) is used to reconstruct  $\pi^0 \rightarrow \gamma\gamma$  events and constrain the square of the four-momenta of the photon candidates be equal to the neutral pion mass.

Tag modes that are used, together with their branching ratios in the PDG and BESIII Monte Carlo, are listed in Table 2. Some of the particles are not measured directly but reconstructed through other particles in the detector:  $K_s \rightarrow \pi^+\pi^-$ ,  $\pi^0 \rightarrow \gamma\gamma$ ,  $\eta \rightarrow \gamma\gamma$ ,  $\omega \rightarrow \pi^+\pi^-\pi^0$ ,  $\eta' \rightarrow \pi^+\pi^-\eta$ , and  $\eta' \rightarrow \rho\gamma$ . Branching ratios of these intermediate particle decays are given in Table 3.

Decays contributing to the signal final states are listed in Table 1 for  $\pi^+\pi^-\pi^0$  and Table 4 for  $K^+K^-\pi^0$ , along with the intermediate resonances, the normalized branching ratios, and the resulting  $CP$  fraction. These values are already corrected for the excess events mentioned in the previous section.

In order to reduce the background, requirements are placed on the detected particles. A list of these requirements is given in Table 5.

In order to make sure the signal events,  $\pi^+\pi^-\pi^0$  and  $K^+K^-\pi^0$ , reside inside the Dalitz plot (DP) an one-constraint (1C) kinematic fit is performed. A common fitter program provided by IHEP is used for this fit. Two tracks and two EMC showers, together with their uncertainty information, are included in the fit. The  $\pi^0$  as an intermediate state is included. Finally, momentum and energy of all the tracks and showers are constrained to give the  $D^0$  mass. The 1C kinematic fit is almost always successful and the failure rate is negligible.

This analysis takes advantage of single- and double-tag candidates. A single-tag (ST) candidate is where only one of the neutral  $D$  candidates is reconstructed without a requirement on the other side of the decay. A double-tag (DT) candidate is where both  $D$  mesons are reconstructed through hadronic decays. For the DT candidates used in this analysis, one of the  $D$  mesons is required to decay to our signal modes,  $\pi^+\pi^-\pi^0$  or  $K^+K^-\pi^0$ , and the opposite  $D$  must decay to one of the  $CP$  modes used.

For the  $\pi^+\pi^-\pi^0$  channel, in order to remove the background from  $K_s\pi^0$  decay, a mass veto on the  $\pi^+\pi^-$  system is applied. Events with a dipion invariant mass satisfying  $|M_{\pi^+\pi^-}| < 0.018 \text{ GeV}/c^2$  are discarded. More details on this mass veto are explained in Section 6.2.

**Table 1:** Decays contributing to the  $\pi^+\pi^-\pi^0$  decay in the BESIII decay tables.

CP	BF	Decay	Model	Int. Res. BF (%)	Model	Int. Res. Decay	Final BF (%)	Normalized BF (%)
+	0.009800	$\rho^+\pi^-$	SVS	0.999550	VSS	$\pi^+\pi^0$	0.009796	0.511031
+	0.004970	$\rho^-\pi^+$	SVS	0.999550	VSS	$\pi^-\pi^0$	0.004968	0.259166
+	0.003730	$\rho^0\pi^0$	SVS	0.989609	VSS	$\pi^+\pi^-$	0.003691	0.192570
-	0.000064	$f_0\pi^0$	PHSP	0.509802	PHSP	$\pi^+\pi^-$	0.000033	0.001702
+	0.000040	$\rho(2S)^+\pi^-$	PHSP	0.400000	PHSP	$\pi^+\pi^0$	0.000016	0.000835
+	0.000110	$\rho(2S)^0\pi^0$	PHSP	0.400000	PHSP	$\pi^+\pi^-$	0.000044	0.002295
+	0.000650	$\rho(2S)^-\pi^+$	PHSP	0.400000	PHSP	$\pi^-\pi^0$	0.000260	0.013564
-	0.000100	$f'_0\pi^0$	PHSP	0.393939	PHSP	$\pi^+\pi^-$	0.000039	0.002055
-	0.000560	$f_0(1500)\pi^0$	PHSP	0.231231	PHSP	$\pi^+\pi^-$	0.000129	0.006755
-	0.000340	$f_2\pi^0$	PHSP	0.565000	TSS	$\pi^+\pi^-$	0.000192	0.010022
+	0.001300	$\phi\pi^0$	SVS	0.000074	HELAMP	$\pi^-\pi^+$	0.000000	0.000005
	0.00205*	$\pi\pi\pi^0$	PHSP				not generated	
Total		$\pi^+\pi^-\pi^0$					0.019168	
Total CP+		$\pi^+\pi^-\pi^0$						0.979490

**Table 2:** CP tag modes used and branching fractions in percent, with resonance decay rates and MC reweighting included for the BES MC. The PDG branching ratios do not include the daughter decay branching ratios.

Decay Channel	PDG BF (%)	BES MC BF (%)
$K_s\pi^0$	$1.200 \pm 0.040$	0.843
$\pi^+\pi^-$	$0.141 \pm 0.003$	0.140
$K^+K^-$	$0.401 \pm 0.007$	0.394
$K_s\pi^0\pi^0$	$0.910 \pm 0.110$	0.498
$K_s\eta'(\pi^+\pi^-\eta)$	$0.950 \pm 0.050$	0.110
$K_s\eta'(\rho\gamma)$	$0.950 \pm 0.050$	0.188
$K_s\eta$	$0.485 \pm 0.030$	0.117
$K_s\omega$	$1.110 \pm 0.060$	0.697
$\pi^+\pi^-\pi^0$	$1.470 \pm 0.090$	1.917
$K^+K^-\pi^0$	$0.338 \pm 0.021$	0.330

**Table 3:** Branching fractions of intermediate resonances in %. The PDG branching ratios do not include the daughter decay branching ratios.

Particle	Final State	PDG BF (%)	BES MC BF (%)
$\pi^0$	$\gamma\gamma$	$98.82 \pm 0.03$	98.82
$K_s$	$\pi^+\pi^-$	$69.20 \pm 0.05$	69.15
$\eta'$	$\pi\pi\eta(\gamma\gamma)$	$42.90 \pm 0.70$	43.40
$\eta'$	$\rho(\pi\pi)\gamma$	$29.10 \pm 0.50$	29.30
$\eta$	$\gamma\gamma$	$39.41 \pm 0.20$	39.31
$\omega$	$\pi^+\pi^-\pi^0(\gamma\gamma)$	$89.20 \pm 0.70$	89.69
$\phi$	$K^+K^-$	$48.90 \pm 0.50$	48.88



**Table 4:** Decays contributing to the  $K^+K^-\pi^0$  decay in the BESIII decay tables.

CP	BF	Decay	Model	Int. Res. BF (%)	Model	Int. Res. Decay	Final BF (%)	Normalized BF (%)
+	0.00032	$K^+K^-\pi^0$	PHSP	1.0000			0.00032	0.09697
+	0.00130	$\phi\pi^0$	SVS	0.4890	VSS	$K^-K^+$	0.00063	0.19264
+	0.00150	$K^{*-}K^+$	SVS	0.3330	VSS	$K^-\pi^0$	0.00049	0.15137
+	0.00440	$K^{*+}K^-$	SVS	0.3330	VSS	$K^+\pi^0$	0.00145	0.44401
-	0.00320	$f_0\pi^0$	PHSP	0.1089	PHSP	$K^+K^-$	0.00034	0.10574
-	0.00010	$f'_0\pi^0$	PHSP	0.0257	PHSP	$K^+K^-$	0.00000	0.00078
-	0.00056	$f_0(1500)\pi^0$	PHSP	0.0290	PHSP	$K^+K^-$	0.00002	0.00492
-	0.00034	$f_2\pi^0$	PHSP	0.0230	TSS	$K^+K^-$	0.00001	0.00237
Total		$K^+K^-\pi^0$					0.00326	
Total CP+		$K^+K^-\pi^0$						0.88615

**Table 5:** DTag Candidate Requirements.

	Requirements
Charged tracks	$\cos(\theta) < 0.93$ $V_r < 1 \text{ cm}$ $V_z < 10 \text{ cm}$
Showers	$0 < \text{Time} < 14 \cdot 50 \text{ ns}$ Barrel: Energy $> 25 \text{ MeV}$ Endcap: Energy $> 50 \text{ MeV}$ Barrel: $ \cos(\theta)  < 0.80$ EndCap: $0.84 < \cos(\theta) < 0.92$
$\pi^+$	SimplePID: $\text{Prob}(\pi) > \text{Prob}(K)$ and $\text{Prob}(\pi) > 0$
$K^\pm$	SimplePID: $\text{Prob}(K) > \text{Prob}(\pi)$ and $\text{Prob}(K) > 0$
$K_s$	$0.487 < M < 0.511 \text{ GeV}/c^2$ Vertex fit $\chi^2 < 100$ Secondary vertex $\chi^2 < 100$ Flight significance $L/\sigma > 2$
$\pi^0$	$0.115 < M < 0.150 \text{ GeV}/c^2$ $\chi^2 < 20$ Number of end-cap photons $< 2$

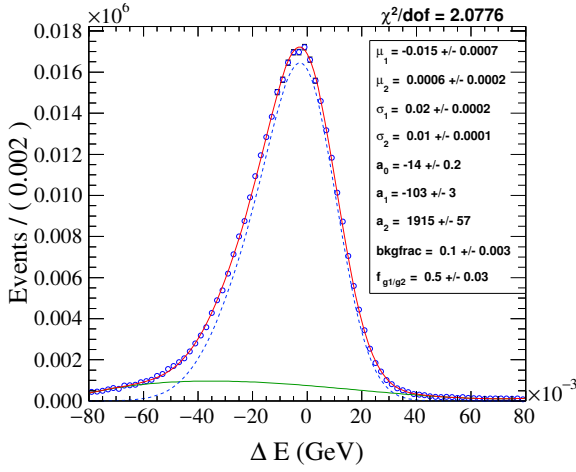
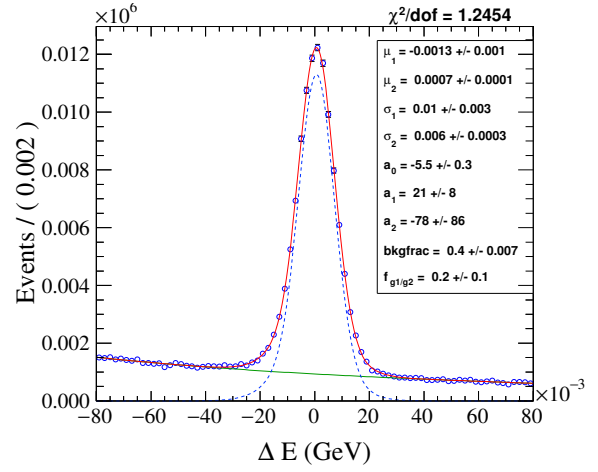
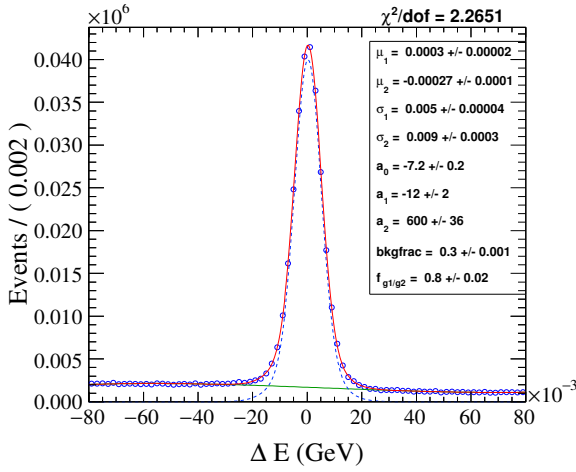
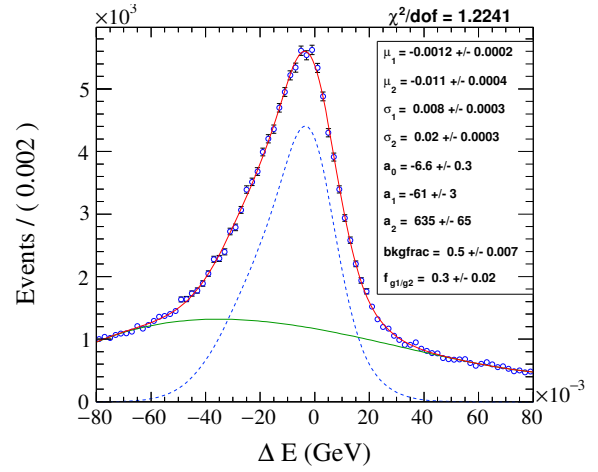
### 3.3 $\Delta E$ Distributions

In order to reduce the background in single- and double-tag candidates,  $\Delta E$  requirements are used. The quantity  $\Delta E$  is the difference between the measured energy of the  $D$  candidate and the beam energy,  $\Delta E \equiv E_D - E_{beam}$ . For a correctly reconstructed candidate, this variable should peak at zero. The requirements on the tag candidates are decided by performing a fit to the  $\Delta E$  distribution for the corresponding single-tag. The final  $\Delta E$  requirements are similar to the ones used in other analyses in BESIII. These requirements are listed in Table 6, and the results of the fits performed are shown in Figures 4-5 for the MC sample and in Figures 6-7 for the data. The fits to the  $\Delta E$  distributions are performed using the RooFit package. A double-Gaussian function is used for the signal region and a second-order polynomial for the background. These fits are only shown to give an idea of the possible ranges on the  $\Delta E$  requirements for the tag and signal modes. No direct information from the fits are used in the analysis.

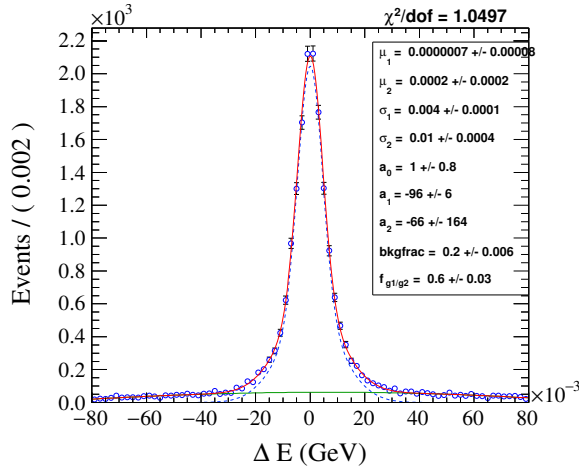
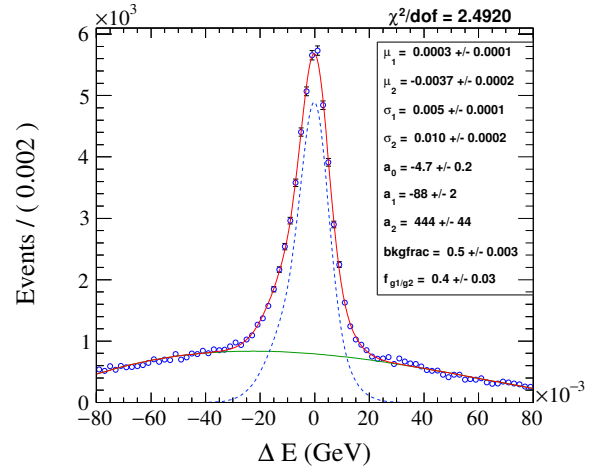
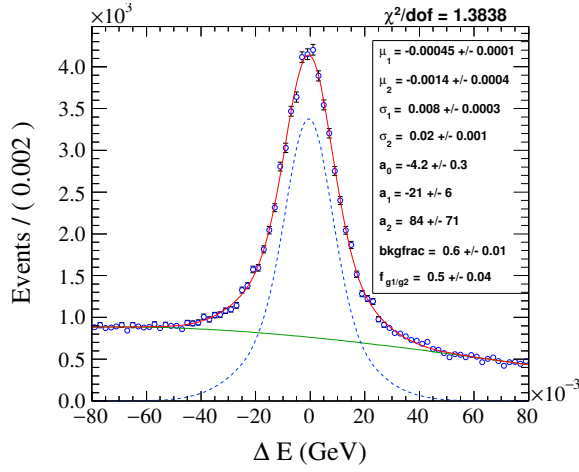
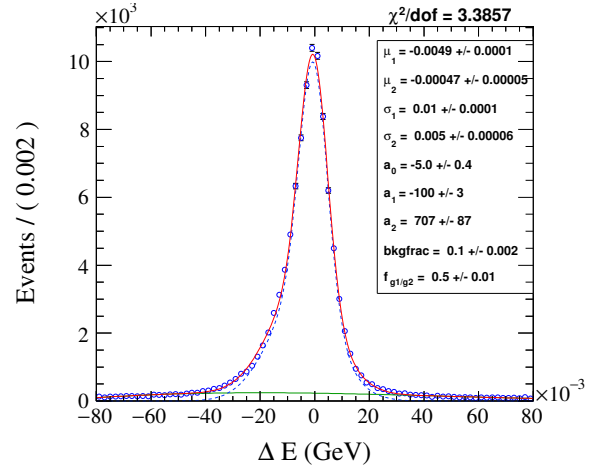
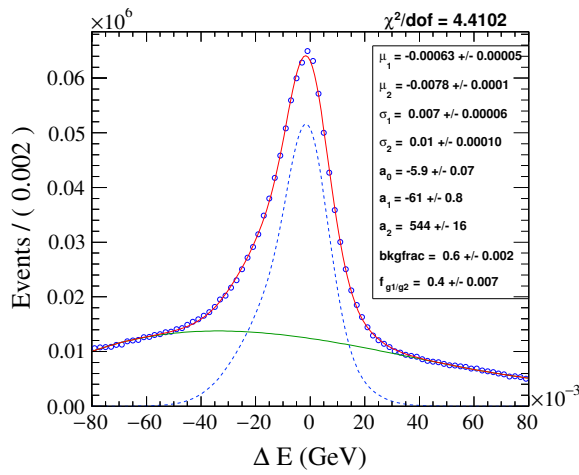
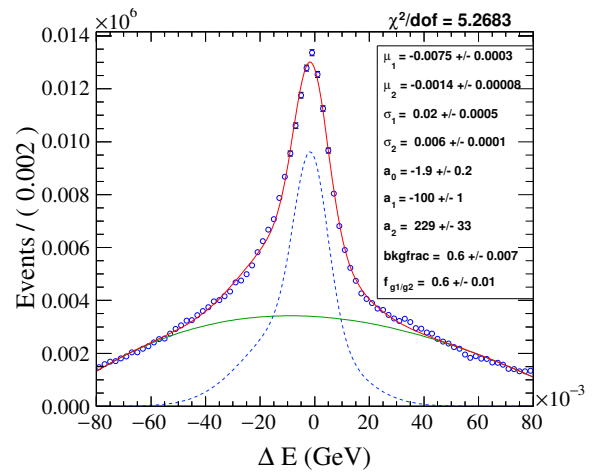
For the decay channels that have a  $\pi^0$  in the final state, the  $\Delta E$  distribution is asymmetric with a low-side tail. This is due to the energy leakage out the back of the EMC detector.

**Table 6:**  $\Delta E$  Requirements

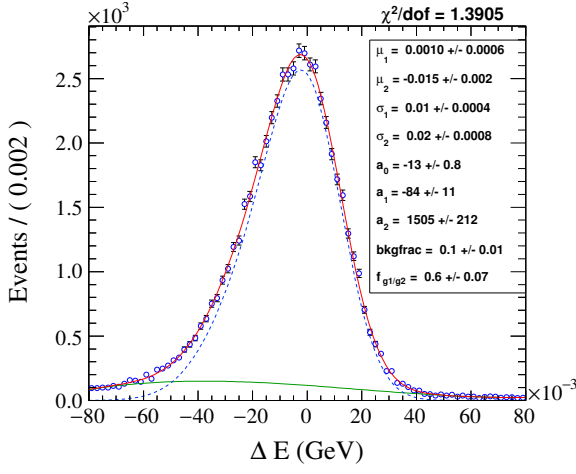
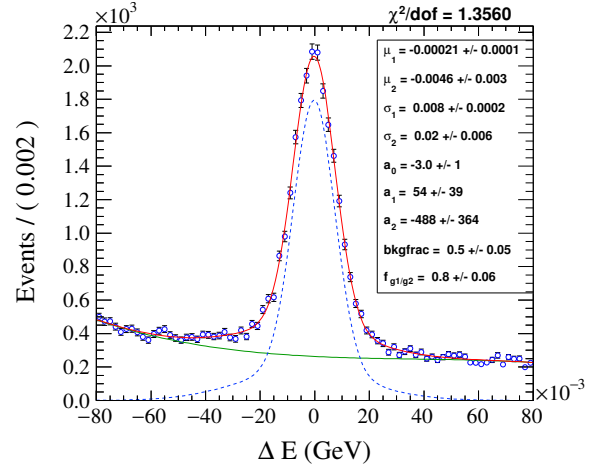
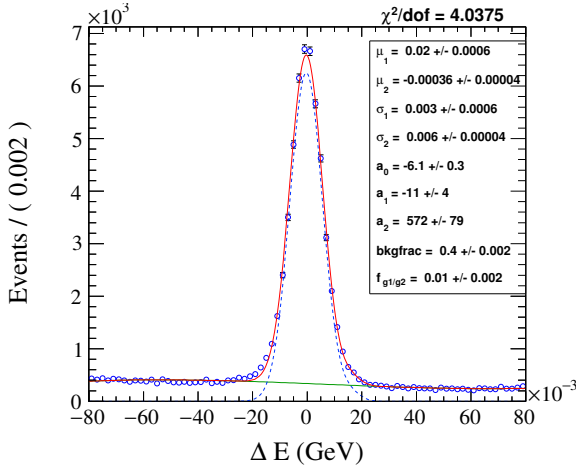
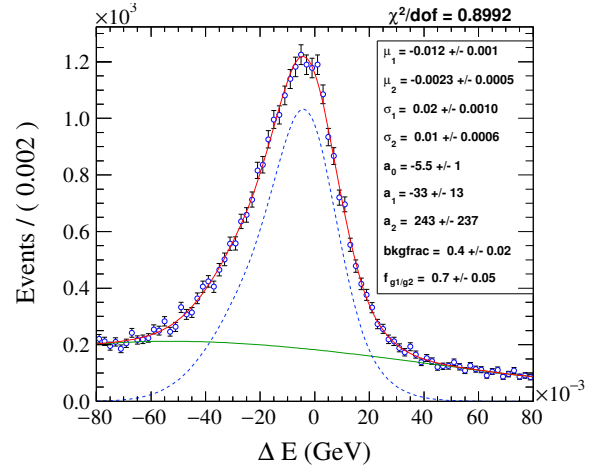
Decay	$\Delta E$ Requirement in $\text{GeV}/c^2$
$K_s \pi^0$	$-0.050 < \Delta E < 0.030$
$\pi^+ \pi^-$	$-0.020 < \Delta E < 0.020$
$K^+ K^-$	$-0.015 < \Delta E < 0.015$
$K_s \pi^0 \pi^0$	$-0.040 < \Delta E < 0.020$
$K_s \eta'(\pi^+ \pi^- \eta)$	$-0.015 < \Delta E < 0.015$
$K_s \eta'(\rho \gamma)$	$-0.030 < \Delta E < 0.020$
$K_s \eta$	$-0.030 < \Delta E < 0.040$
$K_s \omega$	$-0.030 < \Delta E < 0.020$
$\pi^+ \pi^- \pi^0$	$-0.040 < \Delta E < 0.020$
$K^+ K^- \pi^0$	$-0.040 < \Delta E < 0.020$

(a)  $\Delta E$  distribution of  $K_s \pi^0$ (b)  $\Delta E$  distribution of  $\pi^+ \pi^-$ (c)  $\Delta E$  distribution of  $K^+ K^-$ (d)  $\Delta E$  distribution of  $K_s \pi^0 \pi^0$ 

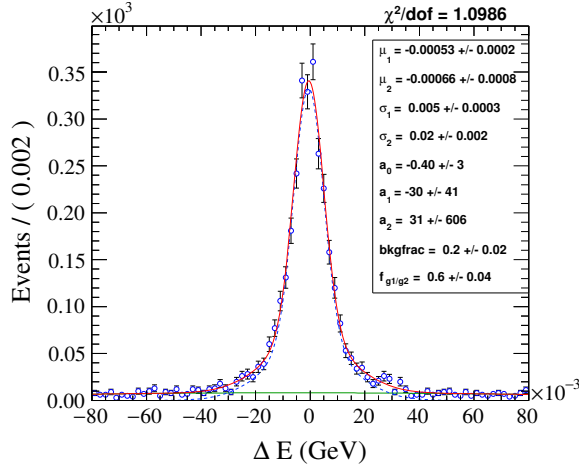
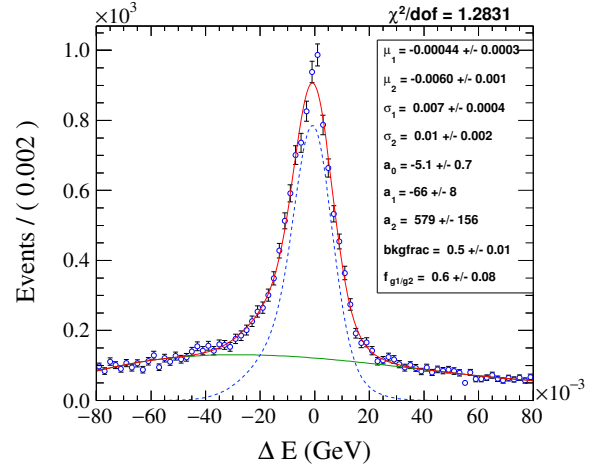
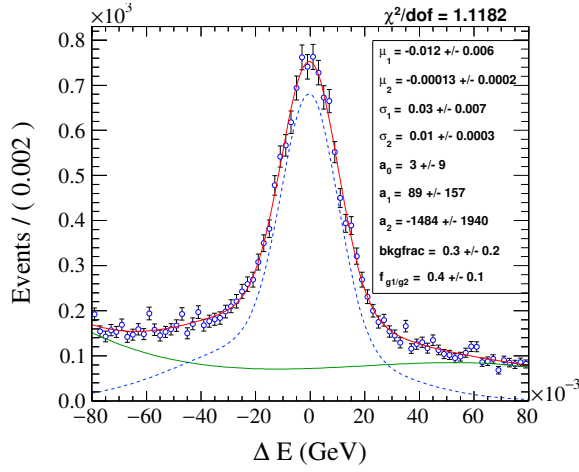
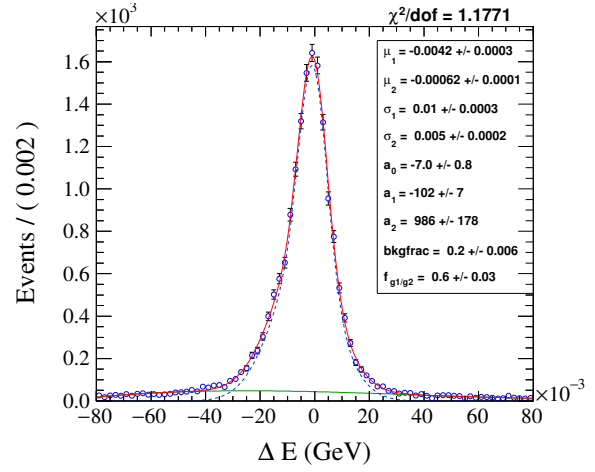
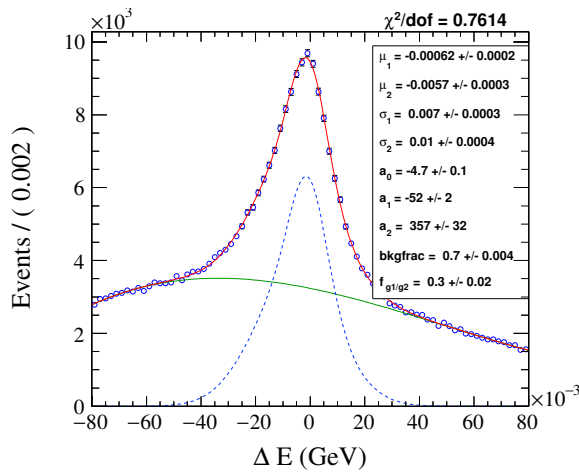
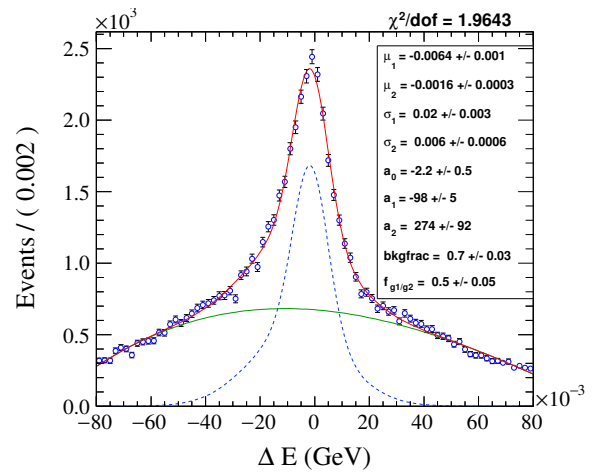
**Figure 4:**  $\Delta E$  distributions of the tag modes for the MC simulation. Blue dashed line is used for the signal shape, green for the background, and red for the whole fit.

(a)  $\Delta E$  distribution of  $K_s \eta' (\pi^+ \pi^- \eta)$ (b)  $\Delta E$  distribution of  $K_s \eta' (\rho^0 \gamma)$ (c)  $\Delta E$  distribution of  $K_s \eta$ (d)  $\Delta E$  distribution of  $K_s \omega$ (e)  $\Delta E$  distribution of  $\pi^+ \pi^- \pi^0$ (f)  $\Delta E$  distribution of  $K^+ K^- \pi^0$ 

**Figure 5:**  $\Delta E$  distributions of the tag and the signal modes for the MC simulation. Blue dashed line is used for the signal shape, green for the background, and red for the whole fit.

(a)  $\Delta E$  distribution of  $K_s \pi^0$ (b)  $\Delta E$  distribution of  $\pi^+ \pi^-$ (c)  $\Delta E$  distribution of  $K^+ K^-$ (d)  $\Delta E$  distribution of  $K_s \pi^0 \pi^0$ 

**Figure 6:**  $\Delta E$  distribution of the tag modes for the data. Blue dashed line is used for the signal shape, green for the background, and red for the whole fit.

(a)  $\Delta E$  distribution of  $K_s \eta' (\pi^+ \pi^- \eta)$ (b)  $\Delta E$  distribution of  $K_s \eta' (\rho^0 \gamma)$ (c)  $\Delta E$  distribution of  $K_s \eta$ (d)  $\Delta E$  distribution of  $K_s \omega$ (e)  $\Delta E$  distribution of  $\pi^+ \pi^- \pi^0$ (f)  $\Delta E$  distribution of  $K^+ K^- \pi^0$ 

**Figure 7:**  $\Delta E$  distribution of the tag and the signal modes for the data. Blue dashed line is used for the signal shape, green for the background, and red for the whole fit.

### 3.4 $K_s$ Selection

Six of the eight  $CP$  tag modes involve a  $K_s$  in this analysis. The  $K_s$  candidates are reconstructed using two oppositely charged tracks which are required to have a point of closest approach to the interaction point less than 20 cm along the  $z$ -axis and an azimuthal angle satisfying  $|\cos(\theta)| < 0.93$ . The vertex fit must have a  $\chi^2$  less than 100. No particle identification is used for the tracks in our  $K_s$  selection.

A secondary vertex fit is also performed on the  $K_s$  candidates which needs to satisfy a  $\chi^2$  requirement of 100, and the flight significance must be larger than 2. The mass of the  $K_s$  candidates is calculated using the four-momentum of the charged tracks, correcting the directions of the two momenta to correspond to the  $\pi^+\pi^-$  vertex. A mass window  $0.487 < M_{K_s} < 0.511 \text{ GeV}/c^2$  is used for the  $K_s$  selection. The  $K_s$  variables for the  $CP$  tags are shown in Figures 8-10.

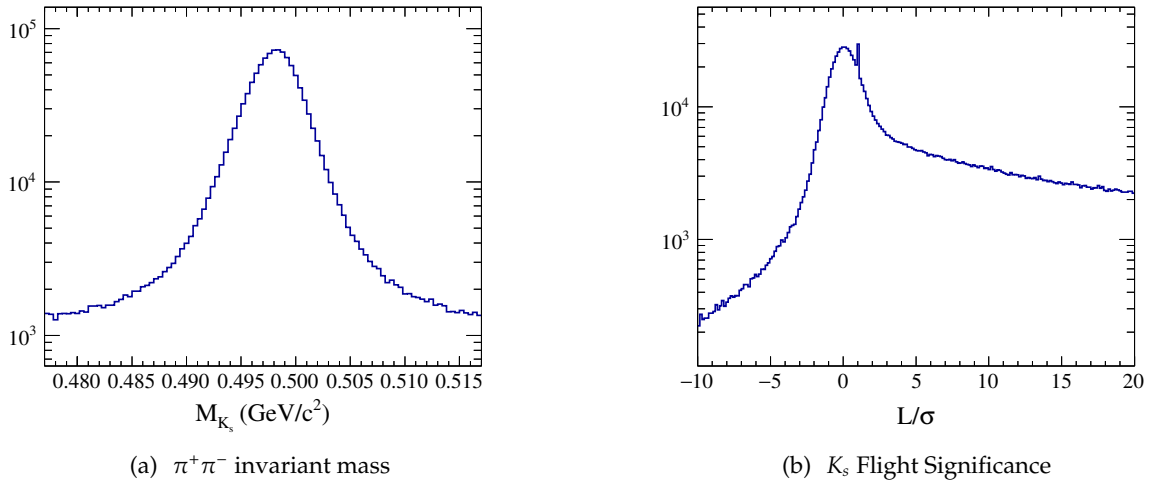


**Figure 8:** The  $K_s$  variables for the  $CP$  tags, mass and flight significance,  $L/\sigma$  from the MC sample.

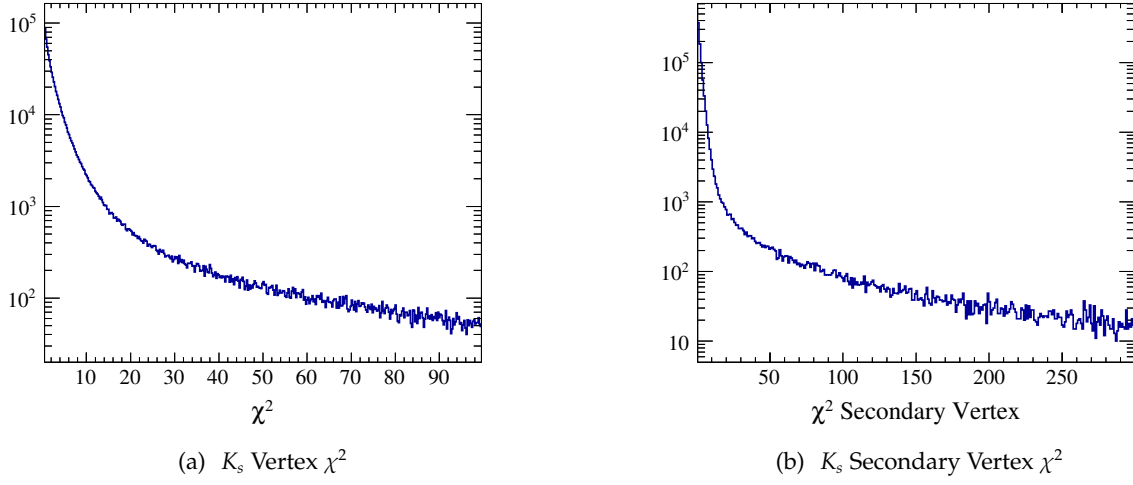


*Figure 9: Tag side  $K_s$  variables, vertex  $\chi^2$  of the MC sample.*

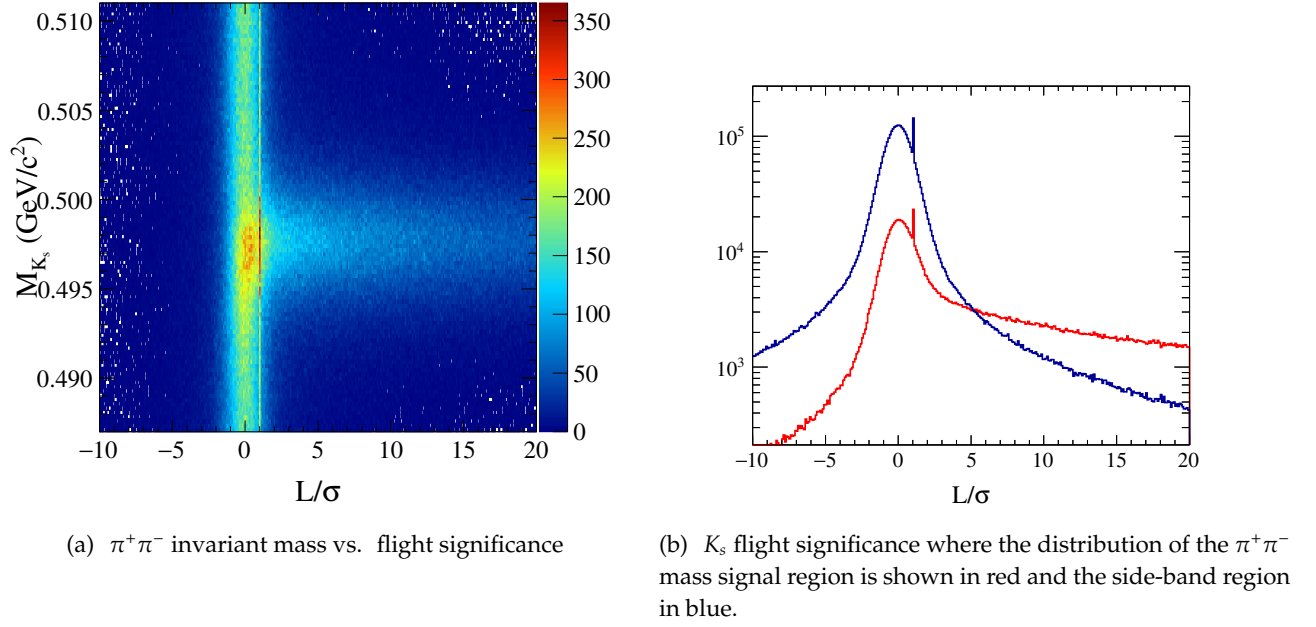


*Figure 10: The  $K_s$  variables for the CP tags from the MC sample*

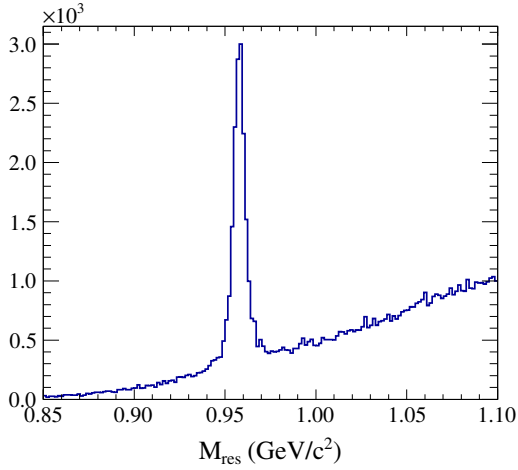


### 3.5 Intermediate Resonances in the Tag Modes

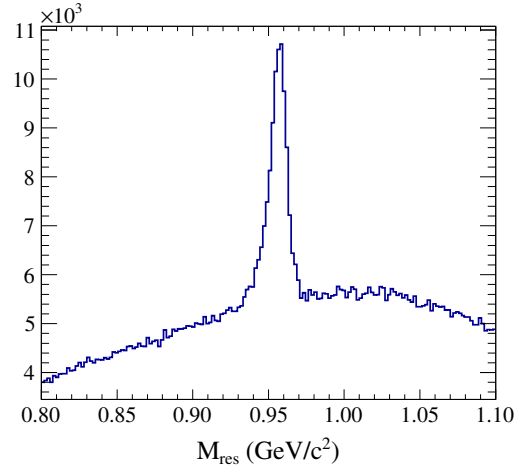
Four of the eight  $CP$  eigenstates used in the analysis involve an intermediate resonance. Therefore, additional requirements are used to reduce the background, due to possible non-resonant decays. The  $\pi^0$  and  $\eta \rightarrow \gamma\gamma$  reconstruction involves a 1C kinematic fit to the resonance mass, where the mass is constrained to be the PDG mass. These requirements are mostly on the value of the reconstructed invariant mass. They are listed in Table 7 and the corresponding distributions are shown in Figures 11 and 12.

**Table 7:** Requirements for resonances.

	Requirements
$\eta'(\pi^+\pi^-\eta)$	$0.938 < M < 0.978 \text{ GeV}/c^2$
$\eta'(\rho\gamma)$	$0.938 < M < 0.978 \text{ GeV}/c^2$
$\eta(\gamma\gamma)$	$0.400 < M < 0.700 \text{ GeV}/c^2$ Number of end-cap photons $< 2$ $\chi^2 < 20$
$\omega(\pi^+\pi^-\pi^0)$	$0.760 < M < 0.805 \text{ GeV}/c^2$



(a)  $\eta'(\pi^+\pi^-\eta)$  mass distribution



(b)  $\eta'(\rho\gamma)$  mass distribution

**Figure 11:** Reconstructed intermediate  $\eta'$  resonance masses for  $\pi^+\pi^-\eta$  and  $\rho\gamma$  decays from the MC sample of the  $CP$  tag mode candidates.

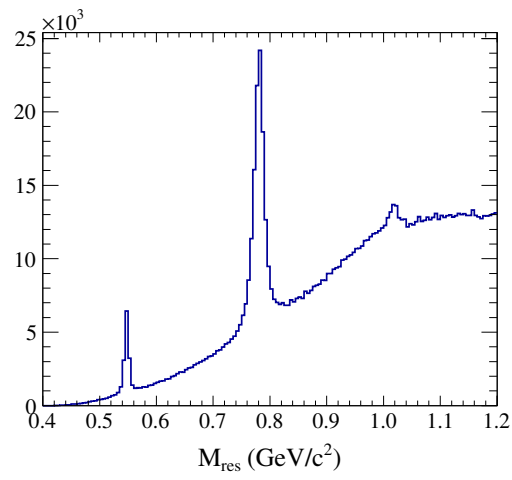


**Figure 12:** The reconstructed  $\omega(\pi^+\pi^-\pi^0)$  invariant mass distribution for the MC sample of the CP tag mode candidates.

## 4 Single Tags

Single-tag yields are required for the  $CP$  fraction measurement. In this section we will explain how the single-tag yields are calculated for the  $CP$  tags.

Tag candidates are reconstructed using the kinematic variable called the beam-constrained mass,  $M_{BC} \equiv \sqrt{E_{beam}^2 - p_D^2}$ , where  $p_D$  is the measured  $D$ -candidate momentum and  $E_{beam}$  is the known beam energy. For a correctly reconstructed event, the variable should peak at the nominal  $D^0$  mass. A maximum-likelihood fit is performed to the  $M_{BC}$  distributions for the tag modes using RooFit. A Crystal Ball function [23], together with a Gaussian, is used to model the signal. An ARGUS function [24] is used to describe the background. Starting values for the signal and background distributions used in the yield fits are initialized using the histogram that is to be fit. Then these initial values of the fit function parameters are scaled with a random value between 0.5 and 1.5 to remove the dependency on the starting values of the fit. The fit, with randomly scaled initial values, is performed a hundred times. The successful fit with a positive-definite error matrix and the best likelihood value is kept.

The function that is used to perform the fits is given below.

$$Signal_{M_{BC}} = CrystalBall(\mu_1, \sigma_1, n, \alpha) * f_{CB/G} + Gaus(\mu_1, \sigma_2) * (1 - f_{CB/G}), \quad (4)$$

where  $f_{CB/G}$  is between 0 and 1, where  $\mu_1$  and  $\sigma_2$  is the mean and the standard deviation of the Gaussian function. The  $n$  and  $\sigma_1$  are parameters of the Crystal Ball function. The form of the Crystal Ball function is given below.

$$f(x; \alpha, n, \bar{x}, \sigma) = N \cdot \begin{cases} \exp\left(-\frac{(x-\bar{x})^2}{2\sigma^2}\right), & \text{for } \frac{x-\bar{x}}{\sigma} > -\alpha \\ \left(\frac{n}{|\alpha|}\right)^n \cdot \exp\left(-\frac{|\alpha|^2}{2}\right) \cdot \left(\frac{n}{|\alpha|} - |\alpha| - \frac{x-\bar{x}}{\sigma}\right)^{-n}, & \text{for } \frac{x-\bar{x}}{\sigma} \leq -\alpha \end{cases} \quad (5)$$

The parameter  $\alpha$  defines the transition between the Gaussian and the power-law functions.

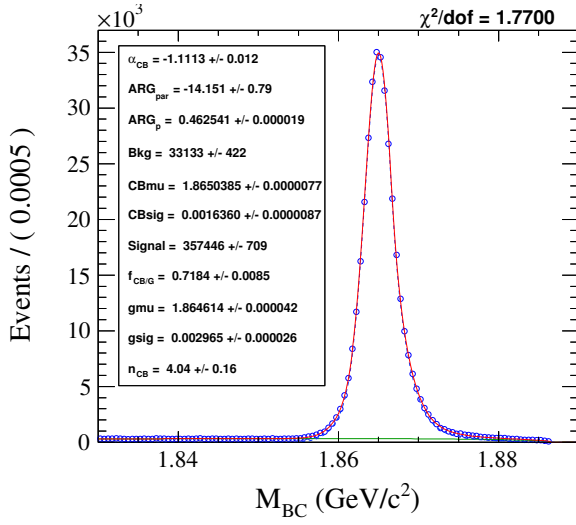
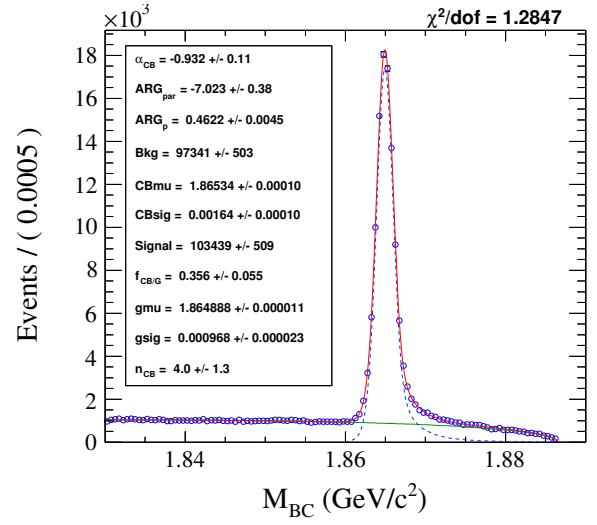
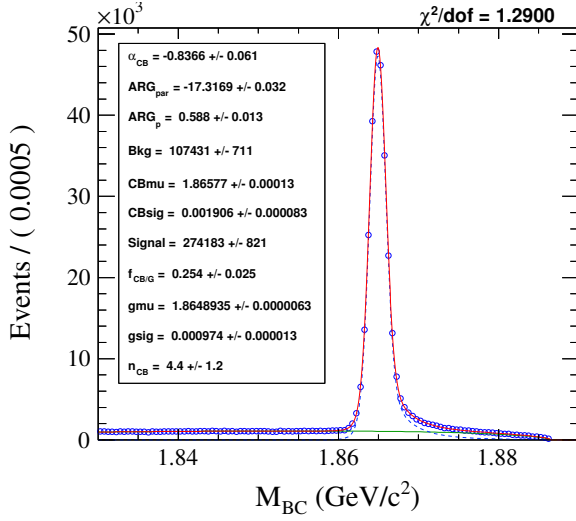
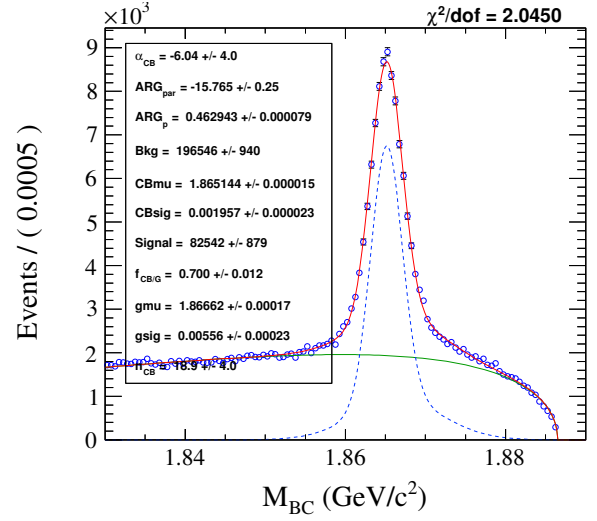
The MC sample is fit to measure the reconstruction efficiency of the single-tag candidates. Plots of these yield fits are given in Figures 13-14. For the data sample yields fits, the parameters that describe the signal shape from the MC fit signal shape are used as input. The MC fit parameters are saved, and for the data fit these parameters are used to describe the signal shape. There is no restriction on the background shape of the data, and the ARGUS background shape is allowed to float. For some of the tag modes, a Gaussian function is used to smear the signal shape to account for the data/MC resolution difference. These yield fits are shown in Figures 15-16. Yield fits to half of the MC sample used as the “fake data” sample used for testing the analysis code, are given in Figures 17-18.

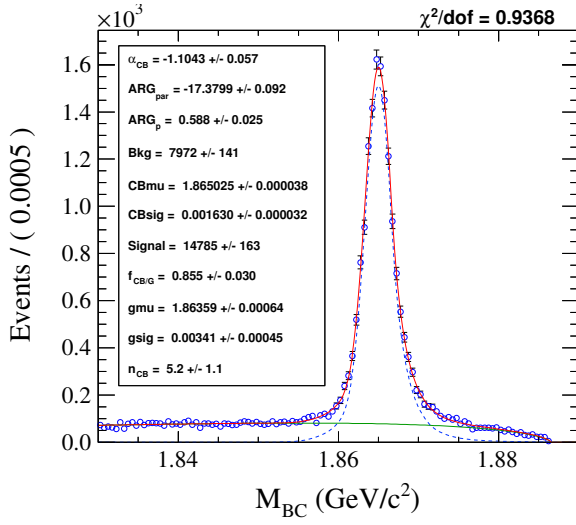
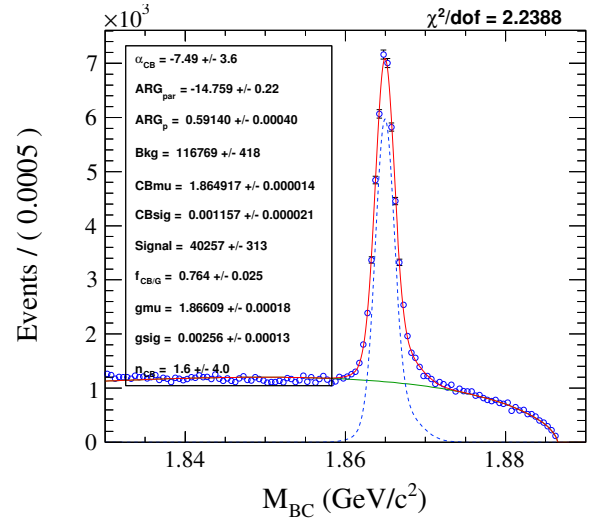
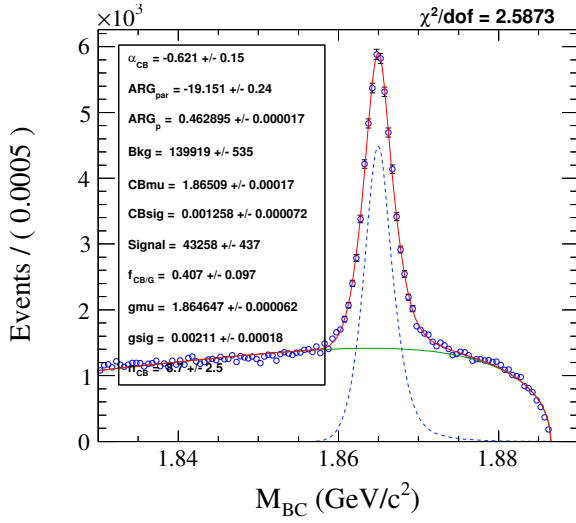
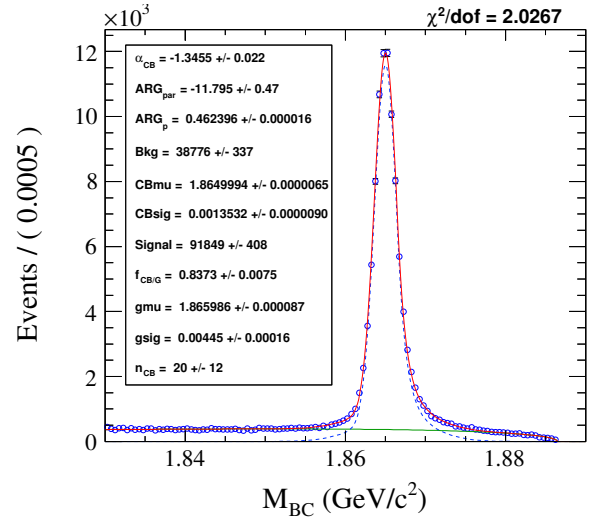
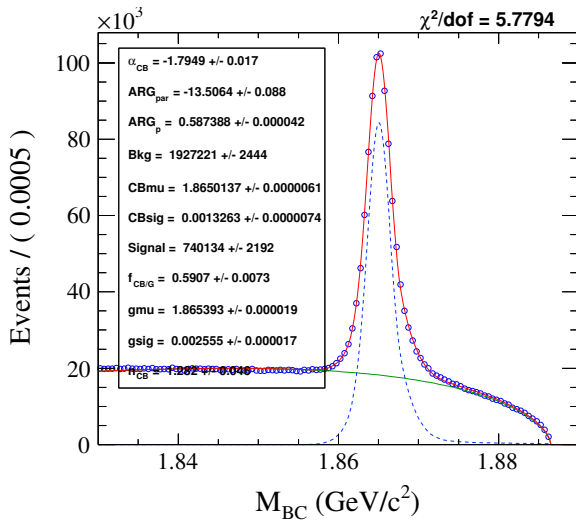
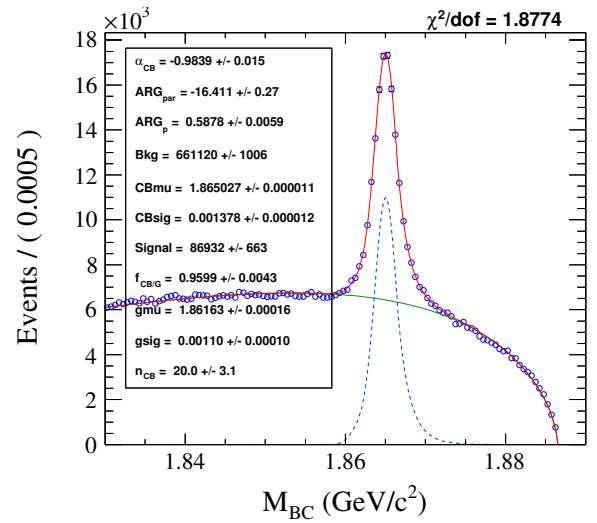
Yields of  $K_s \eta'(\rho\gamma)$  and  $K_s \omega$  for the MC and the data sample include a side-band subtraction which is discussed in Section 4.1.

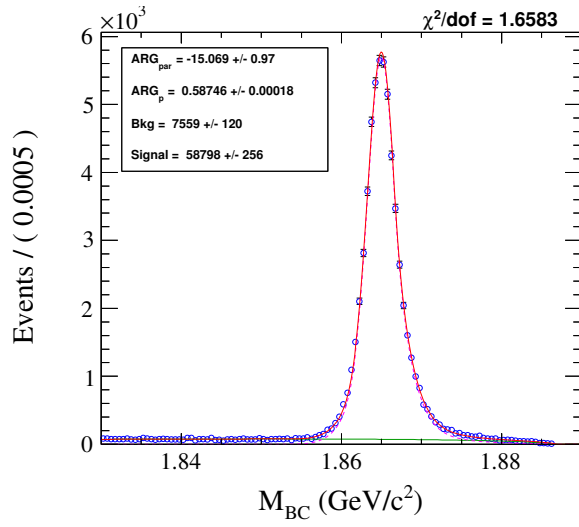
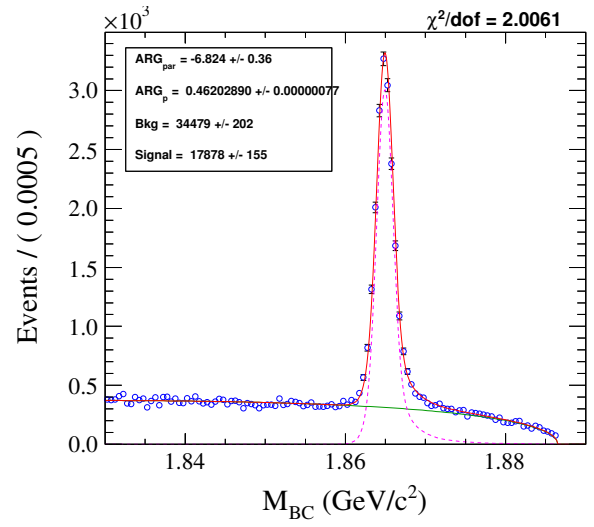
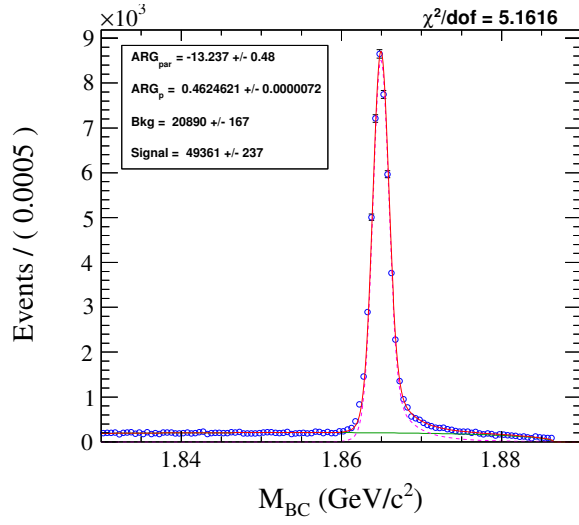
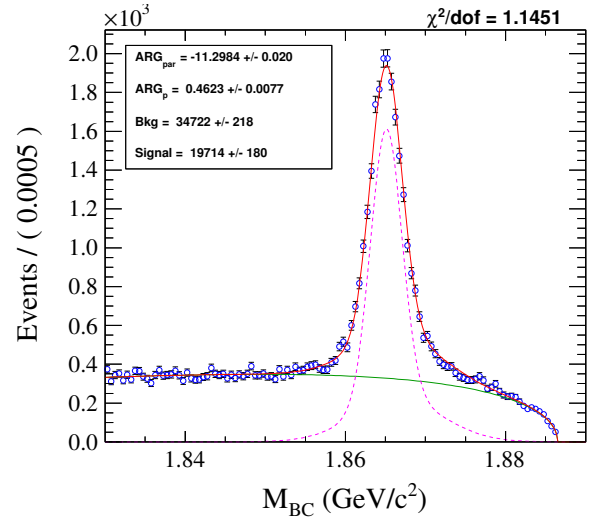
In the yield plots, we also include fits to the ST candidates for the  $\pi^+ \pi^- \pi^0$  and  $K^+ K^- \pi^0$  final states. These plots are just for illustration of the signal modes and yields are not used in the analysis. Yield fits for the  $\pi^+ \pi^- \pi^0$  mode is given in Figures 14(e), 16(e), 18(e) for the efficiency, data, and fake data sample, respectively. Similarly,  $K^+ K^- \pi^0$  mode yield fits are shown in Figures 14(f), 16(f), 18(f) again for efficiency, data, and fake data sample, respectively.

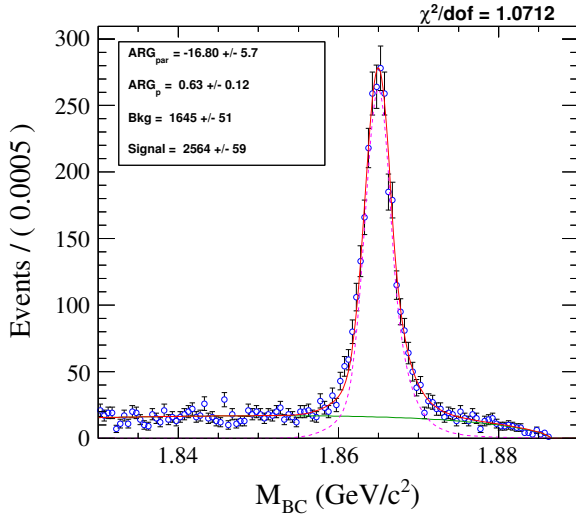
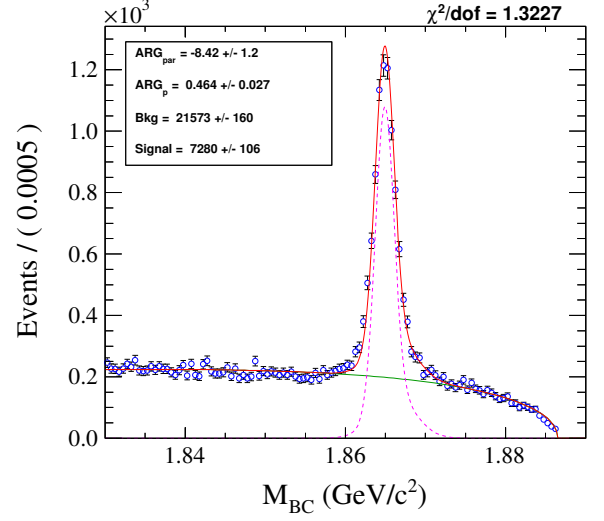
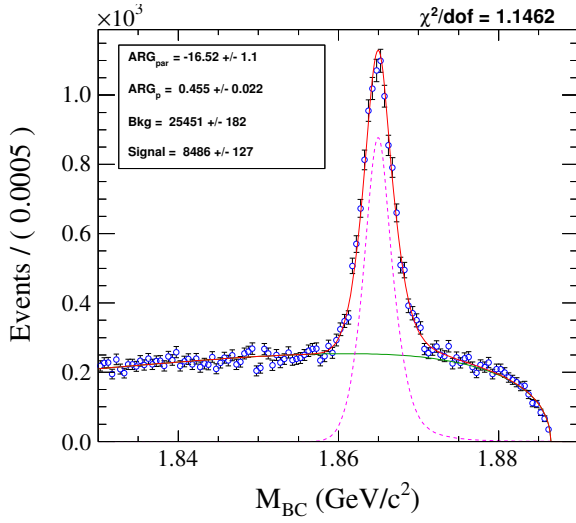
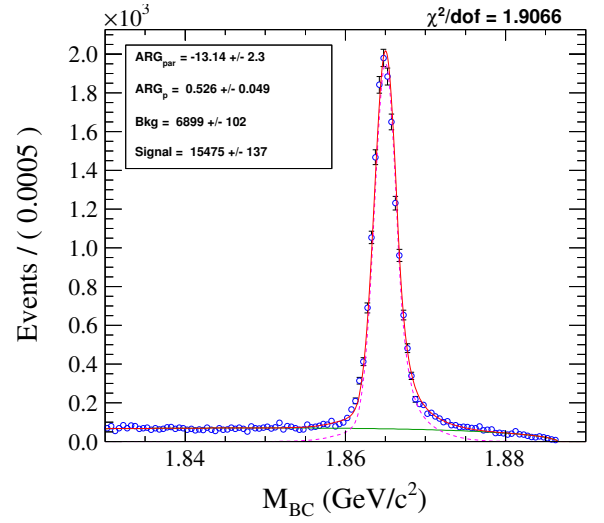
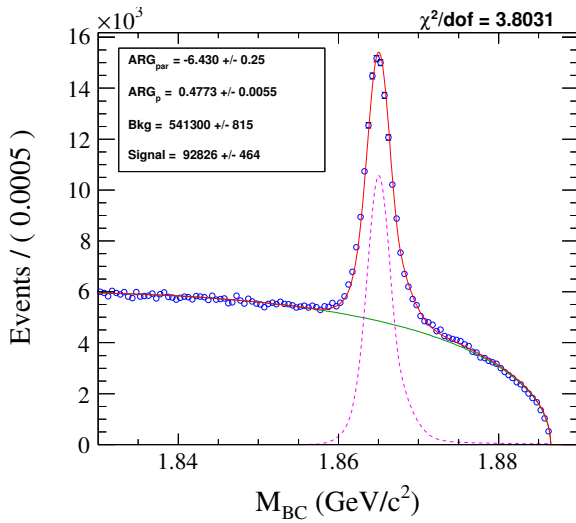
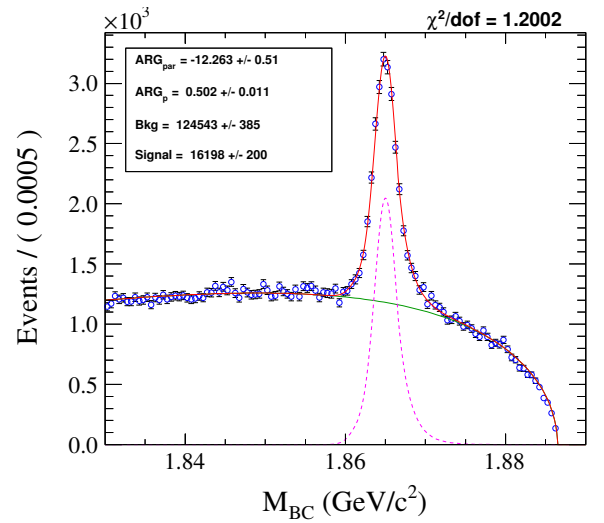
*Table 8: Single Tag Yields.*

Decay Channel	Data Yields	Efficiency MC Sample Yield	Fake Data Sample
$K_s\pi^0$	$(5.880 \pm 0.026) \times 10^4$	$(3.574 \pm 0.007) \times 10^5$	$(3.579 \pm 0.007) \times 10^5$
$\pi^+\pi^-$	$(1.788 \pm 0.016) \times 10^4$	$(1.034 \pm 0.005) \times 10^5$	$(1.034 \pm 0.005) \times 10^5$
$K^+K^-$	$(4.936 \pm 0.024) \times 10^4$	$(2.742 \pm 0.008) \times 10^5$	$(2.737 \pm 0.007) \times 10^5$
$K_s\pi^0\pi^0$	$(1.971 \pm 0.018) \times 10^4$	$(8.25 \pm 0.09) \times 10^4$	$(8.26 \pm 0.08) \times 10^4$
$K_s\eta'(\pi^+\pi^-\eta)$	$(2.56 \pm 0.06) \times 10^3$	$(1.479 \pm 0.016) \times 10^4$	$(1.461 \pm 0.017) \times 10^4$
$K_s\eta'(\rho\gamma)$	$(7.28 \pm 0.11) \times 10^3$	$(4.026 \pm 0.031) \times 10^4$	$(4.40 \pm 0.05) \times 10^4$
$K_s\eta$	$(8.49 \pm 0.13) \times 10^3$	$(4.33 \pm 0.04) \times 10^4$	$(4.32 \pm 0.04) \times 10^4$
$K_s\omega$	$(1.547 \pm 0.014) \times 10^4$	$(9.18 \pm 0.04) \times 10^4$	$(9.29 \pm 0.04) \times 10^4$

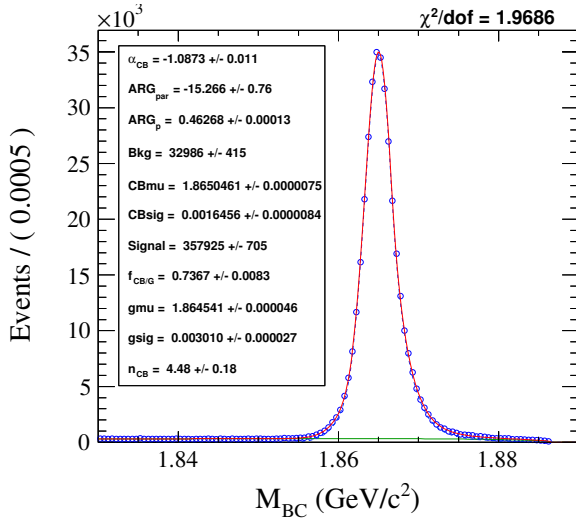
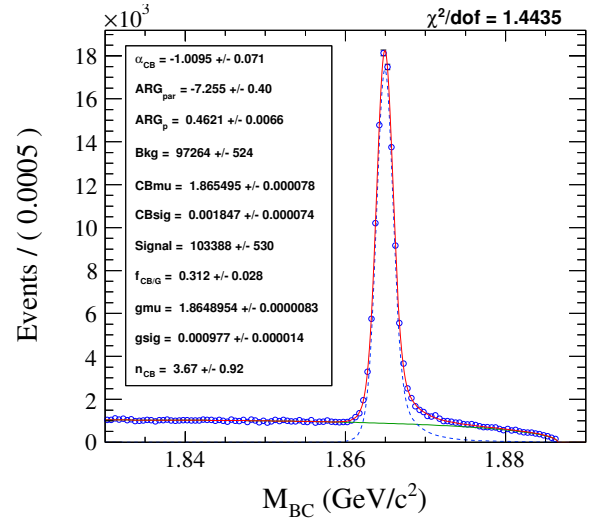
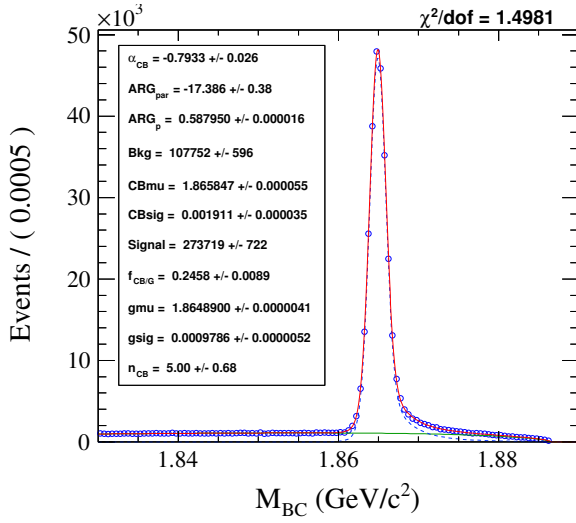
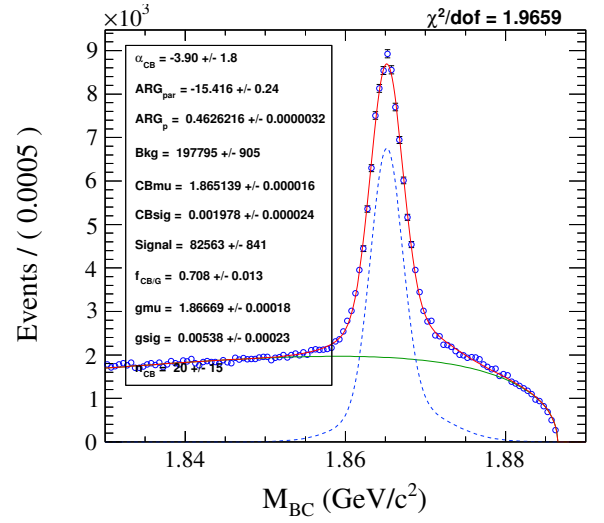
(a)  $M_{BC}$  distribution of  $K_s\pi^0$ (b)  $M_{BC}$  distribution of  $\pi\pi$ (c)  $M_{BC}$  distribution of  $KK$ (d)  $M_{BC}$  distribution of  $K_s\pi^0\pi^0$ **Figure 13:**  $M_{BC}$  fits to the CP tags of the MC sample.

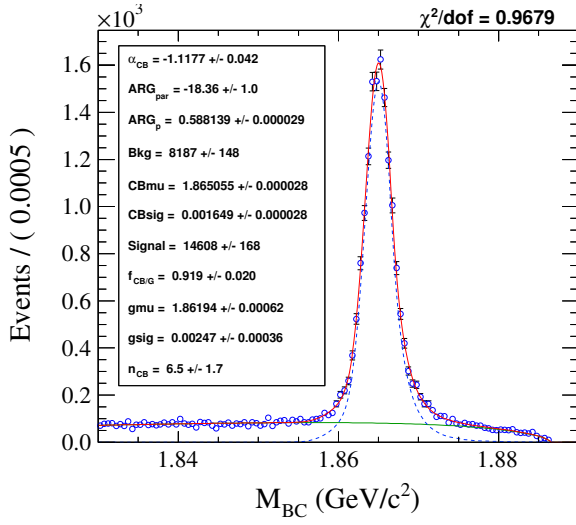
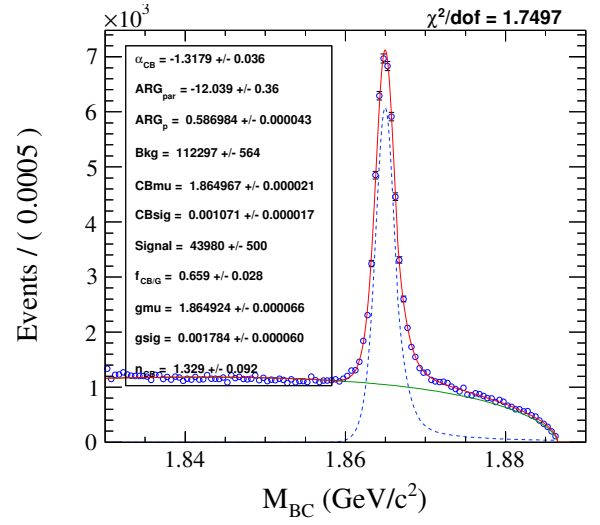
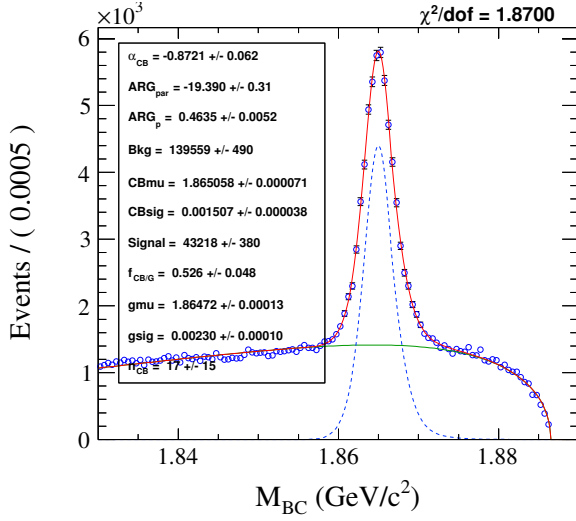
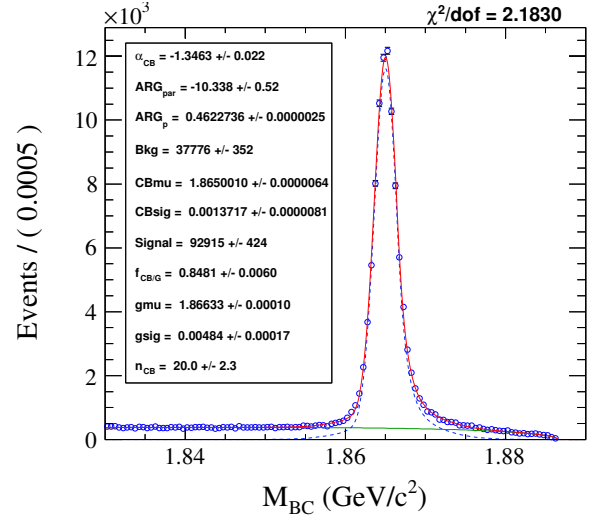
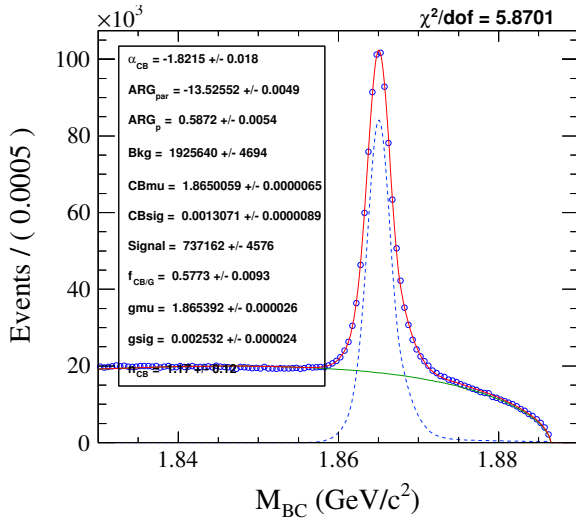
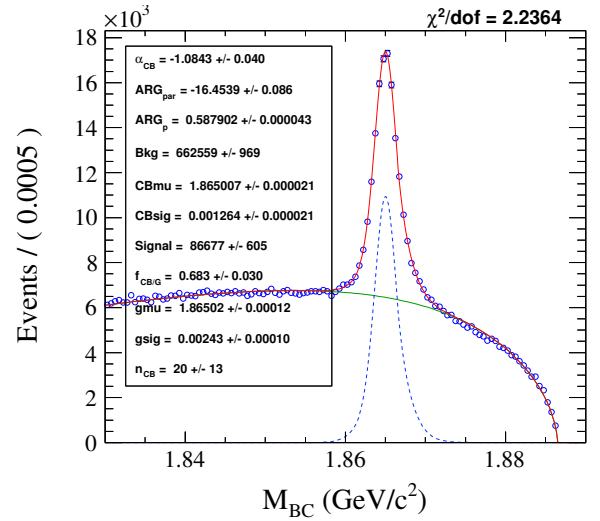
(a)  $M_{BC}$  distribution of  $K_s \eta' (\pi \pi \eta)$ (b)  $M_{BC}$  distribution of  $K_s \eta' (\rho \gamma)$ (c)  $M_{BC}$  distribution of  $K_s \eta$ (d)  $M_{BC}$  distribution of  $K_s \omega$ (e)  $M_{BC}$  distribution of  $\pi^+ \pi^- \pi^0$ (f)  $M_{BC}$  distribution of  $K^+ K^- \pi^0$ Figure 14:  $M_{BC}$  fits to the CP tags of the MC sample.

(a)  $M_{BC}$  distribution of  $K_s\pi^0$ (b)  $M_{BC}$  distribution of  $\pi\pi$ (c)  $M_{BC}$  distribution of  $KK$ (d)  $M_{BC}$  distribution of  $K_s\pi^0\pi^0$ **Figure 15:**  $M_{BC}$  fits to the CP tags of the data sample.

(a)  $M_{BC}$  distribution of  $K_s\eta'(\pi\pi\eta)$ (b)  $M_{BC}$  distribution of  $K_s\eta'(\rho\gamma)$ (c)  $M_{BC}$  distribution of  $K_s\eta$ (d)  $M_{BC}$  distribution of  $K_s\omega$ (e)  $M_{BC}$  distribution of  $\pi^+\pi^-\pi^0$ (f)  $M_{BC}$  distribution of  $K^+K^-\pi^0$ Figure 16:  $M_{BC}$  fits to the CP tags of the data sample.



(a)  $M_{BC}$  distribution of  $K_s\pi^0$ (b)  $M_{BC}$  distribution of  $\pi\pi$ (c)  $M_{BC}$  distribution of  $KK$ (d)  $M_{BC}$  distribution of  $K_s\pi^0\pi^0$ **Figure 17:**  $M_{BC}$  fits to the CP tags of the MC fake data sample.

(a)  $M_{BC}$  distribution of  $K_s\eta'(\pi\pi\eta)$ (b)  $M_{BC}$  distribution of  $K_s\eta'(\rho\gamma)$ (c)  $M_{BC}$  distribution of  $K_s\eta$ (d)  $M_{BC}$  distribution of  $K_s\omega$ (e)  $M_{BC}$  distribution of  $\pi^+\pi^-\pi^0$ (f)  $M_{BC}$  distribution of  $K^+K^-\pi^0$ **Figure 18:**  $M_{BC}$  fits to the CP tags of the MC fake data sample.

### 4.1 Mass Sideband Subtraction

Background levels of the tag modes  $K_s\eta'(\rho\gamma)$  and  $K_s\omega$  are larger due to the non-resonant decay contributions to the final states. We subtract this type of background by performing a mass-sideband subtraction for the intermediate resonances  $\eta'$  and  $\omega$  for  $K_s\eta'(\rho\gamma)$  and  $K_s\omega$ , respectively.

Three  $M_{BC}$  distributions are prepared, corresponding to three regions in the resonance mass distribution; low-sideband, high-sideband, and signal region. These  $M_{BC}$  distributions are then fit to calculate the yield using the same method explained earlier in this section. A separate fit is performed on the resonance mass distribution to measure the background fraction (areas) in these three regions. A fourth-order polynomial is used for the background, and MC truth shape convolved with a Gaussian is used for the signal. Background areas, together with the  $M_{BC}$  yields, are then used to calculate the amount that is going to be subtracted. The formula used for this calculation, which assumes a linear variation of the fraction of non-resonant peaking background, is given below.

$$\frac{Y_0}{A_0} = \left( \frac{m_2 - m_0}{m_2 - m_1} \right) \frac{Y_1}{A_1} + \left( \frac{m_0 - m_1}{m_2 - m_1} \right) \frac{Y_2}{A_2}, \quad (6)$$

where  $Y_0$  and  $A_0$  are the yield and background area for the signal region;  $Y_1$  and  $A_1$  are the corresponding values for the low side; and  $Y_2$  and  $A_2$  for the high side. The  $m_i$  parameters are the central value of each mass region for the low, signal, and the high sidebands. The calculated  $Y_0$  is then subtracted from the single-tag yield of tag mode.

Individual details of the subtraction process is given in the following sections.

#### 4.1.1 Mass Sideband Subtraction for $K_s\eta'(\rho\gamma)$

The  $\eta' \rightarrow \rho\gamma$  invariant mass distribution is plotted in Figure 19 for the MC sample. The various regions are defined as  $0.850 < M_{\eta'} < 0.900 \text{ GeV}/c^2$  for the low-side,  $0.938 < M_{\eta'} < 0.978 \text{ GeV}/c^2$  for the signal region, and  $1.000 < M_{\eta'} < 1.050 \text{ GeV}/c^2$  for the high-side region.

For the MC sample, the resulting scales and yields are given in Table 9. Fits to the  $M_{BC}$  distributions of these sideband regions and the signal region are given in Figure 20 for the signal region and Figure 21 for the sidebands.

Similar information for the data sample is given in Table 10 and mass distribution is shown in Figure 22. Fits to the  $M_{BC}$  distributions of these sideband regions and the signal region is given in Figure 23 for signal region and Figure 24 for the sidebands for the data sample.

**Table 9:** Sideband subtraction numbers of  $K_s\eta'(\rho\gamma)$  for the MC sample.

	Low side	Signal region	High side
Background scale	0.156	0.143	0.183
Yield	$(9.3 \pm 1.9) \times 10^2$	$(4.026 \pm 0.031) \times 10^4$	$(2.89 \pm 0.21) \times 10^3$
Final yield		$(3.894 \pm 0.034) \times 10^4$	

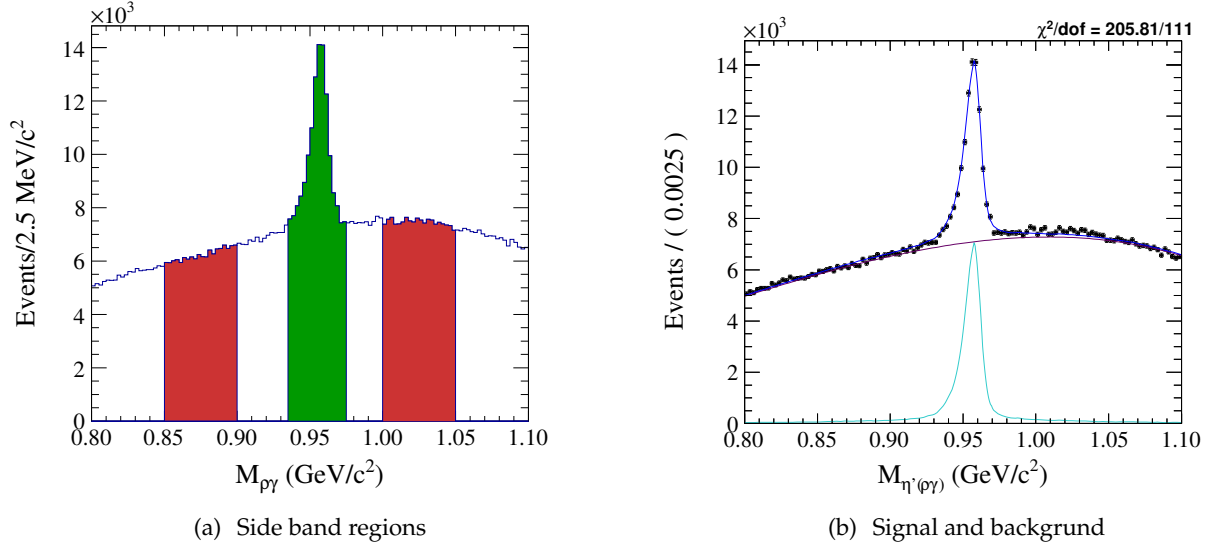


**Figure 19:** The  $\eta' \rightarrow \rho\gamma$  mass distribution for the  $K_s\eta'(\rho\gamma)$  decay using the MC sample. In the left plot, green is the signal region, red denotes the sideband regions. On the right, signal events and background are shown.

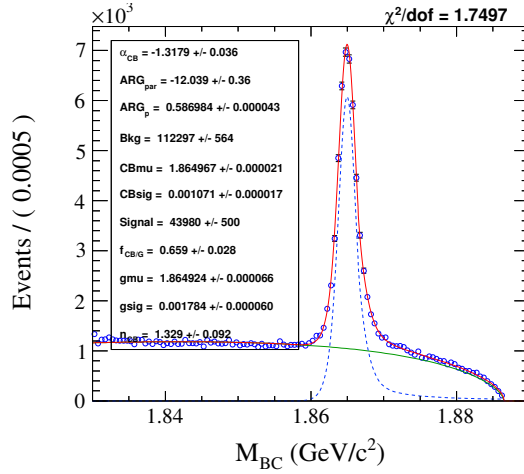


**Figure 20:** Fit to the  $M_{BC}$  distribution for the  $K_s\eta'(\rho\gamma)$  signal region of the MC sample.

**Table 10:** Sideband subtraction numbers of  $K_s\eta'(\rho\gamma)$  for the data sample.

	Low side	Signal region	High side
Background scale	0.150	0.142	0.187
Yield	$(2.3 \pm 0.5) \times 10^2$	$(7.83 \pm 0.11) \times 10^3$	$(4.9 \pm 0.8) \times 10^2$
Final yield		$(7.56 \pm 0.11) \times 10^3$	

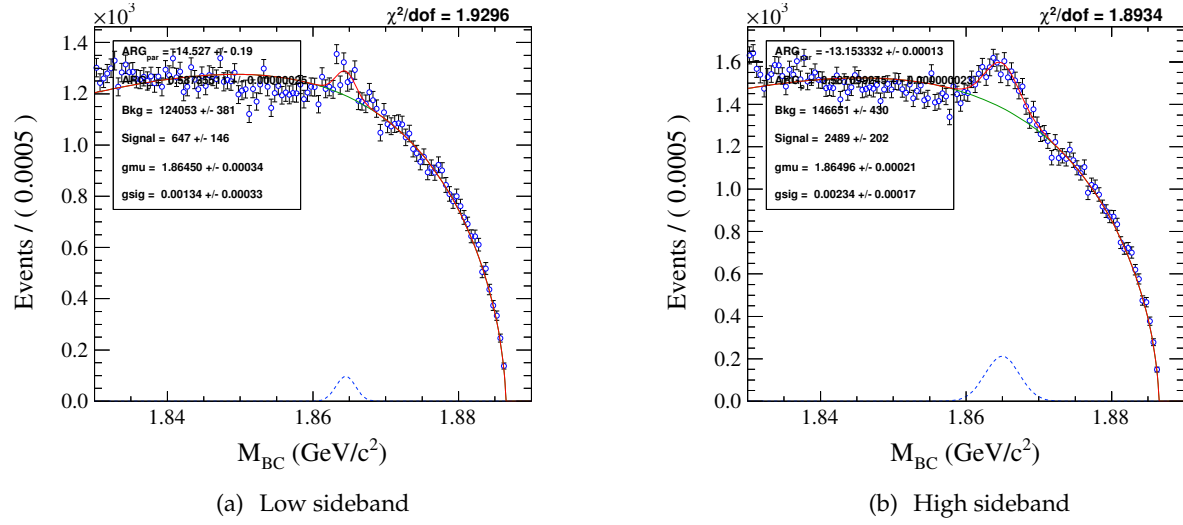


**Figure 21:** Fit to the  $M_{BC}$  distribution for the  $K_s \eta'(\rho\gamma)$  sideband regions in the  $\eta' \rightarrow \rho\gamma$  mass distribution for the MC sample.

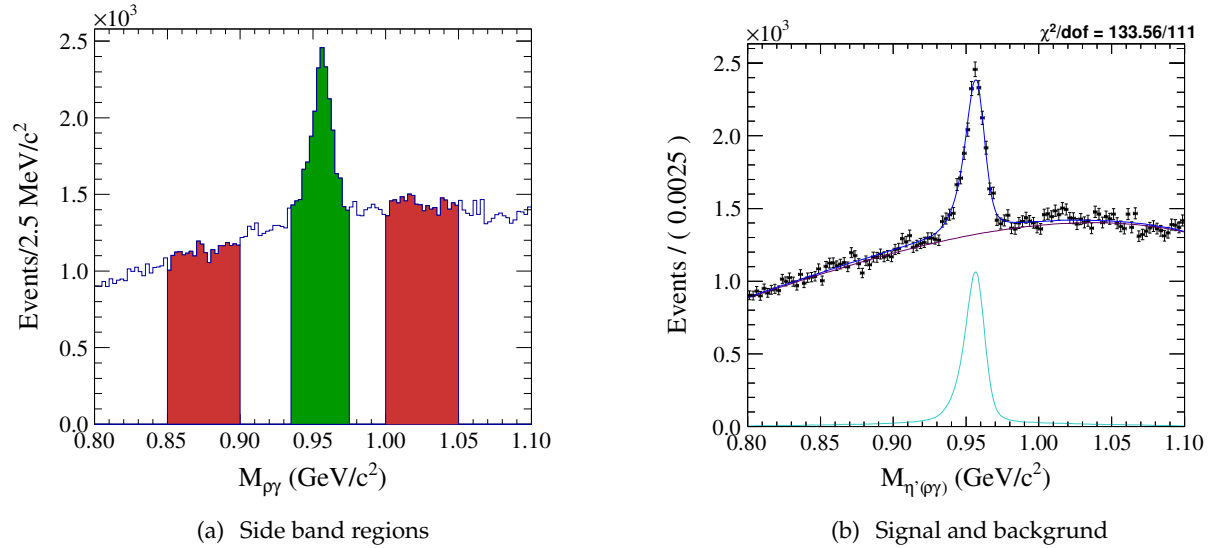


**Figure 22:** The  $\eta' \rightarrow \rho\gamma$  mass distribution for the  $K_s \eta'(\rho\gamma)$  decay using data sample. In the left plot green is the signal region, red denotes the sideband regions. On the right, signal events and background is shown for the data sample.

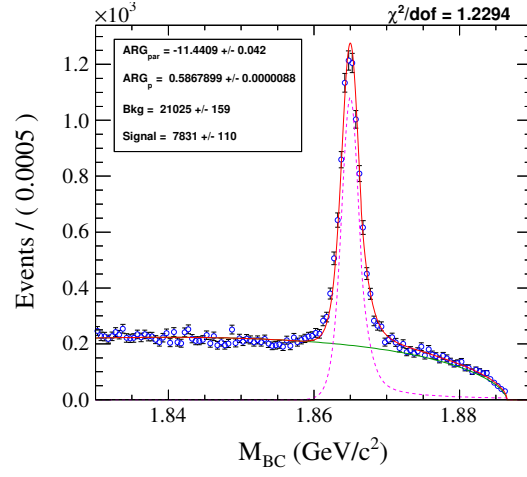
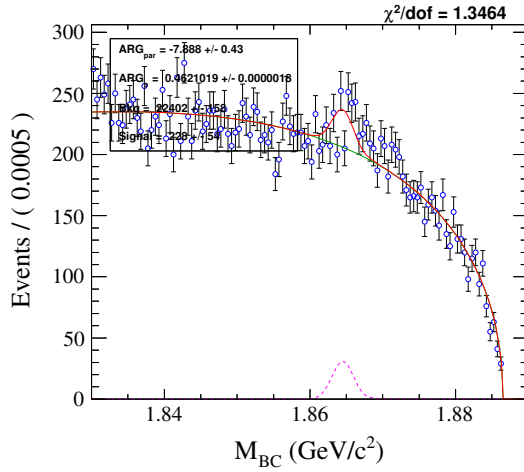
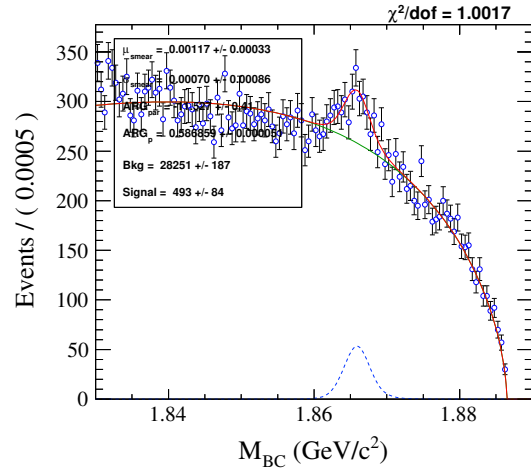


**Figure 23:** Fit to the  $M_{BC}$  distribution for the  $K_s\eta'(\rho\gamma)$  signal region in the  $\eta'$  mass distribution of the data sample.



(a) Low sideband



(b) High sideband

**Figure 24:** Fit to the  $M_{BC}$  distribution for the  $K_s\eta'(\rho\gamma)$  sideband regions in the  $\eta'$  mass distribution of the data sample.

#### 4.1.2 Mass Sideband Subtraction for $K_s\omega$

The  $\omega \rightarrow \pi^+\pi^-\pi^0$  mass distribution is plotted in Figure 25 for the MC sample. Side band regions are defined between  $0.600 < M_\omega < 0.730 \text{ GeV}/c^2$  for the low side,  $0.760 < M_\omega < 0.805 \text{ GeV}/c^2$  for the signal region, and  $0.830 < M_\omega < 0.8525 \text{ GeV}/c^2$  for the high side region.

For the MC sample resulting scales and yields are given in the Table 11. Fits to the  $M_{BC}$  distributions of these sideband regions and the signal region is given in Figure 26 for signal region and Figure 27 for the sidebands.

Similar information for the data sample is given in Table 12 and mass distribution is shown in Figure 28. Fits to the  $M_{BC}$  distributions of these sideband regions and the signal region is given in Figure 29 for signal region and Figure 30 for the sidebands for the data sample.

**Table 11:** Sideband subtraction numbers of  $K_s\omega$  for the MC sample.

	Low side	Signal region	High side
Background scale	0.179	0.123	0.082
Yield	$(1.709 \pm 0.025) \times 10^4$	$(9.18 \pm 0.04) \times 10^4$	$(9.83 \pm 0.27) \times 10^3$
Final yield		$(7.81 \pm 0.05) \times 10^4$	

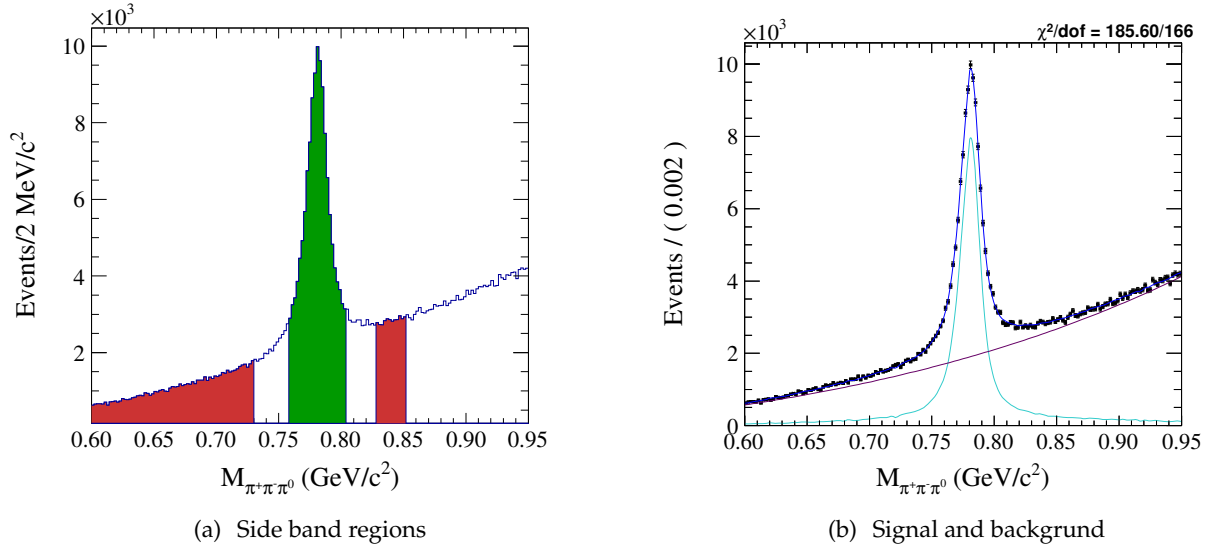


**Figure 25:** The  $\omega \rightarrow \pi^+\pi^-\pi^0$  mass distribution for the  $K_s\omega$  decay using the MC sample. In the left plot green is the signal region, red denotes the sideband regions. On the right, signal events and background is shown.

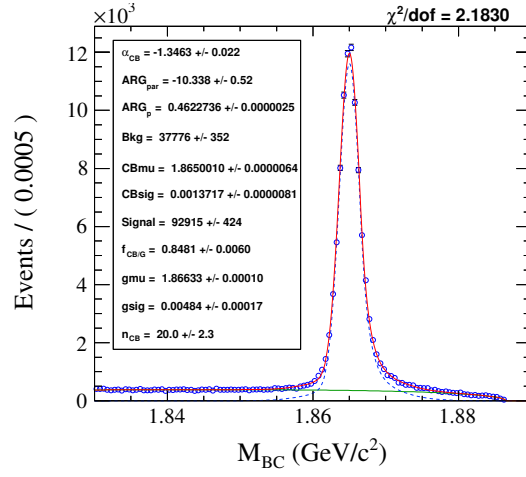


**Figure 26:** Fit to the  $M_{BC}$  distribution for the  $K_s\omega$  signal region in the  $\omega \rightarrow \pi^+\pi^-\pi^0$  mass distribution of the MC sample.

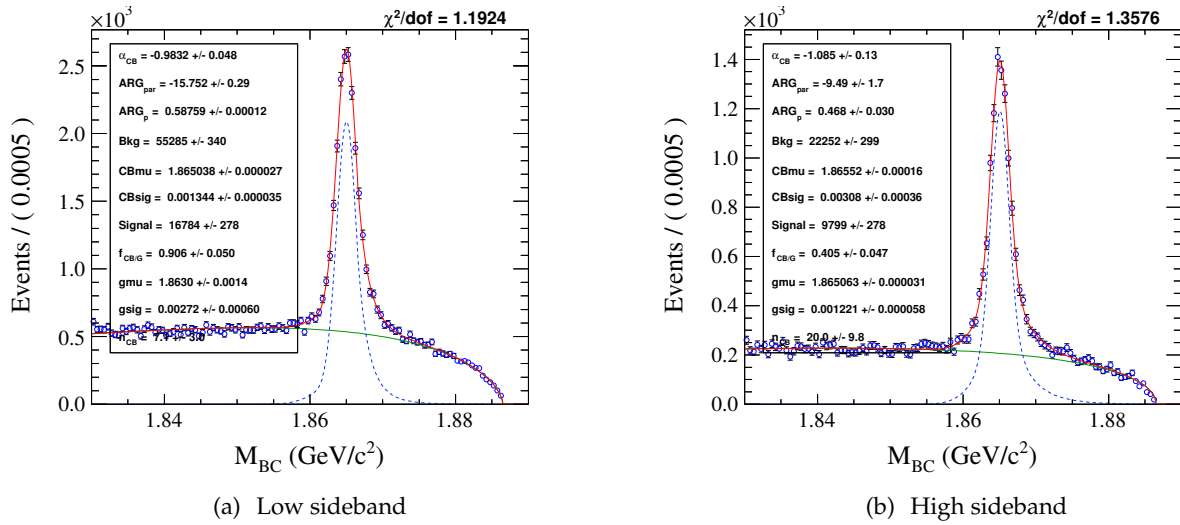


**Figure 27:** Fit to the  $M_{BC}$  distribution for the  $K_s\omega$  sideband regions in the  $\omega \rightarrow \pi^+\pi^-\pi^0$  mass distribution of the MC sample.

**Table 12:** Sideband subtraction numbers of  $K_s\omega$  for the data sample.

	Low side	Signal region	High side
Background scale	0.159	0.121	0.085
Yield	$(1.07 \pm 0.05) \times 10^3$	$(1.552 \pm 0.013) \times 10^4$	$(1.20 \pm 0.05) \times 10^3$
Final yield		$(1.409 \pm 0.015) \times 10^4$	



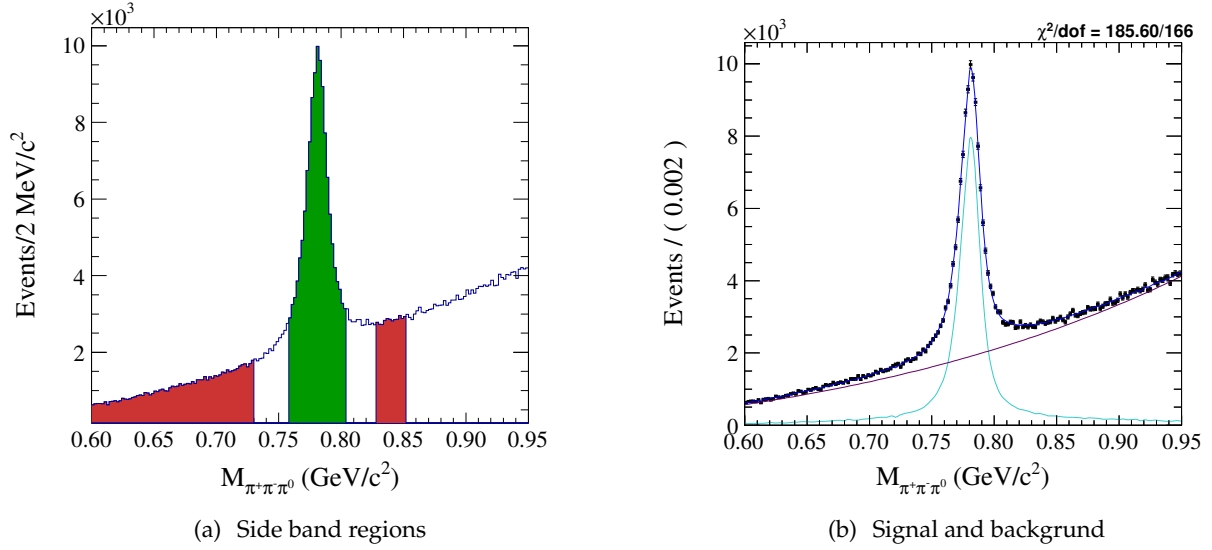


**Figure 28:** The  $\omega \rightarrow \pi^+\pi^-\pi^0$  mass distribution for the  $K_s\omega$  decay using the data sample. In the left plot green is the signal region, red denotes the sideband regions. On the right, signal events and background is shown for the data sample.

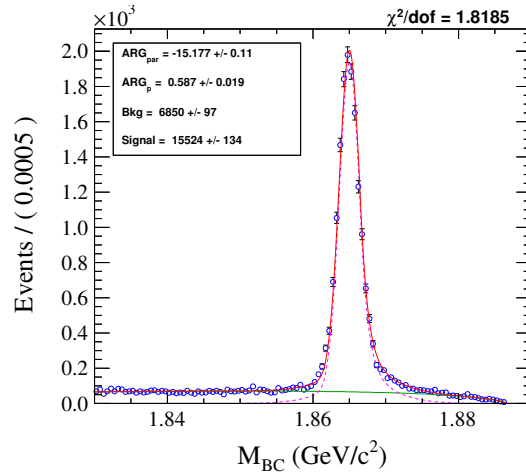


**Figure 29:** Fit to the  $M_{BC}$  distribution for the  $K_s\omega$  signal region in the  $\omega$  mass distribution of the data sample.

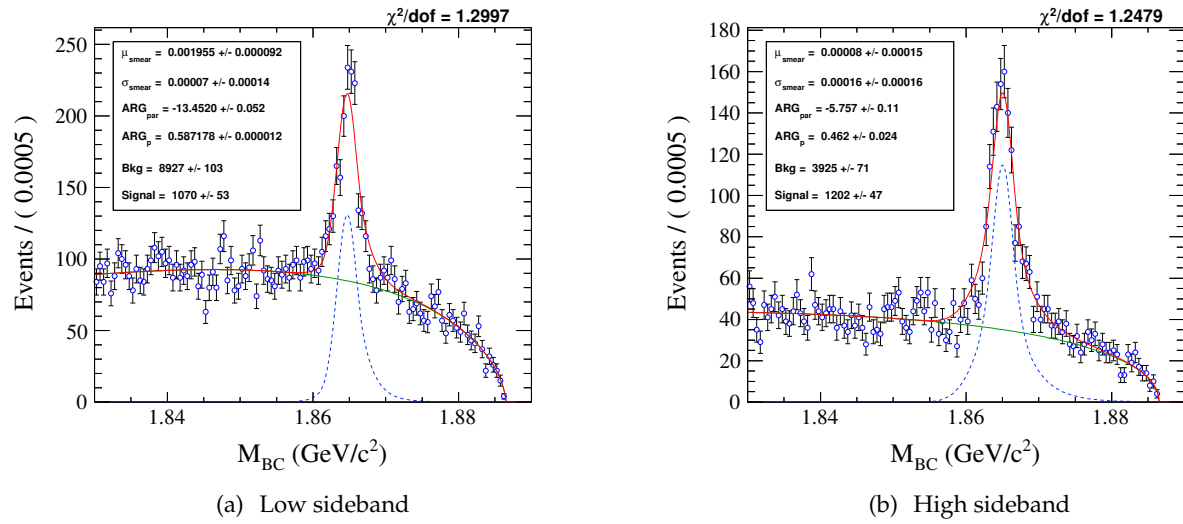


**Figure 30:** Fit to the  $M_{BC}$  distribution for the  $K_s\omega$  sideband regions in the  $\omega \rightarrow \pi^+\pi^-\pi^0$  mass distribution of the data sample.

## 5 Double Tags

When both  $D^0$  and  $\bar{D}^0$  hadronic decays are reconstructed in a single event, it is called a double-tag (DT) candidate. Double tags are also required for the  $CP$  fraction measurement. Therefore, we calculate the yield of a signal event decay opposite to a  $CP$  tag for both  $\pi^+\pi^-\pi^0$  and  $K^+K^-\pi^0$  decay.

For this analysis we consider DT events with one  $D$  decaying to our signal channel  $\pi^+\pi^-\pi^0$  or  $K^+K^-\pi^0$ , where the opposite  $D$  decays to one of the possible channels given in Table 2. Charge-conjugate modes are also considered throughout the analysis. Three  $CP$ -even, and five  $CP$ -odd tag modes are used.

Requirements for the tag side are the same as the single-tag requirements given in Table 6. The  $\Delta E$  requirement is enforced for the tag side as well as the signal side. Double tag yields are then calculated using a sideband subtraction method, introduced by CLEO-c [25], using the two-dimensional  $M_{BC}$  distribution of the DT candidates.

For the sideband subtraction, various regions are defined in the 2D  $M_{BC}$  distribution. These regions are listed in Table 13 and shown in Figure 31.

Figures 32-47 show the distributions for both  $\pi^+\pi^-\pi^0$  and  $K^+K^-\pi^0$  double-tag combinations.

Scale factors for the sidebands are calculated using the information from the single-tag  $M_{BC}$  fits. The scale of the region  $A$  is the ratio between the ARGUS background underneath the signal region, and the background integrated over region  $A$  of the single tag  $M_{BC}$ . Similarly for the scaling of region  $B$ , information is used from the single-tag  $M_{BC}$  fit to the tag mode. The scale factor of region  $C$  is the average of the  $A$  and  $B$  scale factors,  $\text{Scale}_C = (\text{Scale}_A + \text{Scale}_B)/2$ . Finally, scale factor of region  $D$  is just the ratio of areas of corresponding regions. The  $D$  region should be viewed as the uniform background that is present throughout the two-dimensional  $M_{BC}$  distribution. Areas  $A$  and area  $B$  are equal at  $0.00025 \text{ (GeV}/c^2)^2$ , area  $C$  is  $0.00016 \text{ (GeV}/c^2)^2$ , and area  $D$  is  $0.00038 \text{ (GeV}/c^2)^2$ . The yield,  $Y$  is then given by the formula below:

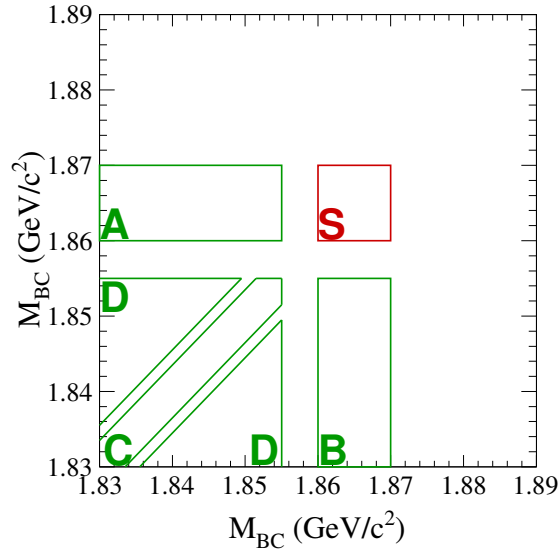
$$Y = \left( S - D \cdot \frac{\text{Area}_S}{\text{Area}_D} \right) - \text{Scale}_A \cdot \left( A - D \cdot \frac{\text{Area}_A}{\text{Area}_D} \right) - \text{Scale}_B \cdot \left( B - D \cdot \frac{\text{Area}_B}{\text{Area}_D} \right) - \text{Scale}_C \cdot \left( C - D \cdot \frac{\text{Area}_C}{\text{Area}_D} \right), \quad (7)$$

where  $S$ ,  $A$ ,  $B$ ,  $C$ , and  $D$  represent the counts in the corresponding regions. These counts for the sideband regions of the MC sample are given in Table 14 for  $\pi^+\pi^-\pi^0$  DT combinations, and in Table 15 for  $K^+K^-\pi^0$ . Similar information is given in Table 16 for data DT  $\pi^+\pi^-\pi^0$  candidates and Table 17 for  $K^+K^-\pi^0$ . Two-dimensional  $M_{BC}$  distributions are given in Figures 32-47 for both  $\pi^+\pi^-\pi^0$  and  $K^+K^-\pi^0$  double-tag combinations.

The resulting yields are given in Table 18 for double-tag events with  $\pi^+\pi^-\pi^0$ , and in Table 19 for  $K^+K^-\pi^0$  double-tag combinations.

**Table 13:** Double-tag Sideband Regions

	$M_{BC}$ Range	$\delta M_{BC} =  M_{BC1} - M_{BC2} $ (GeV/ $c^2$ )
Signal	$1.860 < M_{BC1} < 1.870$ GeV/ $c^2$ $1.860 < M_{BC2} < 1.870$ GeV/ $c^2$	
Region A	$1.830 < M_{BC1} < 1.855$ GeV/ $c^2$ $1.860 < M_{BC2} < 1.870$ GeV/ $c^2$	
Region B	$1.860 < M_{BC1} < 1.870$ GeV/ $c^2$ $1.830 < M_{BC2} < 1.855$ GeV/ $c^2$	
Region C	$1.830 < M_{BC1} < 1.855$ GeV/ $c^2$ $1.830 < M_{BC2} < 1.855$ GeV/ $c^2$	$\leq 0.0035$
Region D	$1.830 < M_{BC1} < 1.855$ GeV/ $c^2$ $1.830 < M_{BC2} < 1.855$ GeV/ $c^2$	$\geq 0.0055$

**Figure 31:** Regions in the  $M_{BC}$  distribution.**Table 14:** Double-tag counts for signal and sideband regions. For  $\pi^+\pi^-\pi^0$  vs. tag modes for the MC sample.

Mode	S	A	B	C	D	All
$K_s\pi^0$	4388	29	6	25	2	4986
$\pi^-\pi^+$	193	5	11	387	33	1038
$K^-K^+$	310	17	18	411	35	1226
$K_s\pi^0\pi^0$	86	4	1	62	22	326
$K_s\eta'(\pi^-\pi^+\eta)$	187	0	2	1	1	216
$K_s\eta'(\rho\gamma)$	612	4	9	8	5	696
$K_s\eta$	612	5	53	8	9	876
$K_s\omega$	1172	7	4	18	0	1326

**Table 15:** Double Tag counts for signal and sideband regions. For  $K^+K^-\pi^0$  vs. tag modes for the MC sample.

Mode	S	A	B	C	D	All
$K_s\pi^0$	503	8	0	7	4	595
$\pi^-\pi^+$	82	5	2	137	13	376
$K^-K^+$	89	8	1	49	9	226
$K_s\pi^0\pi^0$	28	0	2	5	3	58
$K_s\eta'(\pi^-\pi^+\eta)$	25	2	0	0	0	33
$K_s\eta'(\rho\gamma)$	61	2	2	0	1	83
$K_s\eta$	55	3	6	1	1	101
$K_s\omega$	99	3	0	2	1	116

**Table 16:** Double Tag counts for signal and sideband regions. For  $\pi^+\pi^-\pi^0$  vs. tag modes for the data sample.

Mode	S	A	B	C	D	All
$K_s\pi^0$	503	8	0	7	4	595
$\pi^-\pi^+$	82	5	2	137	13	376
$K^-K^+$	89	8	1	49	9	226
$K_s\pi^0\pi^0$	28	0	2	5	3	58
$K_s\eta'(\pi^-\pi^+\eta)$	25	2	0	0	0	33
$K_s\eta'(\rho\gamma)$	61	2	2	0	1	83
$K_s\eta$	55	3	6	1	1	101
$K_s\omega$	99	3	0	2	1	116

**Table 17:** Double Tag counts for signal and sideband regions. For  $K^+K^-\pi^0$  vs. tag modes for the data sample.

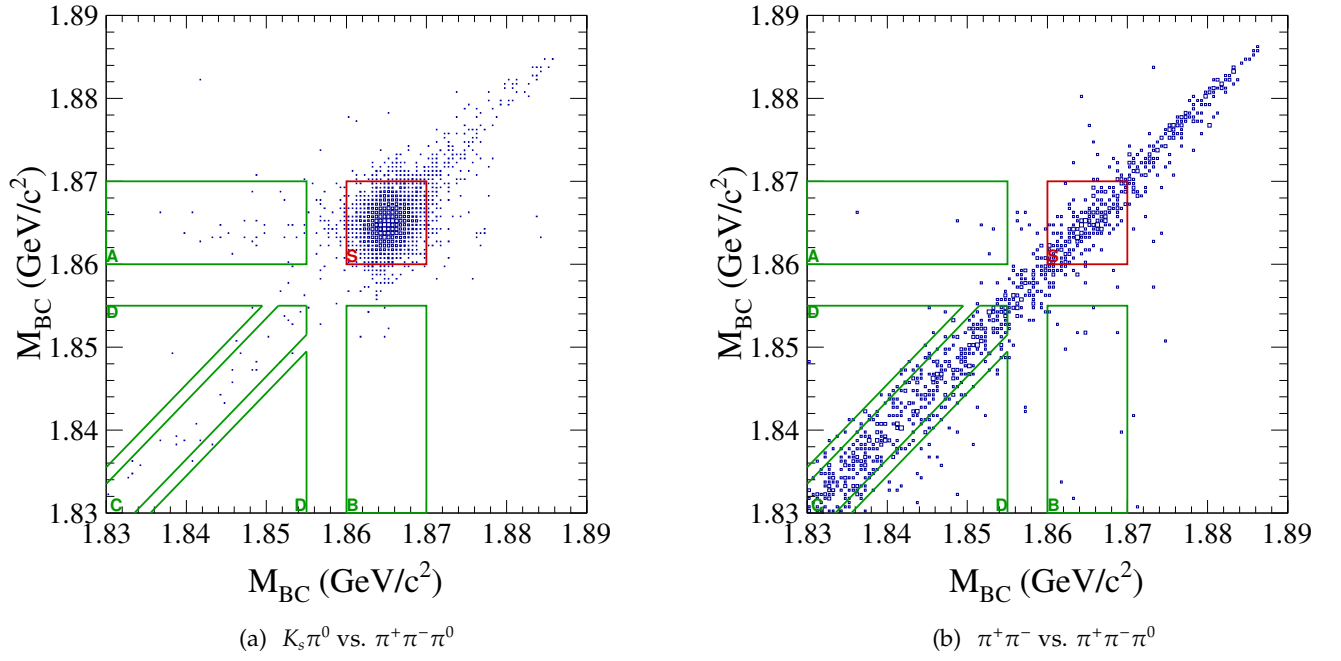
Mode	S	A	B	C	D	All
$K_s\pi^0$	53	3	0	0	1	74
$\pi^-\pi^+$	36	0	2	21	9	112
$K^-K^+$	49	1	2	15	3	97
$K_s\pi^0\pi^0$	12	1	0	0	0	16
$K_s\eta'(\pi^-\pi^+\eta)$	4	0	0	0	0	4
$K_s\eta'(\rho\gamma)$	6	0	0	0	0	11
$K_s\eta$	8	0	1	0	0	13
$K_s\omega$	21	0	0	1	0	26

**Table 18:** Double Tag yields for  $\pi^+\pi^-\pi^0$  vs. tag modes, before the mass side band subtraction for  $K_s\eta'(\rho\gamma)$  and  $K_s\omega$ .

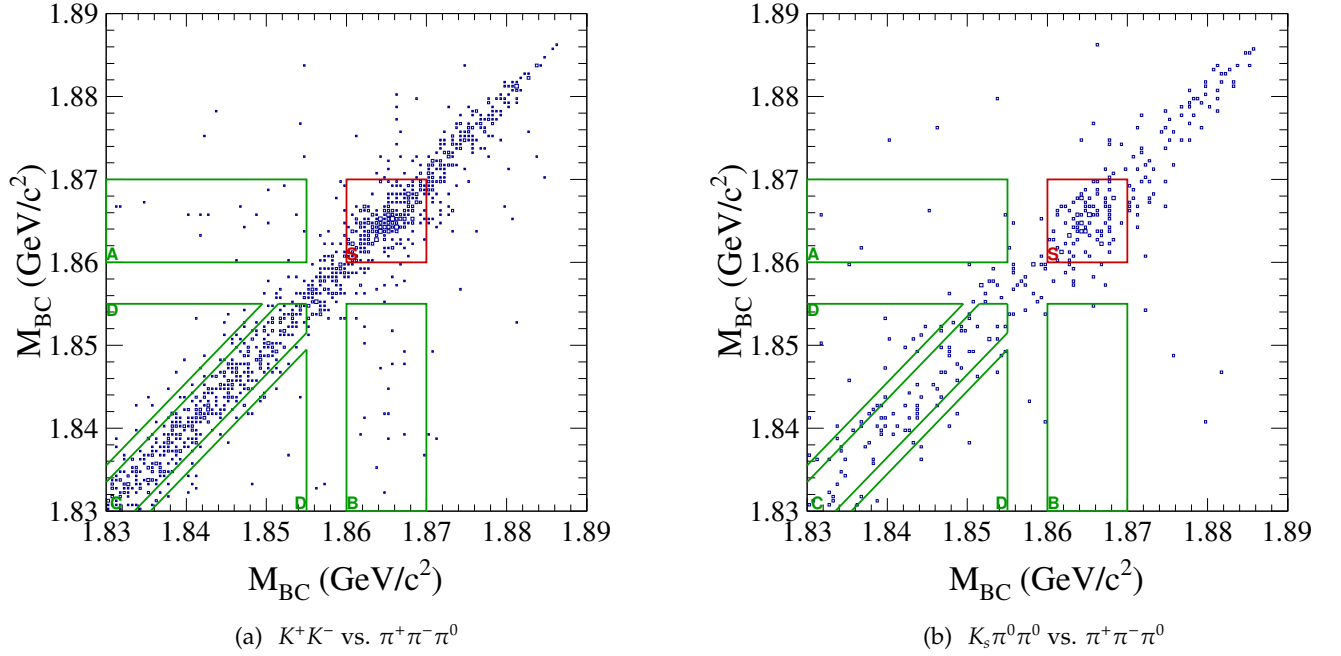
Mode	Data yields	MC yields	Fake data yields
$K_s\pi^0$	$490 \pm 22$	$(4.51 \pm 0.07) \times 10^3$	$(4.37 \pm 0.07) \times 10^3$
$\pi^+\pi^-$	$18 \pm 6$	$65 \pm 16$	$61 \pm 16$
$K^+K^-$	$40 \pm 9$	$132 \pm 19$	$153 \pm 20$
$K_s\pi^0\pi^0$	$16 \pm 5$	$58 \pm 10$	$69 \pm 10$
$K_s\eta'(\pi^+\pi^-\eta)$	$21 \pm 5$	$202 \pm 14$	$186 \pm 14$
$K_s\eta'(\rho\gamma)$	$74 \pm 9$	$542 \pm 23$	$606 \pm 25$
$K_s\eta$	$91 \pm 10$	$621 \pm 26$	$587 \pm 25$
$K_s\omega$	$120 \pm 11$	$1166 \pm 34$	$1161 \pm 34$

**Table 19:** Double Tag yields for  $K^+K^-\pi^0$  vs. tag modes, before the mass side band subtraction for  $K_s\eta'(\rho\gamma)$  and  $K_s\omega$ .

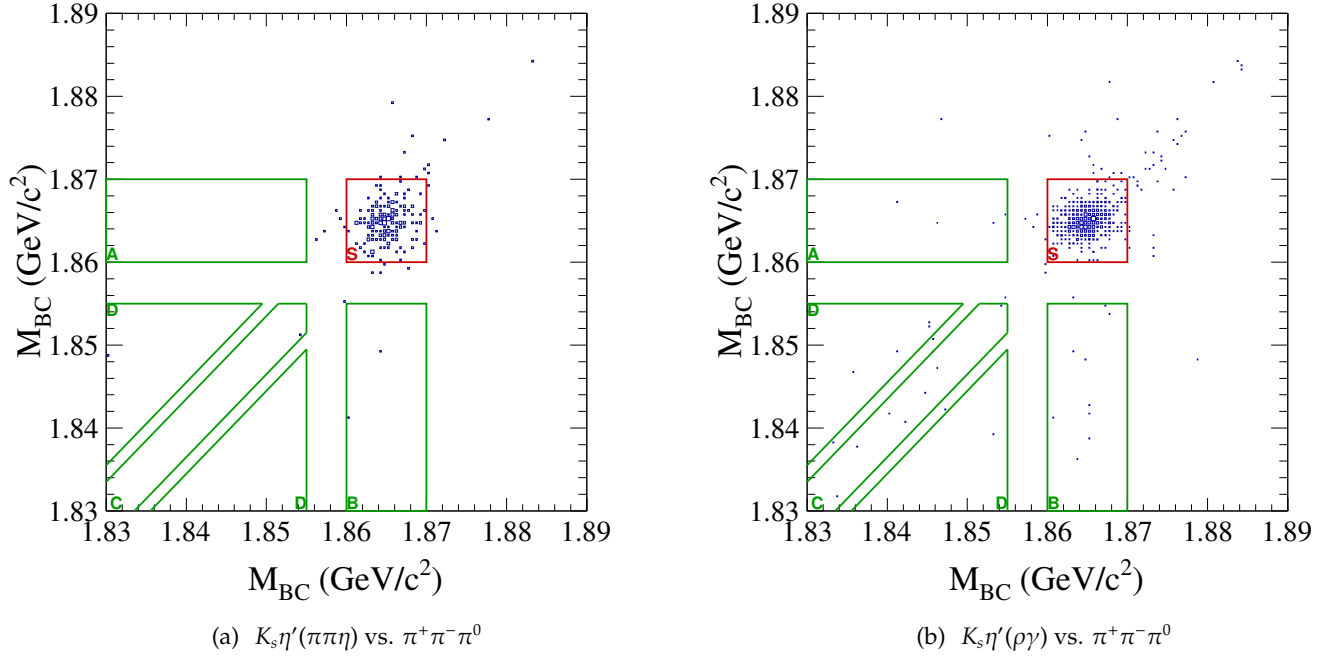
Mode	Data yields	MC yields	Fake data yields
$K_s\pi^0$	$52 \pm 7$	$433 \pm 21$	$499 \pm 22$
$\pi^+\pi^-$	$31 \pm 6$	$50 \pm 10$	$34 \pm 10$
$K^+K^-$	$43 \pm 7$	$81 \pm 11$	$70 \pm 10$
$K_s\pi^0\pi^0$	$11.6 \pm 3.5$	$32 \pm 6$	$26 \pm 5$
$K_s\eta'(\pi^+\pi^-\eta)$	$4.0 \pm 2.0$	$25 \pm 5$	$24 \pm 5$
$K_s\eta'(\rho\gamma)$	$6.0 \pm 2.4$	$61 \pm 8$	$60 \pm 8$
$K_s\eta$	$7.6 \pm 2.9$	$62 \pm 8$	$51 \pm 8$
$K_s\omega$	$21 \pm 5$	$123 \pm 11$	$97 \pm 10$

5.1  $\pi^+\pi^-\pi^0$  vs. tag modes

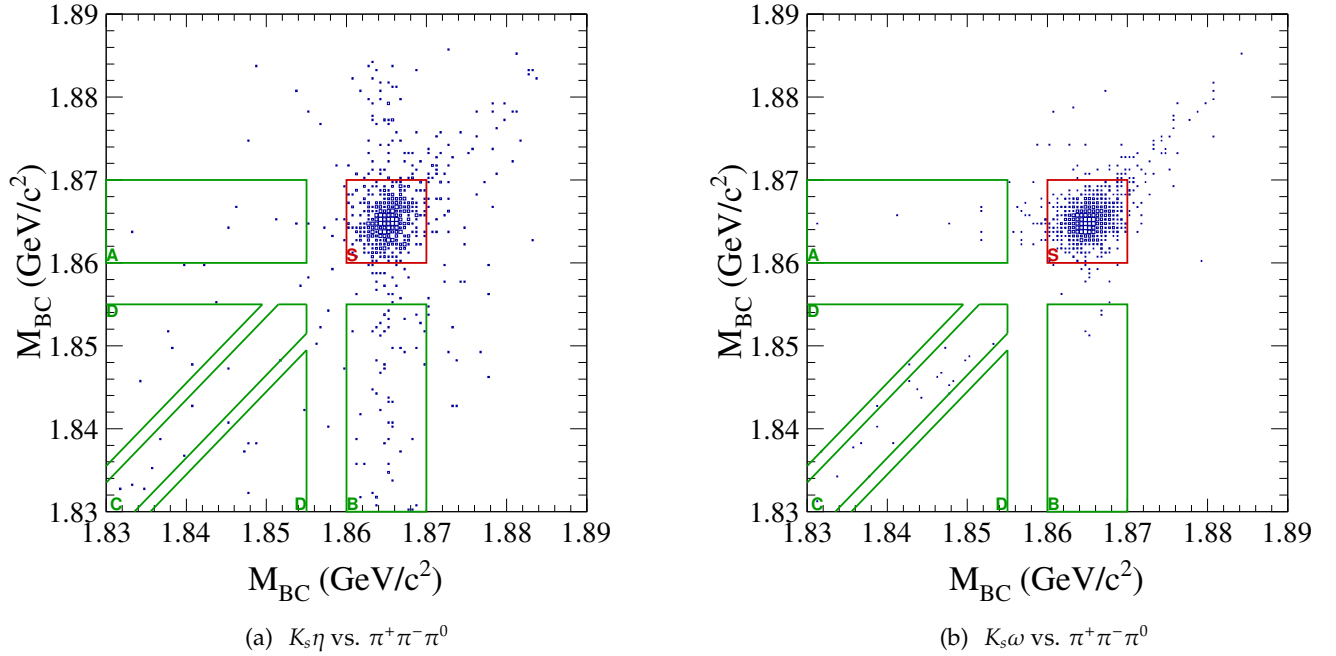
**Figure 32:** Two dimensional  $M_{BC}$  distributions for  $\pi^+\pi^-\pi^0$  DT candidates for the MC. Red for the signal region, and green for four side band regions.



**Figure 33:** Two dimensional  $M_{BC}$  distributions for  $\pi^+\pi^-\pi^0$  DT candidates for the MC. Red for the signal region, and green for four side band regions.

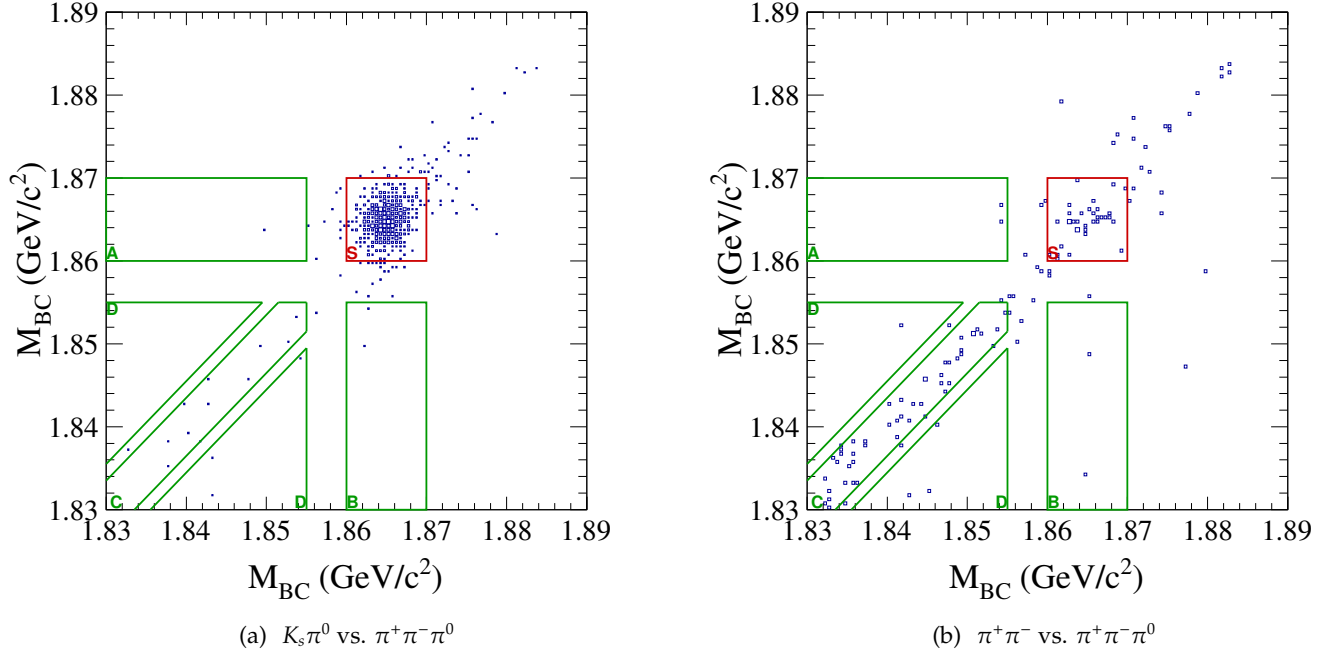


**Figure 34:** Two dimensional  $M_{BC}$  distributions for  $\pi^+ \pi^- \pi^0$  DT candidates for the MC. Red for the signal region, and green for four side band regions.

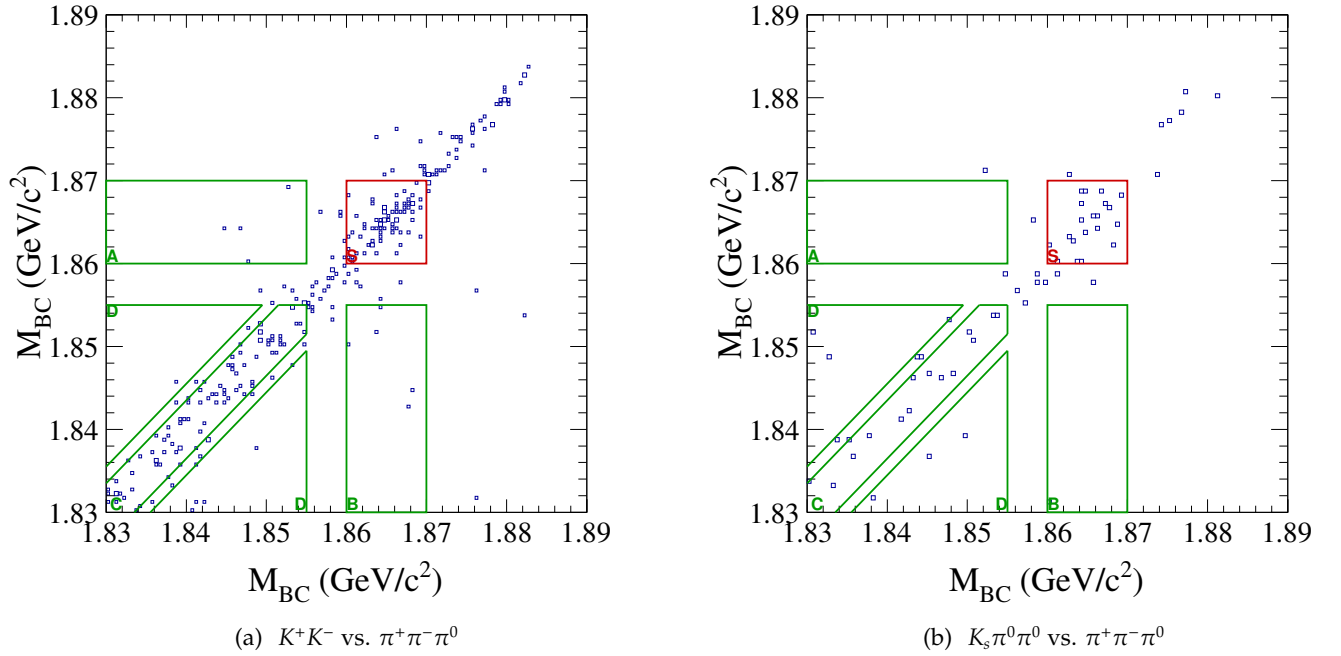


**Figure 35:** Two dimensional  $M_{BC}$  distributions for  $\pi^+ \pi^- \pi^0$  DT candidates for the MC. Red for the signal region, and green for four side band regions.

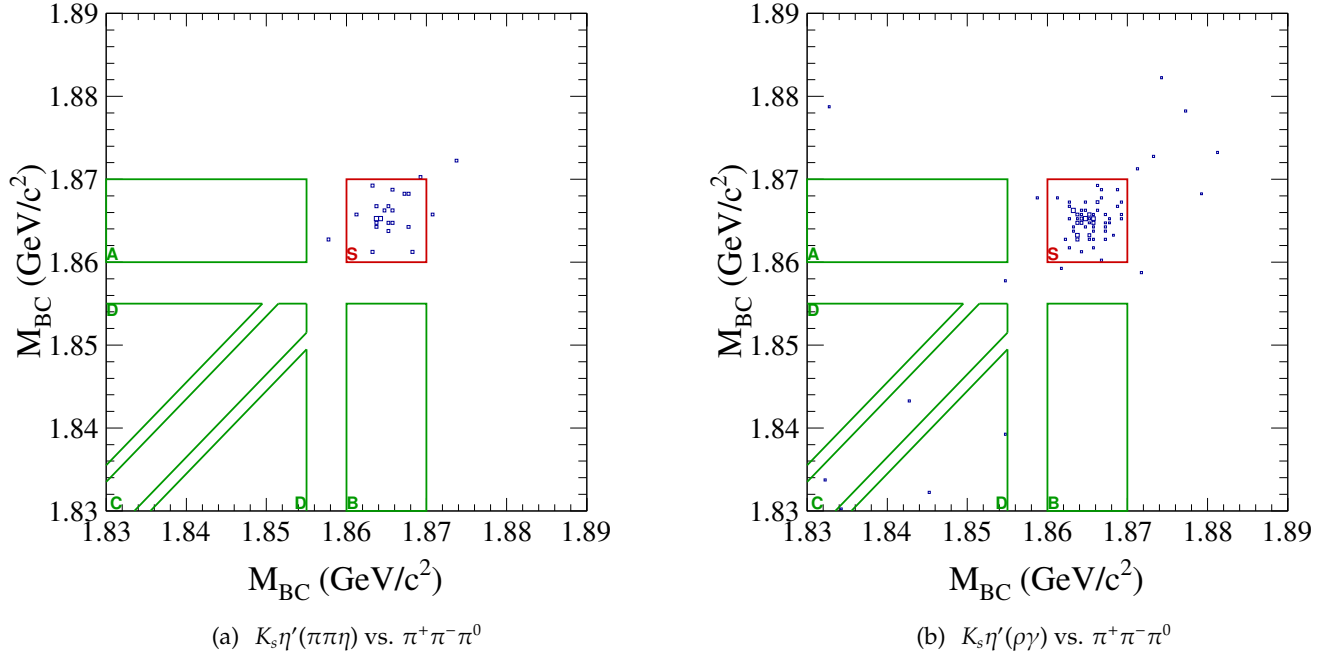




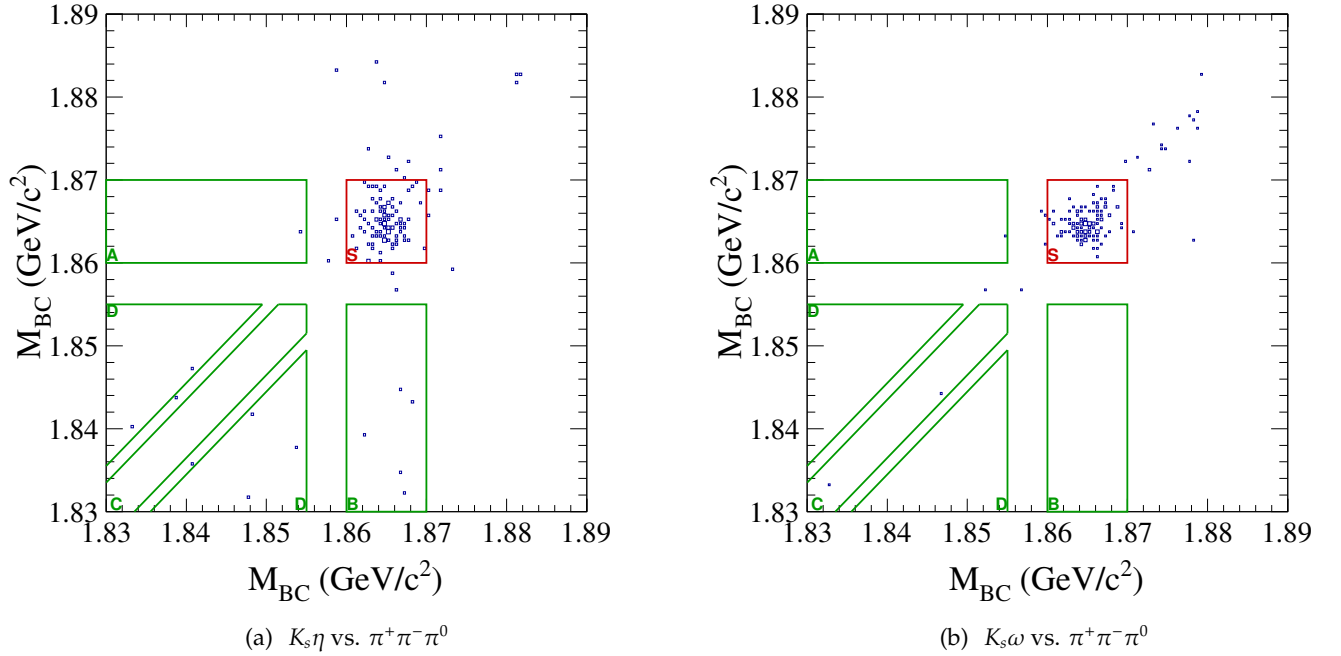
**Figure 36:** Two dimensional  $M_{BC}$  distributions for  $\pi^+\pi^-\pi^0$  DT candidates for the data sample. Red for the signal region, and green for four side band regions.



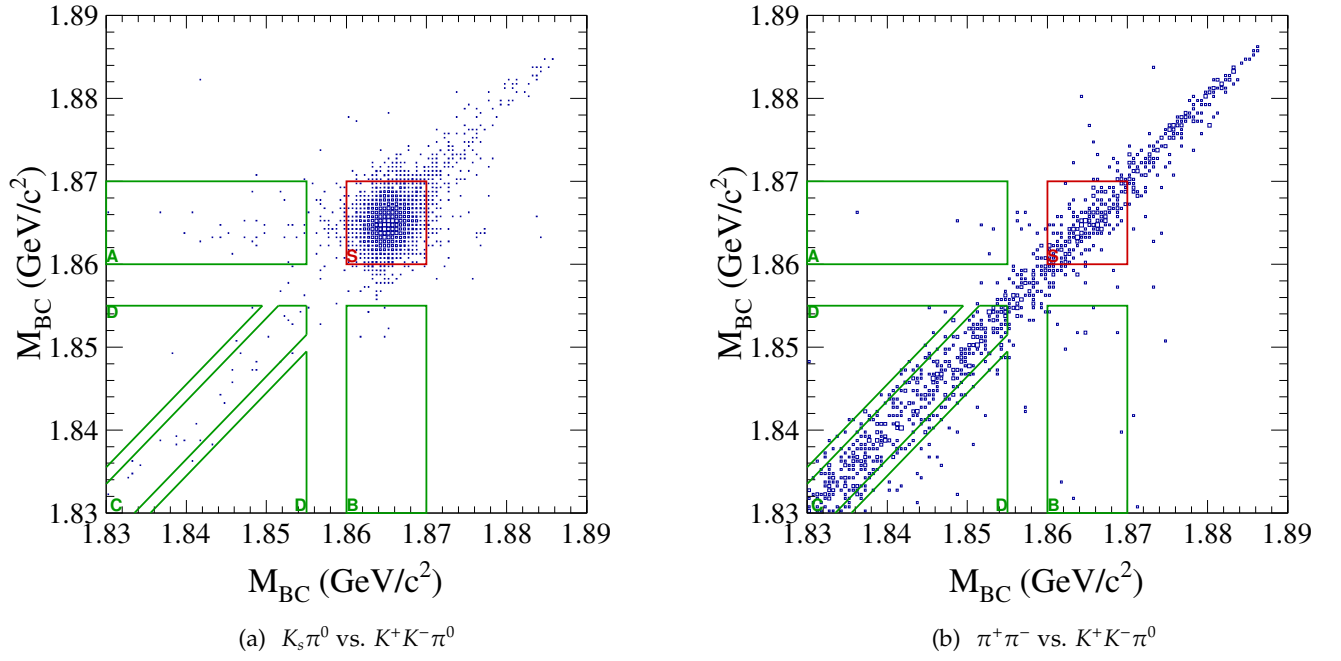
**Figure 37:** Two dimensional  $M_{BC}$  distributions for  $\pi^+\pi^-\pi^0$  DT candidates for the data sample. Red for the signal region, and green for four side band regions.



**Figure 38:** Two dimensional  $M_{BC}$  distributions for  $\pi^+ \pi^- \pi^0$  DT candidates for the data sample. Red for the signal region, and green for four side band regions.



**Figure 39:** Two dimensional  $M_{BC}$  distributions for  $\pi^+ \pi^- \pi^0$  DT candidates for the data sample. Red for the signal region, and green for four side band regions.

5.2  $K^+K^-\pi^0$  vs. tag modes

**Figure 40:** Two dimensional  $M_{BC}$  distributions for  $K^+K^-\pi^0$  DT candidates for the MC. Red for the signal region, and green for four side band regions.

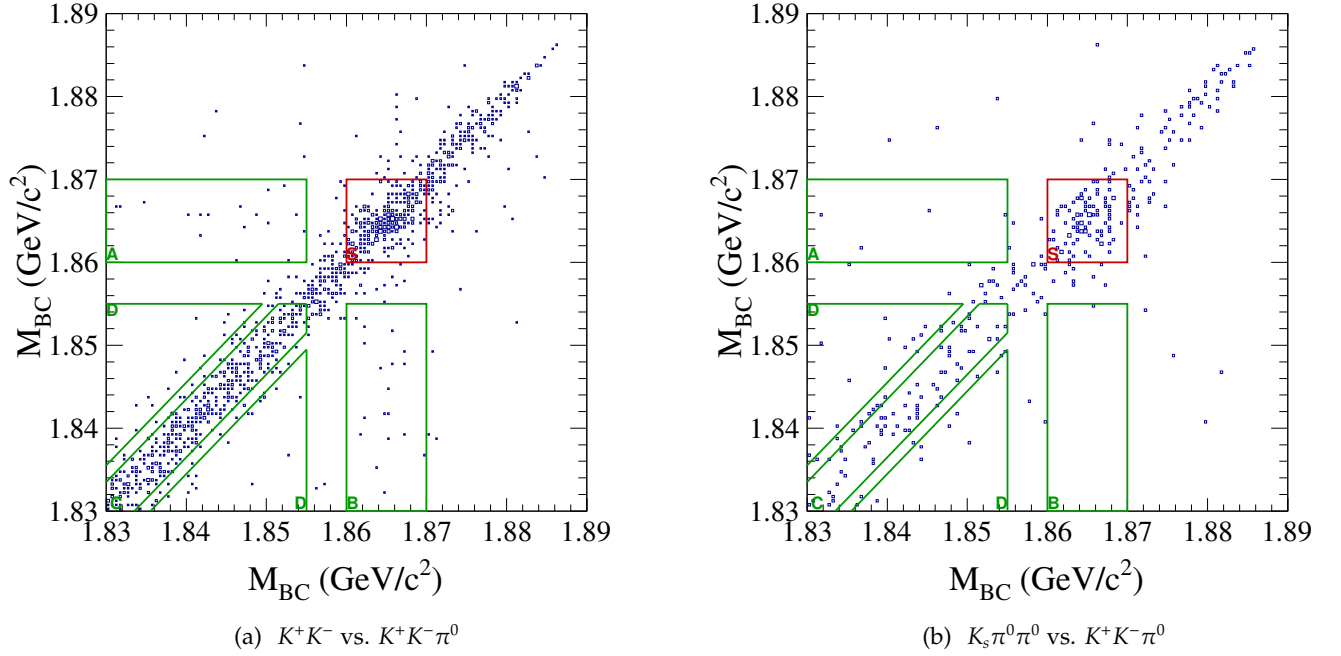


**Figure 41:** Two dimensional  $M_{BC}$  distributions for  $K^+K^-\pi^0$  DT candidates for the MC. Red for the signal region, and green for four side band regions.

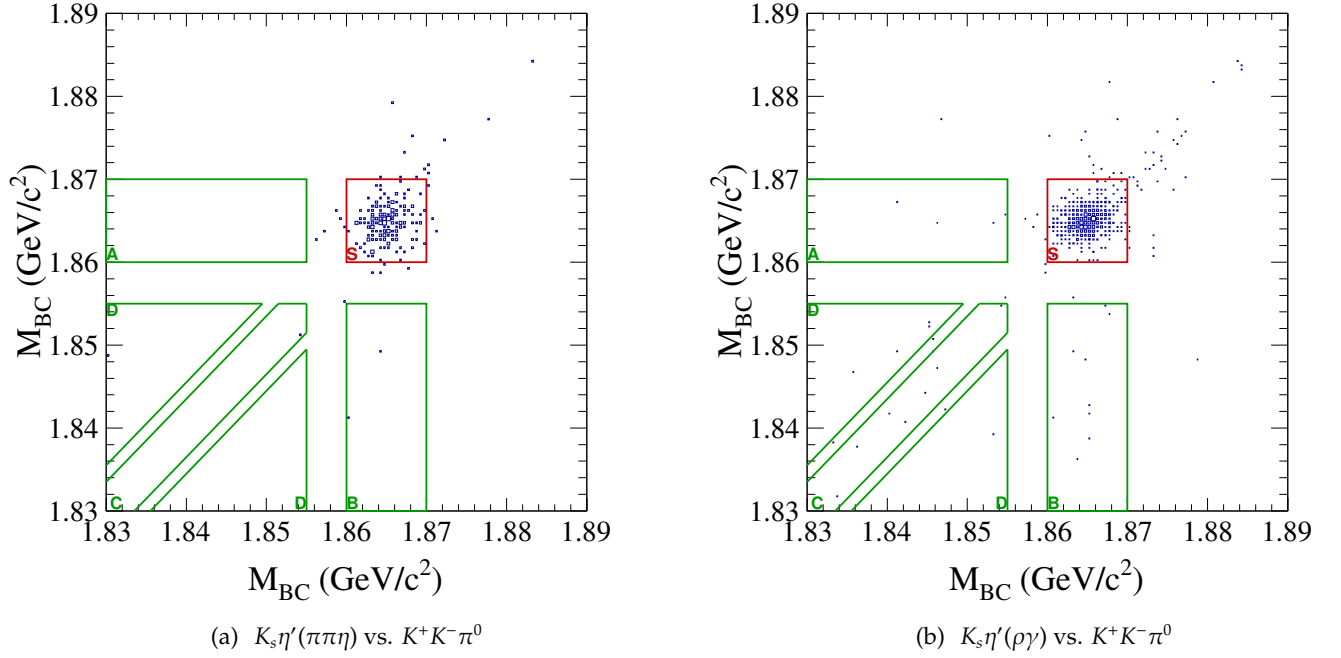


**Figure 42:** Two dimensional  $M_{BC}$  distributions for  $K^+K^-\pi^0$  DT candidates for the MC. Red for the signal region, and green for four side band regions.

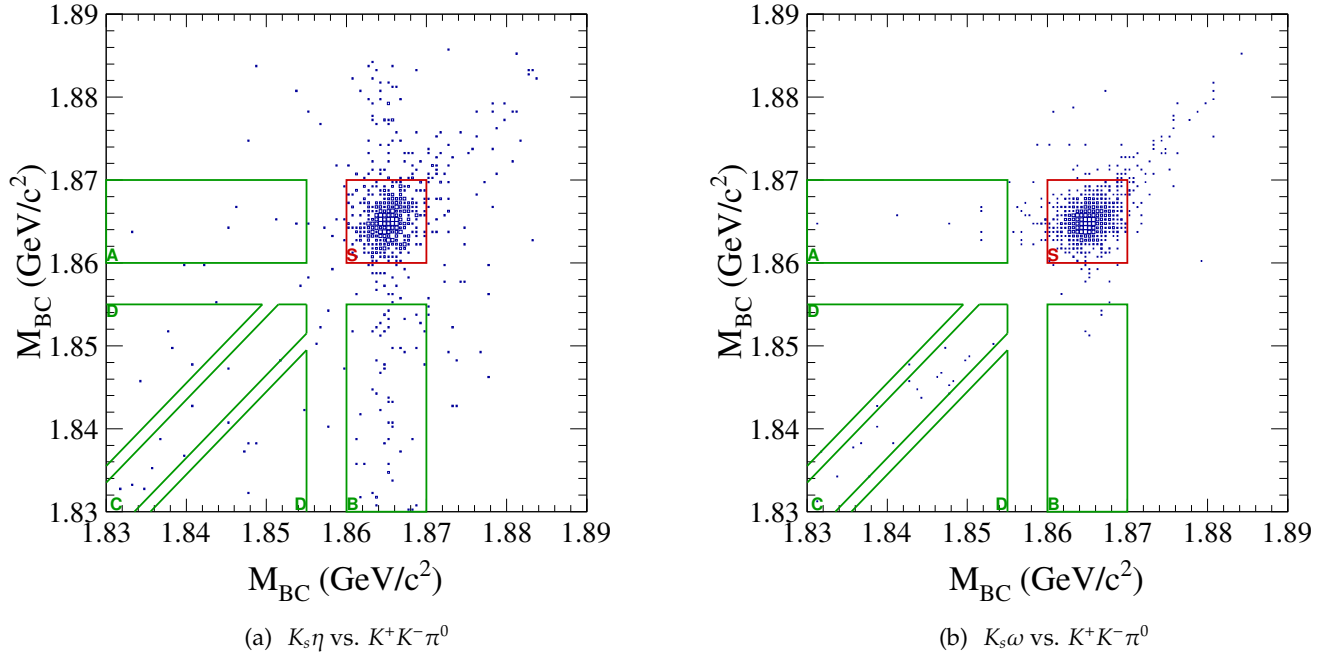


**Figure 43:** Two dimensional  $M_{BC}$  distributions for  $K^+K^-\pi^0$  DT candidates for the MC. Red for the signal region, and green for four side band regions.

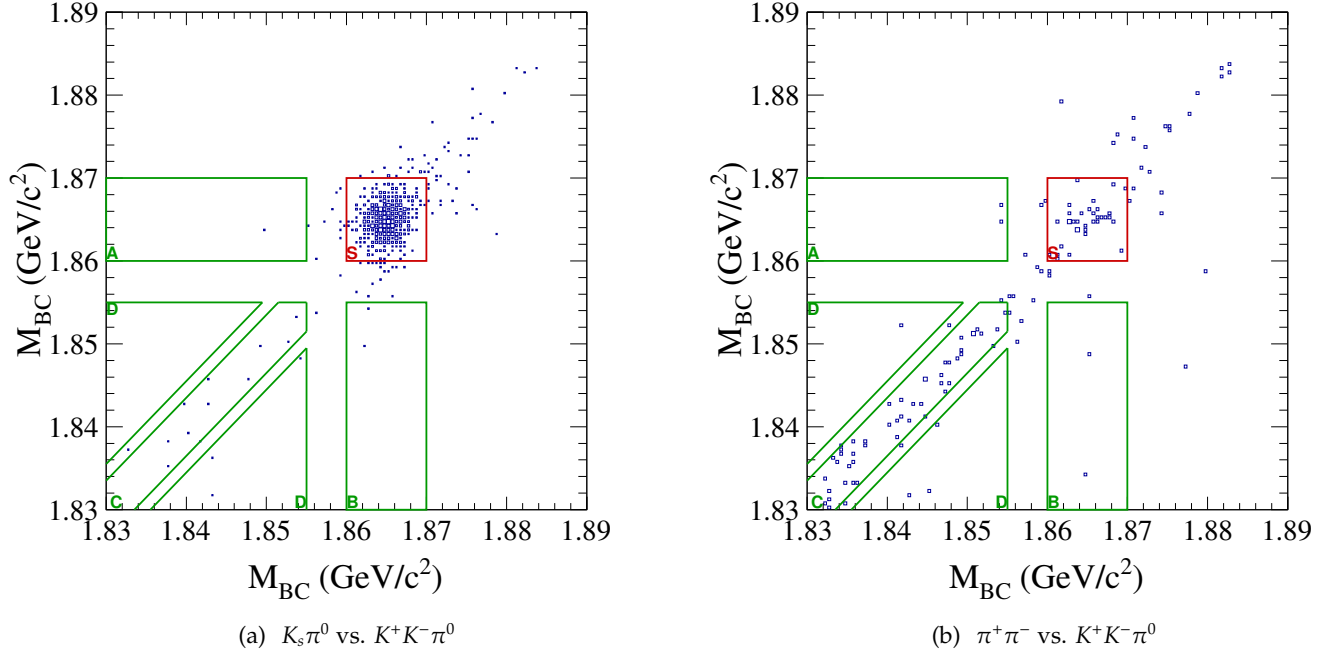


**Figure 44:** Two dimensional  $M_{BC}$  distributions for  $K^+K^-\pi^0$  DT candidates for the data sample. Red for the signal region, and green for four side band regions.

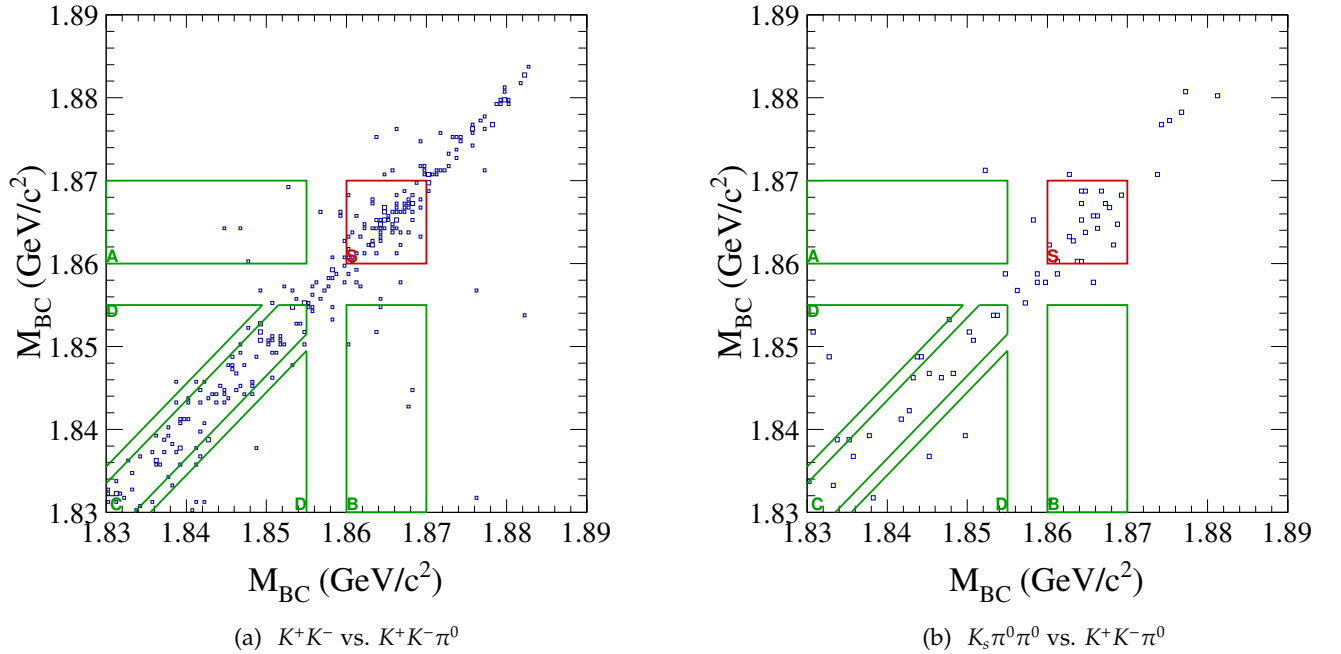


**Figure 45:** Two dimensional  $M_{BC}$  distributions for  $K^+K^-\pi^0$  DT candidates for the data sample. Red for the signal region, and green for four side band regions.

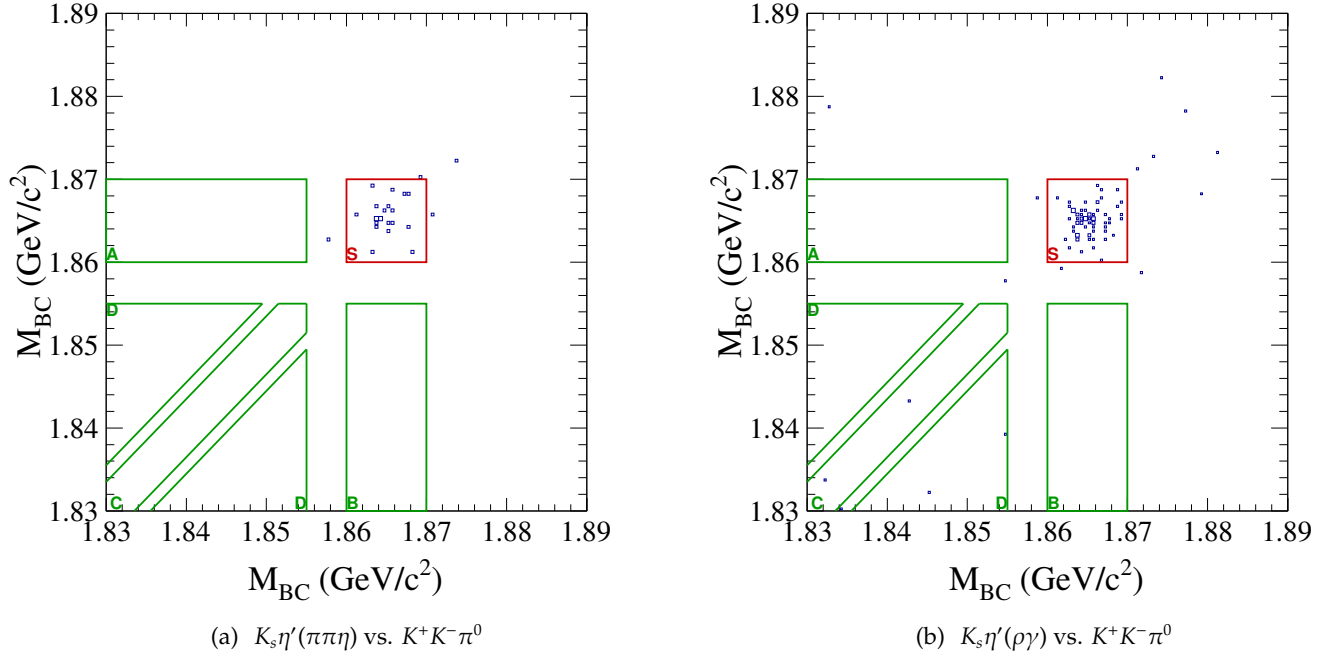


**Figure 46:** Two dimensional  $M_{BC}$  distributions for  $K^+K^-\pi^0$  DT candidates for the data sample. Red for the signal region, and green for four side band regions.

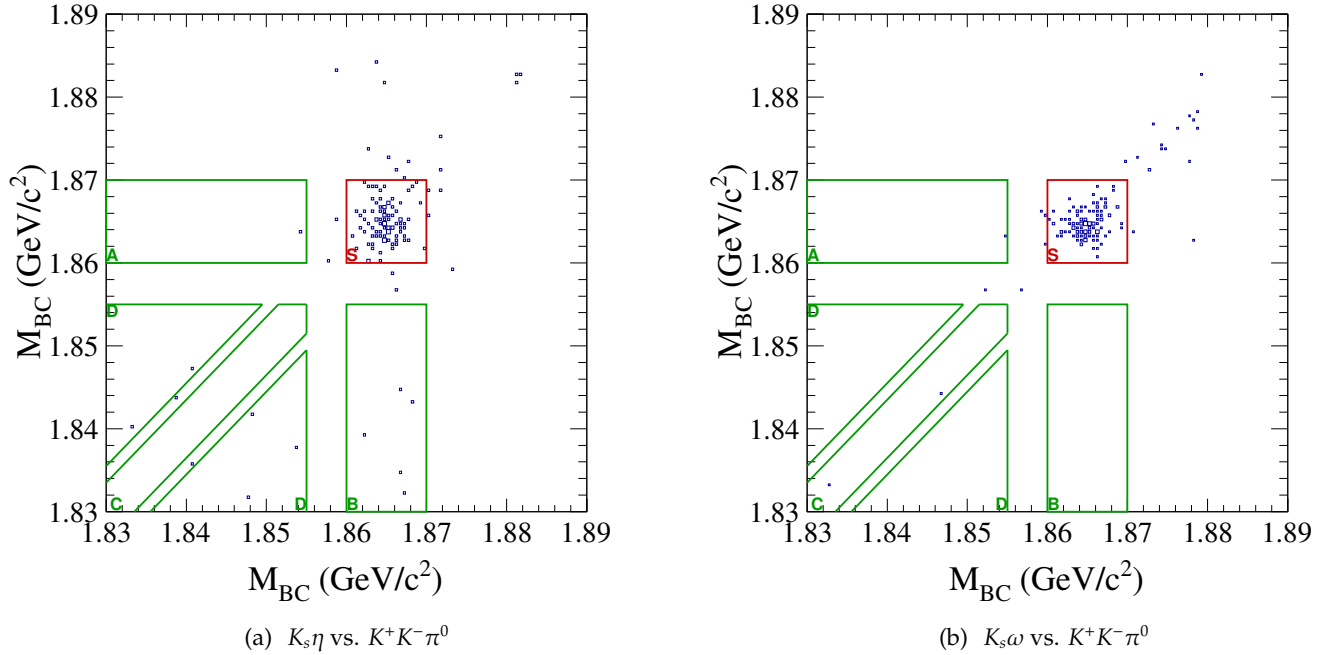


**Figure 47:** Two dimensional  $M_{BC}$  distributions for  $K^+K^-\pi^0$  DT candidates for the data sample. Red for the signal region, and green for four side band regions.

### 5.3 Mass Sideband Subtraction for Double Tags

As described in Section 4.1, background due to non-resonant decays to the  $K_s\eta'(\rho\gamma)$  and  $K_s\omega$  channels are large. A similar mass sideband subtraction is also performed for the DT candidates.

Instead of the three  $M_{BC}$  fits that correspond to the low, high, and signal region, three 2D  $M_{BC}$  distributions are prepared for the double-tag candidates. Same DT yield procedure that incorporates the counts of the  $S$ ,  $A$ ,  $B$ ,  $C$ , and  $D$  regions in the 2D  $M_{BC}$  distributions is used. The 2D  $M_{BC}$  yields are then scaled according to the  $M_\omega$  fit to calculate the corresponding value to be subtracted from the number of signal events in the  $M_{\omega\rightarrow\pi^+\pi^-\pi^0}$  signal region. Details of the mass sideband subtraction were given in Section 4.1. Individual studies for  $\pi^+\pi^-\pi^0$  and  $K^+K^-\pi^0$  double-tag candidates are given in the following sections.

#### 5.3.1 $\pi^+\pi^-\pi^0$ vs. tag modes

The intermediate-resonance mass distributions from MC are shown for the tag modes  $K_s\omega$ , and  $K_s\eta'(\rho\gamma)$  in Figure 48. Similar distributions are plotted in Figure 49 for the data sample.

Yields for the mass sidebands and the resulting yield after the subtraction is given Table 20 for  $K_s\eta'(\rho\gamma)$  and in Table 22 for  $K_s\omega$  double-tag candidates from the MC. Similar information for the data sample is given in Table 21 for  $K_s\eta'(\rho\gamma)$  and Table 23 for  $K_s\omega$ .

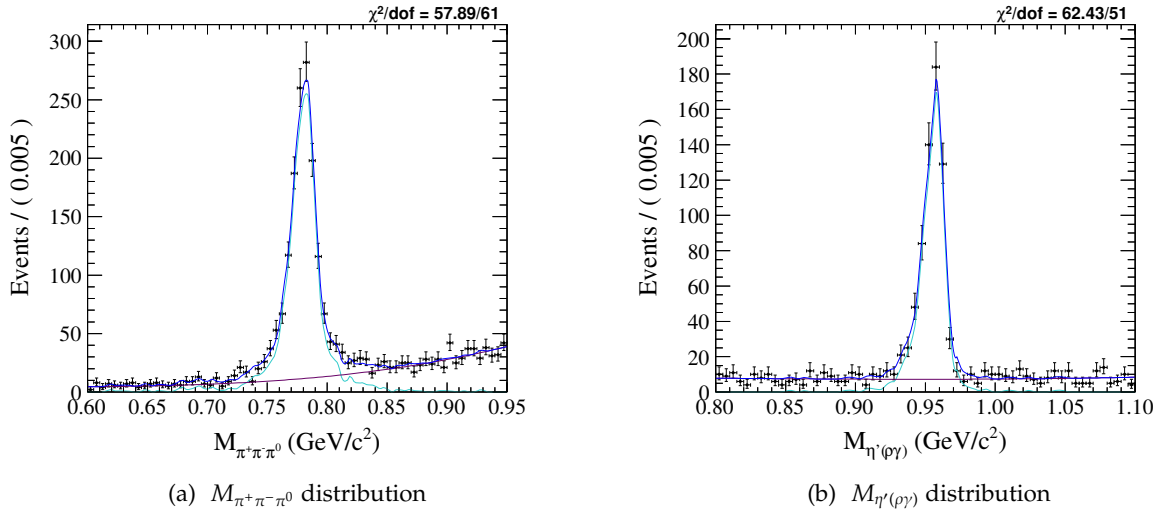


**Figure 48:** The  $\pi^+\pi^-\pi^0$  invariant mass distribution in  $K_s\omega$  vs.  $\pi^+\pi^-\pi^0$  DT events from the MC on the left. The  $\eta'$  mass distribution in  $K_s\eta'(\rho\gamma)$  vs.  $\pi^+\pi^-\pi^0$  DT events from the MC on the right. Magenta is used for background and cyan for the signal.

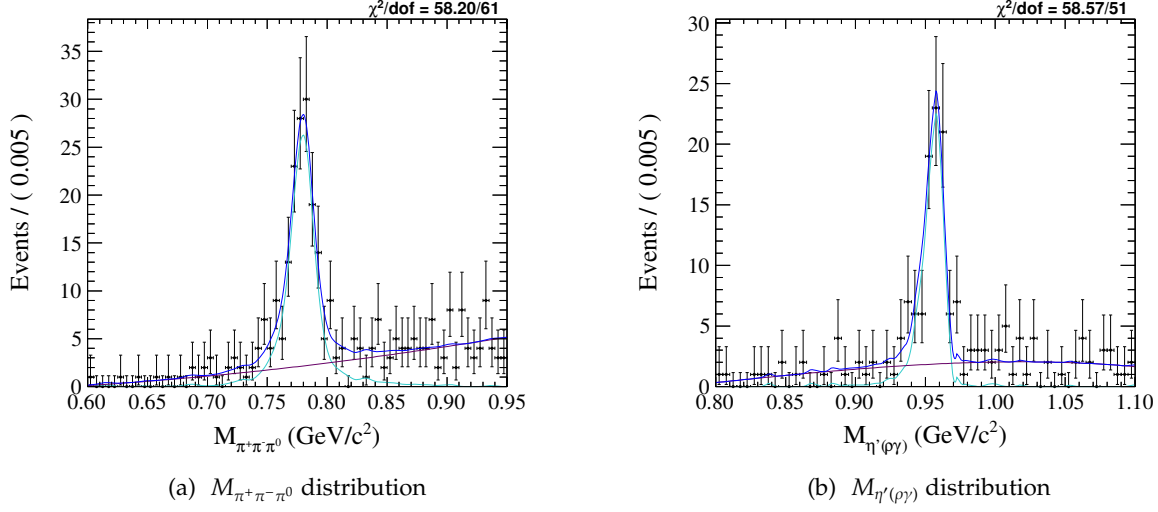


**Figure 49:** The  $\pi^+\pi^-\pi^0$  invariant mass distribution in  $K_s\omega$  vs.  $\pi^+\pi^-\pi^0$  DT events from the data on the left. The  $\eta'$  mass distribution in  $K_s\eta'$  vs.  $\pi^+\pi^-\pi^0$  DT events for the data on the right. Magenta is used for background and cyan for the signal.

**Table 20:** Sideband subtraction numbers for  $K_s\eta'$  vs.  $\pi^+\pi^-\pi^0$  from the MC.

	Low side	Signal region	High side
Background scale	0.150	0.142	0.187
Yield	$21 \pm 5$	$606 \pm 25$	$29 \pm 6$
Final yield		$586 \pm 25$	

**Table 21:** Sideband subtraction numbers for  $K_s\eta'$  vs.  $\pi^+\pi^-\pi^0$  for the data sample.

	Low side	Signal region	High side
Background scale	0.128	0.161	0.219
Yield	$0.3 \pm 1.2$	$74 \pm 9$	$2.9 \pm 2.3$
Final yield		$73 \pm 9$	

**Table 22:** Sideband subtraction numbers for  $K_s\omega$  vs.  $\pi^+\pi^-\pi^0$  from the MC.

	Low side	Signal region	High side
Background scale	0.168	0.120	0.081
Yield	$162 \pm 13$	$1161 \pm 34$	$95 \pm 10$
Final yield		$(1.03 \pm 0.04) \times 10^3$	



**Table 23:** *Sideband subtraction numbers for  $K_s\omega$  vs.  $\pi^+\pi^-\pi^0$  for the data sample.*

	Low side	Signal region	High side
Background scale	0.121	0.124	0.089
Yield	$11 \pm 4$	$120 \pm 11$	$6.6 \pm 2.9$
Final yield		$110 \pm 11$	

### 5.3.2 $K^+K^-\pi^0$ vs. tag modes

The intermediate resonance mass distributions are shown for the tag modes  $K_s\omega$  and  $K_s\eta'(\rho\gamma)$  in Figure 50. Similar distributions are plotted in Figure 51 for the data sample. The first two of these modes are selected due to their high peaking background in single tag selection. The last mode is shown for demonstration of the case where peaking background is not a significant issue. The  $K^+K^-\pi^0$  double-tag candidates of the data sample have very low statistics and the values that are subtracted from the signal region yields are either very small, or negligible.

Yields for the mass sidebands and the resulting yield after the subtraction is given in Table 24 for  $K_s\eta'(\rho\gamma)$  and Table 26 for  $K_s\omega$  double-tag candidates from the MC. Similar information for the data can be found in Table 25 for  $K_s\eta'(\rho\gamma)$  and Table 27 for  $K_s\omega$ .

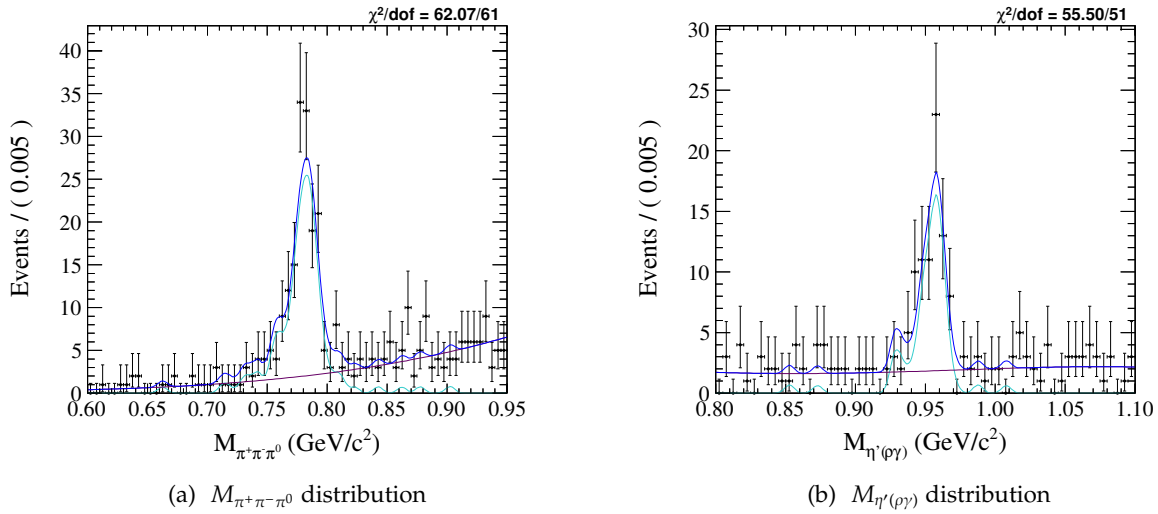


**Figure 50:** The  $\pi^+\pi^-\pi^0$  invariant mass distribution in  $K_s\omega$  vs.  $K^+K^-\pi^0$  DT events from the MC on the left. The  $\eta'$  mass distribution in  $K_s\eta'$  vs.  $K^+K^-\pi^0$  DT events from the MC on the right. Magenta is used for background and cyan for the signal.

**Table 24:** Sideband subtraction numbers for  $K_s\eta'(\rho\gamma)$  vs.  $K^+K^-\pi^0$  from the MC.

	Low side	Signal region	High side
Background scale	0.170	0.151	0.173
Yield	$6.3 \pm 2.8$	$60 \pm 8$	$11.1 \pm 3.5$
Final yield		$53 \pm 8$	

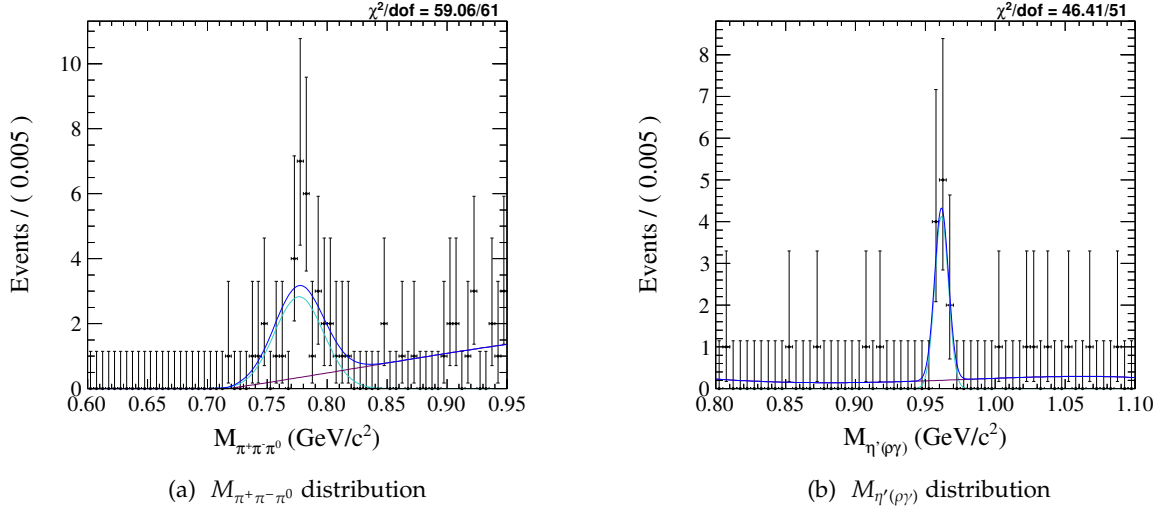


**Figure 51:** The  $\pi^+\pi^-\pi^0$  invariant mass distribution in  $K_s\omega$  vs.  $K^+K^-\pi^0$  DT events for the data on the left. The  $\eta'$  mass distribution in  $K_s\eta'$  vs.  $K^+K^-\pi^0$  DT events for the data on the right. Magenta is used for background and cyan for the signal.

**Table 25:** Sideband subtraction numbers for  $K_s\eta'(\rho\gamma)$  vs.  $K^+K^-\pi^0$  for the data sample.

	Low side	Signal region	High side
Background scale	0.114	0.123	0.215
Yield	$-0.7 \pm 0.1$	$6.0 \pm 2.4$	$1.4 \pm 1.1$
Final yield		$6.3 \pm 2.5$	

**Table 26:** Sideband subtraction numbers for  $K_s\omega$  vs.  $K^+K^-\pi^0$  from the MC.

	Low side	Signal region	High side
Background scale	0.175	0.127	0.084
Yield	$16 \pm 5$	$97 \pm 10$	$9.2 \pm 3.2$
Final yield		$84 \pm 11$	

**Table 27:** Sideband subtraction numbers for  $K_s\omega$  vs.  $K^+K^-\pi^0$  for the data sample.

	Low side	Signal region	High side
Background scale	0.000	0.137	0.133
Yield	$0.0 \pm 0$	$21 \pm 5$	$1.0 \pm 1.0$
Final yield		$20 \pm 5$	

## 6 Peaking Background

Peaking backgrounds are studied for both the signal modes and for the  $CP$  tags that are used in the analysis. Studies are divided into three main sections: peaking background for  $CP$  tags, for  $\pi^+\pi^-\pi^0$ , and for  $K^+K^-\pi^0$ .

The peaking background is caused by events that satisfy all the requirements of the analysis, but originated from a different decay. This is investigated using MC simulation where the generator level information can be used to determine what decay channel was generated. This will be called the MC truth information throughout the text.

### 6.1 Peaking-background Study for $CP$ Single Tags

Single-tag  $CP$  candidates are reconstructed in the same way as explained in Section 4. The  $M_{BC}$  distributions from MC are then fit to calculate the yields. Three different fits are performed. First, all the events reconstructed for that mode are fit, then only the signal only events, and finally the peaking background events. Truth information is used to gather the corresponding  $M_{BC}$  distributions of the peaking background for the  $CP$  tags. These distributions are also fit and the resulting yields are used to calculate the peaking background percentages in the  $CP$  single-tag modes. Yields and corresponding peaking background fractions are given in Table 28. We perform the calculation  $((S + pBG) - S)/S$  to measure the background fraction, different than just using  $pBG/S$ . This is because the “peaking background”, can have a larger width and be off-center from the  $D$  mass. This makes  $pBG$  harder to fit and we are interested in the effects of this wider, off-center shape to the total distribution of  $S + pBG$ , because that is what we would use as our nominator of the efficiency definition.

The fits performed are shown in Figures 52-55. Some of the fits are challenging because of the lack of a clear signal shape. For such fits, we try a double-Gaussian or single-Gaussian as the signal shape. If the  $M_{BC}$  distribution has almost non-visible signal shape, only ARGUS background is used to fit the background. For the signal yield calculation for such fits, the background yield in the signal region ( $1.86 < M_{BC} < 1.87 \text{ GeV}/c^2$ ) is subtracted from the number of entries in the same region. This method is used in the  $K_s$  mass sideband study, which is detailed in Section 6.1.6, and also for some of the peaking background only fits.

The peaking background fractions for some of the modes are below 1%. This is small enough that our efficiency definition should take care of it. For the numerator of the efficiency we use the  $S + pBG$  yields, and therefore, the resulting efficiency is higher than just using the  $S$  yields. This definition of the efficiency will take care of these additional events so that it is equivalent to an explicit subtraction of the background. More details about the efficiency is given in Section 7. For the  $CP$  tags that have larger background fractions, detailed studies are explained in the following sections.

Background for the  $\pi^+\pi^-$  mode is small, about 0.5%. The  $M_{BC}$  distribution for the peaking background show a very small peak on top of the ARGUS shape. Background for the  $K^+K^-$  mode is also small, about 0.9%. However, the  $M_{BC}$  distribution again does not have a clear ARGUS shape. For  $K_s\eta$ , the peaking-background shape is similar to  $K^+K^-$ , and the resulting fraction is

negligible.

**Table 28:**  $M_{BC}$  yields and the resulting peaking background (pBG) ratios for CP tags.

Mode	CP	pBG yield	Signal only yield	(S + pBG) yield	pBG/S	((S + pBG) - S)/S
$K_s\pi^0$	CP-	$(5.5 \pm 0.9) \times 10^2$	$(3.570 \pm 0.007) \times 10^5$	$(3.587 \pm 0.007) \times 10^5$	$0.00153 \pm 0.00024$	0.005
$\pi^+\pi^-$	CP+	$(1.7 \pm 0.8) \times 10^2$	$(1.0297 \pm 0.0035) \times 10^5$	$(1.025 \pm 0.005) \times 10^5$	$0.0017 \pm 0.0008$	-0.005
$K^+K^-$	CP+	$(2.20 \pm 0.16) \times 10^3$	$(2.698 \pm 0.006) \times 10^5$	$(2.742 \pm 0.007) \times 10^5$	$0.0081 \pm 0.0006$	0.016
$K_s\pi^0\pi^0$	CP+	$(6.7 \pm 0.6) \times 10^3$	$(7.40 \pm 0.04) \times 10^4$	$(8.15 \pm 0.08) \times 10^4$	$0.090 \pm 0.008$	0.102
$K_s\eta'(\pi^+\pi^-\eta)$	CP-	$(0.3 \pm 1.8) \times 10^2$	$(1.459 \pm 0.015) \times 10^4$	$(1.476 \pm 0.020) \times 10^4$	$0.002 \pm 0.012$	0.011
$K_s\eta'(\rho\gamma)$	CP-	$(3.49 \pm 0.17) \times 10^3$	$(4.072 \pm 0.027) \times 10^4$	$(4.39 \pm 0.04) \times 10^4$	$0.086 \pm 0.004$	0.078
$K_s\eta$	CP-	$(2.92 \pm 0.19) \times 10^3$	$(4.522 \pm 0.024) \times 10^4$	$(4.305 \pm 0.035) \times 10^4$	$0.064 \pm 0.004$	-0.048
$K_s\omega$	CP-	$(1.223 \pm 0.021) \times 10^4$	$(8.06 \pm 0.04) \times 10^4$	$(9.19 \pm 0.04) \times 10^4$	$0.1517 \pm 0.0027$	0.140

**Table 29:** Individual contribution of the tags to the total background and the ST yield. pBG' is the peaking background calculated using the formula  $(S + pBG) - S$ .

Tag	CP	pBG/ $\Sigma pBG_{CP}$	(S + pBG)/ $\Sigma(S + pB)_{CP}$	pBG'/ $\Sigma S_{CP}$
$\pi^+\pi^-$	CP+	$0.019 \pm 0.009$	$0.224 \pm 0.001$	-0.001
$K^+K^-$	CP+	$0.242 \pm 0.024$	$0.599 \pm 0.002$	0.010
$K_s\pi^0\pi^0$	CP+	$0.738 \pm 0.082$	$0.178 \pm 0.002$	0.017
$K_s\pi^0$	CP-	$0.028 \pm 0.005$	$0.649 \pm 0.002$	0.003
$K_s\eta'(\pi^+\pi^-\eta)$	CP-	$0.002 \pm 0.009$	$0.027 \pm 0.000$	0.000
$K_s\eta'(\rho\gamma)$	CP-	$0.182 \pm 0.009$	$0.079 \pm 0.001$	0.006
$K_s\eta$	CP-	$0.152 \pm 0.010$	$0.078 \pm 0.001$	-0.004
$K_s\omega$	CP-	$0.636 \pm 0.017$	$0.166 \pm 0.001$	0.021

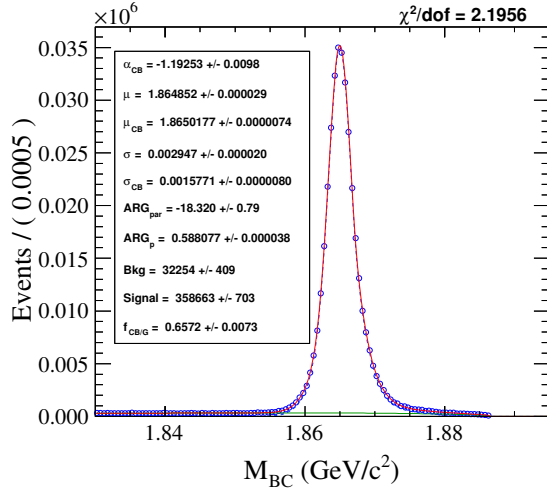
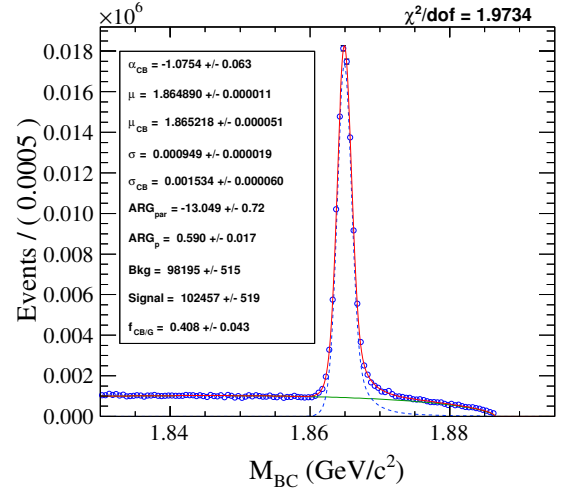
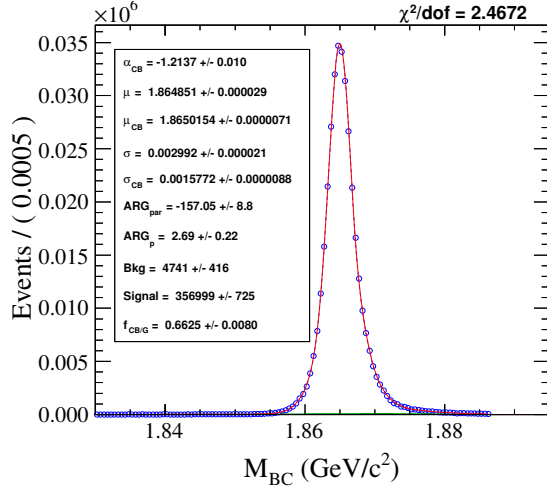
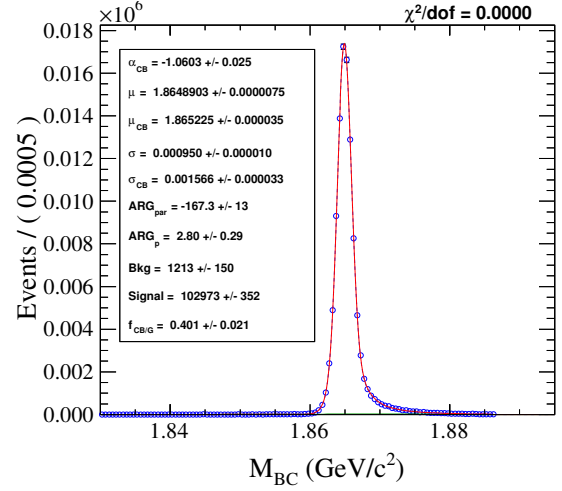
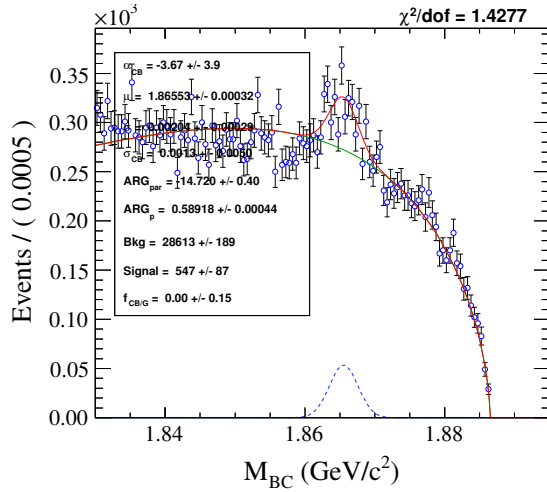
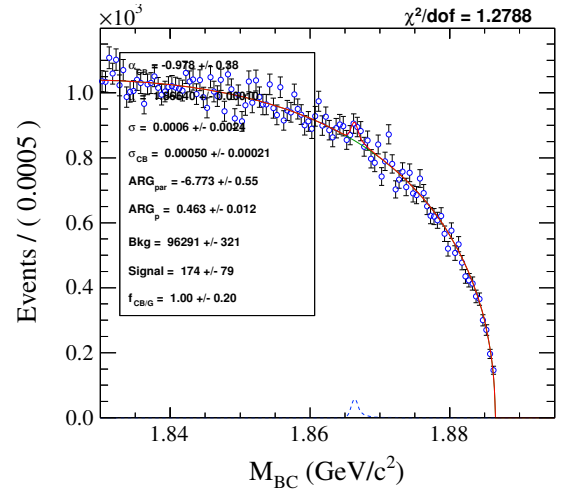
(a)  $K_s\pi^0$  yield(b)  $\pi^-\pi^+$  yield(c) Signal for  $K_s\pi^0$ (d) Signal for  $\pi^-\pi^+$ (e) Peaking background for  $K_s\pi^0$ (f) Peaking background for  $\pi^-\pi^+$ 

Figure 52: ST candidate, signal only, and peaking background fits of CP tags.

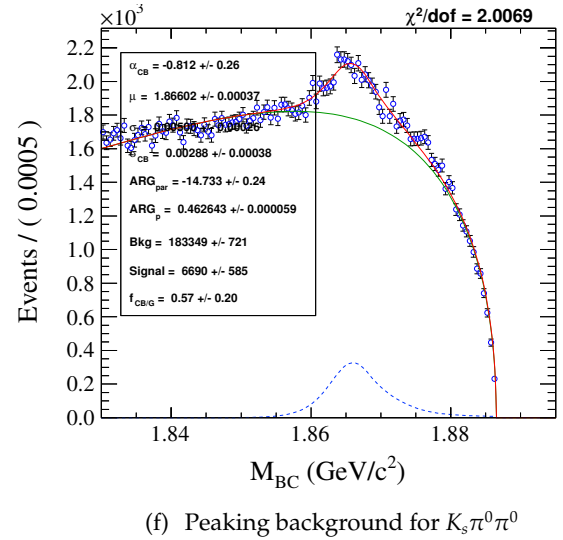
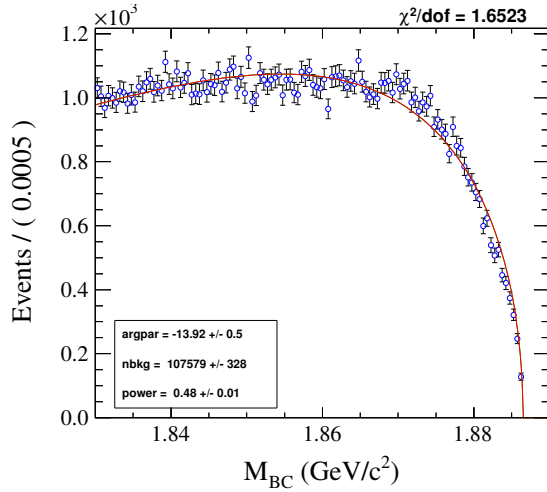
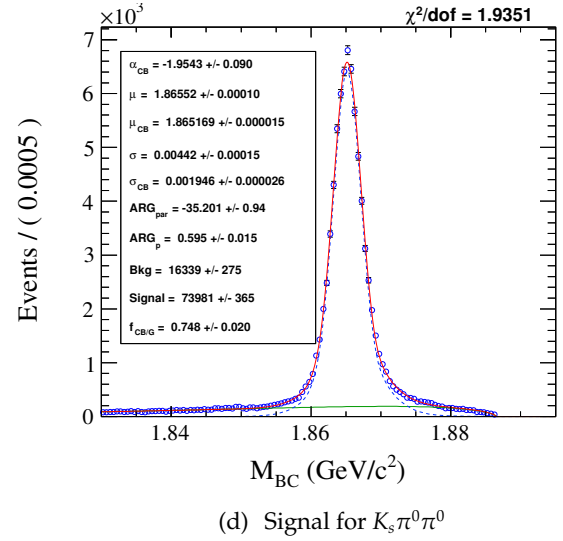
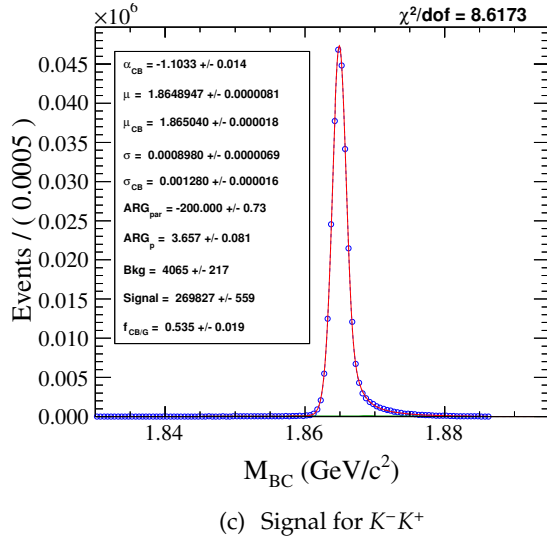
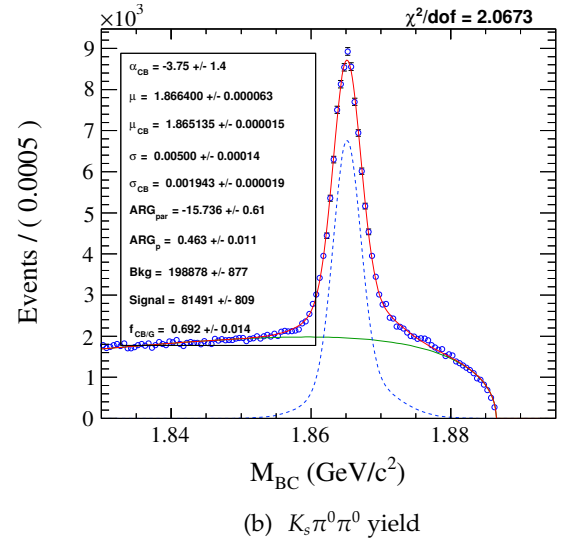
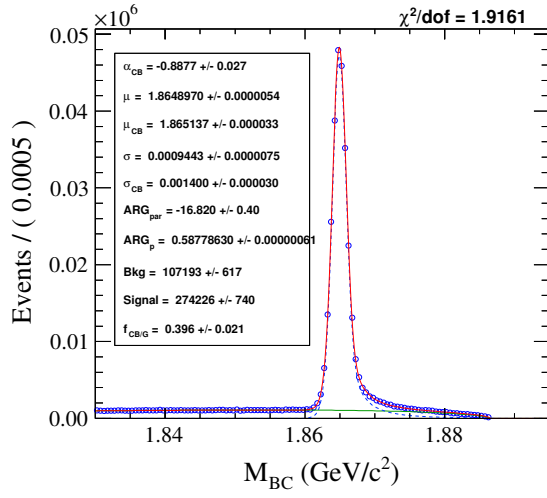
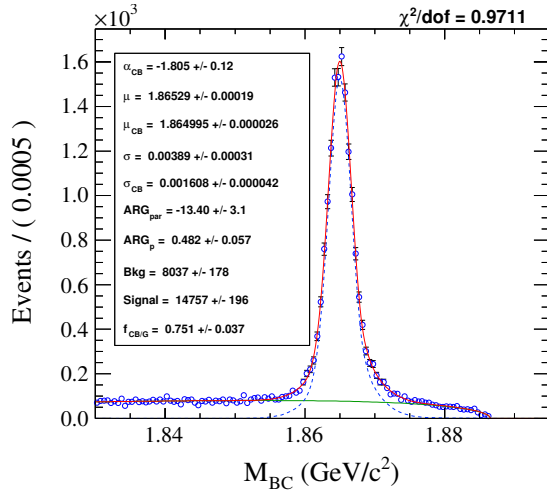
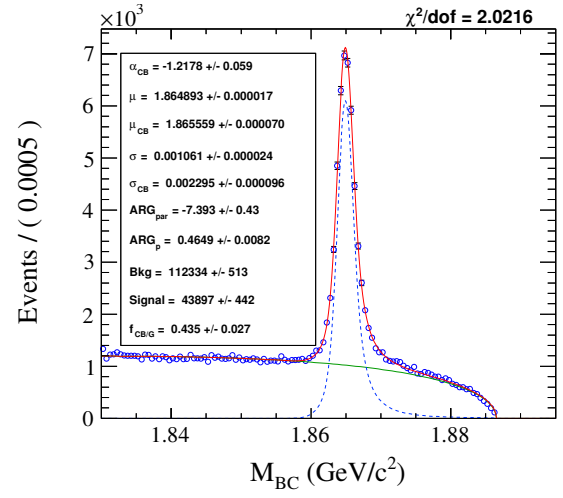
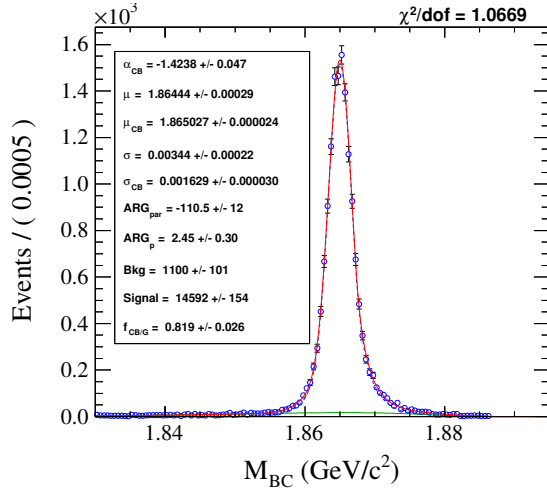
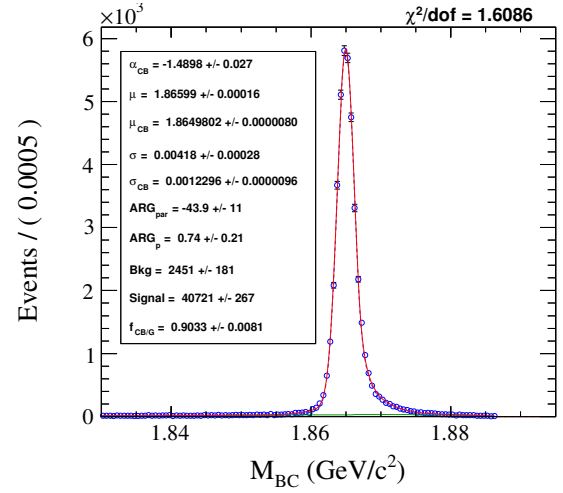
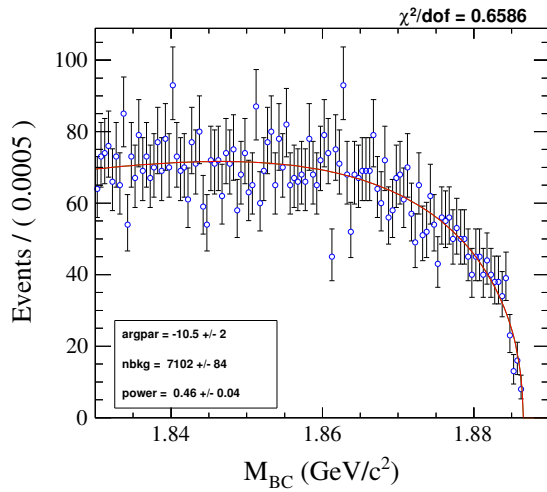
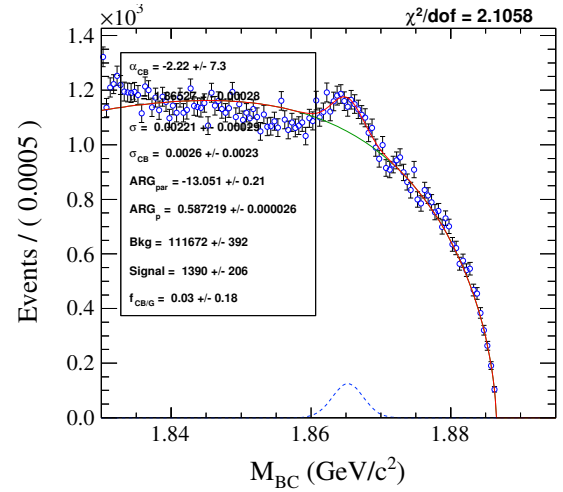
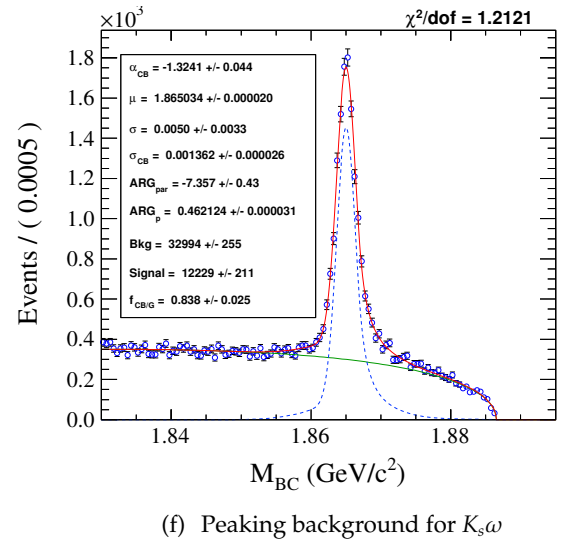
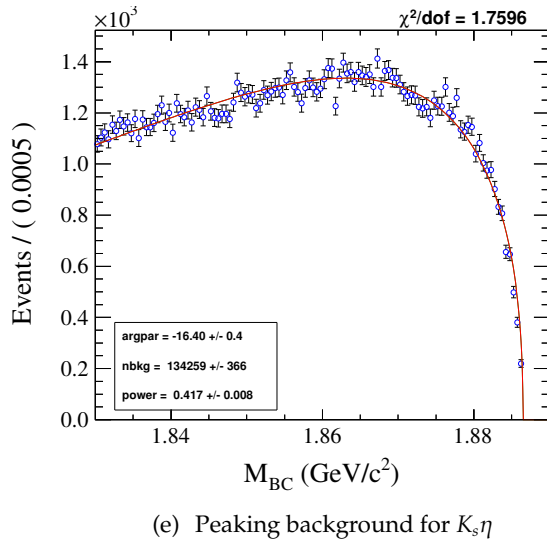
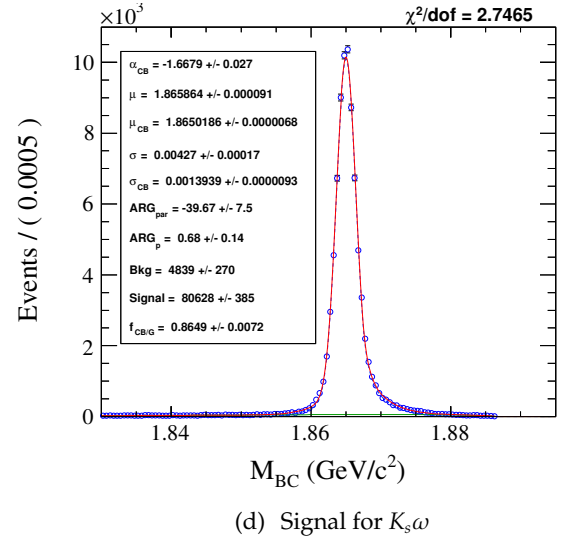
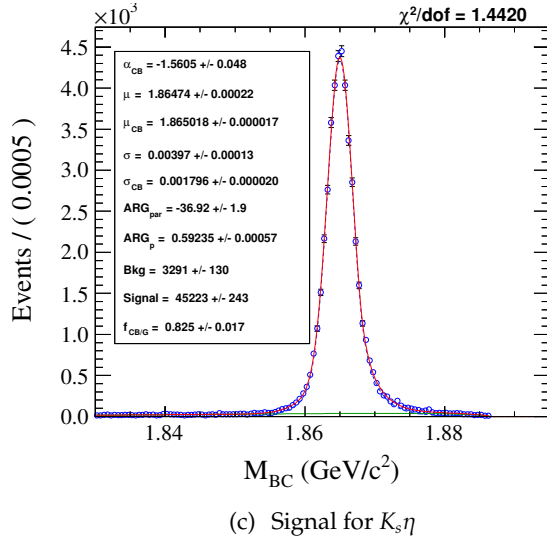
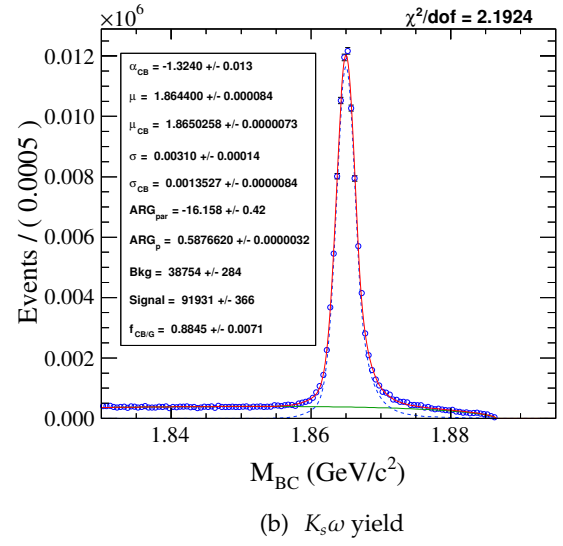
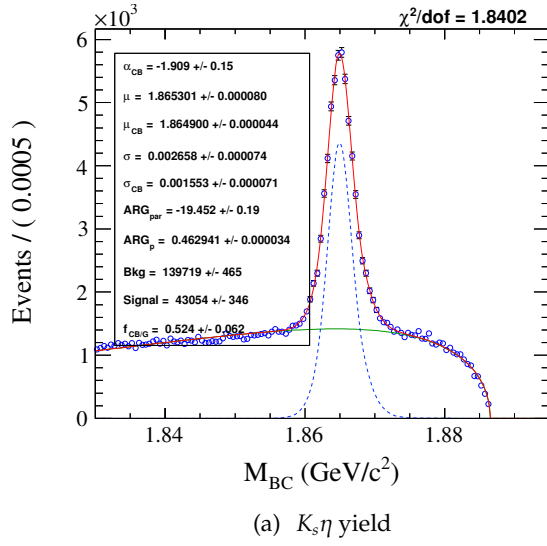


Figure 53: ST candidate, signal only, and peaking background fits of CP tags.

(a)  $K_s \eta' (\pi^+ \pi^- \eta)$  yield(b)  $K_s \eta' (\rho \gamma)$  yield(c) Signal for  $K_s \eta' (\pi^+ \pi^- \eta)$ (d) Signal for  $K_s \eta' (\rho \gamma)$ (e) Peaking background for  $K_s \eta' (\pi^+ \pi^- \eta)$ (f) Peaking background for  $K_s \eta' (\rho \gamma)$ **Figure 54:** ST candidate, signal only, and peaking background fits of CP tags.





**Figure 55:** ST candidate, signal only, and peaking background fits of CP tags.

### 6.1.1 Peaking Background for Combined $CP$ Tags

$CP$ -tag candidates are combined to perform analogous  $pBG$  fits: ST candidates, signal only, and peaking background for both  $CP$  tag combinations. These fits are shown in Figure 56 for both  $CP+$  and  $CP-$ . Background fractions are given in Table 30.

**Table 30:** Yields from the fits and the resulting peaking-background fractions for the combined  $CP+$  and  $CP-$  tags.

$CP$	$pBG$ yield	Signal only yield	$(S + pBG)$ yield	$pBG/S$	$((S + pBG) - S)/S$
$CP+$	$(8.7 \pm 0.5) \times 10^3$	$(4.447 \pm 0.008) \times 10^5$	$(4.531 \pm 0.011) \times 10^5$	$0.0195 \pm 0.0010$	0.019
$CP-$	$(1.093 \pm 0.027) \times 10^4$	$(5.395 \pm 0.009) \times 10^5$	$(5.556 \pm 0.012) \times 10^5$	$0.0203 \pm 0.0005$	0.030

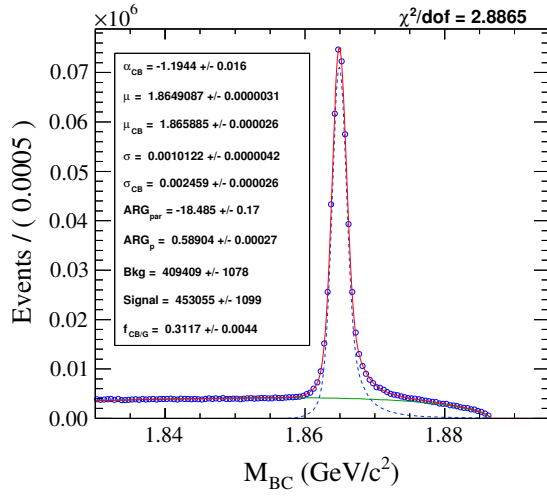
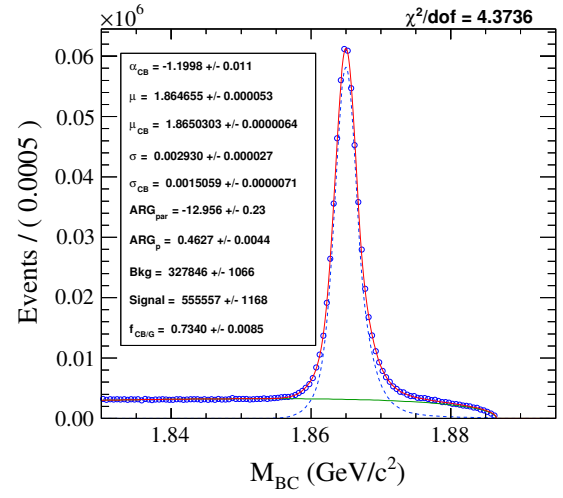
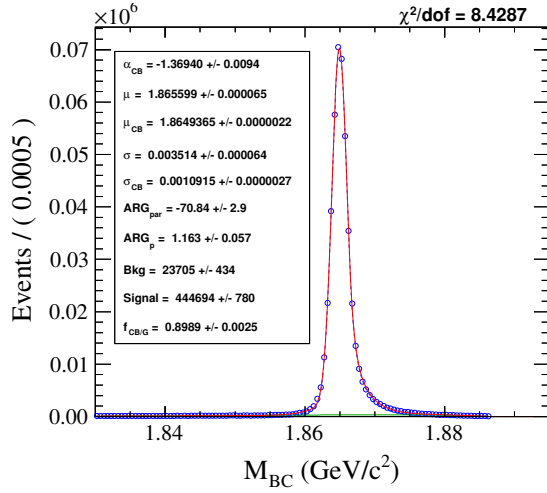
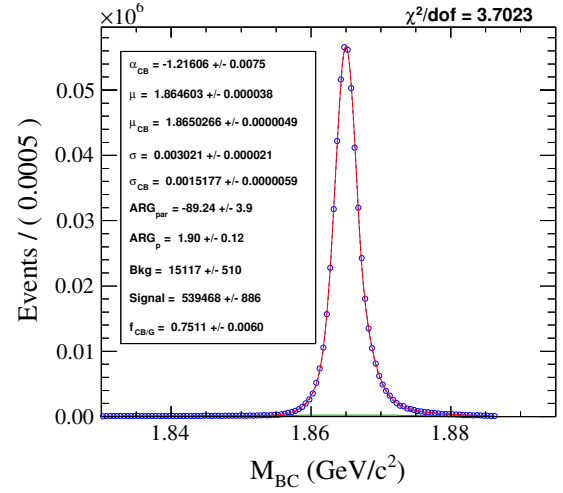
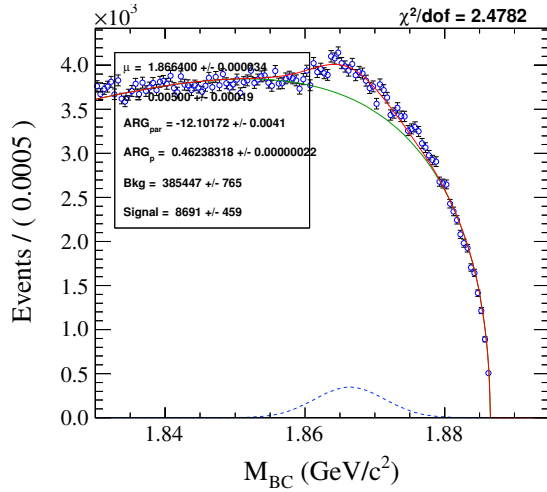
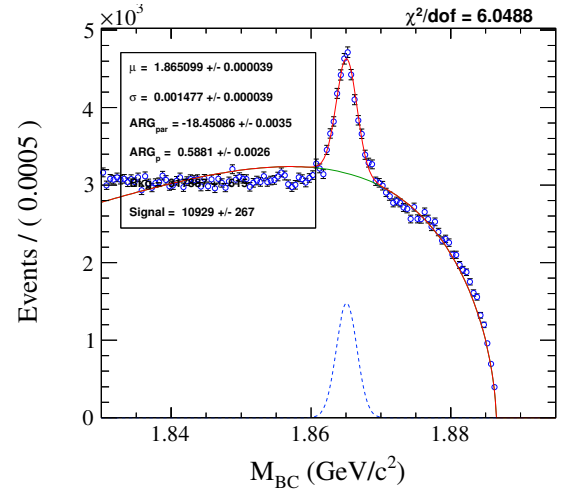
(a) Total yield  $CP+$ (b) Total yield  $CP-$ (c) Signal only for  $CP+$ (d) Signal only for  $CP-$ (e) Peaking background for  $CP+$ (f) Peaking background for  $CP-$ 

Figure 56: ST candidate, signal only, and the peaking background fits to the CP combined tags.

### 6.1.2 Peaking Background for $K_s\pi^0\pi^0$

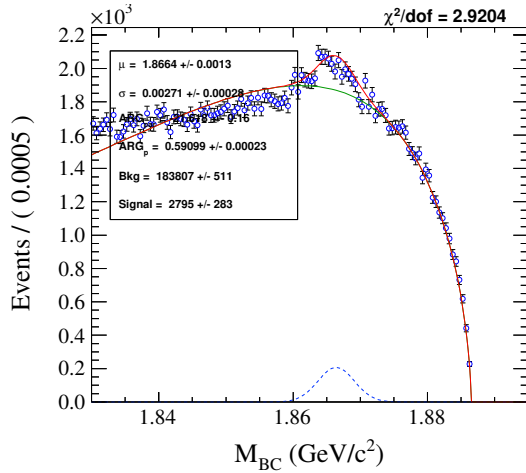
The  $K_s\pi^0\pi^0$  mode has 11.7% background. Possible contributions to the background are  $\pi^-\pi^+\pi^0\pi^0$ ,  $K_sK_s$ ,  $K_s\pi^-\pi^+$ ,  $\omega\pi^0$ , and  $\eta\pi^0$  decays. These decays are studied using the MC truth information and the results are presented in Tables 31 and 32. Corresponding fits are shown in Figures 57 and 58. Out of the possible decay channels that are studied, none of them dominates the background and the result is inconclusive. Efficiency definition explained in 7 will take additional candidates into account.

**Table 31:** Peaking-background study yields for the  $K_s\pi^0\pi^0$  mode.

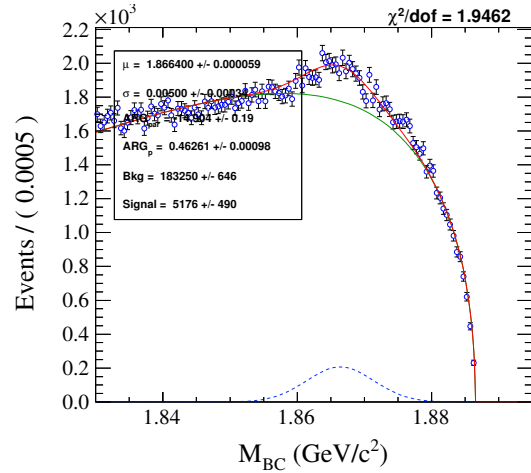
Mode	CP	pBG yield	Signal only yield	(S + pBG) yield	pBG/S	((S + pBG) - S)/S
$K_s\pi^0\pi^0$	CP+	$(6.7 \pm 0.6) \times 10^3$	$(7.40 \pm 0.04) \times 10^4$	$(8.15 \pm 0.08) \times 10^4$	$0.090 \pm 0.008$	0.102

**Table 32:** Peaking background fractions for  $K_s\pi^0\pi^0$  mode.

Contribution to pBG	Yield	Fraction of total bg
All but $\pi^-\pi^+\pi^0\pi^0$	$(2.80 \pm 0.28) \times 10^3$	$0.418 \pm 0.056$
All but $K_sK_s$	$(5.2 \pm 0.5) \times 10^3$	$0.774 \pm 0.100$
All but $K_s\pi^-\pi^+$	$(5.9 \pm 1.0) \times 10^3$	$0.880 \pm 0.174$
All but ( $\pi^-\pi^+\pi^0\pi^0$ , $K_sK_s$ , $K_s\pi^-\pi^+$ , $\omega\pi^0$ , and $\eta\pi^0$ )	$(6.5 \pm 3.1) \times 10^2$	$0.097 \pm 0.048$

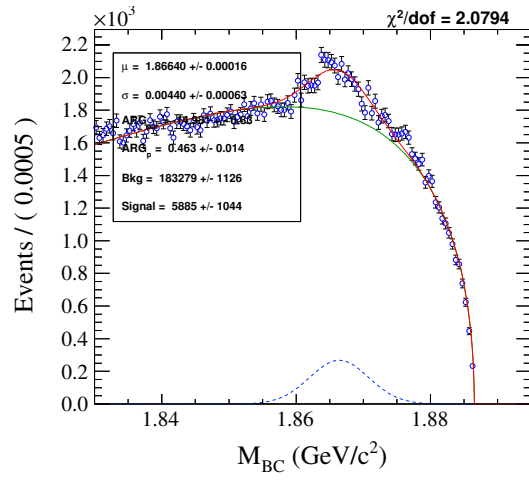
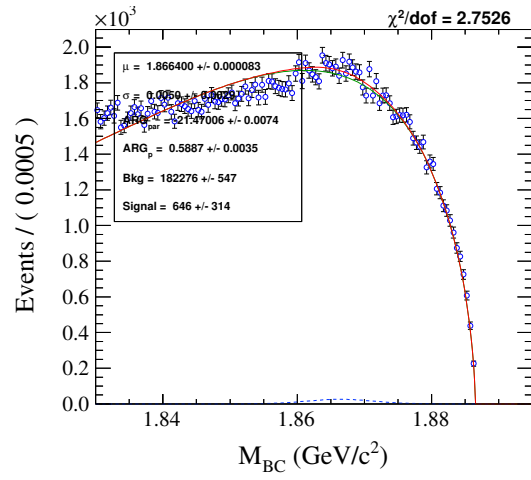


(a)  $K_s\pi^0\pi^0$  candidates with signal and  $\pi^-\pi^+\pi^0\pi^0$  removed.



(b)  $K_s\pi^0\pi^0$  candidates with signal,  $K_sK_s$  removed.

**Figure 57:**  $M_{BC}$  fit to the peaking background of  $K_s\pi^0\pi^0$  with various contributions removed.

(a)  $K_s\pi^0\pi^0$  candidates with signal and  $K_s\pi^-\pi^+$  removed.(b)  $K_s\pi^0\pi^0$  candidates with signal,  $\pi^-\pi^+\pi^0\pi^0$ ,  $K_sK_s$ ,  $K_s\pi^-\pi^+$ ,  $\omega\pi^0$ , and  $\eta\pi^0$  removed**Figure 58:**  $M_{BC}$  fit to the peaking background of  $K_s\pi^0\pi^0$  with various contributions removed.

### 6.1.3 Peaking Background for $K_s\eta'(\pi^+\pi^-\eta)$

The  $K_s\eta'(\pi^+\pi^-\eta)$  mode has about 2% background before sideband subtraction. The  $\eta'$  mass distribution is plotted in Figure 59. Side band regions are defined as  $0.85 < M_{\eta'} < 0.90 \text{ GeV}/c^2$  (low side),  $0.938 < M_{\eta'} < 0.978$  for the signal region, and  $1.00 < M_{\eta'} < 1.05 \text{ GeV}/c^2$  for the (high side). Fits are performed to the corresponding  $M_{BC}$  distributions of these mass regions and given in Figure 60 for signal region and Figure 61 for the sidebands. The two-dimensional distribution of  $M_{BC}$  vs.  $M_{\eta'}$  is shown in Figure 62.

The peaking background fraction is very small for this mode and therefore no mass sideband subtraction is performed.

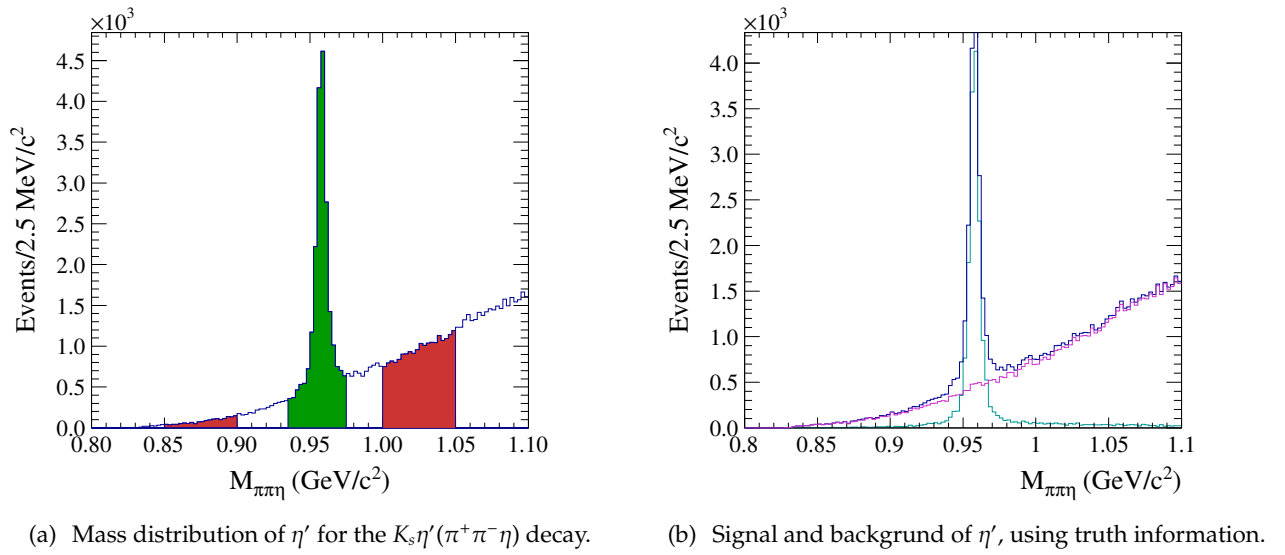


**Figure 59:** Left: the  $\eta'$  mass distribution for the  $K_s\eta'(\pi^+\pi^-\eta)$  candidates. Green is the signal region, red denotes the sideband regions. Right: signal events (red) and background (green), and total (blue).

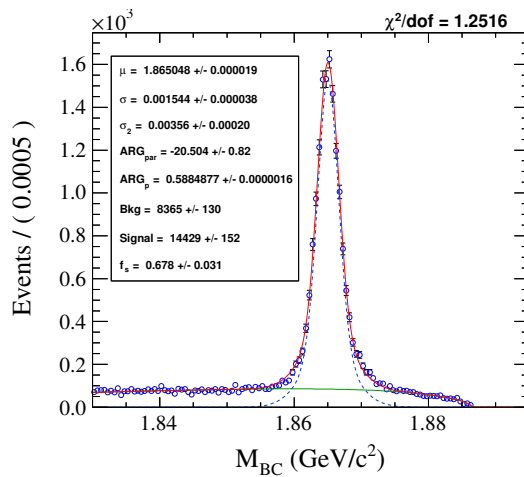


**Figure 60:**  $M_{BC}$  fit to the  $K_s\eta'(\pi^+\pi^-\eta)$  signal region in the  $\eta'$  mass distribution.

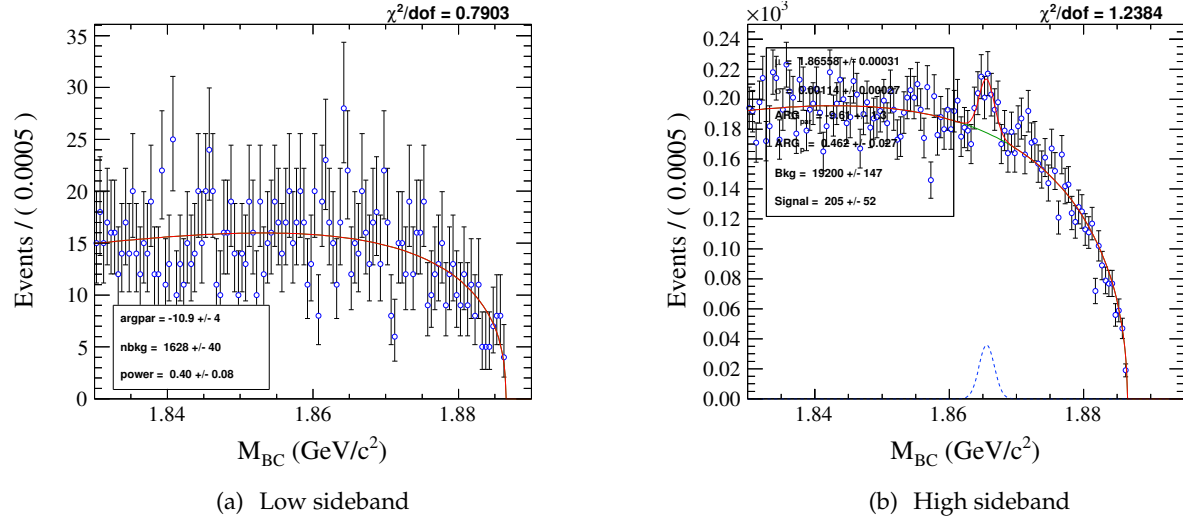


**Figure 61:**  $M_{BC}$  fit to the  $K_s \eta' (\pi^+ \pi^- \eta)$  sideband regions in the  $\eta'$  mass distribution.

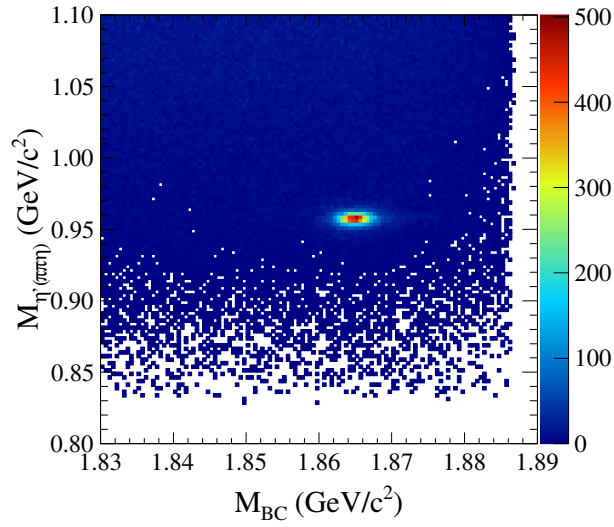


**Figure 62:**  $M_{BC}$  vs  $M_{\eta'}$  distribution of  $K_s \eta' (\pi^+ \pi^- \eta)$ .

### 6.1.4 Peaking Background for $K_s\eta'(\rho\gamma)$

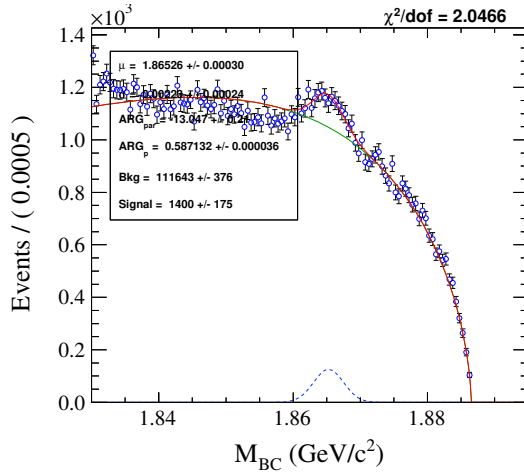
The  $K_s\eta'(\rho\gamma)$  mode has about 3.5% background before the mass sideband subtraction. This subtraction is explained in Section 4.1.1. A separate study was done to classify which decay modes contribute to the peaking background using the MC truth information. Suspected decay modes that could be contributing to the peaking background for this mode are  $K_s\pi^-\pi^+\pi^0$ ,  $K_s\omega(\pi^-\pi^+\pi^0)$ , and  $K_s\eta(\pi^-\pi^+\pi^0)$ . Only the first channel is studied separately and others are combined. Results are presented in Tables 33 and 34, and the corresponding fits are shown in Figures 63 and 64. Results show that more than half of the background is due to the decay  $K_s\pi^-\pi^+\pi^0$ . The mass sideband subtraction performed for this mode will reduce the peaking background.

**Table 33:** Yields for the peaking-background study yields for the  $K_s\eta'(\rho\gamma)$  mode.

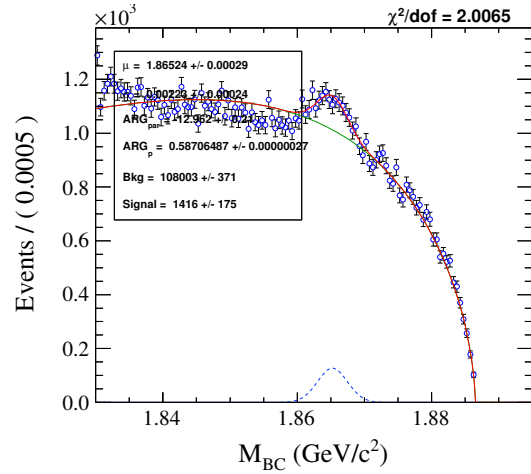
Mode	CP	pBG yield	Signal only yield	(S + pBG) yield	pBG/S	((S + pBG) - S)/S
$K_s\eta'(\rho\gamma)$	CP-	$(3.49 \pm 0.17) \times 10^3$	$(4.072 \pm 0.027) \times 10^4$	$(4.39 \pm 0.04) \times 10^4$	$0.086 \pm 0.004$	0.078

**Table 34:** Peaking background fractions for the  $K_s\eta'(\rho\gamma)$  mode.

Contribution to Bg	Yield	Fraction of total pBG
All but $K_s\pi^-\pi^+\pi^0$	$(1.40 \pm 0.18) \times 10^3$	$1.007 \pm 0.195$
All but ( $K_s\pi^-\pi^+\pi^0$ and $K_s\omega$ )	$(1.42 \pm 0.18) \times 10^3$	$1.018 \pm 0.197$
All but ( $K_s\pi^-\pi^+\pi^0$ , $K_s\omega$ , and $K_s\eta$ )	$(1.42 \pm 0.17) \times 10^3$	$1.019 \pm 0.193$



(a)  $K_s\eta'(\rho\gamma)$  with signal and  $K_s\pi^-\pi^+\pi^0$  removed.



(b)  $K_s\eta'(\rho\gamma)$  with signal,  $K_s\pi^-\pi^+\pi^0$ , and  $K_s\omega$  removed.

**Figure 63:** Fit to the  $M_{BC}$  distribution for peaking background of  $K_s\eta'(\rho\gamma)$  with various contributions removed.



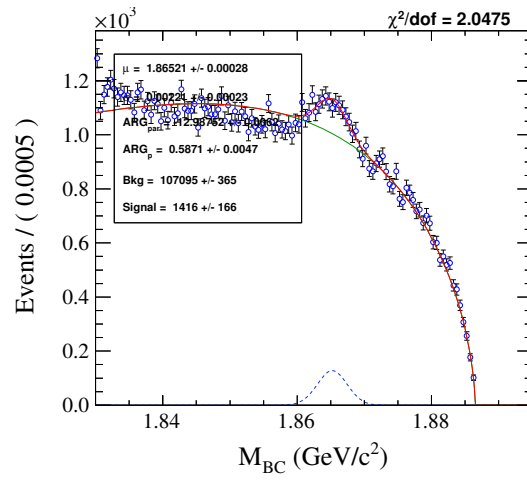


**Figure 64:**  $M_{\text{BC}}$  fit to the  $K_s \eta' (\rho \gamma)$  with signal,  $K_s \pi^- \pi^+ \pi^0$ ,  $K_s \omega$ , and  $K_s \eta$  removed.

### 6.1.5 Peaking Background Study of $K_s\omega$

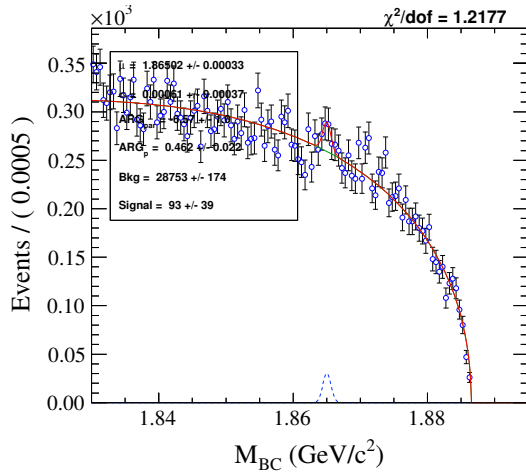
The  $K_s\omega$  mode has about 14.5% background before sideband subtraction. A mass sideband study was carried out, as detailed in Section 4.1.2. A separate study is performed to classify which decay modes contribute to the peaking background. Suspected decay modes that contribute to the peaking background for this mode are  $K_s\pi^-\pi^+\pi^0$  and  $K_sK_s\pi^0$ . Results are presented in Table 35 and corresponding fits are shown in Figures 65 and 66. Results show that almost all the background for this mode is due to the decay channel  $K_s\pi^-\pi^+\pi^0$ , where the non-resonant  $\pi^+\pi^-\pi^0$  is mistaken for an  $\omega$  decay. The mass sideband subtraction reduces this background.

**Table 35:** Yields from the peaking-background study yield for the  $K_s\omega$  mode.

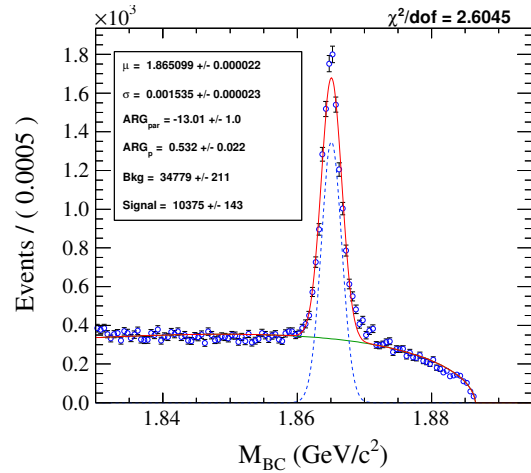
Mode	CP	pBG yield	Signal only yield	(S + pBG) yield	pBG/S	((S + pBG) - S)/S
$K_s\omega$	CP-	$(1.223 \pm 0.021) \times 10^4$	$(8.06 \pm 0.04) \times 10^4$	$(9.19 \pm 0.04) \times 10^4$	$0.1517 \pm 0.0027$	0.140

**Table 36:** Peaking background fractions for the  $K_s\eta'(\rho\gamma)$  mode.

Contribution to Bg	Yield	Fraction of total bg
All but $K_s\pi^-\pi^+\pi^0$	$(9 \pm 4) \times 10^1$	$0.008 \pm 0.003$
All but $K_sK_s\pi^0$	$(1.038 \pm 0.014) \times 10^4$	$0.848 \pm 0.019$
All but ( $K_s\pi^-\pi^+\pi^0$ and $K_sK_s\pi^0$ )	$(7 \pm 4) \times 10^1$	$0.006 \pm 0.003$



(a)  $K_s\omega$  with signal and  $K_s\pi^-\pi^+\pi^0$  removed.



(b)  $K_s\omega$  with signal,  $K_sK_s\pi^0$  removed.

**Figure 65:**  $M_{BC}$  fit to the peaking background of  $K_s\omega$  with various contributions removed.

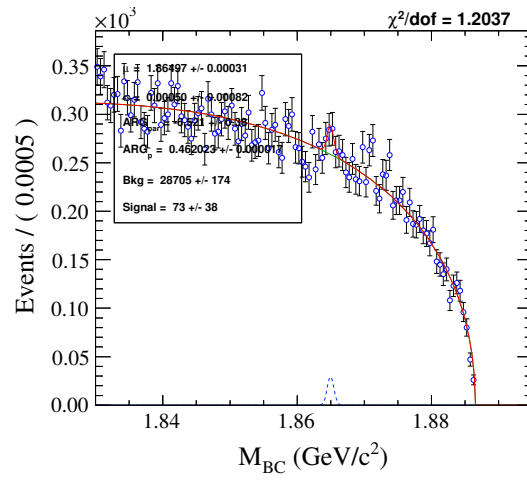


*Figure 66:  $M_{BC}$  fit to the  $K_s\omega$  with signal with  $K_s\pi^-\pi^+\pi^0$  and  $K_sK_s\pi^0$  removed.*

### 6.1.6 Mass Sideband Study of $K_s$ for the Tag Modes

Six out of eight tag modes include a  $K_s$ . Therefore sideband regions in the  $K_s$  mass distribution are investigated to see if non-resonant  $\pi^+\pi^-$  decays contribute to the peaking background. Low-mass side region is defined as  $0.400 < M_{\pi^+\pi^-} < 0.424 \text{ GeV}/c^2$ , high-side as  $0.576 < M_{\pi^+\pi^-} < 0.600 \text{ GeV}/c^2$ , and the signal region as  $0.487 < M_{\pi^+\pi^-} < 0.511 \text{ GeV}/c^2$ . Yields of the  $M_{BC}$  fits are summarized in Table 37 for the MC sample and in Table 38 for the data. All the other requirements on the  $K_s$  selection are still in place and listed in Table 7.

Fits used in the calculations are shown in Figures 67-69 for the MC sample and in Figures 70-72 for the data sample. Most of the low- and high-sideband distributions for the data sample do not have a clear signal shape, and therefore, are fit only using an ARGUS background function. The yields are calculated as explained in Section 6.1. This method is also used for some of the MC sideband regions.

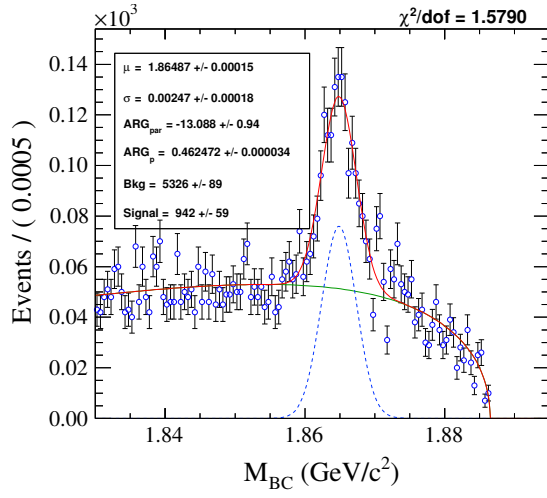
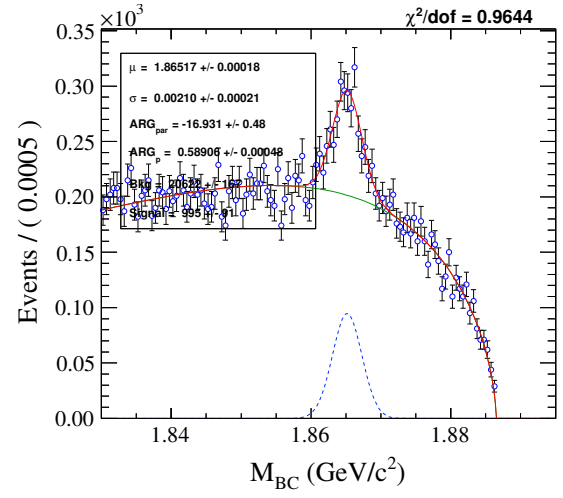
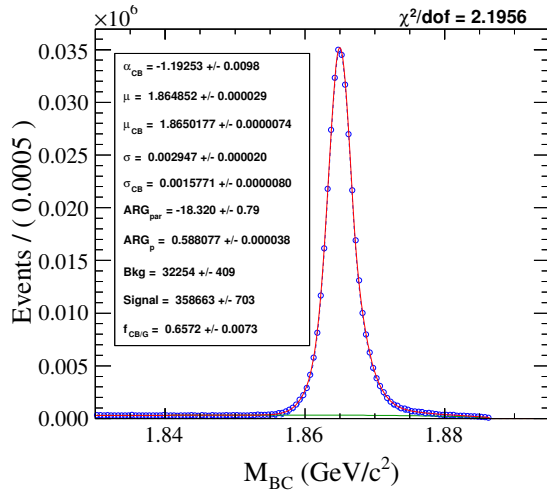
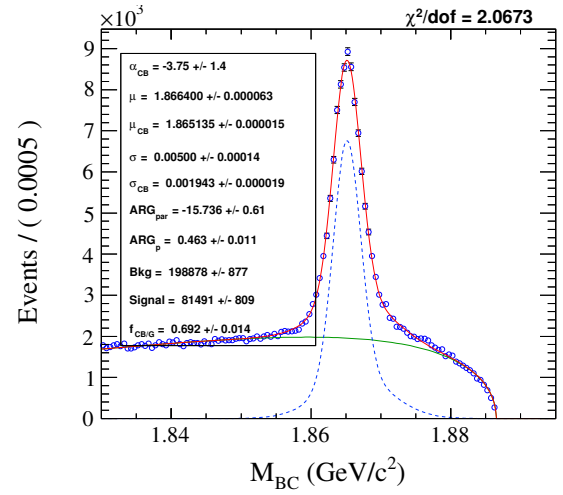
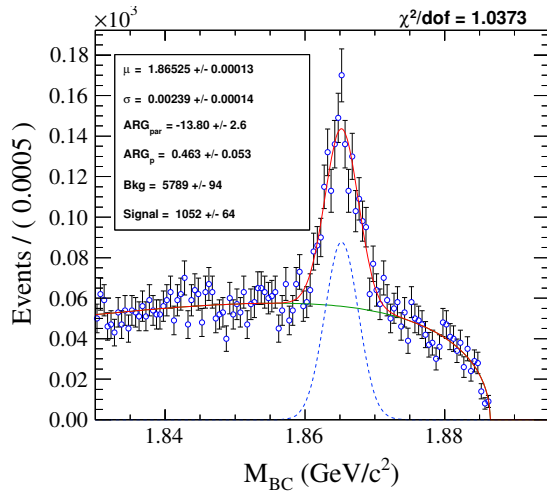
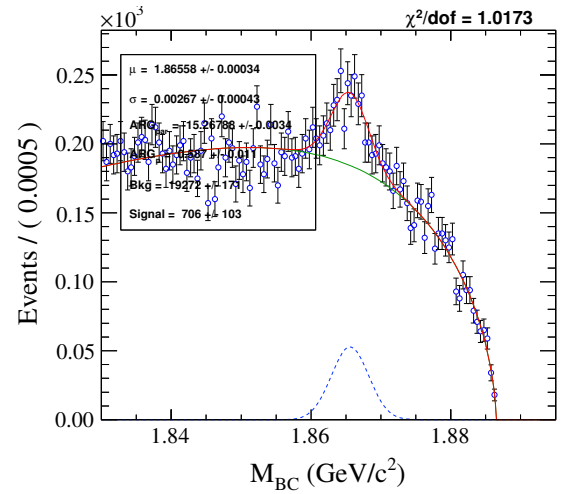
The peaking-background fraction due to the non-resonant  $\pi^+\pi^-$  decays is below a percent for almost all the tag modes in the MC, with very similar results for the data. We consider this peaking-background contribution to be negligible and no subtraction is performed. Efficiency definition in the analysis should take care of any excess events. More details are given in Section 7.

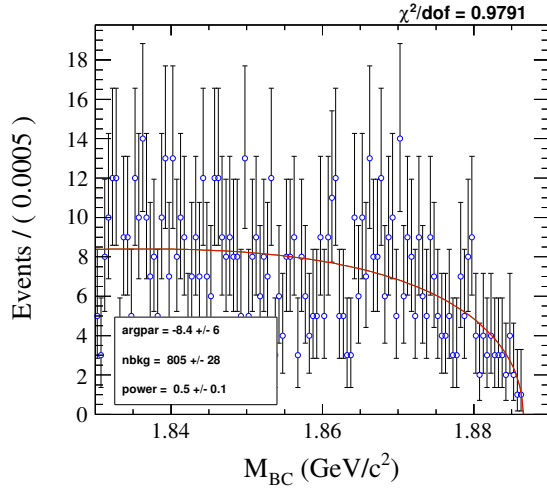
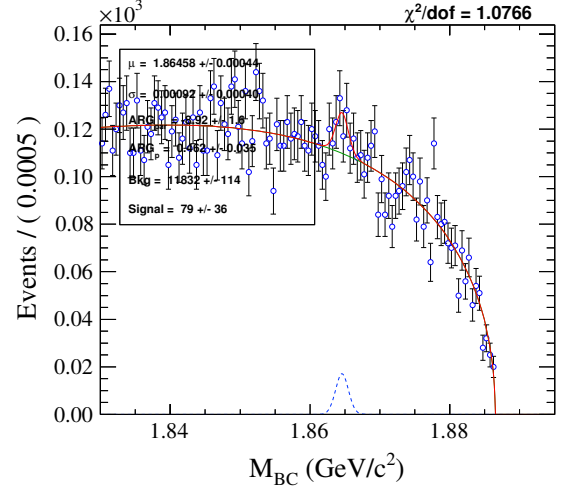
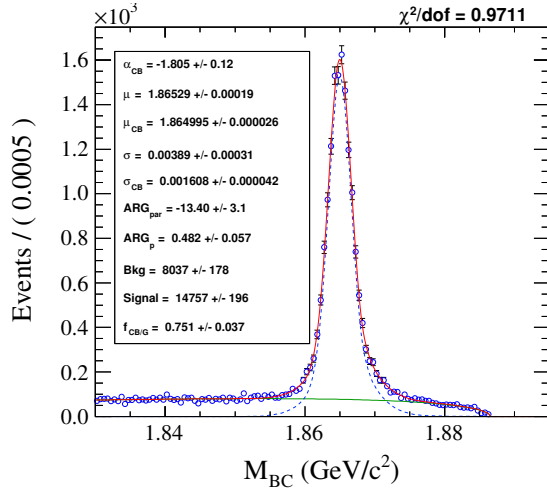
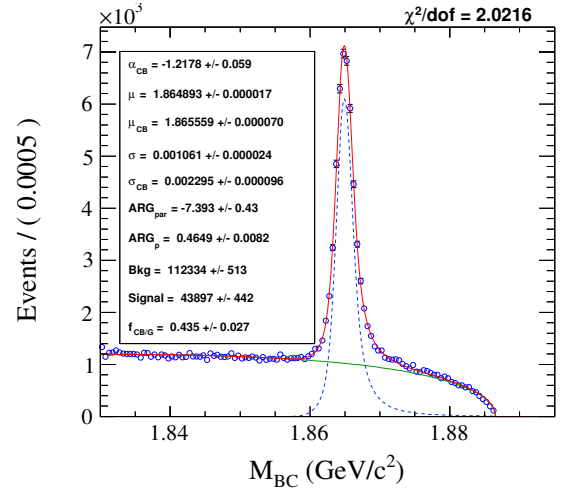
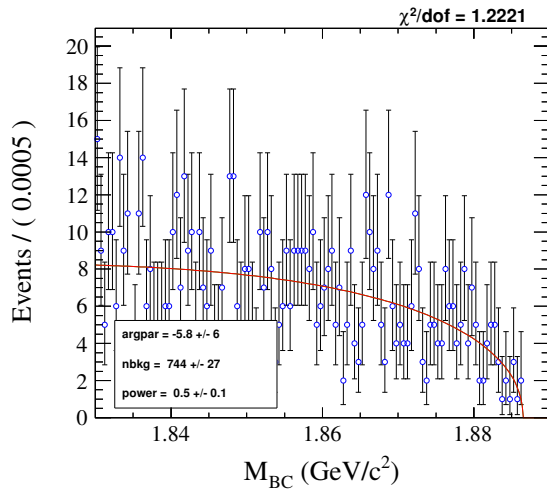
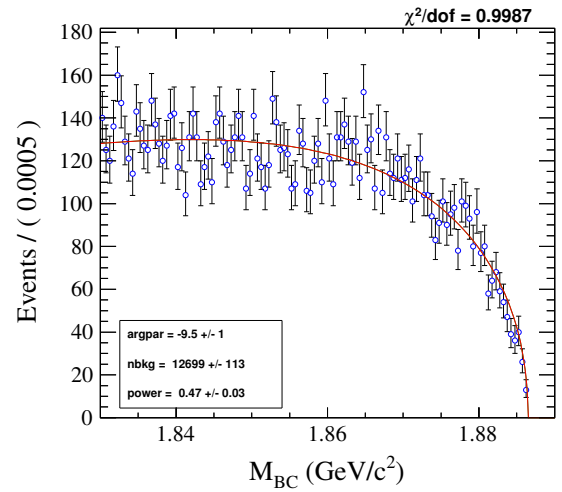
**Table 37:** Yields from the three mass regions of the  $\pi^+\pi^-$  distributions and their resulting peaking-background fractions from the MC.

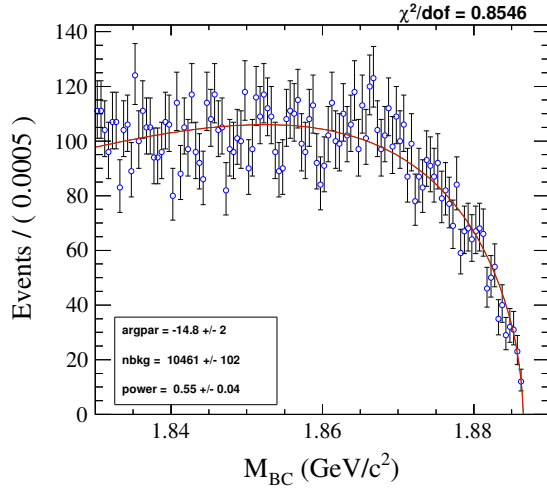
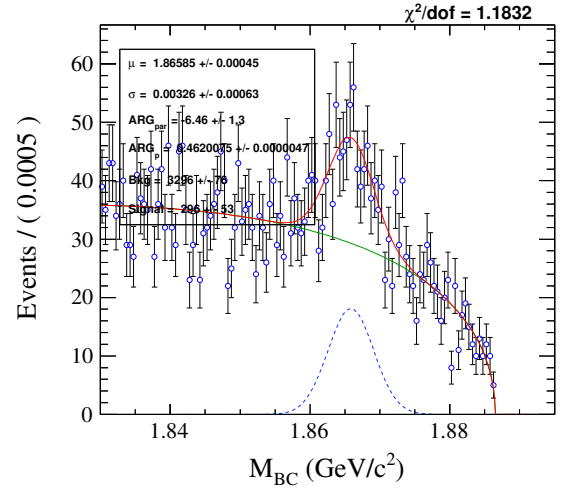
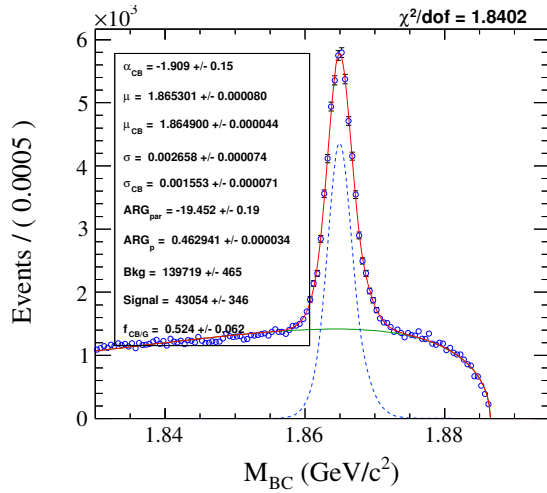
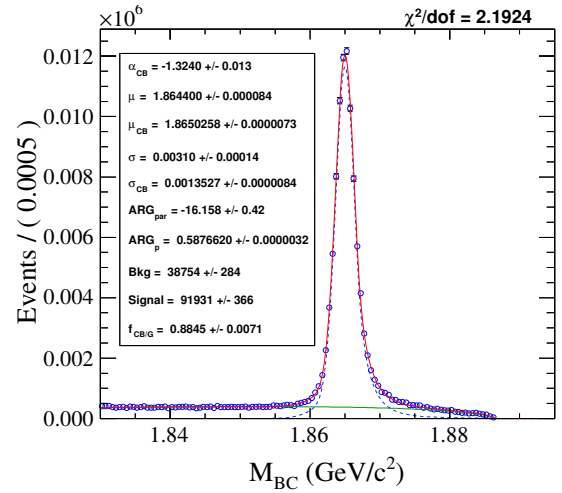
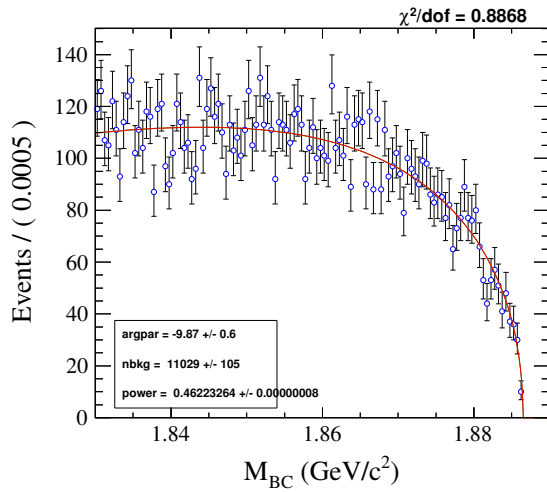
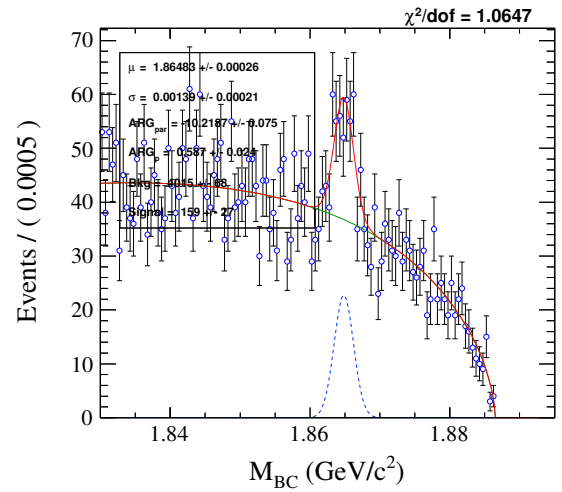
Tag	Low-side Yield	Signal Yield	High-side Yield	Fraction of Bg (average)
$K_s\pi^0$	$(9.4 \pm 0.6) \times 10^2$	$(3.587 \pm 0.007) \times 10^5$	$(1.05 \pm 0.06) \times 10^3$	$0.003 \pm 0.000$
$K_s\pi^0\pi^0$	$(9.9 \pm 0.9) \times 10^2$	$(8.15 \pm 0.08) \times 10^4$	$(7.1 \pm 1.0) \times 10^2$	$0.010 \pm 0.001$
$K_s\eta'(\pi^+\pi^-\eta)$	$33 \pm 14$	$(1.476 \pm 0.020) \times 10^4$	$11 \pm 13$	$0.001 \pm 0.001$
$K_s\eta'(\rho\gamma)$	$(8 \pm 4) \times 10^1$	$(4.39 \pm 0.04) \times 10^4$	$(3.7 \pm 0.6) \times 10^2$	$0.005 \pm 0.001$
$K_s\eta$	$(2.9 \pm 0.5) \times 10^2$	$(4.305 \pm 0.035) \times 10^4$	$(2.4 \pm 0.5) \times 10^2$	$0.006 \pm 0.001$
$K_s\omega$	$(3.0 \pm 0.5) \times 10^2$	$(9.19 \pm 0.04) \times 10^4$	$159 \pm 27$	$0.002 \pm 0.000$

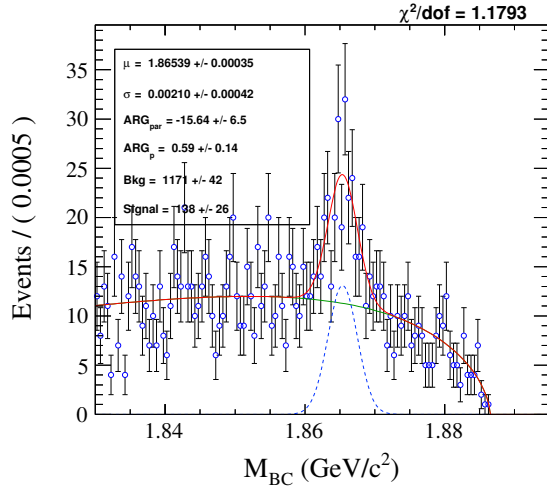
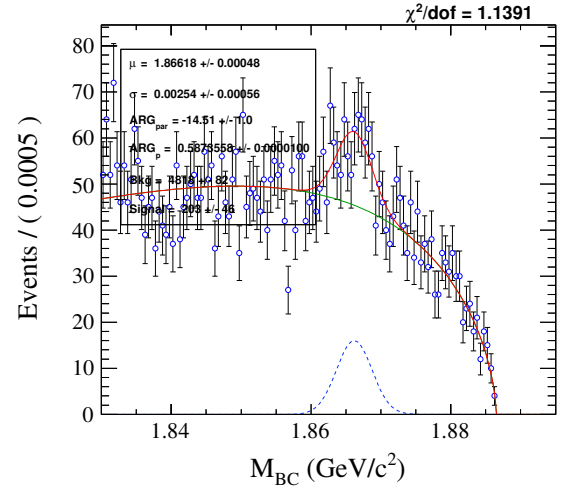
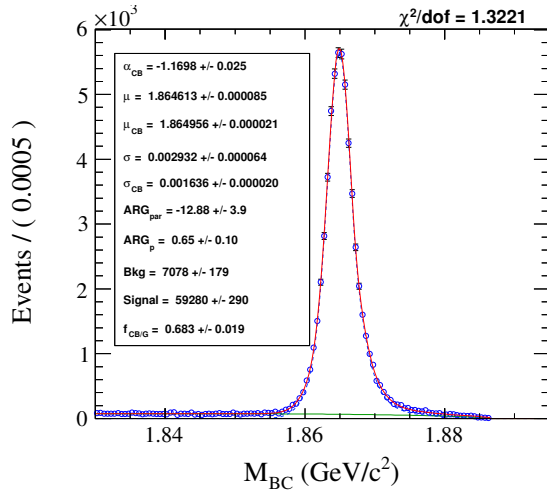
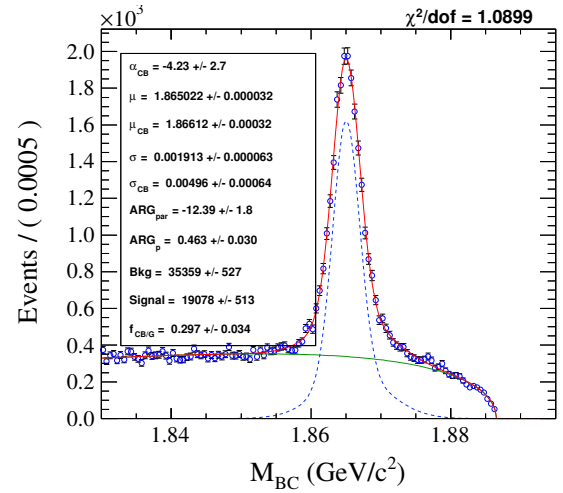
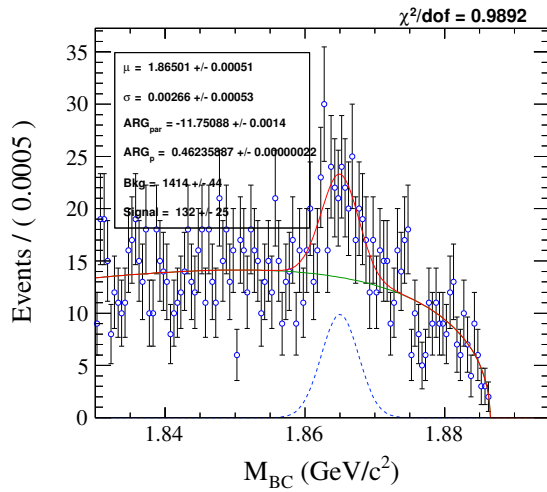
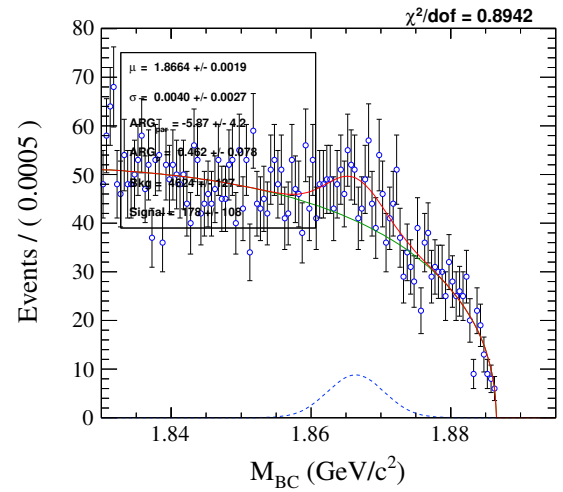
**Table 38:** Yields from the three mass regions of the  $\pi^+\pi^-$  distributions and their resulting peaking-background fractions from the data sample.

Tag	Low-side Yield	Signal Yield	High-side Yield	Fraction of Bg (average)
$K_s\pi^0$	$138 \pm 26$	$(5.928 \pm 0.029) \times 10^4$	$132 \pm 25$	$0.002 \pm 0.000$
$K_s\pi^0\pi^0$	$(2.0 \pm 0.5) \times 10^2$	$(1.91 \pm 0.05) \times 10^4$	$(1.8 \pm 1.1) \times 10^2$	$0.010 \pm 0.003$
$K_s\eta'(\pi^+\pi^-\eta)$	$8 \pm 7$	$(2.55 \pm 0.08) \times 10^3$	$8 \pm 7$	$0.003 \pm 0.002$
$K_s\eta'(\rho\gamma)$	$39 \pm 25$	$(8.1 \pm 0.4) \times 10^3$	$50 \pm 27$	$0.005 \pm 0.002$
$K_s\eta$	$62 \pm 25$	$(8.49 \pm 0.20) \times 10^3$	$49 \pm 25$	$0.007 \pm 0.002$
$K_s\omega$	$32 \pm 14$	$(1.561 \pm 0.020) \times 10^4$	$39 \pm 16$	$0.002 \pm 0.001$

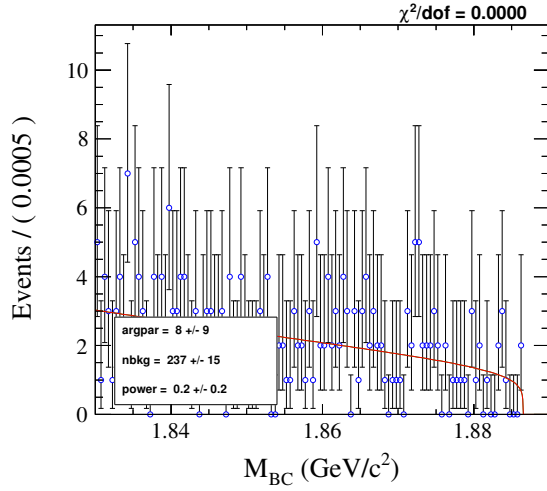
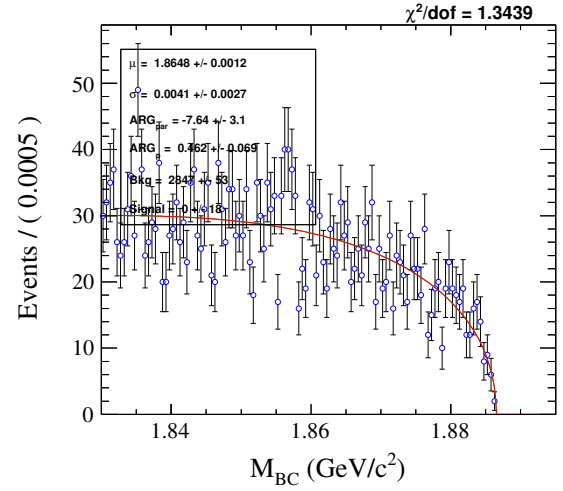
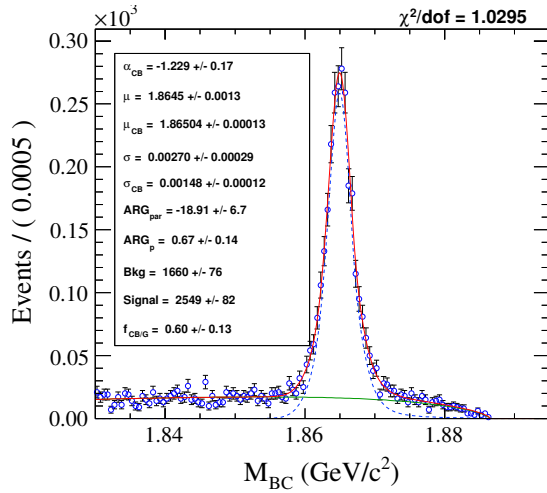
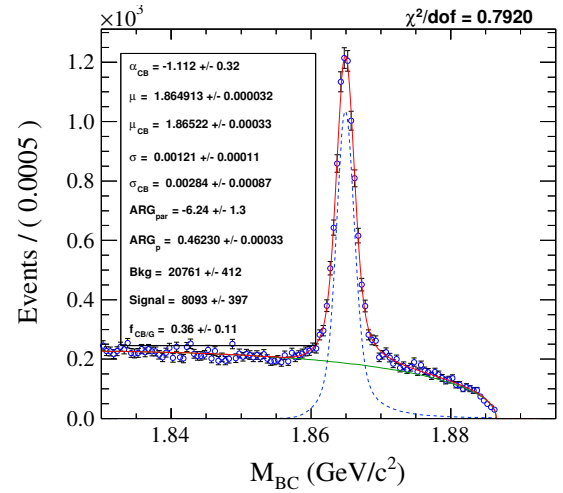
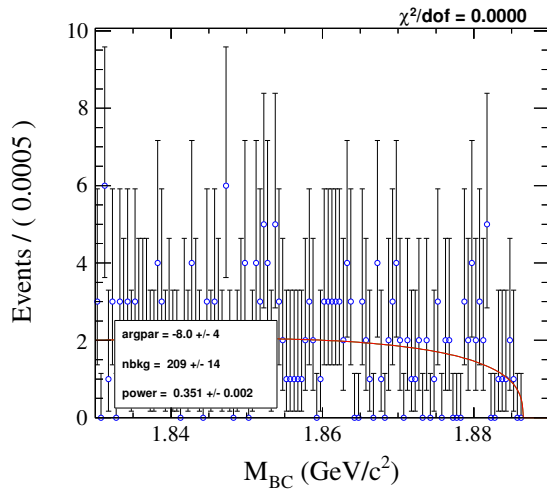
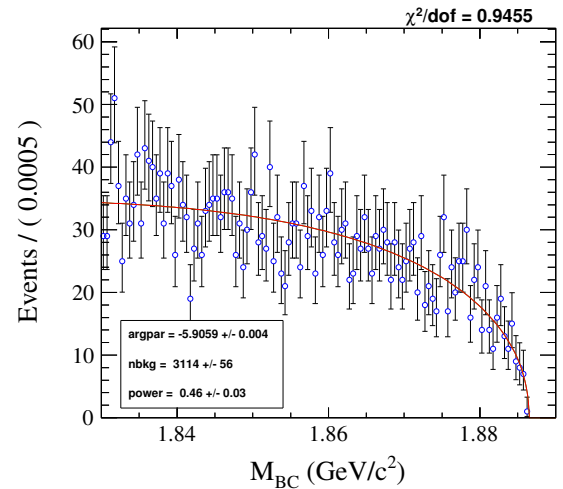
(a)  $K_s\pi^0$  low side yield(b)  $K_s\pi^0\pi^0$  low side yield(c) Signal region for  $K_s\pi^0$ (d) Signal region for  $K_s\pi^0\pi^0$ (e) High side yield  $K_s\pi^0$ (f) High side yield  $K_s\pi^0\pi^0$ **Figure 67:** Side band and the signal region yield fits for the  $K_s$  study for the MC.

(a)  $K_s \eta' (\pi^+ \pi^- \eta)$  low side yield(b)  $K_s \eta' (\pi^+ \pi^- \eta)$  low side yield(c) Signal region for  $K_s \eta' (\pi^+ \pi^- \eta)$ (d) Signal region for  $K_s \eta' (\rho \gamma)$ (e) High side yield  $K_s \eta' (\pi^+ \pi^- \eta)$ (f) High side yield  $K_s \eta' (\rho \gamma)$ **Figure 68:** Side band and the signal region yield fits for the  $K_s$  study for the MC.

(a)  $K_s\eta$  low side yield(b)  $K_s\omega$  low side yield(c) Signal region for  $K_s\eta$ (d) Signal region for  $K_s\omega$ (e) High side yield  $K_s\eta$ (f) High side yield  $K_s\omega$ Figure 69: Side band and the signal region yield fits for the  $K_s$  study for the MC.

(a)  $K_s\pi^0$  low side yield(b)  $K_s\pi^0\pi^0$  low side yield(c) Signal region for  $K_s\pi^0$ (d) Signal region for  $K_s\pi^0\pi^0$ (e) High side yield  $K_s\pi^0$ (f) High side yield  $K_s\pi^0\pi^0$ **Figure 70:** Side band and the signal region yield fits for the  $K_s$  study for the data sample.



(a)  $K_s \eta' (\pi^+ \pi^- \eta)$  low side yield(b)  $K_s \eta' (\pi^+ \pi^- \eta)$  low side yield(c) Signal region for  $K_s \eta' (\pi^+ \pi^- \eta)$ (d) Signal region for  $K_s \eta' (\rho \gamma)$ (e) High side yield  $K_s \eta' (\pi^+ \pi^- \eta)$ (f) High side yield  $K_s \eta' (\rho \gamma)$ **Figure 71:** Side band and the signal region yield fits for the  $K_s$  study for the data sample.

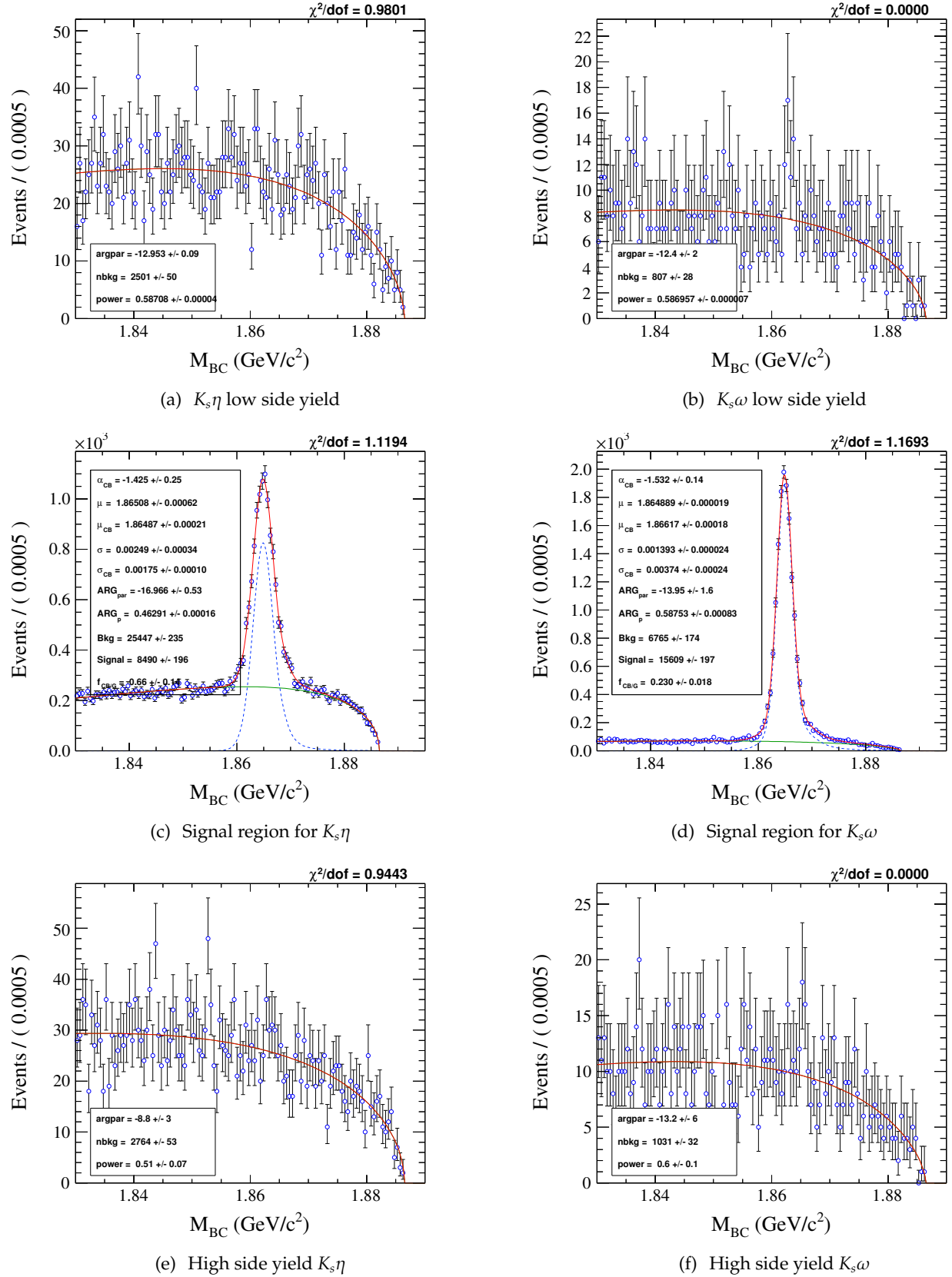


**Figure 72:** Side band and the signal region yield fits for the  $K_s$  study for the data sample.

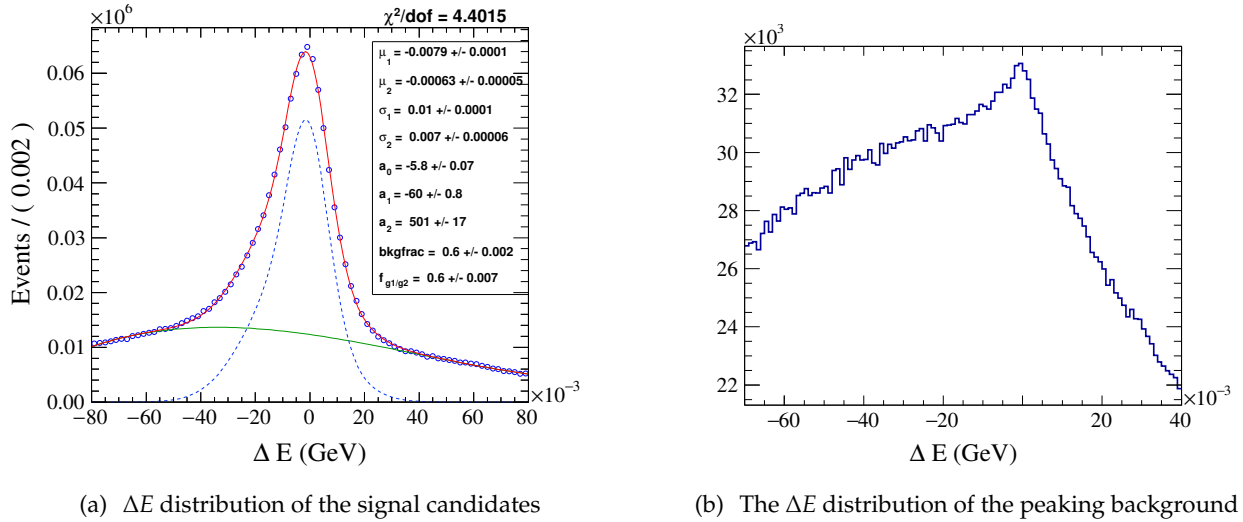
## 6.2 Peaking Background Study for $\pi^+\pi^-\pi^0$

Quantifying the peaking background in the  $\pi^+\pi^-\pi^0$  decay is important. Wrong  $CP$  contributions can dilute the  $F_+$  measurement since the value of  $F_+$  is close to 1.0. Single-tag events of the  $\pi^+\pi^-\pi^0$  signal mode are not used in this analysis, but their high statistics can be used to get a better understanding of the major contributions to the peaking background in the DT sample. Single tags can also provide a test bench for possible background vetoes such as for  $D^0 \rightarrow K_s(\pi^+\pi^-)\pi^0$ .

### 6.2.1 Single-tag Candidate

The  $\Delta E$  distributions for  $\pi^+\pi^-\pi^0$  ST candidates and the peaking background are given in Figure 73.

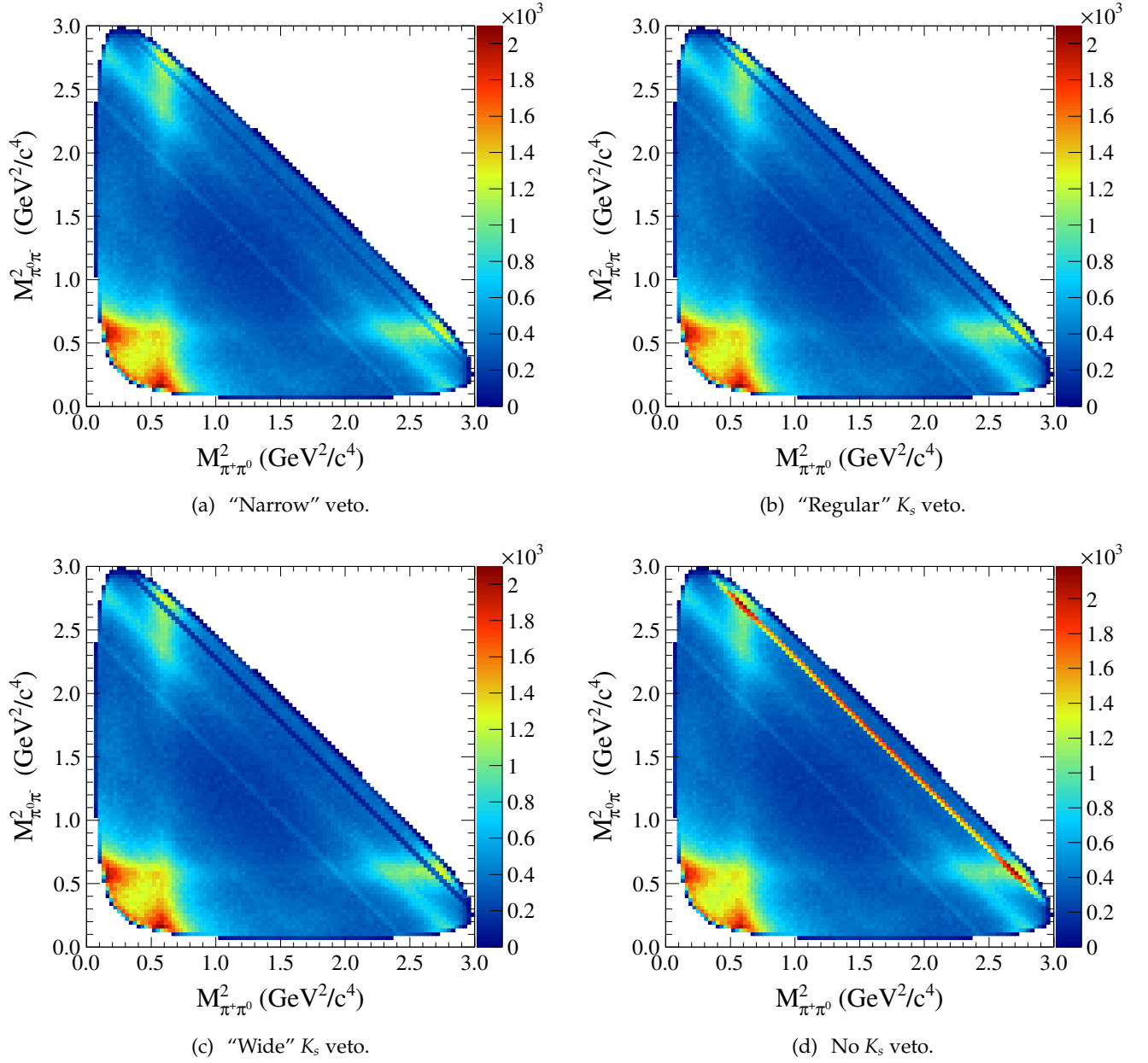
The dominant peaking background for the  $\pi^+\pi^-\pi^0$  mode is from the  $K_s\pi^0$  decay. To reduce this contribution, which has the opposite  $CP$  eigenvalue, various  $K_s$  mass vetoes are investigated. These vetoes are summarized in Table 39, where “Regular” veto means the nominal requirement on the  $\pi^+\pi^-\pi^0$  candidates. MC truth information is used to check the efficiency of these  $K_s$  mass requirements. It should be noted that a  $K_s$  veto is not expected to remove all the background since it targets only one source. The  $K_s$  veto is performed using the  $\pi^+\pi^-$  mass at the  $K_s$  vertex. However in the Dalitz plots shown in this section use the  $\pi^+\pi^-$  variable shows the mass at the IP. A  $\pi^+\pi^-\pi^0$  Dalitz plot with various  $K_s$  requirements is shown in Figure 74.



**Figure 73:** The  $\Delta E$  distribution of the ST  $\pi^+\pi^-\pi^0$  candidates from the MC for the signal (left) and peaking background (right).

**Table 39:**  $K_s$  vetoes for  $\pi^+\pi^-\pi^0$ .  $M_{K_sPDG}$  is taken to be  $0.4976 \text{ GeV}/c^2$ .

Veto event if $K_s$ mass is between	Naming Convention
No cut	No cut
$ M_{\pi^+\pi^-} - M_{PDG}  < 0.012 \text{ GeV}/c^2$	Narrow
$ M_{\pi^+\pi^-} - M_{PDG}  < 0.018 \text{ GeV}/c^2$	Regular
$ M_{\pi^+\pi^-} - M_{PDG}  < 0.024 \text{ GeV}/c^2$	Wide

**Figure 74:** Dalitz plot of  $\pi^+\pi^-\pi^0$  using all the MC sample with using various  $K_s$  veto.

**6.2.1.1 Peaking-background Yields for Single-tag  $\pi^+\pi^-\pi^0$**  : Various  $M_{BC}$  fits are performed to investigate the peaking background for the ST  $\pi^+\pi^-\pi^0$  candidates. MC truth information, together with various  $K_s$  mass vetoes, are used and the results are summarized in Table 40. Fits are shown in Figure 75 for plots without the use of the MC truth information, Figure 76 for candidates with the  $\pi^+\pi^-\pi^0$  removed, and Figure 77 for candidates with  $\pi^+\pi^-\pi^0$  and  $K_s\pi^0$  removed.

Given the information given in Table 40, peaking background fraction for the  $\pi^+\pi^-\pi^0$  mode is measured to be 1.3%.

**Table 40:** *Single-tag peaking-background study of  $\pi^+\pi^-\pi^0$  from the MC.*

$K_s$ veto	$(S + pBG)$	No signal		No signal and no $K_s\pi^0$	
		$S$ yield	$((S + pBG) - S)/S$	$S$ yield	$((S + pBG) - S)/S$
Narrow	$(7.526 \pm 0.015) \times 10^5$	$(7.343 \pm 0.011) \times 10^5$	$0.025 \pm 0.003$	$(7.463 \pm 0.011) \times 10^5$	$0.008 \pm 0.003$
Regular	$(7.339 \pm 0.013) \times 10^5$	$(7.283 \pm 0.011) \times 10^5$	$0.008 \pm 0.002$	$(7.373 \pm 0.011) \times 10^5$	$-0.005 \pm 0.002$
Wide	$(7.263 \pm 0.014) \times 10^5$	$(7.217 \pm 0.011) \times 10^5$	$0.006 \pm 0.002$	$(7.293 \pm 0.011) \times 10^5$	$-0.004 \pm 0.002$
No veto	$(9.148 \pm 0.014) \times 10^5$	$(7.517 \pm 0.011) \times 10^5$	$0.217 \pm 0.002$	$(9.132 \pm 0.012) \times 10^5$	$0.002 \pm 0.002$

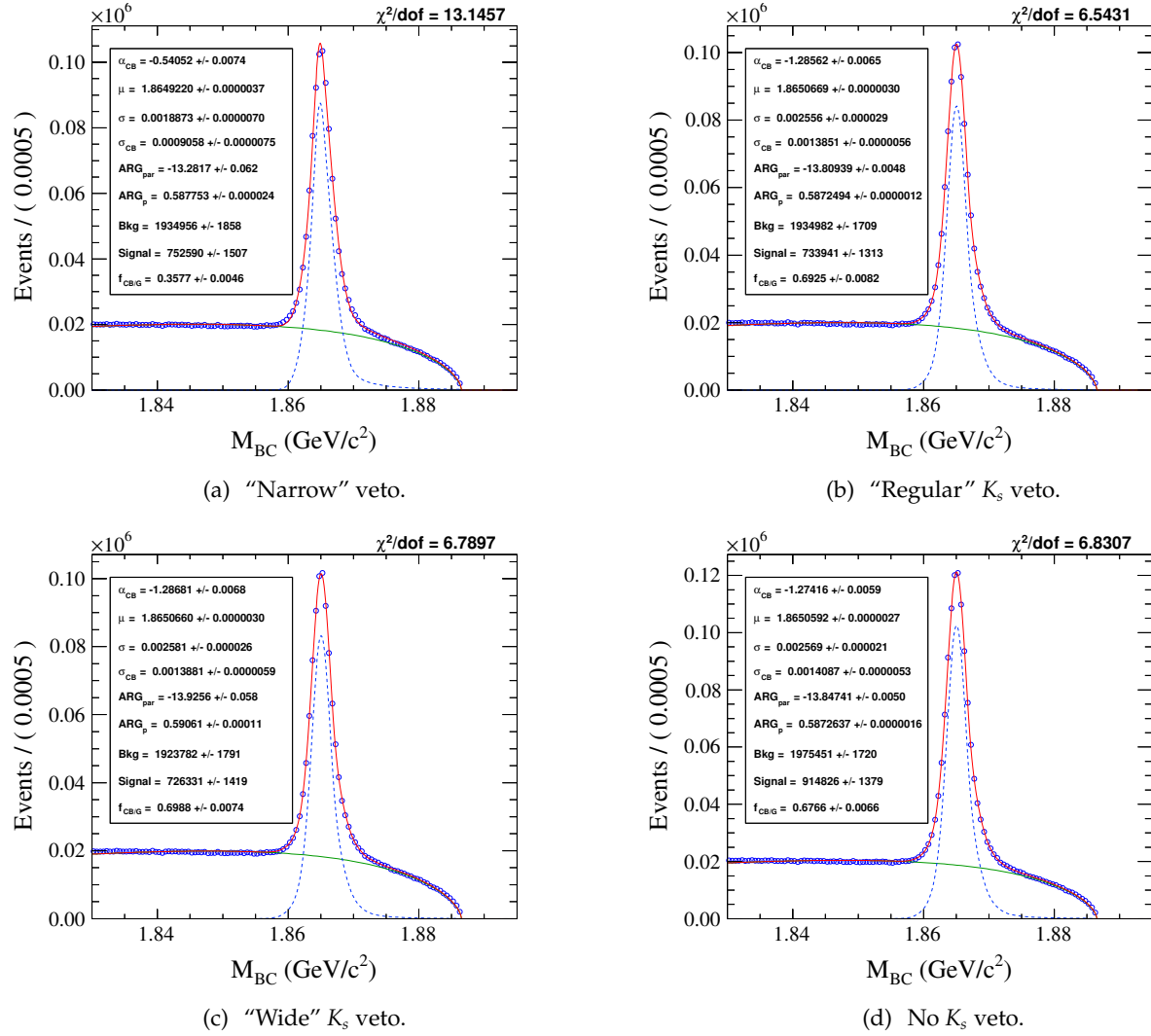
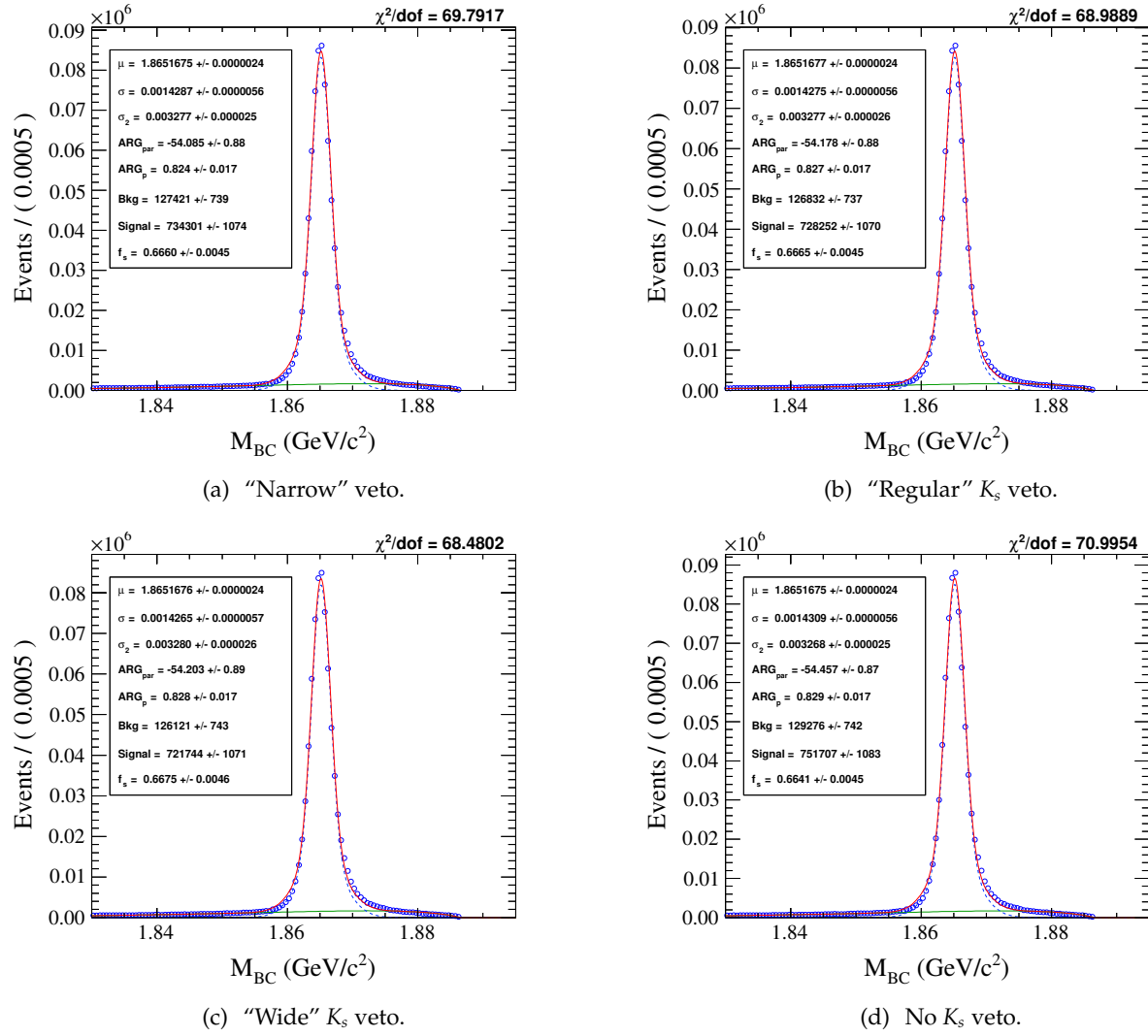
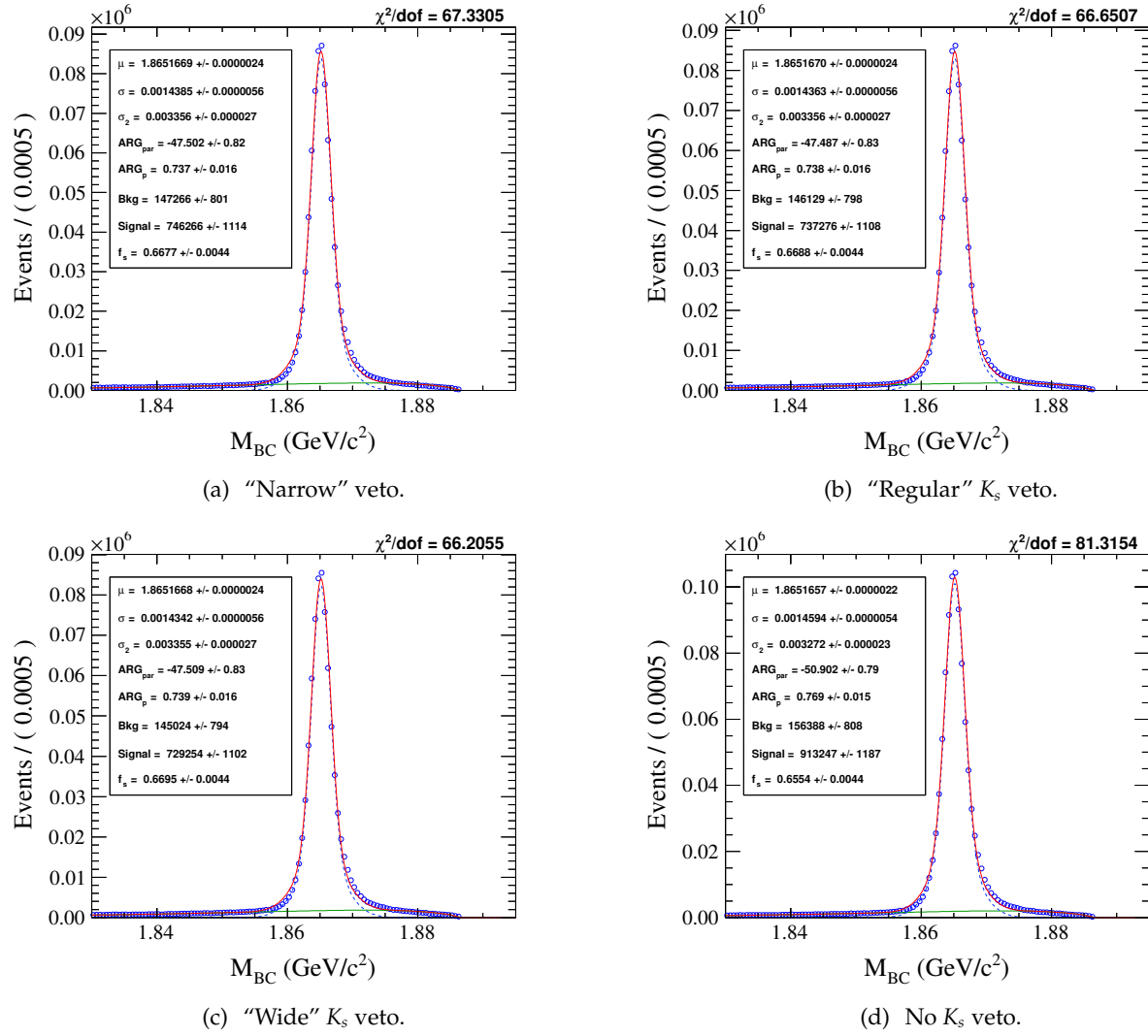


Figure 75:  $\pi^+\pi^-\pi^0$  yield fits with different  $K_s$  vetoes using the MC sample.



**Figure 76:** Peaking background for  $\pi^+\pi^-\pi^0$  using the MC sample, with different  $K_s$  vetoes.



**Figure 77:** Peaking background for  $\pi^+\pi^-\pi^0$  using the MC sample, with  $K_s\pi^0$  removed using truth information, showing the remaining backgrounds.



**6.2.1.2  $K_s\pi^0$  Background in  $\pi^+\pi^-\pi^0$**  : We discussed how the  $K_s\pi^0$  background is handled. In this section, the Dalitz plot distributions of the generated  $K_s\pi^0$  events are shown. MC truth information is used to select  $K_s\pi^0$  events that are reconstructed in the  $\pi^+\pi^-\pi^0$  mode.

All the  $\pi^+\pi^-\pi^0$  candidates with truth information matching a  $K_s\pi^0$  decay and with the opposite  $D$  not decaying to  $\pi^+\pi^-\pi^0$  or  $K_s\pi^0$  are shown in Figure 78. No  $K_s$  mass veto is applied in the plot.

Three different  $K_s$  vetoes, with different mass windows, are then applied to see the effects on the  $K_s\pi^0$  background. The resulting Dalitz plots are given in Figure 79(a) for the regular  $K_s$  veto, Figure 79(b) for the wider veto, and Figure 80 for the widest veto.

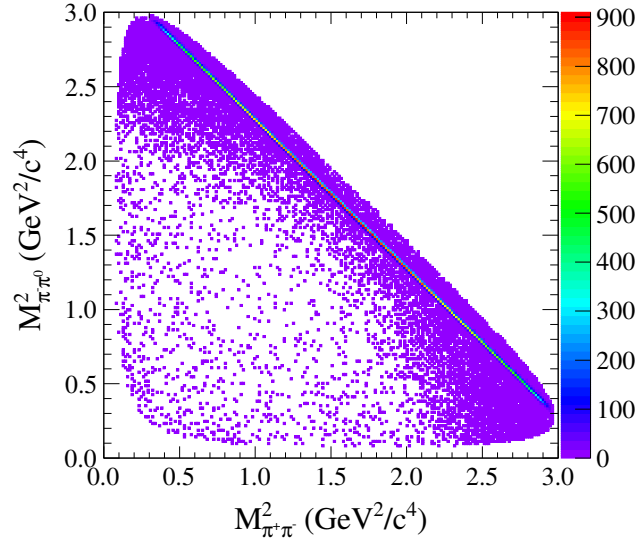


**Figure 78:** Dalitz plot of  $\pi^+\pi^-\pi^0$  candidates, without any  $K_s$  veto, that are generated as  $K_s\pi^0$  decays.

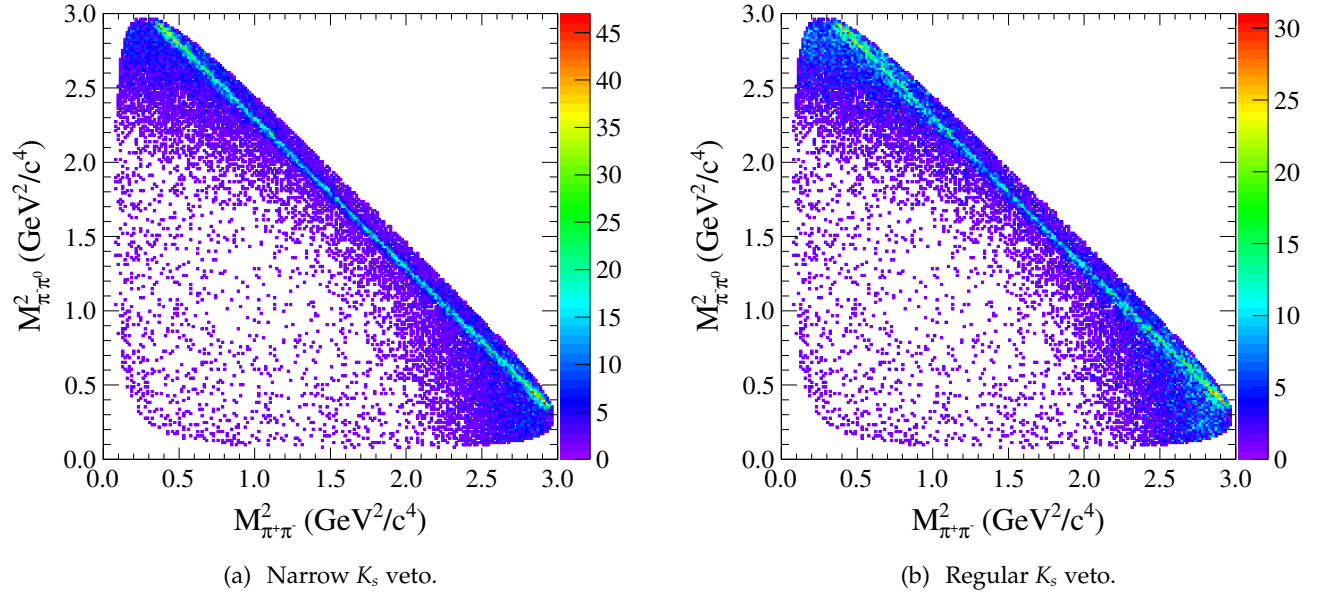


*Figure 79:  $K_s\pi^0$  events in DP of  $\pi^+\pi^-\pi^0$ .*

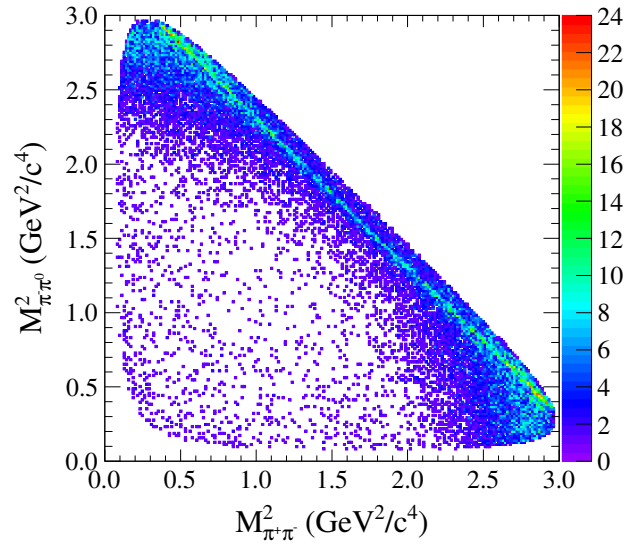


*Figure 80: Wide  $K_s$  veto.*

### 6.2.2 Peaking Background for Double Tags

Peaking backgrounds for double-tag combinations are also studied using the MC truth information. A DT candidate is classified as peaking background if at least one of the  $D$  meson decays is not generated as the tag or the signal mode in question.

Combined results for  $CP+$  and  $CP-$  DT decays are summarized in Table 41. The individual tag-combination results are given in Table 42. Two-dimensional  $M_{BC}$  plots for the  $CP$ -combined DT candidates are shown in Figure 81 for  $CP+$  and Figure 82 for  $CP-$ . Individual two dimensional  $M_{BC}$  plots are given in Appendix C.1. The numbers of events inside the five 2D  $M_{BC}$  regions are listed in Table 43 for all DT candidates, in Table 44 for signal only, and Table 45 for the peaking background.

Noting the high fraction of peaking background in the DT combinations with the tag side being a  $CP+$  eigenstate, a separate study was performed to check the  $K_s\pi^0$  contribution. This type of peaking background and prefers the signal vs.  $CP+$  combination with the  $K_s\pi^0$  in  $CP-$  state. It was found that 42%, 50%, and 25% of the peaking background is due to  $K_s\pi^0$  when the  $\pi^+\pi^-\pi^0$  mode is reconstructed against a  $\pi^+\pi^-$ ,  $K^+K^-$ , and  $K_s\pi^0\pi^0$  tag mode respectively.

**Table 41:** Yields of the DT peaking-background study and the fractions for  $\pi^+\pi^-\pi^0$  vs. combined CP tags.

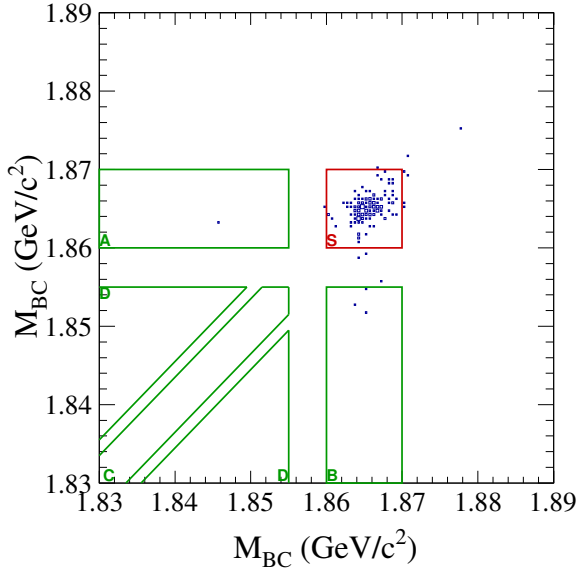
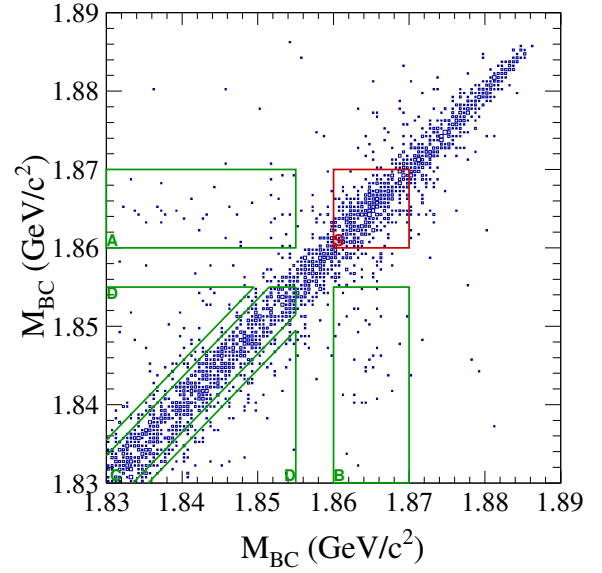
CP	pBG yield	Signal only yield	(S + pBG)	pBG/S	((S + pBG) - S)/S
CP+	$109.5 \pm 23.7$	$138.4 \pm 11.9$	$248.0 \pm 26.5$	$0.791 \pm 0.184$	0.791
CP-	$164.3 \pm 15.0$	$6877.6 \pm 83.1$	$7041.9 \pm 84.4$	$0.024 \pm 0.002$	0.024

**Table 42:** Yields of the DT peaking-background study and the fractions for  $\pi^+\pi^-\pi^0$  vs. individual CP tags.

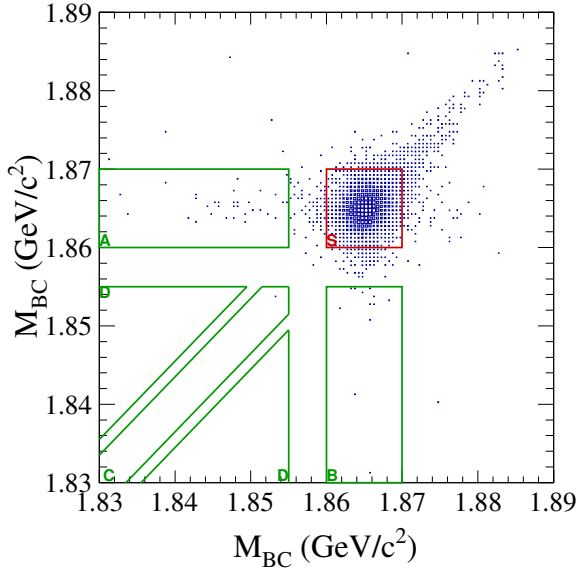
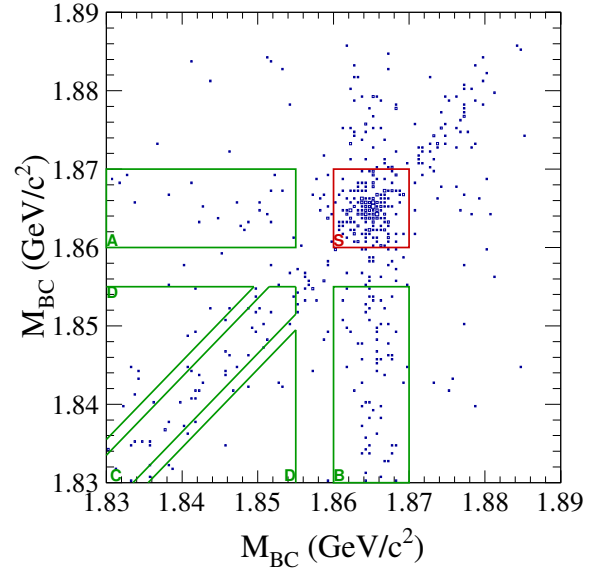
Tag	CP	pBG yield	Signal only yield	(S + pBG)	pBG/S	((S + pBG) - S)/S
$K_s\pi^0$	-	$18.9 \pm 5.7$	$4489.5 \pm 67.1$	$4508.4 \pm 67.3$	$0.004 \pm 0.001$	0.004
$\pi\pi$	+	$26.1 \pm 14.4$	$39.3 \pm 6.3$	$65.4 \pm 15.7$	$0.664 \pm 0.381$	0.664
$KK$	+	$52.0 \pm 16.3$	$79.6 \pm 9.0$	$131.6 \pm 18.6$	$0.653 \pm 0.217$	0.653
$K_s\pi^0\pi^0$	+	$38.1 \pm 9.1$	$19.6 \pm 4.5$	$57.6 \pm 10.1$	$1.943 \pm 0.644$	1.943
$K_s\eta'(\pi\pi\eta)$	-	$0.2 \pm 1.1$	$202.0 \pm 14.3$	$202.2 \pm 14.4$	$0.001 \pm 0.006$	0.001
$K_s\eta'(\rho\gamma)$	-	$23.8 \pm 5.4$	$518.2 \pm 22.8$	$541.9 \pm 23.4$	$0.046 \pm 0.011$	0.046
$K_s\eta$	-	$20.2 \pm 7.6$	$601.1 \pm 24.6$	$621.3 \pm 25.8$	$0.034 \pm 0.013$	0.034
$K_s\omega$	-	$99.1 \pm 10.4$	$1066.7 \pm 32.7$	$1165.8 \pm 34.3$	$0.093 \pm 0.010$	0.093

**Table 43:** Numbers of the events in the five regions of 2D  $M_{BC}$  distribution for all  $\pi^+\pi^-\pi^0$  vs. CP tags.

CP	S	A	B	C	D	All
CP+	552	37	36	833	106	2456
CP-	7100	53	76	37	16	8165

(a)  $CP+$  vs.  $\pi^+\pi^-\pi^0$  true events.(b) Peaking background for  $CP+$  vs.  $\pi^+\pi^-\pi^0$  candidates.

**Figure 81:** Double tag candidates with  $CP+$  vs.  $\pi^+\pi^-\pi^0$  candidates and peaking background distribution using all the MC sample.

(a)  $CP-$  vs.  $\pi^+\pi^-\pi^0$  true events.(b) Peaking background for  $CP-$  vs.  $\pi^+\pi^-\pi^0$  candidates.

**Figure 82:** Double tag candidates with  $CP-$  vs.  $\pi^+\pi^-\pi^0$  candidates and peaking background distribution using all the MC sample.

**Table 44:** Region counts for the 2D  $M_{BC}$  distribution for the signal only  $\pi^+\pi^-\pi^0$  vs. CP tags events.

CP	S	A	B	C	D	All
CP+	140	1	3	0	0	155
CP−	6895	32	13	1	0	7641

**Table 45:** Region counts for the 2D  $M_{BC}$  distribution for the peaking background events for  $\pi^+\pi^-\pi^0$  vs. CP tags.

CP	S	A	B	C	D	All
CP+	412	36	33	833	106	2301
CP−	205	21	63	36	16	524

### 6.3 Peaking Background for $K^+K^-\pi^0$

Understanding the peaking background in the  $K^+K^-\pi^0$  mode is important. DT candidates are used in the analysis, but looking at the ST  $\pi^+\pi^-\pi^0$  candidates can give an insight into possible contributors to the peaking background for this mode.

#### 6.3.1 Single-tag Candidates

$\Delta E$  and  $M_{BC}$  distributions of the single-tag candidates and the peaking background are given in Figure 83 and Figures 84-85, respectively. The resulting peaking-background fractions are given in Table 46. No significant peaking background is observed for this signal mode.

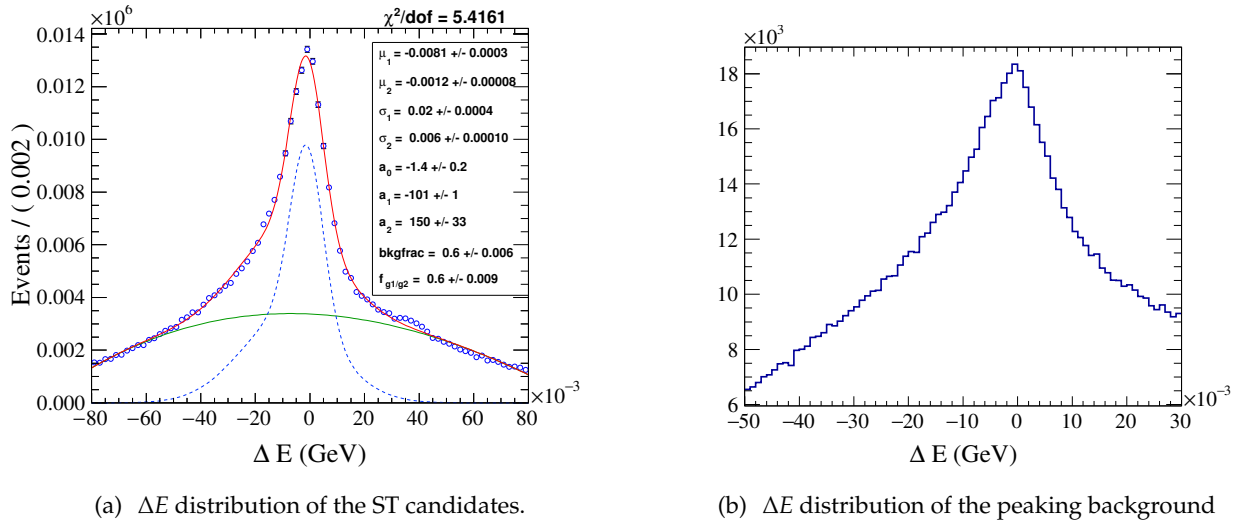


**Figure 83:**  $\Delta E$  distributions of the ST  $K^+K^-\pi^0$  events (left and peaking background (right)

**Table 46:** Single-tag peaking-background study of  $K^+K^-\pi^0$ .

Mode	pBG yield	Signal only yield	(S + pBG) yield	pBG/S	((S + pBG) - S)/S
$K^+K^-\pi^0$	$(1.31 \pm 0.04) \times 10^4$	$(9.62 \pm 0.04) \times 10^4$	$(1.006 \pm 0.017) \times 10^5$	$0.136 \pm 0.004$	0.046

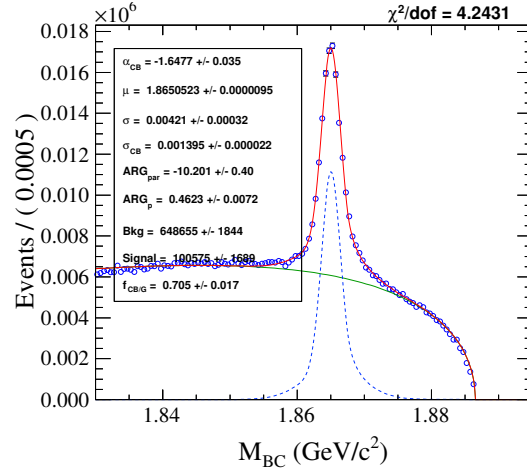
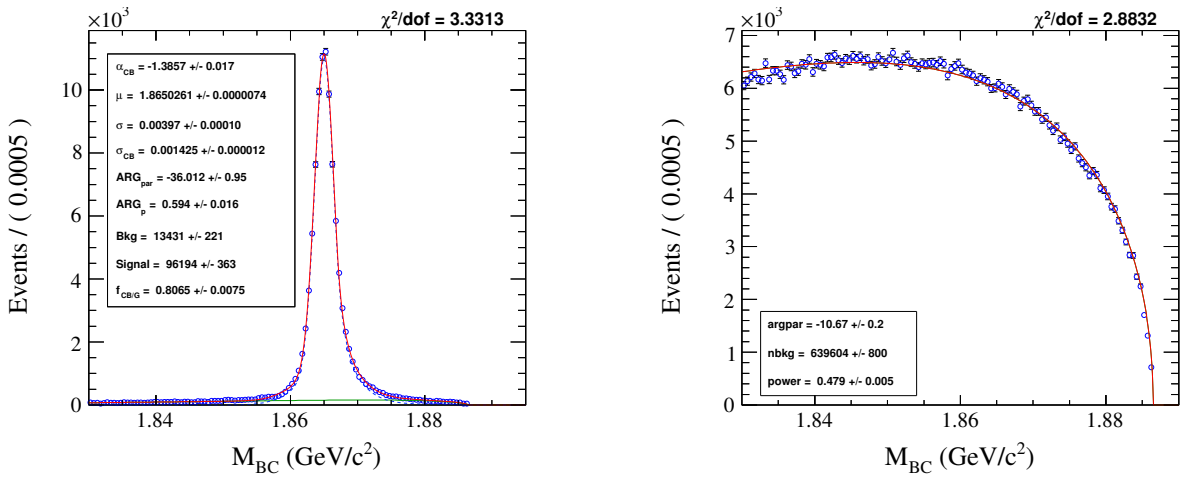


Figure 84: Single-tag candidates for  $K^+K^-\pi^0$  decay



(a)  $M_{BC}$  distribution for signal only candidates of  $K^+K^-\pi^0$  (b)  $M_{BC}$  distribution of the peaking background for  $K^+K^-\pi^0$

Figure 85: Signal only and the peaking background distribution for the  $K^+K^-\pi^0$  candidates

### 6.3.2 Double-tag Peaking Background for $K^+K^-\pi^0$

Two-dimensional  $M_{BC}$  distributions of the double-tag candidates and the peaking-background events are shown in Figure 86 for the  $CP+$  combinations and in Figure 87 for  $CP-$ . The corresponding yields in the 2D  $M_{BC}$  regions are given in Table 48 for all the DT candidates, Table 49 for signal only, and Table 50 for the peaking background.

The resulting  $CP$  combined yields and the background fractions are given in Table 51. Similar information is displayed in Table 47 for individual tag modes.

For individual 2D  $M_{BC}$  distributions for the double-tags, see Appendix C.2.

**Table 47:** Yields from the DT peaking-background study yields and the fractions for  $K^+K^-\pi^0$  vs. individual  $CP$  tags.

Tag	$CP$	$pBG$ yield	Signal only yield	$(S + pBG)$	$pBG/S$	$((S + pBG) - S)/S$
$K_s\pi^0$	–	$8.9 \pm 3.3$	$424.4 \pm 20.7$	$433.3 \pm 20.9$	$0.021 \pm 0.008$	0.021
$\pi^+\pi^-$	+	$18.1 \pm 8.8$	$32.0 \pm 5.7$	$50.1 \pm 10.5$	$0.564 \pm 0.293$	0.564
$K^+K^-$	+	$-3.3 \pm 0.0$	$84.6 \pm 9.2$	$81.3 \pm 11.0$	$-0.039 \pm 0.004$	-0.039
$K_s\pi^0\pi^0$	+	$7.1 \pm 3.4$	$25.0 \pm 5.0$	$32.1 \pm 6.0$	$0.286 \pm 0.146$	0.286
$K_s\eta'(\pi^+\pi^-\eta)$	–	$-0.4 \pm 0.0$	$25.0 \pm 5.0$	$24.6 \pm 5.0$	$-0.016 \pm 0.003$	-0.016
$K_s\eta'(\rho\gamma)$	–	$3.3 \pm 2.2$	$58.0 \pm 7.6$	$61.3 \pm 7.9$	$0.056 \pm 0.039$	0.056
$K_s\eta$	–	$-0.4 \pm 0.0$	$62.0 \pm 7.9$	$61.6 \pm 8.4$	$-0.006 \pm 0.001$	-0.006
$K_s\omega$	–	$11.1 \pm 3.7$	$112.2 \pm 10.6$	$123.3 \pm 11.3$	$0.099 \pm 0.034$	0.099

**Table 48:** Region counts in the 2D  $M_{BC}$  distribution for all  $K^+K^-\pi^0$  vs.  $CP$  tags.

$CP$	$S$	$A$	$B$	$C$	$D$	All
CP+	234	16	11	179	20	664
CP–	716	12	12	10	5	881

**Table 49:** Region counts in the 2D  $M_{BC}$  distribution for signal only  $K^+K^-\pi^0$  vs.  $CP$  tags.

$CP$	$S$	$A$	$B$	$C$	$D$	All
CP+	142	1	0	0	0	153
CP–	684	6	0	0	0	765

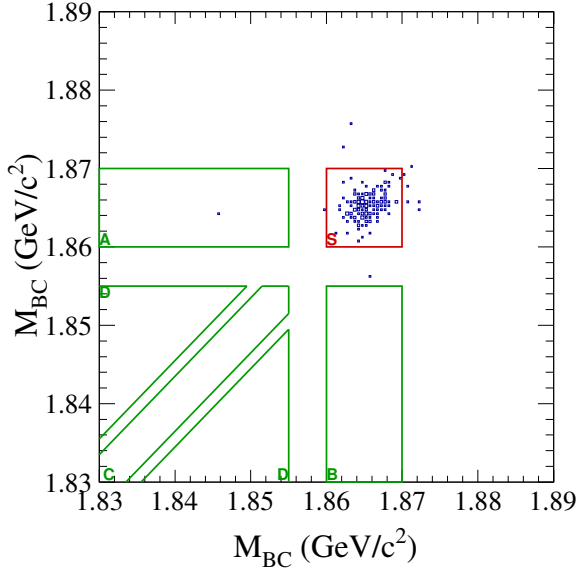
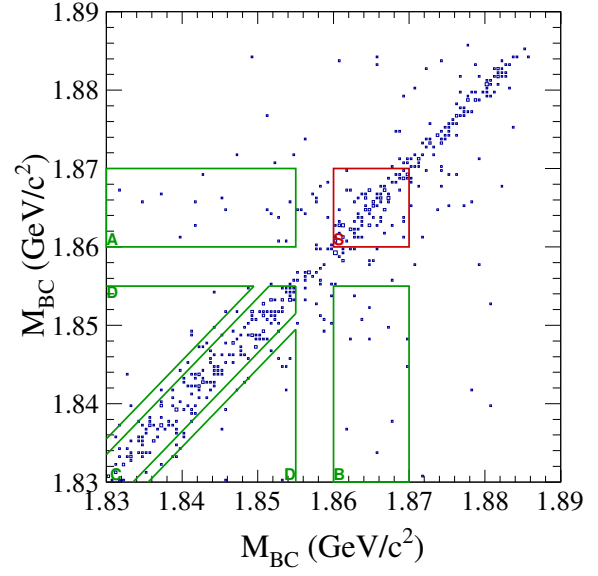
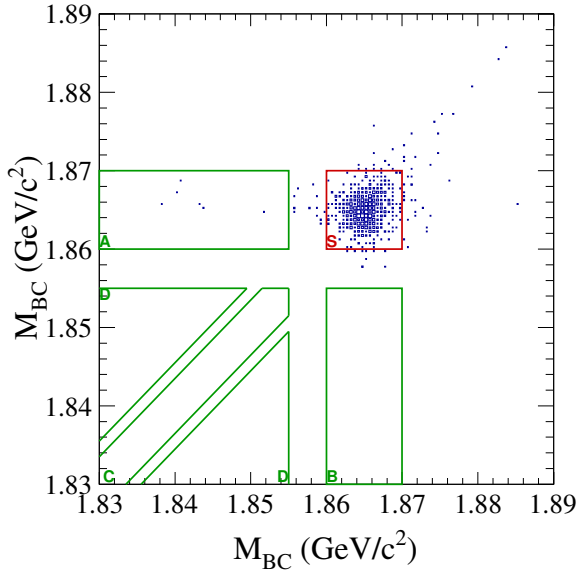
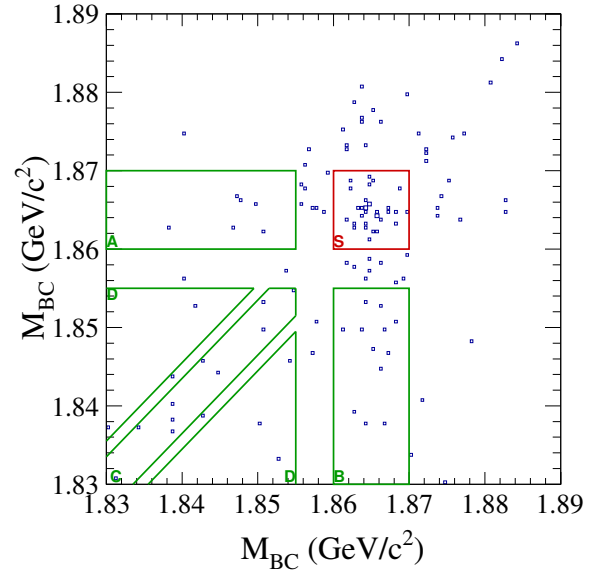
**Table 50:** Region counts in the 2D  $M_{BC}$  distribution for peaking background  $K^+K^-\pi^0$  vs.  $CP$  tags.

$CP$	$S$	$A$	$B$	$C$	$D$	All
CP+	92	15	11	179	20	511
CP–	32	6	12	10	5	116



**Table 51:** DT peaking background study yields and fractions for  $K^+K^-\pi^0$  vs. combined CP tags.

CP	pBG yield	Signal only yield	(S + pBG)	pBG/S	((S + pBG) - S)/S
CP+	$19.4 \pm 11.3$	$141.6 \pm 11.9$	$161.0 \pm 16.4$	$0.137 \pm 0.081$	0.137
CP-	$22.9 \pm 6.1$	$681.6 \pm 26.2$	$704.6 \pm 26.9$	$0.034 \pm 0.009$	0.034

(a) CP+ vs.  $K^+K^-\pi^0$  true events.(b) Peaking background for CP+ vs.  $K^+K^-\pi^0$  candidates.**Figure 86:** Double-tag candidates of CP+ vs  $K^+K^-\pi^0$  using the MC sample.(a) CP- vs  $K^+K^-\pi^0$  true events.(b) Peaking background for CP- vs  $K^+K^-\pi^0$  candidates.**Figure 87:** Double-tag candidates of CP- vs  $K^+K^-\pi^0$  using the MC sample.

## 7 Efficiency calculations

### 7.1 Efficiency of single-tag yields

The efficiency for detecting single-tags is calculated from the ratio of the number of signal candidate to the number of events generated for a tag mode,  $\epsilon = (S + pBG)/G$ , where  $S, pBG, G$  are the MC Signal, MC peaking background, and MC Generated signal events, respectively.

Single-tag efficiency numbers are given in Table 52. Sideband subtraction was performed for the modes  $K_s\eta'(\rho\gamma)$  and  $K_s\omega$ . This procedure is explained in Section 4.1 for ST and Section 5.3 for DT candidates. No subtraction is performed for the other tag modes to remove the peaking background. The definition of the efficiency take cares of the increased number of reconstructed events, resulting in a higher efficiency value. If we use the MC to predict the peaking backgrounds, this method is mathematically identical to subtracting the background based on the MC. Later, we will consider the systematic uncertainties in the MC prediction (present in either method).

The efficiency is used to correct the yields for the data and the MC sample. The MC yields are also corrected since half of the MC sample is used as fake data, as explained in Section 3, and these yields are used in the in/out test of the measurement. Corrected yields are given in Table 53.

**Table 52:** The detection efficiencies of single-tags modes from the MC, after sideband subtraction.

Decay Channel	Efficiency %
$K_s\pi^0$	$35.75 \pm 0.07$
$\pi^+\pi^-$	$65.71 \pm 0.34$
$K^+K^-$	$61.85 \pm 0.16$
$K_s\pi^0\pi^0$	$14.67 \pm 0.15$
$K_s\eta'(\pi^+\pi^-\eta)$	$11.26 \pm 0.13$
$K_s\eta'(\rho\gamma)$	$19.28 \pm 0.23$
$K_s\eta$	$31.24 \pm 0.27$
$K_s\omega$	$9.59 \pm 0.06$

**Table 53:** Corrected single-tag yields.

Decay Channel	Data Corrected Yields	MC corrected yields
$K_s\pi^0$	$(1.644 \pm 0.008) \times 10^5$	$(9.997 \pm 0.028) \times 10^5$
$\pi^+\pi^-$	$(2.721 \pm 0.027) \times 10^4$	$(1.574 \pm 0.011) \times 10^5$
$K^+K^-$	$(7.98 \pm 0.04) \times 10^4$	$(4.433 \pm 0.018) \times 10^5$
$K_s\pi^0\pi^0$	$(1.344 \pm 0.018) \times 10^5$	$(5.63 \pm 0.08) \times 10^5$
$K_s\eta'(\pi^+\pi^-\eta)$	$(2.28 \pm 0.06) \times 10^4$	$(1.313 \pm 0.021) \times 10^5$
$K_s\eta'(\rho\gamma)$	$(3.92 \pm 0.08) \times 10^4$	$(2.020 \pm 0.030) \times 10^5$
$K_s\eta$	$(2.72 \pm 0.05) \times 10^4$	$(1.385 \pm 0.019) \times 10^5$
$K_s\omega$	$(1.469 \pm 0.018) \times 10^5$	$(8.14 \pm 0.07) \times 10^5$

## 7.2 Double-tag efficiency

The efficiencies of the double-tags are calculated after the sideband subtraction and again given by the ratio of the number of reconstructed events to the number of generated double-tag events. The efficiency is defined as  $(S + pBG)/G$ , where  $S, pBG, G$  are the MC Signal, MC Peaking background, and MC Generated signal events. This definition absorbs the peaking background subtraction into the efficiency, and the resulting efficiency values will be higher than they would be otherwise.

Next, we discuss some necessary rescaling of the MC. In the DT efficiency calculation, the signal value  $S$ , must be considered carefully, since the  $CP$ -eigenstate branching fractions for signal can be wrong for two reasons: the MC may differ from the PDG in the total signal branching fraction (BF), and it may also differ in the value of  $F_+$ . The  $CP+$  ( $CP-$ ) BFs for a given mode involve both factors; specifically:

$$B_{CP+} = F_+ B_{total} \quad (8)$$

$$B_{CP-} = (1 - F_+) B_{total} \quad (9)$$

. For each of the signal modes, there are two “input” quantities,  $B_{total}$  and  $F_+$ , and two “output” quantities,  $B_{CP+}$  and  $B_{CP-}$ . The  $B_{total}$  denotes the total BF for the final state  $\pi^+\pi^-\pi^0$  or  $K^+K^-\pi^0$ , and  $B_{CP\pm}$  is the branching fraction of a particular  $CP$  eigenvalue to the signal final state. Branching fractions for the signal modes are given in Table 2.

We measure the quantity  $(S + pBG)$ , but need to rescale only the  $S$  value. This requires a separate determination of  $S$ . As noted in Section 6, we avoid any direct determination of  $pBG$ , since the peaking-background shapes can differ from the signal shape, and we are only need to know the effect of including  $pBG$  events in fits to the yield. In data, we only fit the  $S + pBG$  distribution. In the MC, the only use of  $S$ -only fits, comes from the generated truth information, is in the rescaling, as discussed here.

For the reasons explained above, the true corrected  $CP+$  signal yield must be multiplied by the factor  $x_+ = (F_D B_D)/(F_M B_M)$ . Here, the  $M$  subscript denotes, the MC,  $D$  is data,  $B$  is the branching fraction, and  $F$  is  $F_+$ . Note that  $B_D$  is just the PDG BF, but  $F_D$  is what is measured in this analysis. Since  $F_D$  is needed to determine the correction, we will need to iterate. Multiplying  $S$  by  $x_+$  is the same as adding  $(x_+ - 1)S$  to  $S$ . Thus, we can replace the original numerator,  $S_M + pBG_M$ , of our efficiency, by  $(S_M + pBG_M) + (x_+ - 1)S_M$ .

In the case of a  $CP-$  signal, the procedure is similar, except that  $F$  is replaced by  $(1 - F)$  everywhere in the expression for the scale  $x$ . So for  $CP-$  scaling factor becomes  $x_- = [(1 - F_D)B_D]/[(1 - F_M)B_M]$ . We then replace  $(S_M + pBG_M)$  by  $(S_M + pBG_M) + (x_- - 1)S_M$ .

The resulting efficiencies, after the iteration, are given in Table 54 for  $\pi^+\pi^-\pi^0$  and Table 55 for  $K^+K^-\pi^0$ . The corresponding corrected yields are given in Tables 56-57.

**Table 54:** Double-tag efficiency of tag modes vs.  $\pi^+\pi^-\pi^0$  for MC, including the scaling factor  $x_{\pm}$ .

Mode	Efficiency %
$K_s\pi^0$	$9.24 \pm 0.18$
$\pi^+\pi^-$	$54 \pm 12$
$K^+K^-$	$43 \pm 6$
$K_s\pi^0\pi^0$	$12.7 \pm 2.1$
$K_s\eta'(\pi^+\pi^-\eta)$	$3.20 \pm 0.30$
$K_s\eta'(\rho\gamma)$	$4.85 \pm 0.29$
$K_s\eta$	$9.5 \pm 0.5$
$K_s\omega$	$2.67 \pm 0.12$

**Table 55:** Double-tag efficiency of tag modes vs.  $K^+K^-\pi^0$  for MC, including the scaling factor  $x_{\pm}$ .

Mode	Efficiency %
$K_s\pi^0$	$7.3 \pm 0.4$
$\pi^+\pi^-$	$42 \pm 6$
$K^+K^-$	$32.5 \pm 2.5$
$K_s\pi^0\pi^0$	$9.5 \pm 1.1$
$K_s\eta'(\pi^+\pi^-\eta)$	$3.1 \pm 0.7$
$K_s\eta'(\rho\gamma)$	$4.3 \pm 0.7$
$K_s\eta$	$7.0 \pm 1.0$
$K_s\omega$	$2.35 \pm 0.25$

**Table 56:** Double-tag corrected yields of tag modes vs.  $\pi^+\pi^-\pi^0$ .

Mode	Corrected data yield	Corrected fake data yield
$K_s\pi^0$	$(5.30 \pm 0.26) \times 10^3$	$(3.59 \pm 0.08) \times 10^4$
$\pi^+\pi^-$	$33 \pm 14$	$(1.2 \pm 0.4) \times 10^2$
$K^+K^-$	$94 \pm 25$	$(3.9 \pm 0.7) \times 10^2$
$K_s\pi^0\pi^0$	$(1.3 \pm 0.4) \times 10^2$	$(5.7 \pm 1.3) \times 10^2$
$K_s\eta'(\pi^+\pi^-\eta)$	$(6.6 \pm 1.6) \times 10^2$	$(4.4 \pm 0.5) \times 10^3$
$K_s\eta'(\rho\gamma)$	$(1.50 \pm 0.20) \times 10^3$	$(9.2 \pm 0.6) \times 10^3$
$K_s\eta$	$(9.5 \pm 1.1) \times 10^2$	$(4.72 \pm 0.28) \times 10^3$
$K_s\omega$	$(4.1 \pm 0.5) \times 10^3$	$(2.93 \pm 0.14) \times 10^4$

*Table 57: Double-tag corrected yields of tag modes vs.  $K^+K^-\pi^0$  .*

Mode	Corrected data yield	Corrected fake data yield
$K_s\pi^0$	$(7.2 \pm 1.1) \times 10^2$	$(6.4 \pm 0.4) \times 10^3$
$\pi^+\pi^-$	$75 \pm 19$	$(1.2 \pm 0.4) \times 10^2$
$K^+K^-$	$133 \pm 25$	$(3.7 \pm 0.7) \times 10^2$
$K_s\pi^0\pi^0$	$(1.2 \pm 0.4) \times 10^2$	$(4.3 \pm 1.2) \times 10^2$
$K_s\eta'(\pi^+\pi^-\eta)$	$(1.3 \pm 0.7) \times 10^2$	$(7.3 \pm 2.1) \times 10^2$
$K_s\eta'(\rho\gamma)$	$(1.5 \pm 0.6) \times 10^2$	$(1.15 \pm 0.24) \times 10^3$
$K_s\eta$	$(1.1 \pm 0.4) \times 10^2$	$(6.9 \pm 1.4) \times 10^2$
$K_s\omega$	$(8.5 \pm 2.2) \times 10^2$	$(3.4 \pm 0.5) \times 10^3$

## 8 Systematic Uncertainties

### 8.1 Sensitivity of $F^+$ to Changes in $N^+, N^-$

As explained in Section 1.1, the  $CP$  fraction measurement involves the ratio of the quantities  $N^+$  and  $N^-$ , which are the ratios of the corrected yields of double tags to single tags. In this section, we present expressions for the sensitivity of  $F_+ = N^+/(N^+ + N^-)$  to changes in  $N^+, N^-$ . In order to simplify the notation, we will denote the  $CP$  fraction as  $f = A/(A + B)$ . Note that binomial statistics are not appropriate here, since uncertainties in  $A$  and  $B$  are determined from separate fits with different backgrounds. Thus, the uncertainties are not Poisson and are also not anti-correlated as in the binomial case. Instead, a straightforward calculation leads to:

$$\frac{\delta f}{f} = (1 - f) \frac{\delta A}{A} \quad \text{and} \quad \frac{\delta f}{f} = -(1 - f) \frac{\delta B}{B} \quad (10)$$

These formulas are symmetric except for the leading sign. However, if  $A \neq B$ , then the normalizing denominators on the right-hand sides (*i.e.*,  $A$  and  $B$ ) are different, so that the effect on  $f$  of equal absolute changes in  $A$  and  $B$  are very different.

Re-writing Equation 10 in terms of the total  $A + B$ :

$$\frac{\delta f}{f} = \left(\frac{B}{A}\right) \frac{\delta A}{A + B} \quad \text{and} \quad \frac{\delta f}{f} = -\frac{\delta B}{A + B} \quad (11)$$

These equations must be consistent when  $A$  and  $B$  are interchanged. They are, once one recalls that  $f$  is really shorthand for  $f_A$ , the fraction of  $A$ . When one interchanges  $A$  and  $B$ , one also needs to use  $\delta f_A = -\delta f_B$  and  $f_A/f_B = A/B$ , which leads to identical expressions. In these expressions normalized to  $A + B$ , the large  $(1 - f)$  suppression factor is absent. Instead, the large value of  $\delta B/B$  is reduced by changing the normalization to  $(A + B)$ . This is, of course, trivially equivalent, since  $1 - f = B/(A + B)$ , but it gives an alternate way of understanding the sensitivity. In the former case, a value of  $\delta B/B$  of order 1 is suppressed by a small value of  $(1 - f)$ ; in the latter case,  $\delta B/(A + B)$  simply starts out smaller, since the  $(1 - f)$  has now been absorbed into the alternate normalization. There is also some explicit suppression for  $\delta A$  (assuming that  $A > B$ ) from the  $B/A$  factor due to the correlation between  $A$  and  $(A + B)$  (the numerator and denominator of  $f$ ). We prefer to use the equation with the  $(1 - f)$  terms for technical reasons.

### 8.2 Tag-side Efficiency Systematic Uncertainties

Systematic uncertainties in the reconstruction efficiency of the  $CP$  tag modes should almost entirely cancel, and any residual effects are expected to be negligible. The cancellation occurs when the ratio of the number of double tags to single tags, which have the  $CP$  tag modes in common, is measured.

Any non-cancellation that might occur requires three things. First, there must be a violation of the factorization of the efficiency of the two  $D$  mesons. In other words, the DT efficiency is approximately the product of two ST efficiencies. This assumption is not completely true since in single tags, we average over all the decays of the opposite  $D$  meson, while in double tags, it is a

specific decay mode. The multiplicity of the opposite-side  $D$  decay matters, due to overlaps of the decay products. This is expected to be small due to the fine-grained BESIII detector; the largest effects will arise owing to the lack of isolation of signal photons from  $\pi^0$  decays.

Second, this non-factorization must be different for the  $CP+$  and  $CP-$  DT, otherwise it will cancel in the ratio for  $F_+$ .

Third, the MC must incorrectly simulate the previous two effects, such that the efficiency corrections do not compensate for them. The  $D$  kinematics and the general MC simulation quality are both quite good, so the MC will tend to track any effects that are present rather well. The small size of these three effects suppresses possible systematic uncertainties.

One can also compare the average number of tracks,  $\pi^0$ ,  $K_S$ , and  $\gamma$  for  $CP+$  and  $CP-$  tags. The efficiency systematic uncertainties for  $K_S$  is typically measured as an additional effect that is added to the track-finding efficiency systematic. On the other hand, the  $\pi^0$  systematic uncertainties are inclusive and include the  $\gamma$  detection. Thus,  $K_S$  daughters are counted as tracks, while  $\pi^0$  daughters are not counted as photons. One can see that the differences are small, with the exception of  $K_S$ ; they are summarized in Table 58. So the MC is required to track only modest changes in multiplicities.

Finally, as discussed above, the sensitivity to uncertainties reduced on for DT/ST ratio due to the fact that we are measuring a fraction; *i.e.*, the  $(1 - f)$  factor. This reduction is stronger in the more statistically-precise  $\pi^+\pi^-\pi^0$  case. In summary, we conclude that we can neglect any such effects in the tag-side systematic uncertainties.

**Table 58:** Average number of tracks,  $\pi^0$ ,  $K_S$ , and  $\gamma$  per event for  $CP+$  and  $CP-$  single-tags, weighted by the reconstructed yields.

Object	$CP+$ Tags	$CP-$ Tags
Tracks (all)	2.00	2.22
$K_S$	0.22	1.00
$\pi^0$	0.44	0.63
$\gamma$ (non- $\pi^0$ )	0.00	0.08

### 8.3 Signal-side Efficiency Systematic Uncertainties

The efficiency for detecting the signal-side mode does not completely cancel in the double-tag to single-tag ratio. There is some cancellation since the measurement of  $F_+$  involves a ratio of one such DT/ST value (for  $CP+$  signal opposite a  $CP-$  tag) to the sum of both DT/ST values. However, although  $F_+$  is a ratio, the kinematics of the  $CP+$  and  $CP-$  signal events are different, so the cancellation may not be complete. This leads to two possible sources of systematic uncertainties.

First, we assume the data and MC efficiencies agree versus momentum for the spectra of signal tracks and  $\pi^0$ s, but that the spectra are generated incorrectly in the MC and do not match the data. Then, differences in the spectra will couple into any variations in efficiency vs. momentum and result in the wrong momentum-weighted average of the varying, but presumed correct, efficiencies.

Second, the spectra in data and MC simulation may be the same, but the data and MC efficiencies may not agree precisely for all momenta. This will result in taking a correctly weighted average of incorrect efficiencies.

For the first case, the plots in Section 8.3.1 below demonstrate that the spectra are well modeled. We believe than any residual effect is negligible.

For the second case, I refer the reader to systematic uncertainty studies performed by this author and my colleagues in BESIII Collaboration:

- Charged-particle tracking for  $K^\pm, \pi^\pm$  in Ref. [26]
- Charged-particle identification of  $K^\pm, \pi^\pm$  in Ref. [26]
- $\pi^0$  reconstruction in Ref. [27]

Looking at the size of the data-MC mismatches vs. momentum in these references, we conclude that the difference in the  $CP+$  and  $CP-$  averages should be less than:

- 0.5% per track from track-finding
- 0.5% per track from particle identification
- 0.5% per  $\pi^0$

We scale the uncertainties for the number of tracks, treating the two tracks as correlated within the reconstruction and also in the PID, but with the track reconstruction and PID treated as uncorrelated. Thus, adding 1.0%, 1.0%, and 0.5% in quadrature, we find a total systematic uncertainty of 1.5%. The result is the same for each signal mode, since each has two tracks and one  $\pi^0$ .

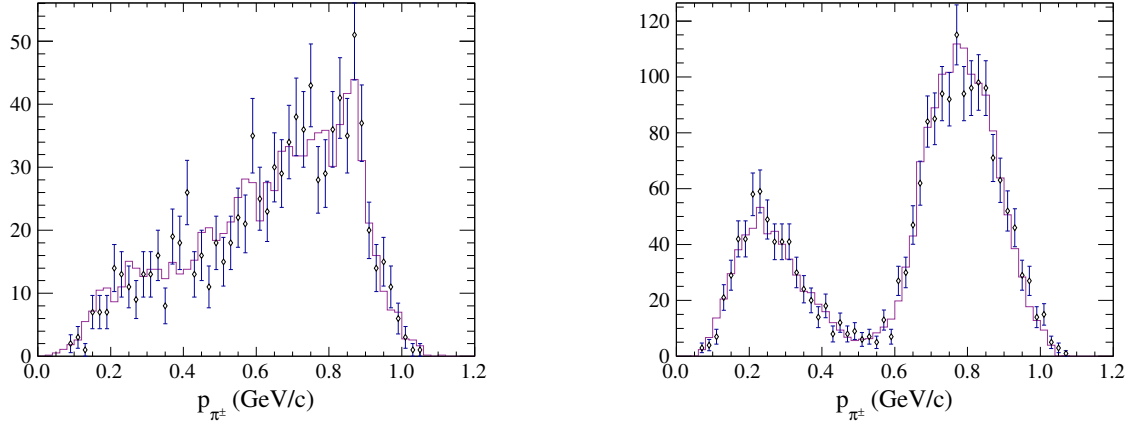
This systematic uncertainty is a relative uncertainty in the measurements of  $A$  and  $B$ . The effect may be ascribed to either  $A$  or  $B$ : the formulas for propagating to  $f$  will of course agree: we choose to use  $\delta f/f = (1 - f)(\delta B/B)$ . For  $\pi^+\pi^-\pi^0$ , using  $f = 0.95$ , we get a fractional uncertainty in  $F_+$  of 0.08%, which we round to 0.1%. For  $K^+K^-\pi^0$ , using  $f = 0.67$ , we find a fractional uncertainty in  $F_+$  of 0.5%. Note that these  $f$  values are smaller than the central values measured to be conservative; *i.e.*, the  $(1 - f) < 1$  factors used are a bit larger, giving a bit less suppression. This is done in part to account for the statistical and systematic uncertainties in these central values.

The efficiency of the signal modes over the Dalitz plot (DP) is also studied and is detailed in Appendix A. The efficiency over the DP is fairly flat and no additional uncertainty is assigned.

### 8.3.1 Momentum spectrum of particles

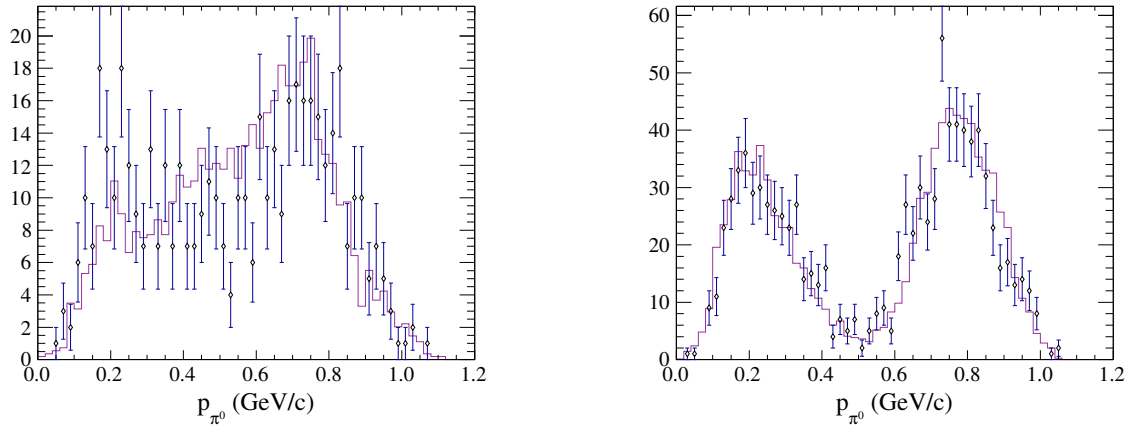
The momentum spectra of the particles in the DT signal events are compared for data and the MC sample. The  $\pi^+$ ,  $\pi^-$ , and  $\pi^0$  momentum distributions for the DT candidates from the  $\pi^+\pi^-\pi^0$  mode are shown in Figures 88 and 89. Kaon and  $\pi^0$  momentum distributions for the DT  $K^+K^-\pi^0$  candidates are shown in Figures 90 and 91.





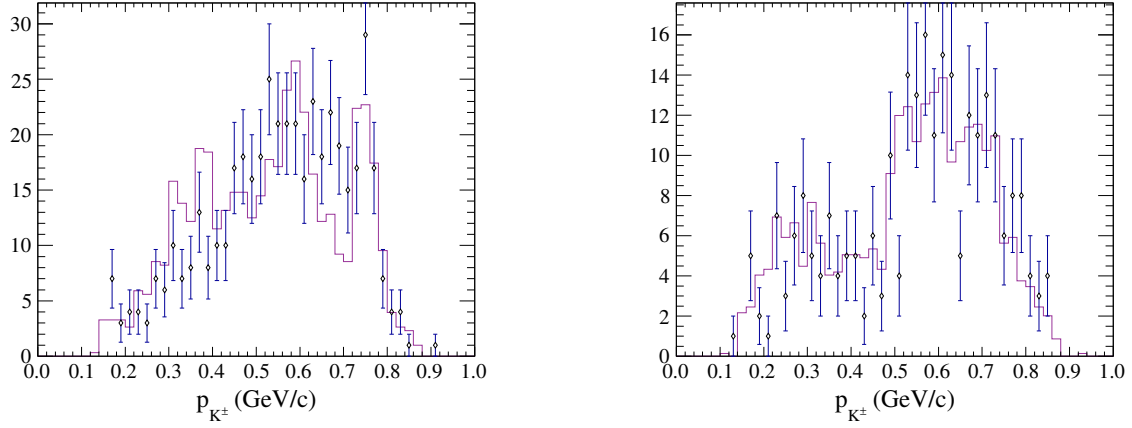
(a) Momentum distribution of  $\pi^+$  and  $\pi^-$  in  $CP+$  vs  $\pi^+\pi^-\pi^0$  events. (b) Momentum distribution of  $\pi^+$  and  $\pi^-$  in  $CP-$  vs  $\pi^+\pi^-\pi^0$  events.

**Figure 88:** Data and MC overlays of charged pion momentum distributions of  $\pi^+\pi^-\pi^0$  events.



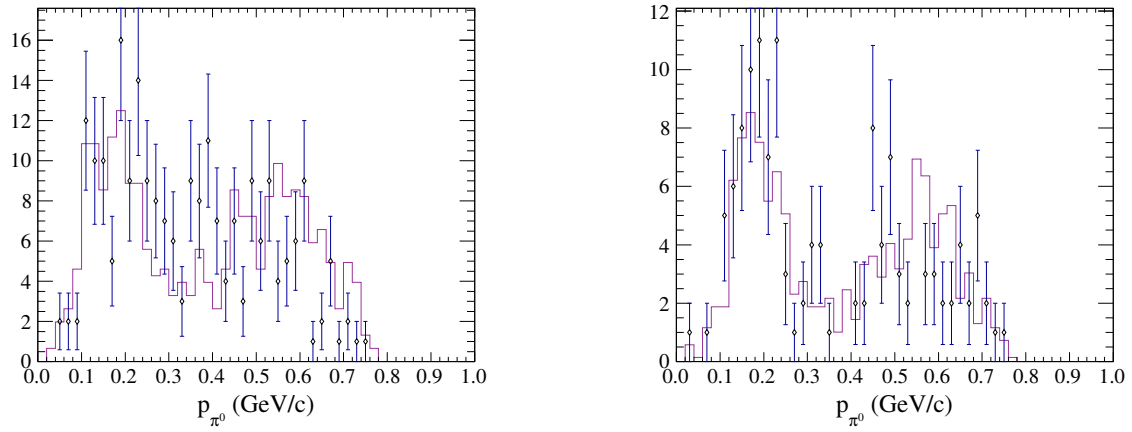
(a) Momentum distribution of  $\pi^0$  in  $CP+$  vs  $\pi^+\pi^-\pi^0$  events. (b) Momentum distribution of  $\pi^0$  in  $CP-$  vs  $\pi^+\pi^-\pi^0$  events.

**Figure 89:** Data and MC overlays of  $\pi^0$  momentum distributions of  $\pi^+\pi^-\pi^0$  events.



(a) Momentum distribution of  $K^+$  and  $K^-$  in  $CP+$  vs  $K^+K^-\pi^0$  events. (b) Momentum distribution of  $K^+$  and  $K^-$  in  $CP-$  vs  $K^+K^-\pi^0$  events.

**Figure 90:** Data and MC overlays of charged kaon momentum distributions of  $K^+K^-\pi^0$  events.



(a) Momentum distribution of  $\pi^0$  in  $CP+$  vs  $K^+K^-\pi^0$  events. (b) Momentum distribution of  $\pi^0$  in  $CP-$  vs  $K^+K^-\pi^0$  events.

**Figure 91:** Data and MC overlays of  $\pi^0$  momentum distributions of  $K^+K^-\pi^0$  events.

### 8.4 Single-tag peaking backgrounds

The peaking-background levels for the single-tag candidates, normalized to total signal for each  $CP$  value, are small, about 3% for both  $CP+$  and  $CP-$  tags. We estimate the systematic uncertainty in this background level by assuming that the peaking backgrounds predicted by the MC are accurate to  $\pm 25\%$ . Thus, we take  $\delta A/A = \delta B/B = 0.75\%$ . For  $\pi^+\pi^-\pi^0$ , we scale this value by  $(1 - f) \simeq 0.05$  and then add the uncertainties in the two  $CP$  tags ( $CP\pm$ ) in quadrature (scaled by  $\sqrt{2}$ ). We arrive at a fractional systematic uncertainty on  $F_+$  of 0.05%, which we round up to 0.1%. Similarly, for the  $K^+K^-\pi^0$  mode, with  $(1 - f) \simeq 0.33$ , we find the fractional systematic uncertainty as 0.4%.

Tag modes,  $K_S\eta'(\rho\gamma)$  and  $K_S\omega$ , that have larger peaking background fractions, are treated empirically via sideband subtractions.

### 8.5 Double tag peaking backgrounds

Naively, the fraction  $pBG$  from the tags and signal add. Of course, the effects of quantum correlations alter this, since like-sign (opposite-sign)  $CP$  pairings are forbidden (enhanced). Furthermore, especially for  $\pi^+\pi^-\pi^0$ , a  $CP-$  signal vs. a  $CP+$  tag is rare due to quantum correlation, so that when we separate DTs by  $CP$ , one combination has much larger peaking background due to the greatly suppressed signal. We present two separate analyses of this issue.

First, we note from Tables 42 and 47 that the central values for the peaking-background fraction vary significantly among the  $CP+$  tags. Thus, we can try using one or two of the three modes instead of all three to measure the  $F_+$  value. Stability of the results will give confidence in the peaking-background predictions. The results of such variations are shown in Table 59.

In the case of the  $\pi^+\pi^-\pi^0$  mode, the statistical uncertainties are completely dominated by the small  $CP+$  tag,  $CP-$  signal yields. Thus, uncertainties on the results on, for example, “ $\pi\pi$  only” and “except for  $\pi\pi$ ” are almost entirely uncorrelated. The differences between all the “only” and “except for” pairs are well under one standard deviation.

In the  $K^+K^-\pi^0$  case, for the two pairs whose fit converge, the uncertainties in the  $CP+$  tag,  $CP-$  signal still dominate, but not quite as much. The differences about one standard deviation.

**Table 59:** Results of systematic studies varying  $CP+$  tags.

Study	$F_+ (\pi^+\pi^-\pi^0)$	$F_+ (K^+K^-\pi^0)$
Nominal Analysis	$0.9680 \pm 0.0065$	$0.7824 \pm 0.0347$
$\pi\pi$ tag only	$0.9650 \pm 0.0140$	$0.7110 \pm 0.0559$
$KK$ tag only	$0.9658 \pm 0.0088$	fails to converge
$K_S\pi^0\pi^0$ tag only	$0.9703 \pm 0.0101$	$0.8170 \pm 0.0534$
Except for $\pi\pi$ tag	$0.9683 \pm 0.0071$	$0.7942 \pm 0.0373$
Except for $KK$ tag	$0.9692 \pm 0.0086$	$0.7928 \pm 0.0430$
Except for $K_S\pi^0\pi^0$ tag	$0.9656 \pm 0.0075$	$0.7505 \pm 0.0372$

Second, we discuss the uncertainties based on the size of the peaking backgrounds relative to

the signal, as summarized in Tables 42 and 47. We base our systematic uncertainty on trusting the MC predictions to be accurate to  $\pm 25\%$ .

For  $CP-$  tags vs. the more common  $CP+$  signal, the peaking backgrounds are small: 3.2% and 3.6% for  $\pi^+\pi^-\pi^0$  and  $K^+K^-\pi^0$ , respectively. If we scale these values by 1/4 to represent our level of intrinsic understanding, and then apply the (slightly conservative, as used above)  $(1 - f)$  factors, we arrive at 0.04% and 0.30%, for the systematic uncertainties respectively.

For  $CP+$  tags vs. the rarer  $CP-$  signal, the peaking backgrounds are rather large: 67% and 8.9% for  $\pi^+\pi^-\pi^0$  and  $K^+K^-\pi^0$ , respectively. Using the same scaling as for the previous case, we obtain about 0.8% and 0.7%, respectively. These dominate over other systematic uncertainties.

Note that the uncertainty on the  $\pi^+\pi^-\pi^0$  branching fraction is 4.2%; for  $K^+K^-\pi^0$ , it is 4.3%. These directly affect the normalization of our MC prediction of the peaking backgrounds, but are small compared to  $\pm 25\%$  value. we have used for estimating the systematic uncertainties.

The branching fractions listed in the BESIII decay table add up to about 100%. Therefore, we assume there is no string fragmentation in the decay process. This gives us more confidence in our MC predictions of the peaking backgrounds.

## 8.6 $K_s$ veto of $\pi^+\pi^-\pi^0$

A  $K_s$  veto is applied in the analysis of the  $\pi^+\pi^-\pi^0$  mode, and three different vetoes are studied, as explained in Section 6.2.

To estimate the systematic uncertainty coming from this requirement the veto is widened from the nominal value of  $\pm 0.018 \text{ GeV}/c^2$  to  $\pm 0.024 \text{ GeV}/c^2$  around the  $K_s$  PDG mass. The complete analysis is repeated, and the results are given in Table 60. The difference in the result is negligible. Any shift in the result could be due to larger changes in the amount of background leaking through the altered veto, and changes due to the region of the signal Dalitz plot being excluded. The assigned systematic uncertainty should cover both of these effects. Since, these different two effects may partially cancel each other, to be safe, we assign a 0.1% uncertainty, which is 40 times larger than the observed shift in the result.

**Table 60:** Results with altered  $K_s$  veto

Study	$F_+(\pi^+\pi^-\pi^0)$
Nominal Analysis	$0.9680 \pm 0.0065$
Wider $K_s$ Veto	$0.9682 \pm 0.0066$

## 8.7 Yield Systematic Uncertainties

Uncertainties related to the yield methods are investigated for both ST and DT. The main concern is about the DT yield method due to the high  $pBG$  fraction and the relatively simple procedure used.

The systematic uncertainty in the method to determine the DT yields can be studied by altering

the  $A, B, C, D$  and  $S$  regions. The scale factor used for the  $C$  region can also be varied since for the rare- $CP$  modes the diagonal band is the dominant structure in the two-dimensional  $M_{BC}$  distribution and these DT combinations also suffer from high  $pBG$  fractions.

We scaled the scale factor used for the  $C$  region by 1.3 to increase the subtraction due to the diagonal band in the two-dimensional  $M_{BC}$  distribution and measured the  $CP$ -even content. Results are given in 61. The difference in the  $CP$ -even content is assigned as systematic uncertainty, which is 0.3% for  $\pi^+\pi^-\pi^0$  and 0.4% for  $K^+K^-\pi^0$ .

**Table 61:** Results with altered  $C$  region scale factor.

Study	$F_+ (\pi^+\pi^-\pi^0)$	$F_+ (K^+K^-\pi^0)$
Nominal Analysis	$0.968 \pm 0.006$	$0.782 \pm 0.035$
Scaled $C$ region count	$0.965 \pm 0.009$	$0.779 \pm 0.036$

## 8.8 Summary of Uncertainties

A summary of all the sources of systematic uncertainties considered is given in Table 62. Individual contributions are added in quadrature to obtain the total uncertainty, also shown in Table 62.

**Table 62:** Summary of the contributions to the systematic uncertainty in %, for the measured  $F_+$  for each of the two signal modes, and the total uncertainty. Systematic uncertainties on the yields are still to be determined.

Source	$\pi^+\pi^-\pi^0$	$K^+K^-\pi^0$
Tag-side Efficiency	$< 0.1\%$	$< 0.1\%$
Signal-side Efficiency	0.1%	0.5%
ST peaking background	0.1%	0.4%
DT peaking background	0.8%	0.7%
$K_S$ Veto	0.1%	N/A
Yields	0.3%	0.4%
Total	0.9%	1.0%

## 8.9 MC in/out Test

An input/output test, where the intrinsic value of  $F_+$  in the BESIII MC sample is measured, has been carried out for the Monte Carlo sample to test the methodology used in this analysis. As mentioned earlier, the BESIII MC sample is divided into two parts, where one part is used for the efficiency measurement and the other sample is used as a fake-data sample. All other steps in the analysis is same as for the data measurement.

The extracted  $F_+$  values are given in Table 63, along with the number of standard deviations ( $\sigma$ ) the extracted value is from the MC input value. The output results are consistent with the MC, and provide us with confidence in the analysis.

**Table 63:** Results of the in/out test from the MC, and  $F_+$  values for the  $\pi^+\pi^-\pi^0$  and  $K^+K^-\pi^0$  final states and the number of standard deviations ( $\sigma$ ) the input and output values differ.

Signal	$F_+$ MC Output Measurement	MC Input	$\sigma$ off
$\pi^+\pi^-\pi^0$	$0.975 \pm 0.004$	0.978	0.87
$K^+K^-\pi^0$	$0.871 \pm 0.019$	0.868	-0.18

## 9 $F_+$ Measurement and Implications

### 9.1 Data Measurement

The corrected yields of single- and double-tags (given in Section 7) are used in Equation 1 to extract the  $CP+$  fraction  $F_+$  of  $\pi^+\pi^-\pi^0$  and  $K^+K^-\pi^0$  decays. Results are given in Table 64. The first measurement of this quantity, described in Ref. [15] (and updated measurement in Ref. [28]), is also given in the same table. The results from the two experiments agree within their uncertainties, while the statistical uncertainty is improved because of the larger the BESIII data. Our systematic uncertainty is larger for  $\pi^+\pi^-\pi^0$ . However, our largest contribution, DT peaking-background is described as “negligible” in [15], which is rather surprising to us.

The effects of  $CP$  violation in the charm system is neglected throughout this measurement, given the experimental upper limits [29] and theoretical expectations [14].

**Table 64:**  $F_+$  values for the  $\pi^+\pi^-\pi^0$  and  $K^+K^-\pi^0$  final states for this analysis and for an earlier experiment.

Signal	$F_+$ Measurement	$F_+$ from Libby <i>et al.</i>
$\pi^+\pi^-\pi^0$	$0.968 \pm 0.006 \pm 0.009$	$0.968 \pm 0.017 \pm 0.006$
$K^+K^-\pi^0$	$0.782 \pm 0.035 \pm 0.008$	$0.731 \pm 0.058 \pm 0.021$

### 9.2 Implications

As mentioned in Section 1, the unitarity triangle angle  $\gamma$  can be measured from a study of  $B^\mp \rightarrow DK^\mp$  decays. By taking advantage of the  $CP+$  fraction measurement done here, related observables of partial-width ratio  $R_{F_+}$  and  $CP$ -asymmetry  $A_{F_+}$  can be written as follows.

$$R_{F_+} \equiv \frac{\Gamma(B^- \rightarrow D_{F_+} K^-) + \Gamma(B^+ \rightarrow D_{F_+} K^+)}{\Gamma(B^- \rightarrow D^0 K^-) + \Gamma(B^+ \rightarrow \bar{D}^0 K^+)} \quad (12)$$

$$(13)$$

$$A_{F_+} \equiv \frac{\Gamma(B^- \rightarrow D_{F_+} K^-) - \Gamma(B^+ \rightarrow D_{F_+} K^+)}{\Gamma(B^- \rightarrow D_{F_+} K^-) + \Gamma(B^+ \rightarrow D_{F_+} K^+)}' \quad (14)$$

where  $D_{F_+}$  is a  $D$  meson decay with  $CP+$  fraction  $F_+$ . Direct analogy can be drawn with the GLW method, where the corresponding observables are  $R_{CP\pm}$  and  $A_{CP\pm}$ . The  $R_{F_+}$  and  $A_{F_+}$  can be rewritten in terms of the  $CP+$  fraction and the angles  $\delta_B$  and  $\gamma$ , when mixing is neglected, as:

$$R_{F_+} = 1 + r_B^2 + (2F_+ - 1) \cdot 2r_B \cos(\delta_B) \cos(\gamma), \quad (15)$$

$$A_{F_+} = (2F_+ - 1) \cdot 2r_B \sin(\delta_B) \sin(\gamma) / R_{F_+}. \quad (16)$$

It is clear that when  $F_+$  is 1 or 0, the above equations simplify to  $R_{CP\pm}$  and  $A_{CP\pm}$ . The factor  $(2F_+ - 1)$  can be thought of as a dilution factor, where in the case of the final state having a  $CP$

fraction of 0.5, this method becomes useless. Therefore, final states such as  $\pi^+\pi^-\pi^0$  and  $K^+K^-\pi^0$ , are excellent candidates for a  $\gamma$  measurement.

An analogy can be drawn with flavor oscillations. Many particle physicists are familiar with measurements of meson-anti-meson mixing, for example, in the  $B^0 - \bar{B}^0$  system [30]. To make such a measurement, one uses a decay mode that distinguishes  $B^0$  from  $\bar{B}^0$ . But one also needs to know the “flavor” at production. This “flavor tagging” has both an efficiency,  $\epsilon$ , for producing an answer, and a dilution,  $DF$ , expressing the correctness of the answer. The dilution is the difference in the number of correct and incorrect tags (right and wrong) over the sum:  $DF = (r - w)/(r + w) = 2f - 1$ , where  $f = r/(r + w)$  is the fraction of correct tags. The name “dilution” arises since this factor “dilutes”, or decreases, the amplitude of observed flavor oscillations. If one randomly guesses, one would have  $f = 0.5$  and  $DF = 0$ .

An analogous dilution occurs when using modes like  $\pi^+\pi^-\pi^0$  and  $K^+K^-\pi^0$  to measure the CKM angle  $\gamma$  in  $B$  decays. The main difference is that, with no effort by the experimenter, nature supplies non-zero dilution. We can simply determine the  $CP$  state, assuming it is 100%  $CP+$ . We are correct  $F_+$  of the time, and incorrect  $1 - F_+$  of the time, for a resulting dilution of  $2F_+ - 1$ .

Another use of the  $F_+$  measurement is described in Ref. [31], where self-conjugate final states are used to determine the indirect  $CP$ -violating observable  $A_\Gamma$  and the mixing observable  $y_{CP}$ , the parameter  $A_\Gamma$  is measured from the difference in the  $D^0$  and  $\bar{D}^0$  lifetimes and  $y_{CP}$  describes  $D^0\bar{D}^0$  oscillations.



## A Determining the Efficiencies over the Dalitz Plot for Signal Single-tag Modes

The detection efficiency over the Dalitz plot is calculated using special MC samples that include only single-tag reconstruction of the signal modes,  $\pi^+\pi^-\pi^0$  and  $K^+K^-\pi^0$ . A hundred thousand events are generated in which the  $D^0$  decays to the signal mode and the opposite  $\bar{D}^0$  decays into  $\nu\bar{\nu}$ . Two samples are generated for  $\pi^+\pi^-\pi^0$  and  $K^+K^-\pi^0$ . These special MC samples ensure there is no background from the opposite  $D$  decay, while maintaining the resonant structure of the signal mode.

All the signal selection criteria are applied as usual. However, we need to remove the background caused by not having a  $M_{BC}$  requirement on the candidates. Two separate  $M_{BC}$  windows are determined for use in a Dalitz plot subtraction to reduce the background in the  $M_{BC}$  distribution. Sideband region is chosen to be between  $|M_{BC} - 1.848| < 0.005 \text{ GeV}/c^2$  and the signal region is defined to be  $|M_{BC} - 1.8645| \text{ GeV}/c^2 < 0.005 \text{ GeV}/c^2$ . The corresponding sideband Dalitz plot, is then subtracted from the signal Dalitz plot using a scale determined from the ST  $M_{BC}$  fit to the signal mode. The resulting Dalitz plot is taken as background free and used to calculate the efficiency. The resulting efficiency for  $\pi^+\pi^-\pi^0$  is displayed in Figure 92 and for  $K^+K^-\pi^0$  in Figure 93.

Distributions that are used to calculate the efficiency of the  $\pi^+\pi^-\pi^0$  mode are given in Figure 94 for the two-dimensional Dalitz plots and in Figure 95 for the projections. Similar plots for the  $K^+K^-\pi^0$  channel are shown in Figure 96 and in Figure 97 for the projections.

The efficiencies over the Dalitz plot are fairly constant for the  $\pi^+\pi^-\pi^0$  mode. For  $K^+K^-\pi^0$ , the most noticeable feature is a lower efficiency at the highest  $K^\pm\pi^0$  masses (Figure 93), visible both in the 2-dimensional plot and the two relevant projections. This dip is because the largest values of  $M_{K^\pm\pi^0}^2$  directly correspond to the smallest  $K^\mp$  energy values, and the tracking efficiency falls off for these low-momentum kaons. This same effect also causes the dip in the efficiency in the  $K^+K^-$  mass projection. Note that the dip is not at the minimum value of  $M_{K^+K^-}^2$ ; this corresponds to the softest  $\pi^0$ , but not the softest  $K^\pm$ .

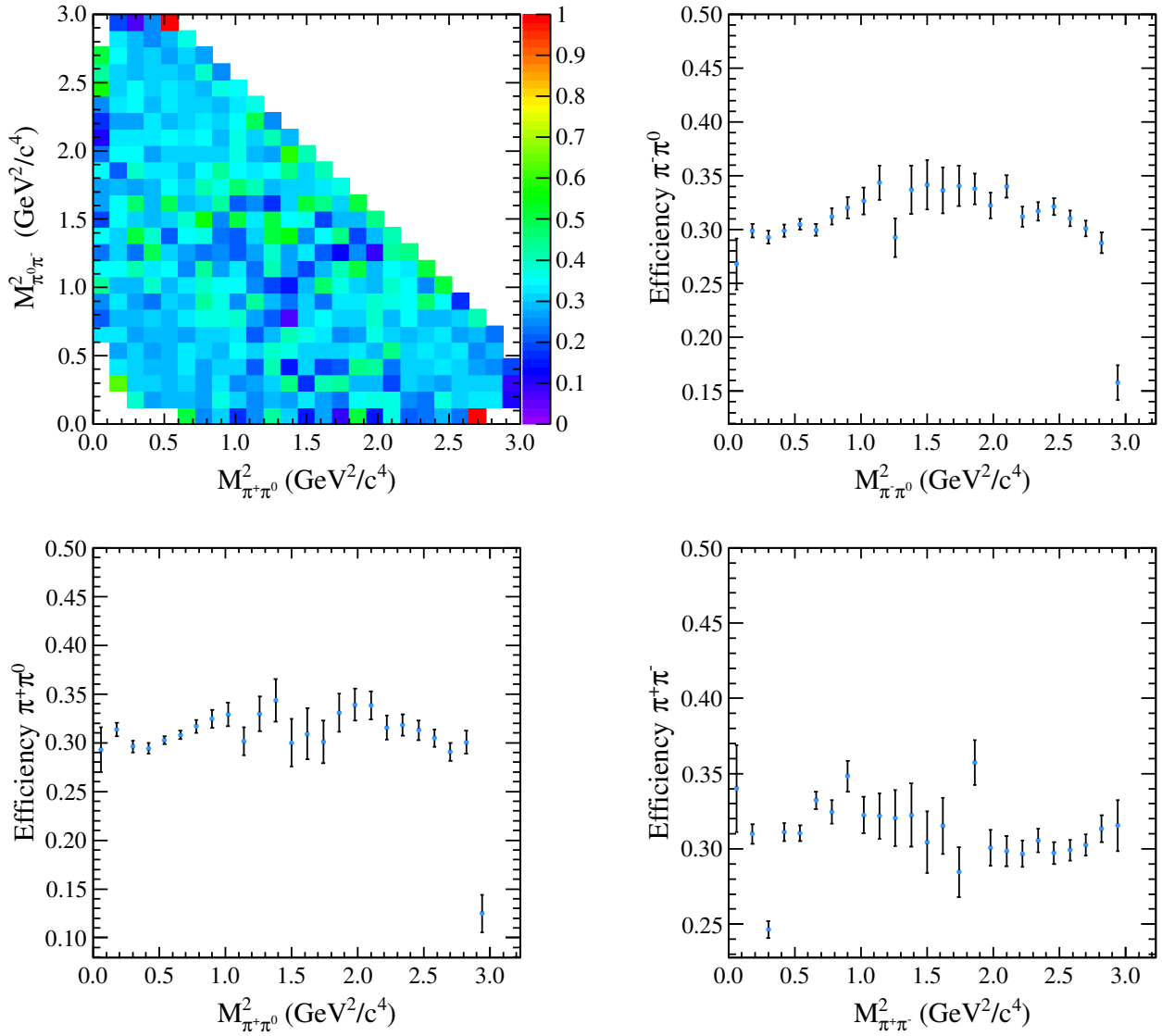
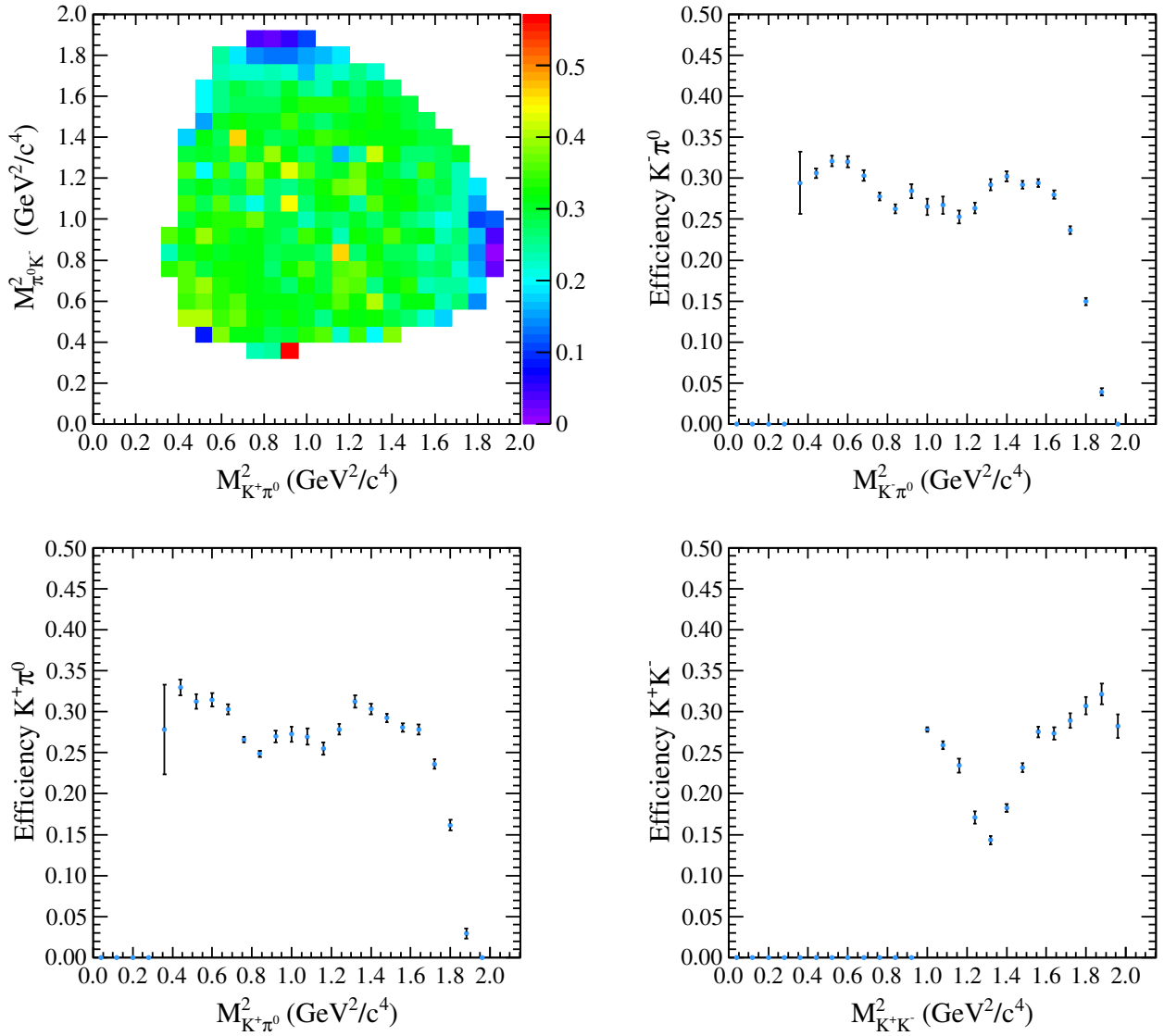
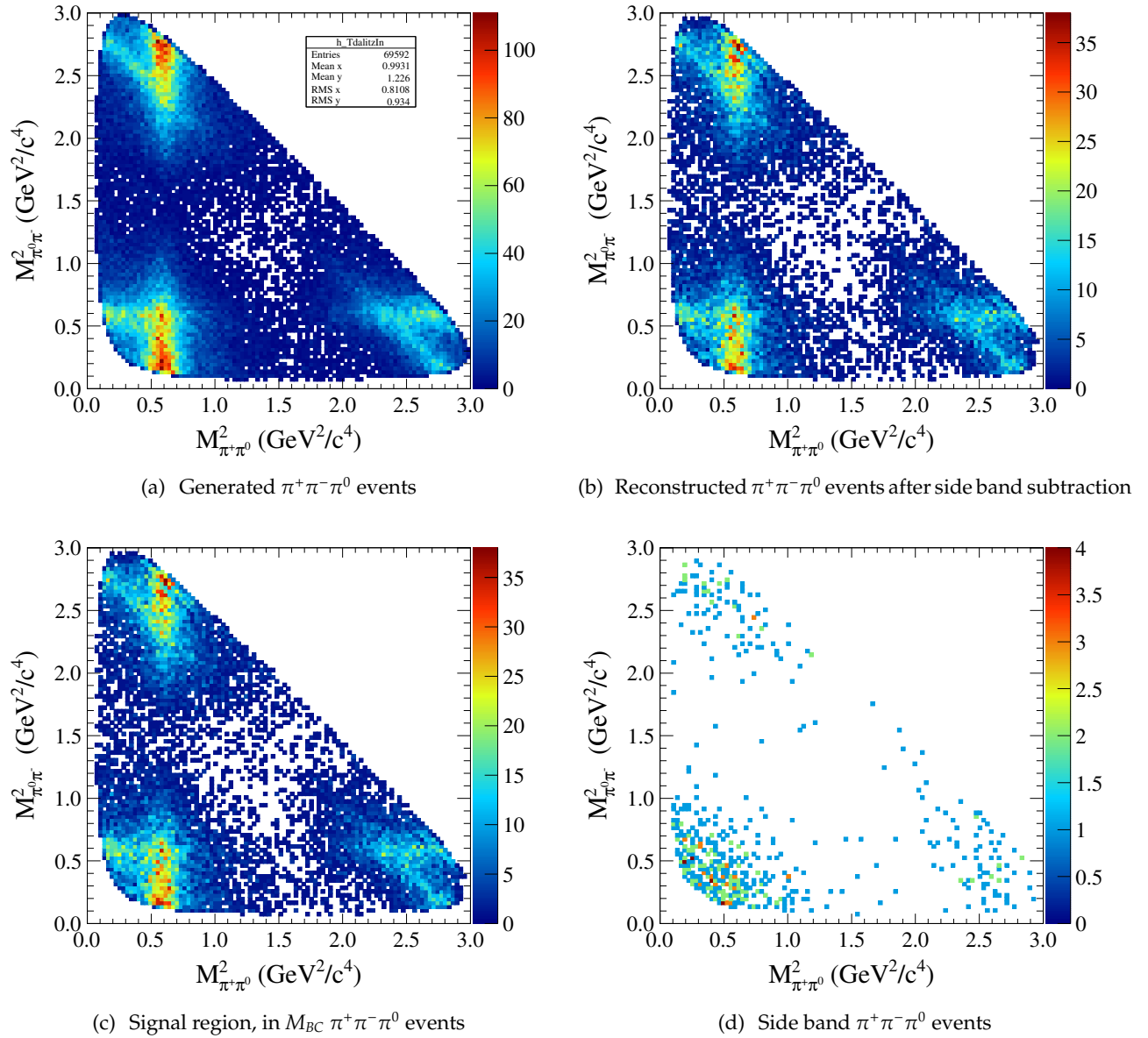


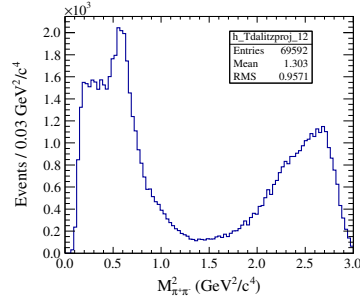
Figure 92: DP efficiency for single tag  $\pi^+\pi^-\pi^0$  events



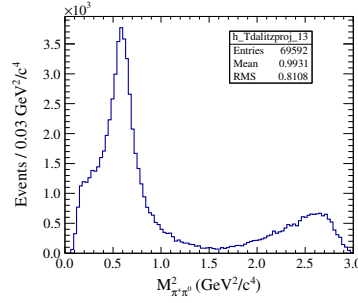
*Figure 93: DP efficiency for single tag  $K^+K^-\pi^0$  events*



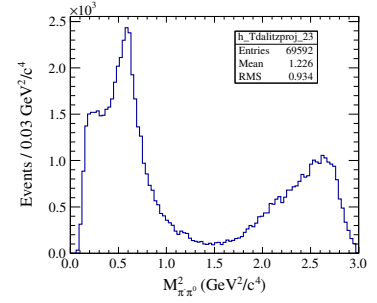
**Figure 94:** Dalitz Plot distributions that are used in the calculation of the DP efficiency for  $\pi^+\pi^-\pi^0$  mode.



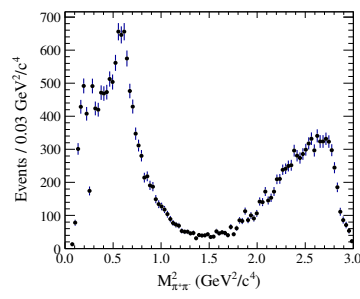
(a) Generated events,  $\pi^+\pi^-$  projection



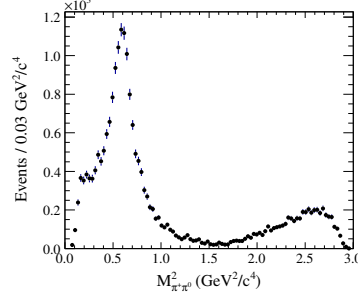
(b) Generated events,  $\pi^+\pi^0$  projection



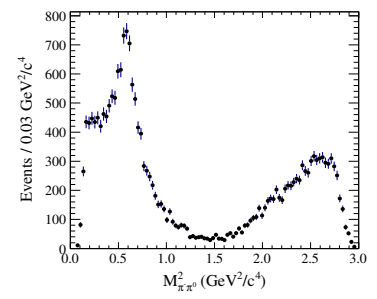
(c) Generated events,  $\pi^-\pi^0$  projection



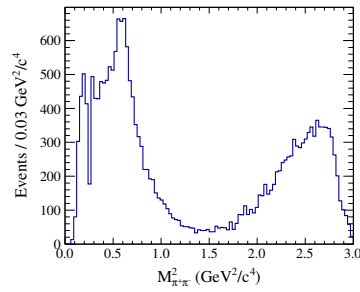
(d) Reconstructed events w/o bg,  $\pi^+\pi^-$  projection



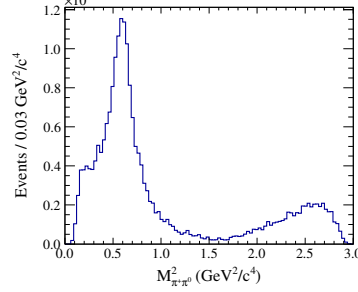
(e) Reconstructed events w/o bg,  $\pi^+\pi^0$  projection



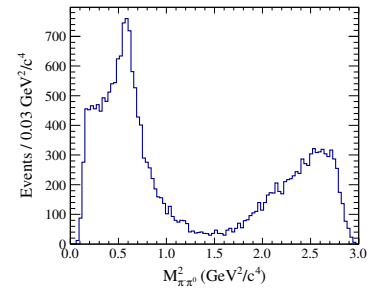
(f) Reconstructed events w/o bg,  $\pi^-\pi^0$  projection



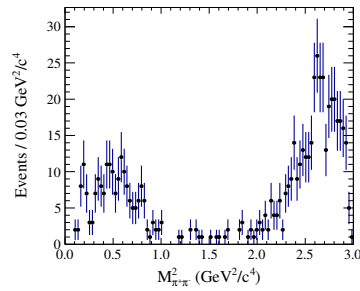
(g) Signal region, in  $M_{BC}$   $\pi^+\pi^-$  projection



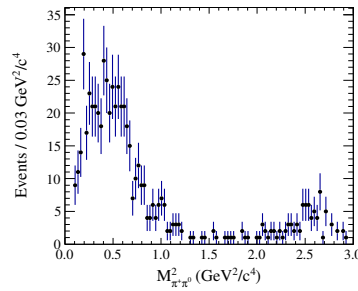
(h) Signal region, in  $M_{BC}$   $\pi^+\pi^0$  projection



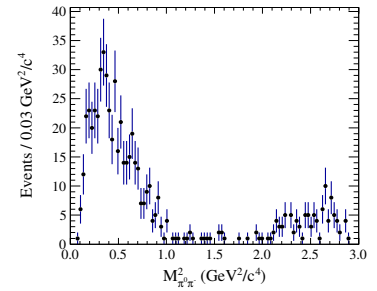
(i) Signal region, in  $M_{BC}$   $\pi^-\pi^0$  projection



(j) Side band,  $\pi^+\pi^-$  projection



(k) Side band,  $\pi^+\pi^0$  projection



(l) Side band,  $\pi^-\pi^0$  projection

**Figure 95:** Dalitz Plot projections that are used in the calculation of the DP efficiency for  $\pi^+\pi^-\pi^0$  mode.

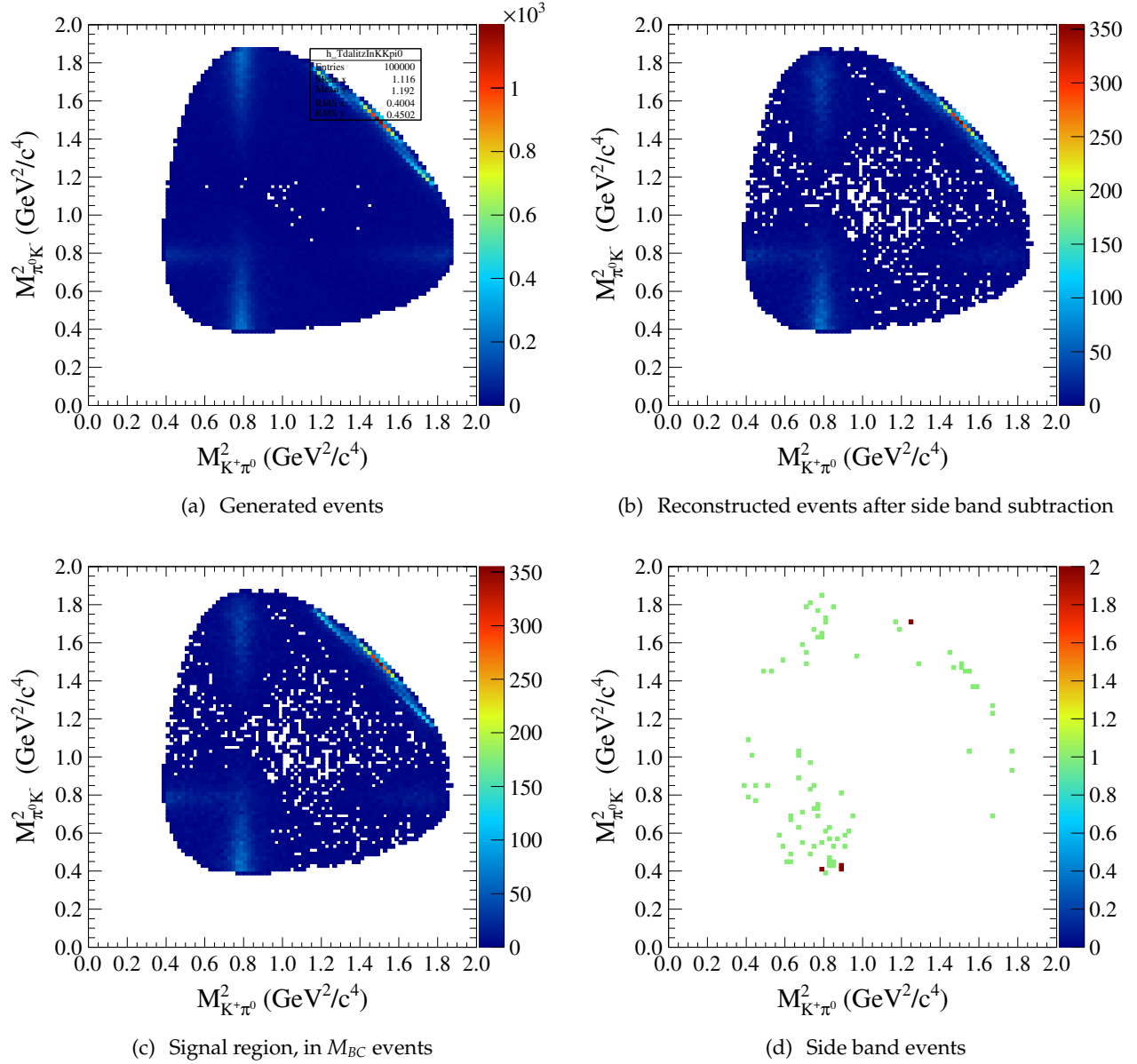
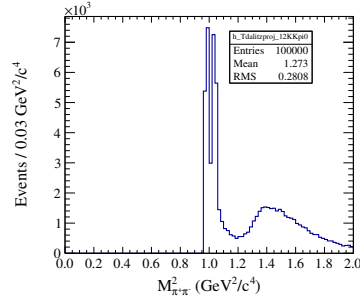
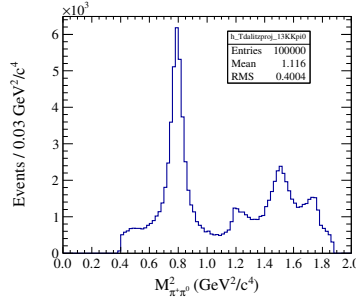


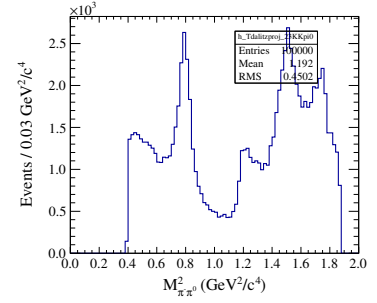
**Figure 96:** Dalitz Plot distributions that are used in the calculation of the DP efficiency for the  $K^+K^-\pi^0$  mode.



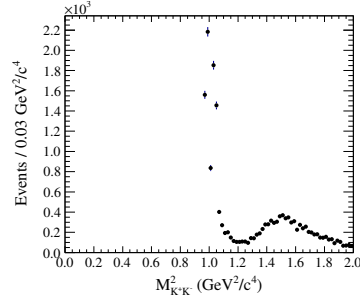
(a) Generated events,  $K^+K^-$  projection



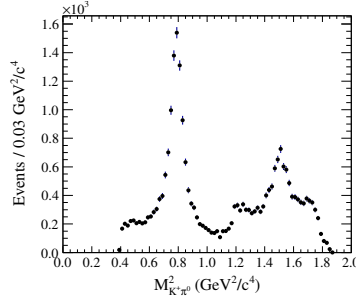
(b) Generated events,  $K^+\pi^0$  projection



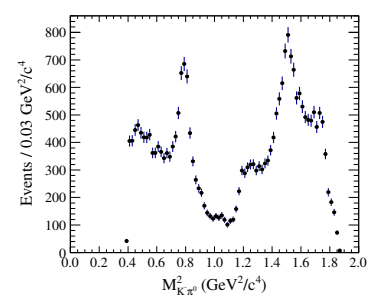
(c) Generated events,  $K^-\pi^0$  projection



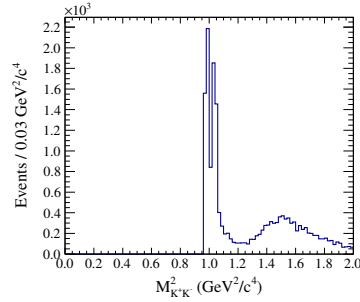
(d) Reconstructed events w/o bg,  $K^+K^-$  projection



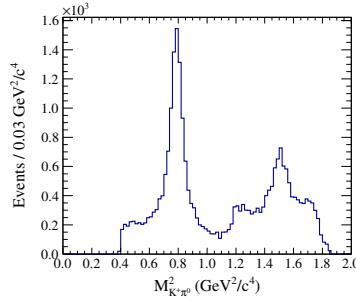
(e) Reconstructed events w/o bg,  $K^+\pi^0$  projection



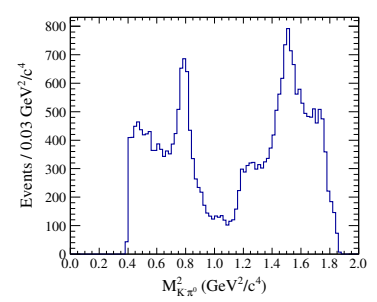
(f) Reconstructed events w/o bg,  $K^-\pi^0$  projection



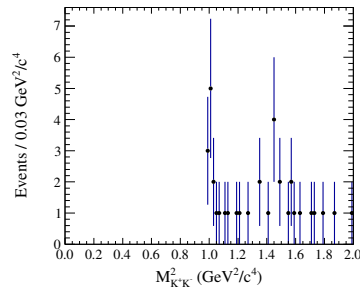
(g) Signal region, in  $M_{BC}$   $K^+K^-$  projection



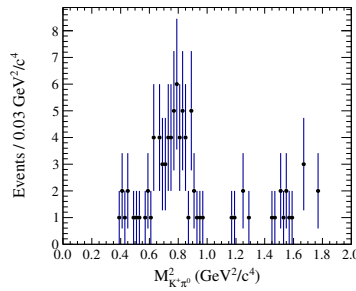
(h) Signal region, in  $M_{BC}$   $K^+\pi^0$  projection



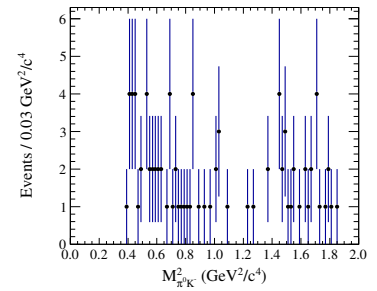
(i) Signal region, in  $M_{BC}$   $K^-\pi^0$  projection



(j) Side band,  $K^+K^-$  projection



(k) Side band  $K^+\pi^0$  projection,



(l) Side band  $K^-\pi^0$  projection,

**Figure 97:** Dalitz Plot projections that are used in the calculation of the DP efficiency for  $K^+K^-\pi^0$  mode.

## B Double Tag Dalitz Plots

### B.1 $\pi^+\pi^-\pi^0$ Double Tag Dalitz Plots

Dalitz plots for  $\pi^+\pi^-\pi^0$  vs.  $CP+$  tags are shown in Figure 98 and  $\pi^+\pi^-\pi^0$  vs.  $CP-$  tags are shown in Figure 99 for the data sample.

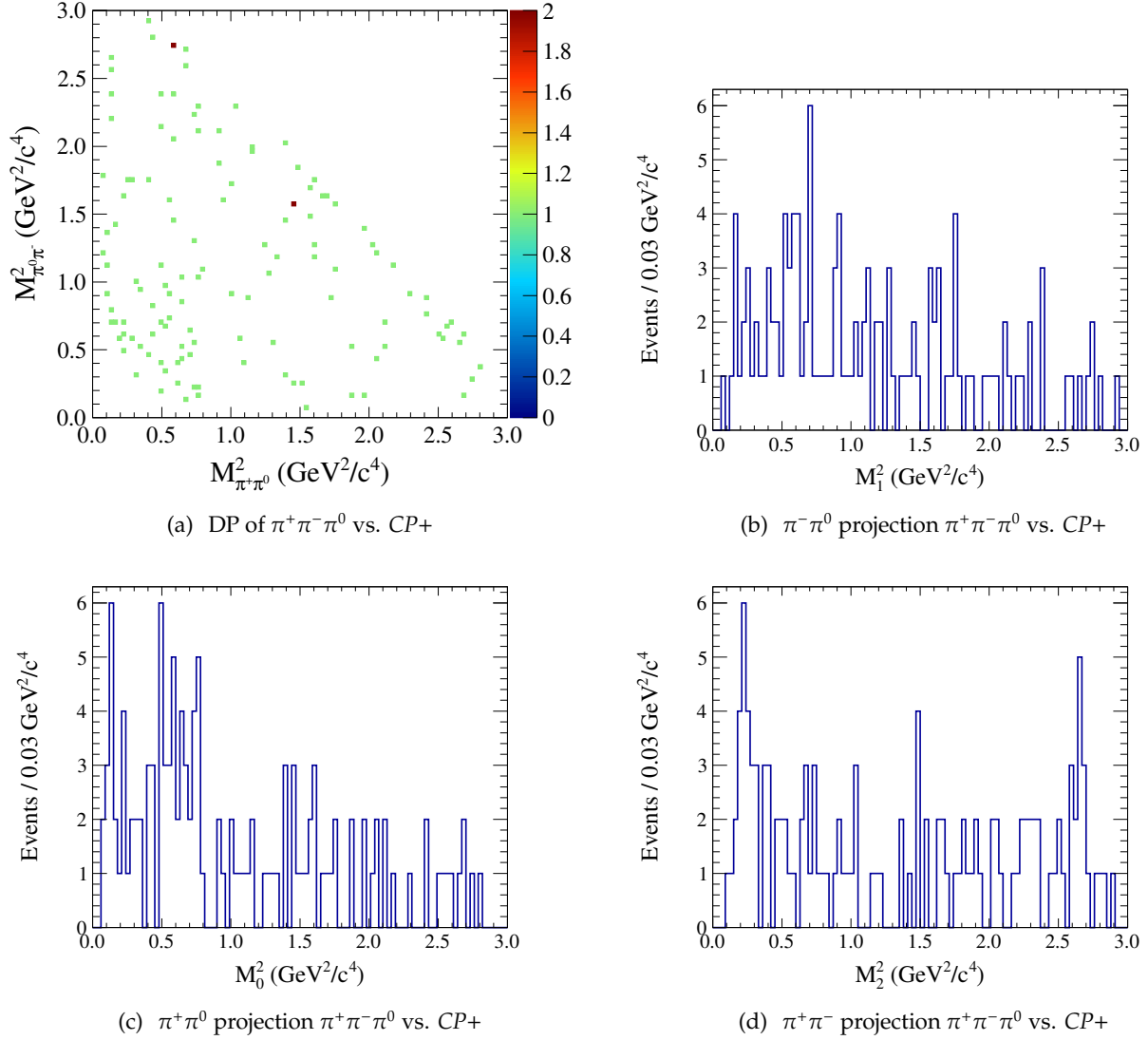
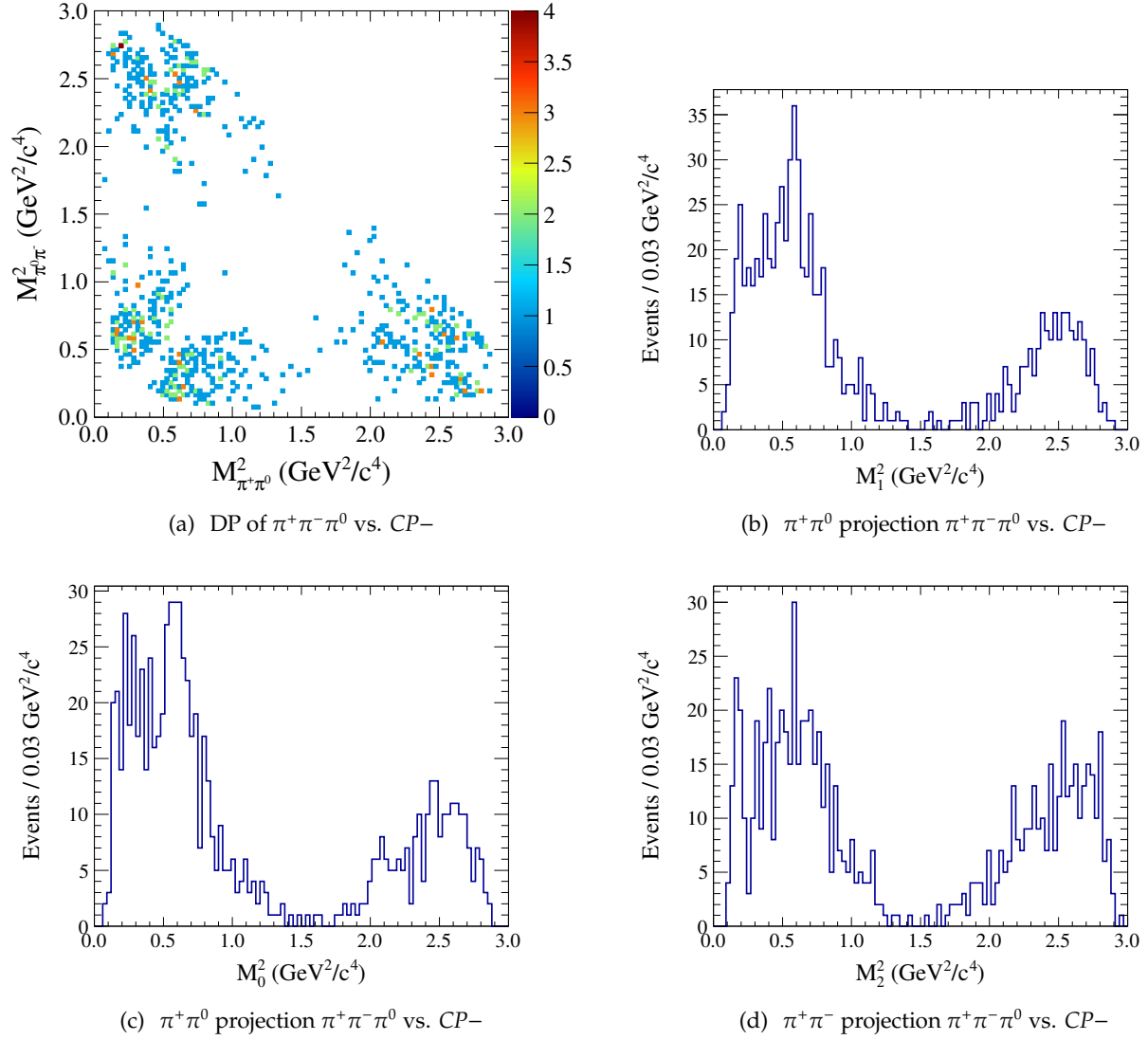


Figure 98:  $\pi^+\pi^-\pi^0$  vs.  $CP+$  events the data sample

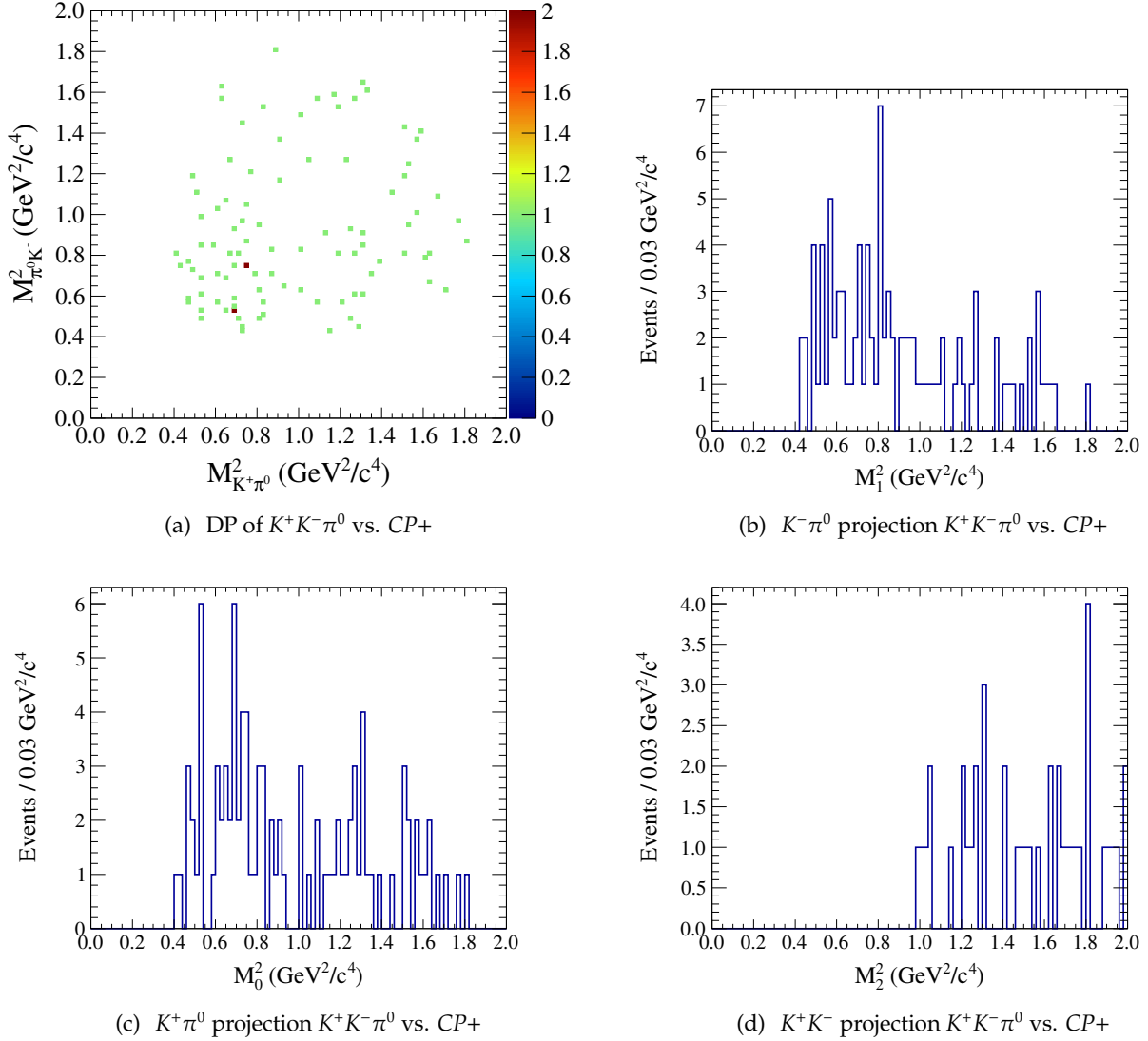




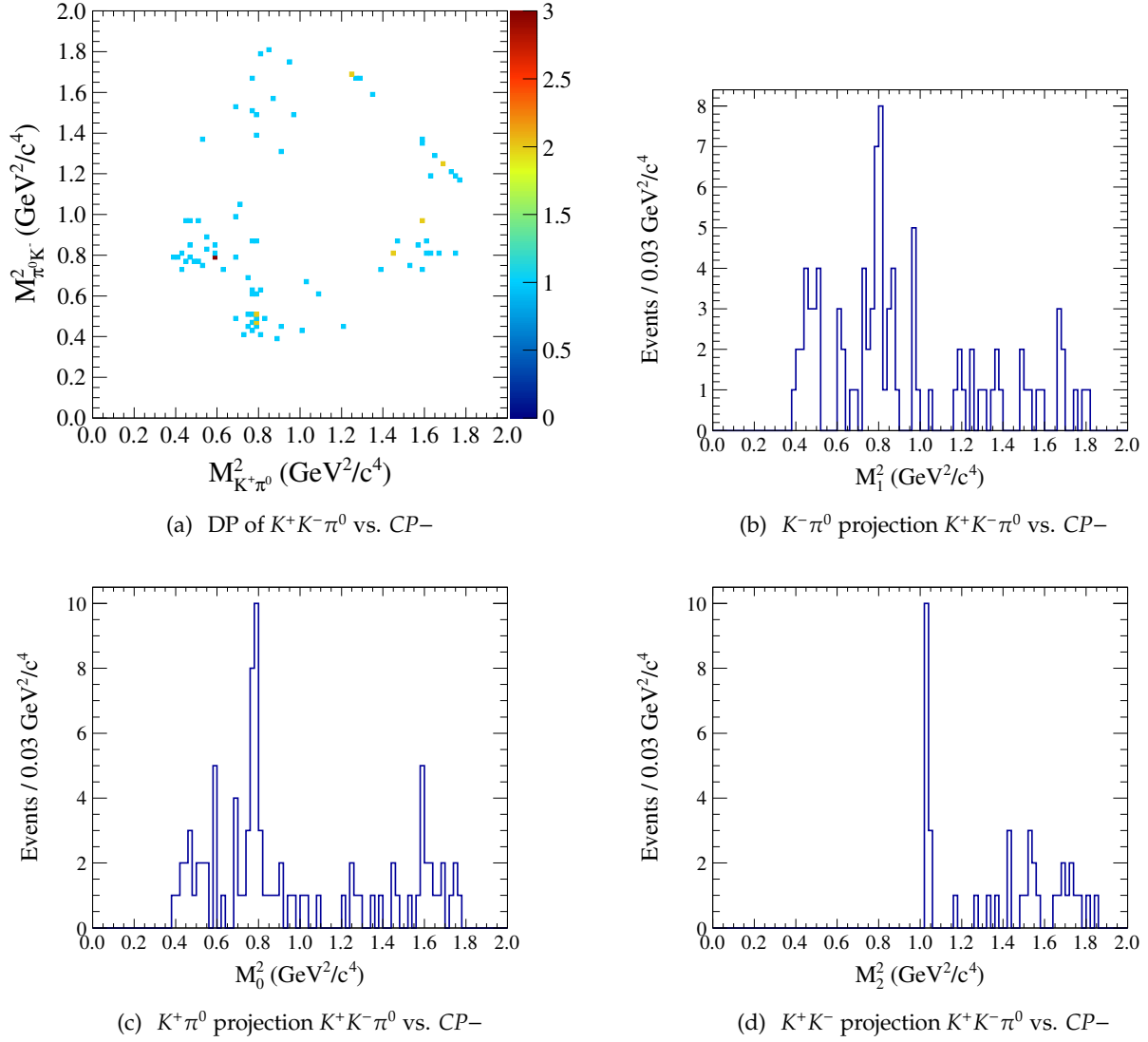
**Figure 99:**  $\pi^+\pi^-\pi^0$  vs.  $CP-$  events for the data sample

## B.2 $K^+K^-\pi^0$ Double Tag Dalitz Plots

Dalitz plots for  $K^+K^-\pi^0$  vs.  $CP+$  tags are shown in Figure 100 and  $K^+K^-\pi^0$  vs.  $CP-$  tags are shown in Figure 101 for the data sample.



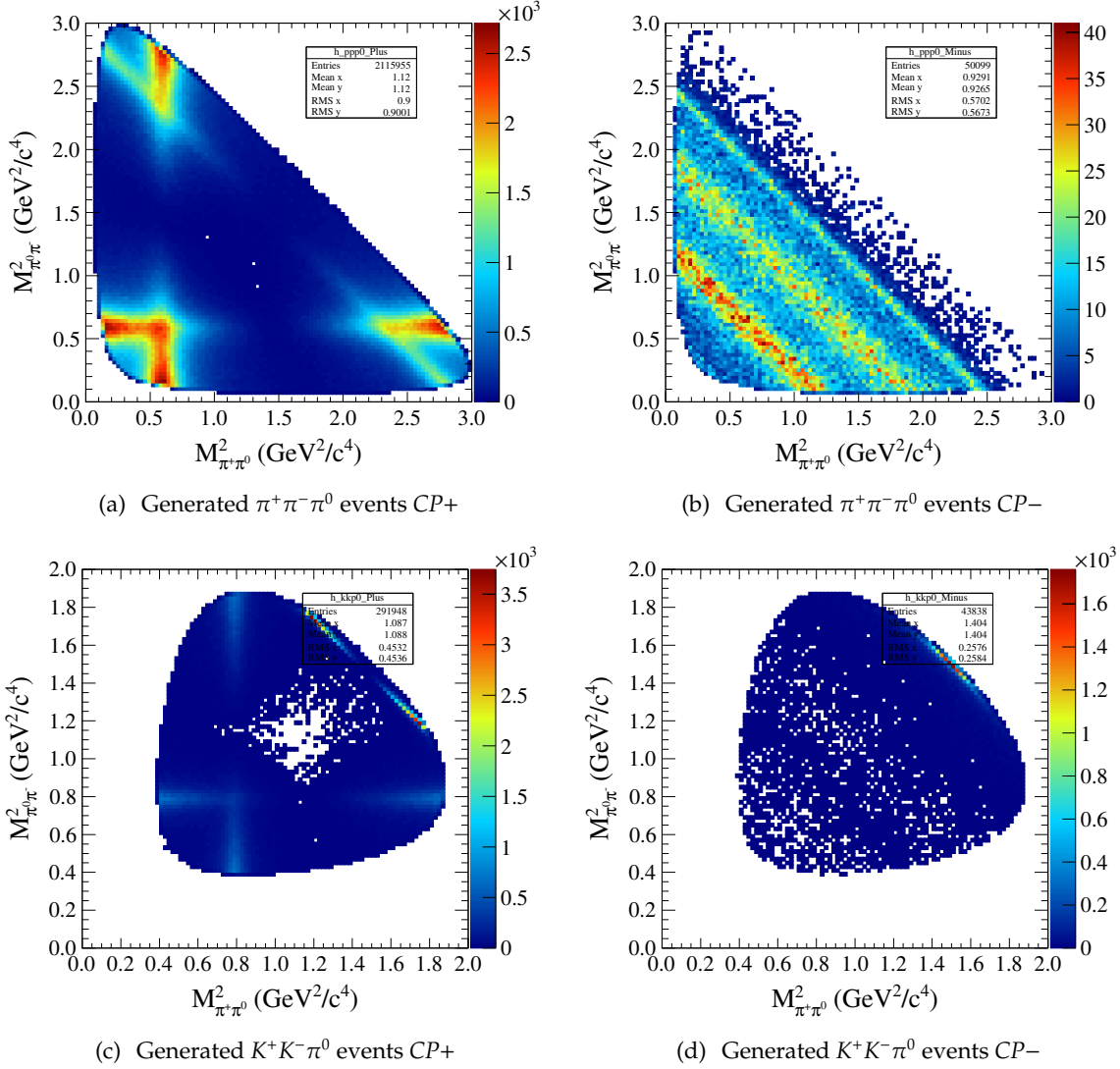
**Figure 100:**  $K^+K^-\pi^0$  vs.  $CP+$  events for the data sample



**Figure 101:**  $K^+K^-\pi^0$  vs.  $CP-$  events for the data sample

### B.3 Dalitz Plot of $CP$ contribution to the signal modes

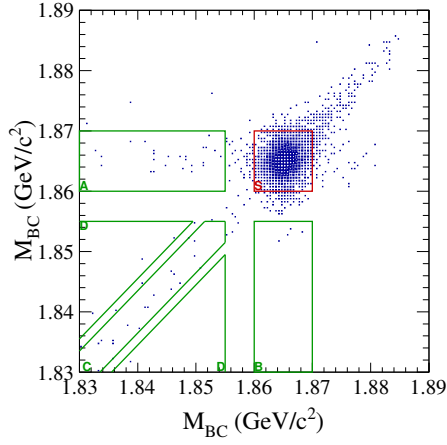
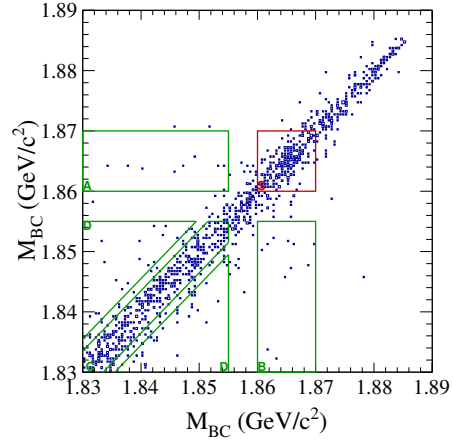
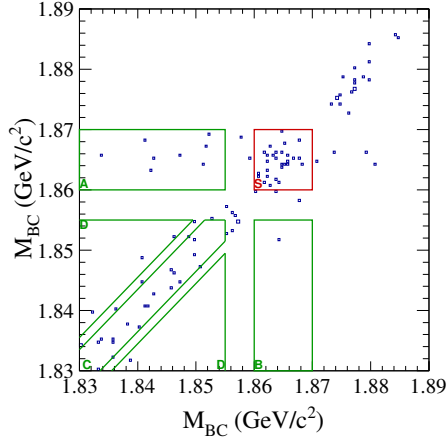
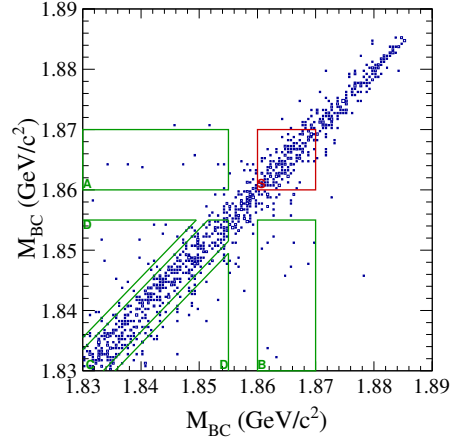
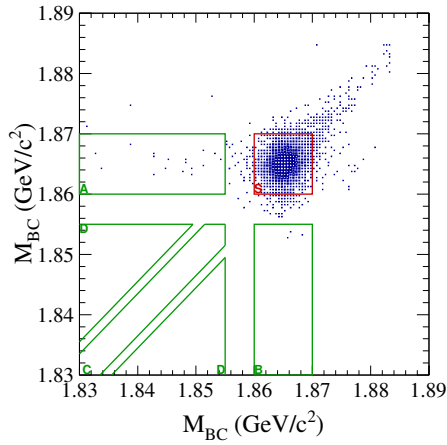
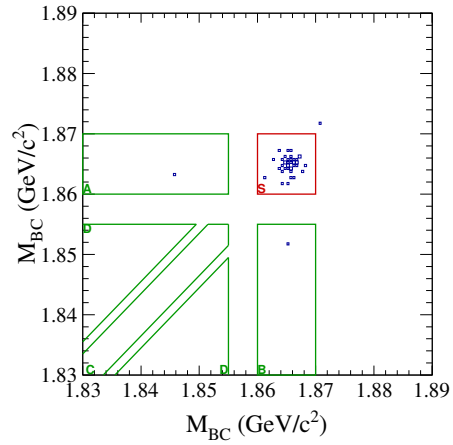
Dalitz plot distributions of the signal modes separated by the  $CP$  content of the intermediate resonances are given in Figure 102 for the MC sample.

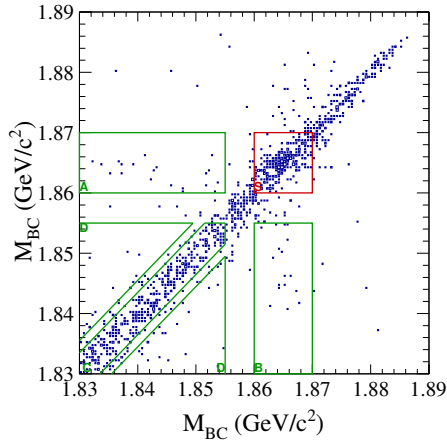
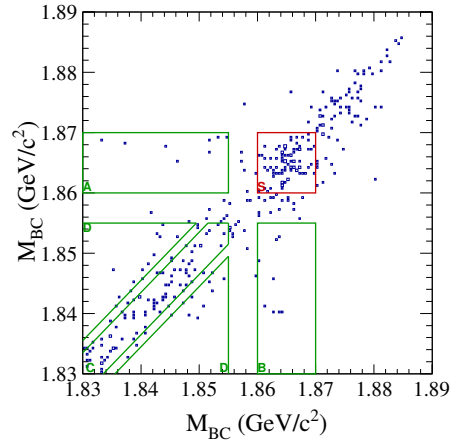
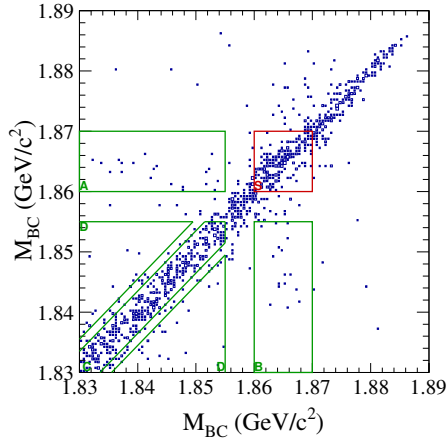
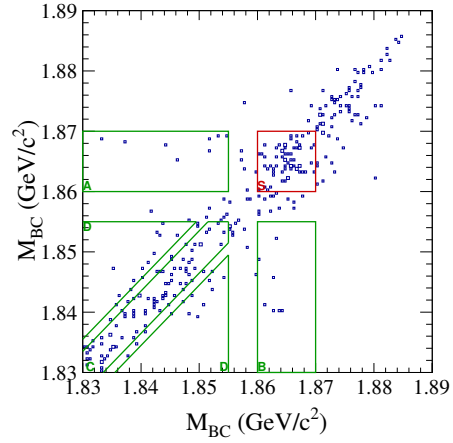
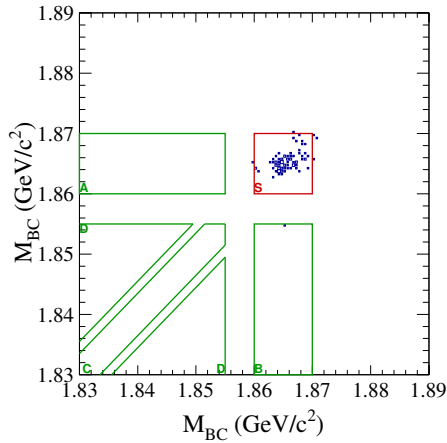
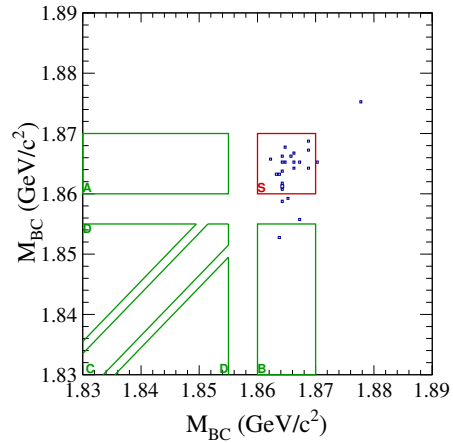


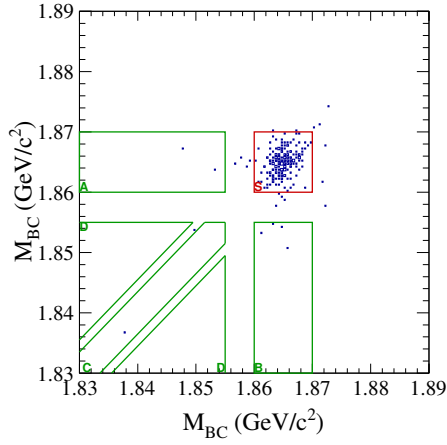
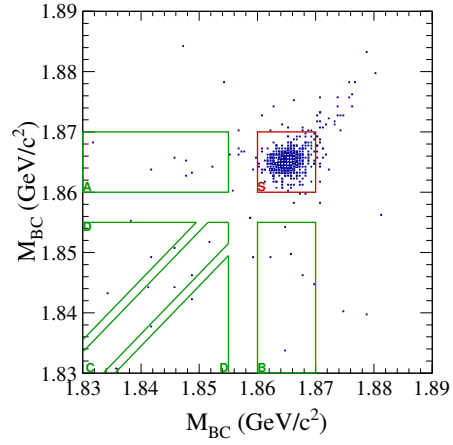
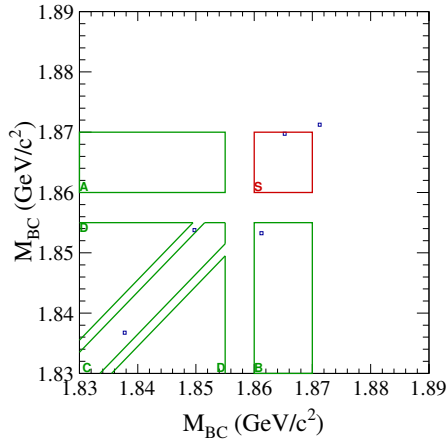
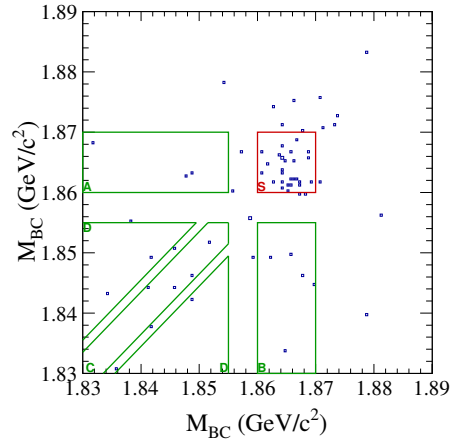
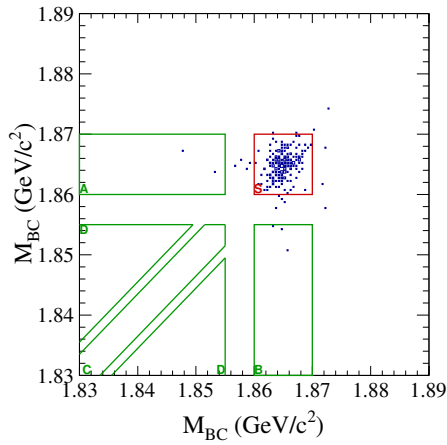
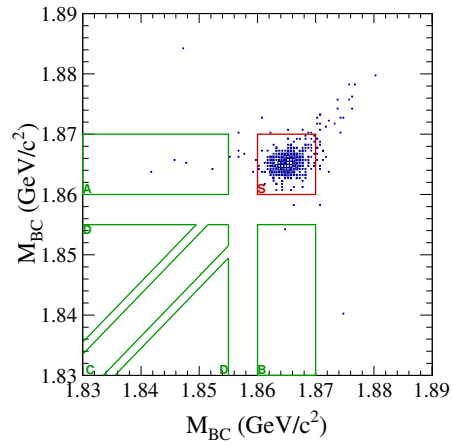
**Figure 102:** Dalitz Plot distributions of the signal modes separated by  $CP$  content for  $\pi^+\pi^-\pi^0$  and  $K^+K^-\pi^0$

## C Peaking Background Box Plots

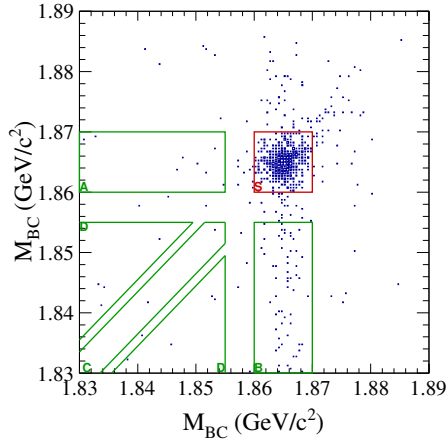
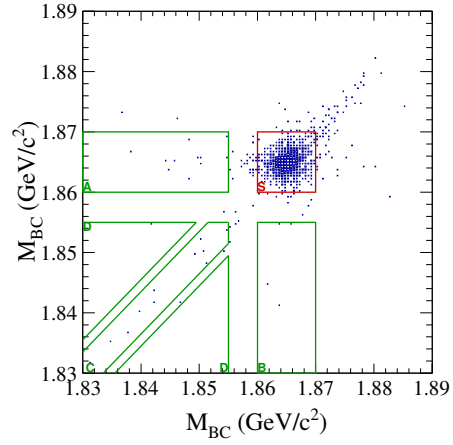
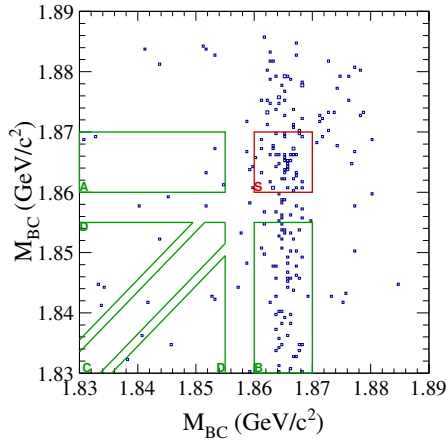
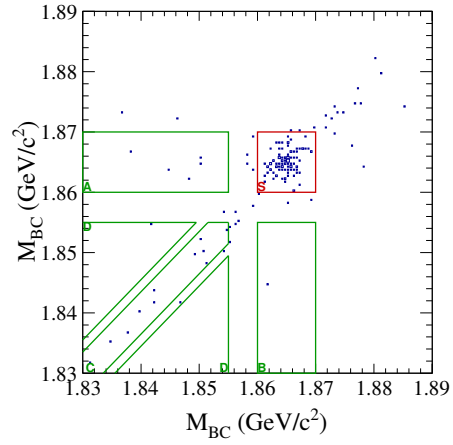
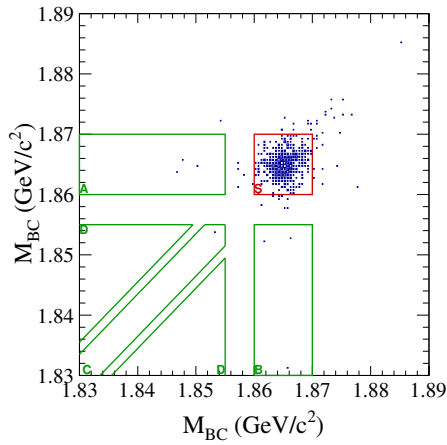
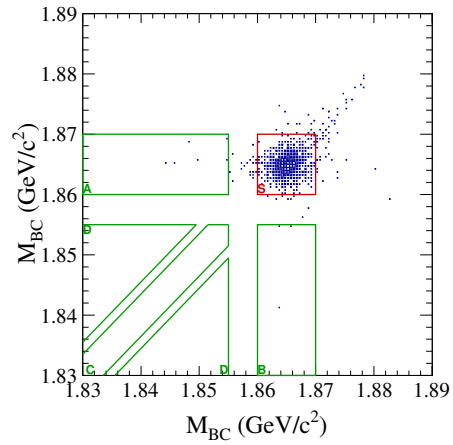
Two dimensional  $M_{BC}$  plots for individual tag combinations are shown in this section.

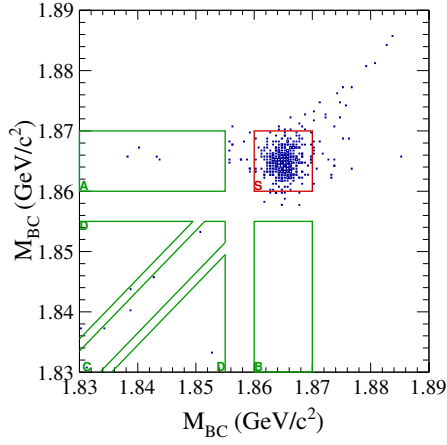
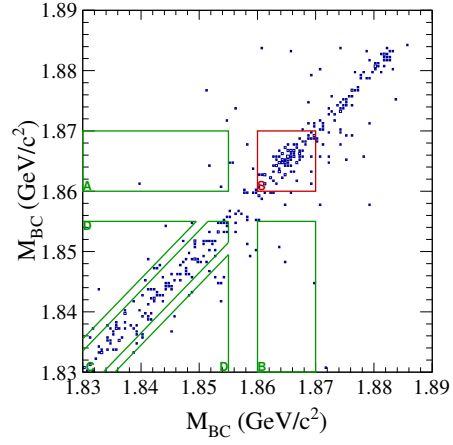
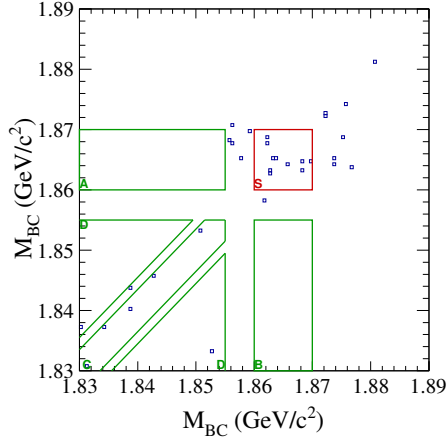
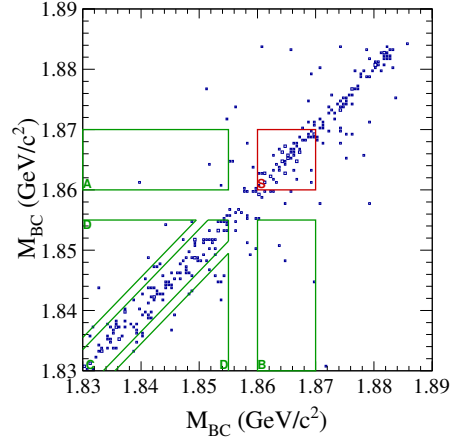
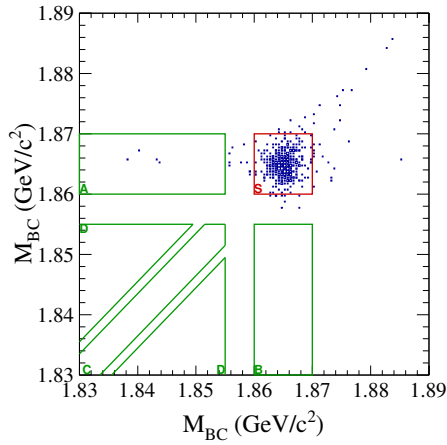
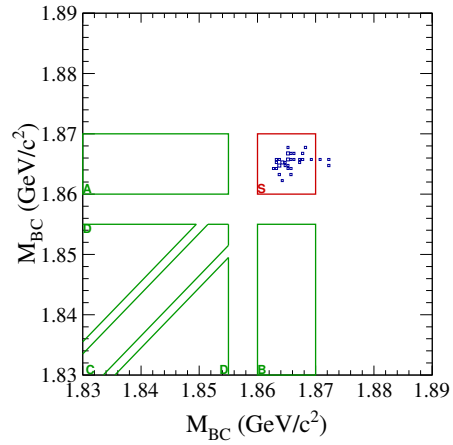
C.1  $\pi^+\pi^-\pi^0$  vs. CP Tag 2D  $M_{BC}$  Distributions(a)  $K_s\pi^0$  vs.  $\pi^+\pi^-\pi^0$ (b)  $\pi\pi$  vs.  $\pi^+\pi^-\pi^0$ (c) Peaking background for  $K_s\pi^0$  vs.  $\pi^+\pi^-\pi^0$ (d) Peaking background for  $\pi\pi$  vs.  $\pi^+\pi^-\pi^0$ (e) Signal for  $K_s\pi^0$  vs.  $\pi^+\pi^-\pi^0$ (f) Signal for  $\pi\pi$  vs.  $\pi^+\pi^-\pi^0$ **Figure 103:** CP tag vs.  $\pi^+\pi^-\pi^0$  peaking background study plots for MC sample.

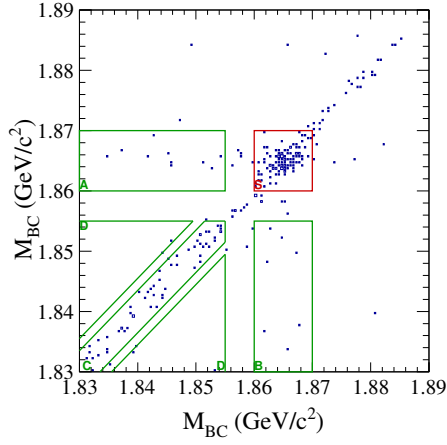
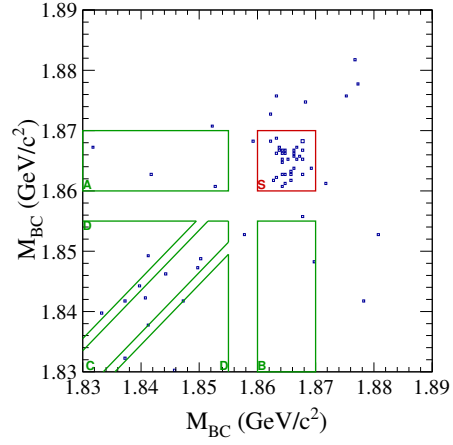
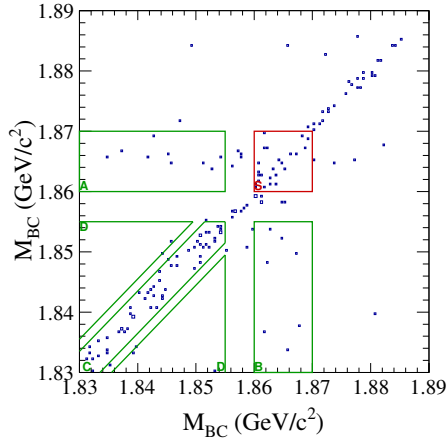
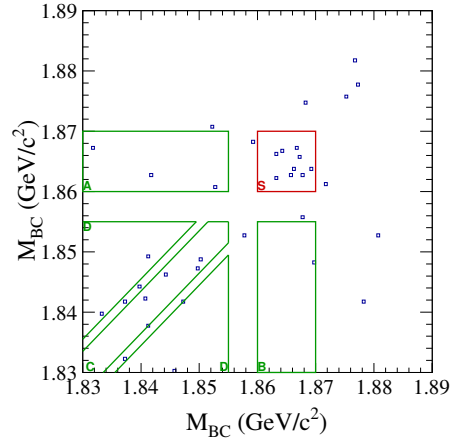
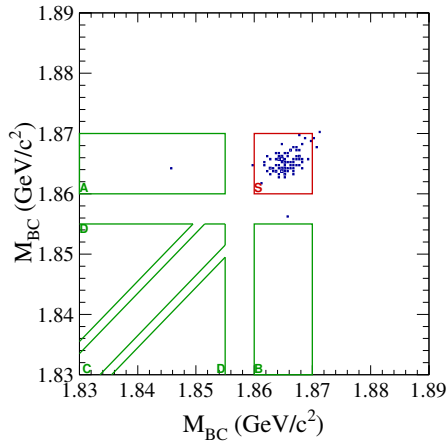
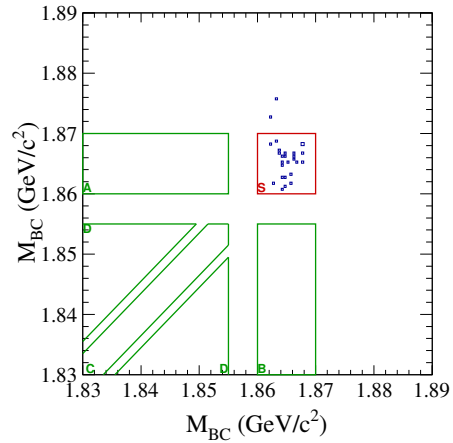
(a)  $KK$  vs.  $\pi^+\pi^-\pi^0$ (b)  $K_s\pi^0\pi^0$  vs.  $\pi^+\pi^-\pi^0$ (c) Peaking background for  $KK$  vs.  $\pi^+\pi^-\pi^0$ (d) Peaking background for  $K_s\pi^0\pi^0$  vs.  $\pi^+\pi^-\pi^0$ (e) Signal for  $KK$  vs.  $\pi^+\pi^-\pi^0$ (f) Signal for  $K_s\pi^0\pi^0$  vs.  $\pi^+\pi^-\pi^0$ **Figure 104:**  $CP$  tag vs.  $\pi^+\pi^-\pi^0$  peaking background study plots for MC sample.

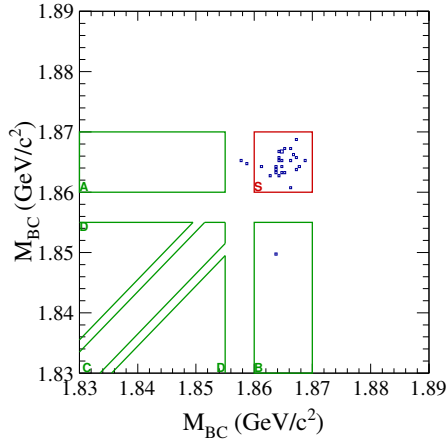
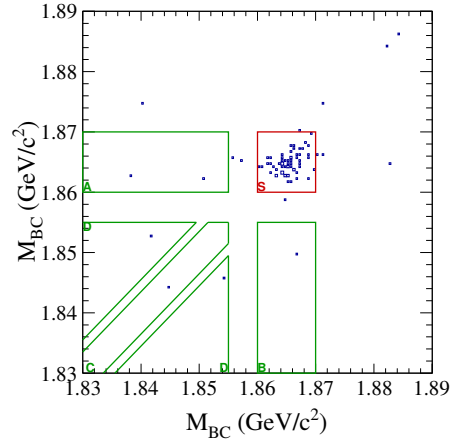
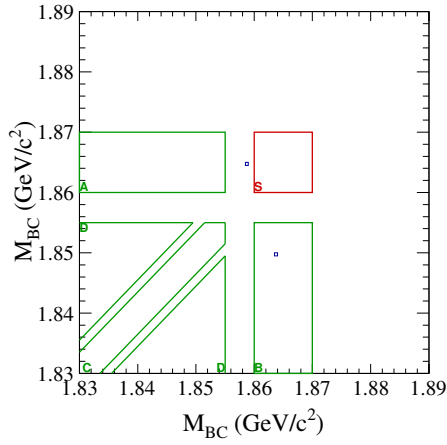
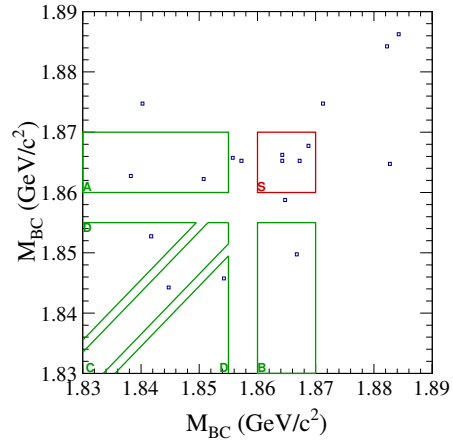
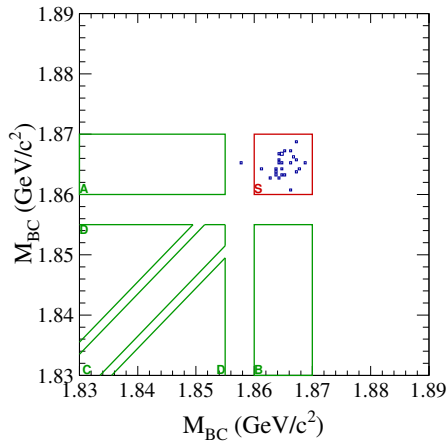
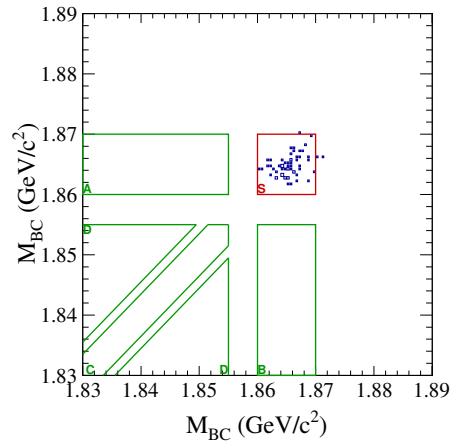
(a)  $K_s\eta'(\pi\pi\eta)$  vs.  $\pi^+\pi^-\pi^0$ (b)  $K_s\eta'(\rho\gamma)$  vs.  $\pi^+\pi^-\pi^0$ (c) Peaking background for  $K_s\eta'(\pi\pi\eta)$  vs.  $\pi^+\pi^-\pi^0$ (d) Peaking background for  $K_s\eta'(\rho\gamma)$  vs.  $\pi^+\pi^-\pi^0$ (e) Signal for  $K_s\eta'(\pi\pi\eta)$  vs.  $\pi^+\pi^-\pi^0$ (f) Signal for  $K_s\eta'(\rho\gamma)$  vs.  $\pi^+\pi^-\pi^0$ **Figure 105:** CP tag vs.  $\pi^+\pi^-\pi^0$  peaking background study plots for MC sample.

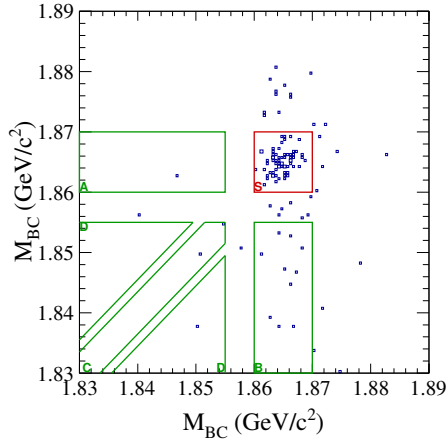
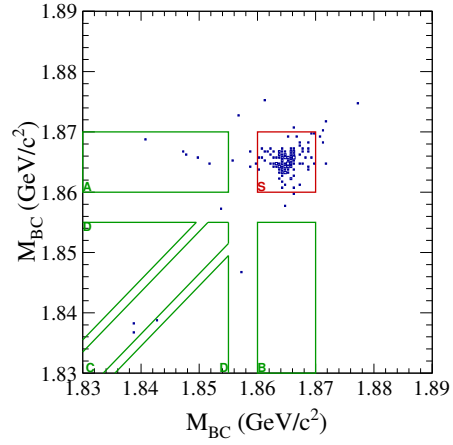
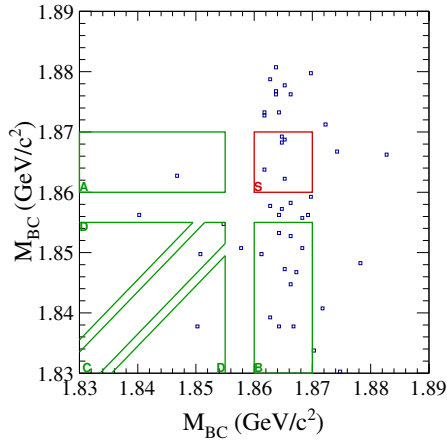
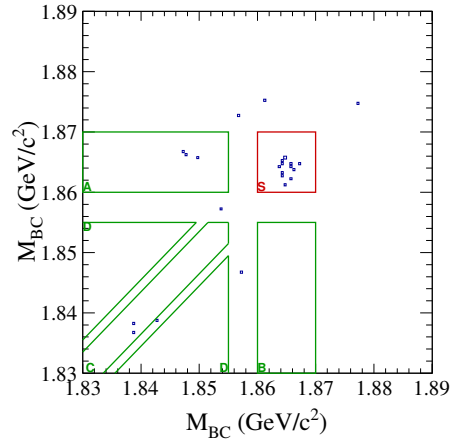
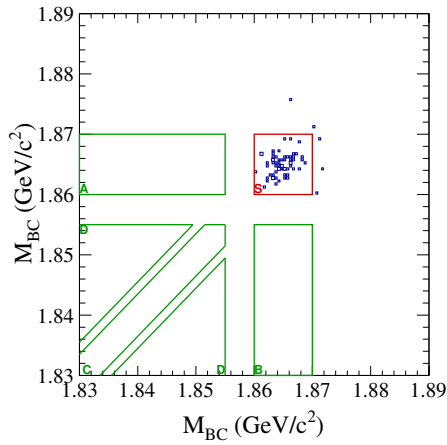
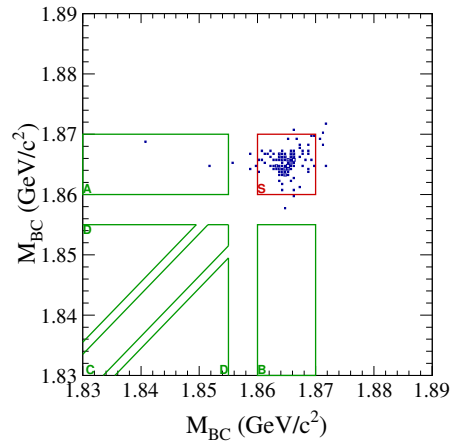


(a)  $K_s\eta$  vs.  $\pi^+\pi^-\pi^0$ (b)  $K_s\omega$  vs.  $\pi^+\pi^-\pi^0$ (c) Peaking background for  $K_s\eta$  vs.  $\pi^+\pi^-\pi^0$ (d) Peaking background for  $K_s\omega$  vs.  $\pi^+\pi^-\pi^0$ (e) Signal for  $K_s\eta$  vs.  $\pi^+\pi^-\pi^0$ (f) Signal for  $K_s\omega$  vs.  $\pi^+\pi^-\pi^0$ **Figure 106:**  $CP$  tag vs.  $\pi^+\pi^-\pi^0$  peaking background study plots for MC sample.

C.2  $K^+K^-\pi^0$  vs.  $CP$  Tag 2D  $M_{BC}$  Distributions(a)  $K_s\pi^0$  vs.  $K^+K^-\pi^0$ (b)  $\pi\pi$  vs.  $K^+K^-\pi^0$ (c) Peaking background for  $K_s\pi^0$  vs.  $K^+K^-\pi^0$ (d) Peaking background for  $\pi\pi$  vs.  $K^+K^-\pi^0$ (e) Signal for  $K_s\pi^0$  vs.  $K^+K^-\pi^0$ (f) Signal for  $\pi\pi$  vs.  $K^+K^-\pi^0$ **Figure 107:**  $CP$  tag vs.  $K^+K^-\pi^0$  peaking background study plots for MC sample.

(a)  $KK$  vs.  $K^+K^-\pi^0$ (b)  $K_s\pi^0\pi^0$  vs.  $K^+K^-\pi^0$ (c) Peaking background for  $KK$  vs.  $K^+K^-\pi^0$ (d) Peaking background for  $K_s\pi^0\pi^0$  vs.  $K^+K^-\pi^0$ (e) Signal for  $KK$  vs.  $K^+K^-\pi^0$ (f) Signal for  $K_s\pi^0\pi^0$  vs.  $K^+K^-\pi^0$ **Figure 108:**  $CP$  tag vs.  $K^+K^-\pi^0$  peaking background study plots for MC sample.

(a)  $K_s \eta'(\pi\pi\eta)$  vs.  $K^+ K^- \pi^0$ (b)  $K_s \eta'(\rho\gamma)$  vs.  $K^+ K^- \pi^0$ (c) Peaking background for  $K_s \eta'(\pi\pi\eta)$  vs.  $K^+ K^- \pi^0$ (d) Peaking background for  $K_s \eta'(\rho\gamma)$  vs.  $K^+ K^- \pi^0$ (e) Signal for  $K_s \eta'(\pi\pi\eta)$  vs.  $K^+ K^- \pi^0$ (f) Signal for  $K_s \eta'(\rho\gamma)$  vs.  $K^+ K^- \pi^0$ **Figure 109:** CP tag vs.  $K^+ K^- \pi^0$  peaking background study plots for MC sample.

(a)  $K_s \eta$  vs.  $K^+ K^- \pi^0$ (b)  $K_s \omega$  vs.  $K^+ K^- \pi^0$ (c) Peaking background for  $K_s \eta$  vs.  $K^+ K^- \pi^0$ (d) Peaking background for  $K_s \omega$  vs.  $K^+ K^- \pi^0$ (e) Signal for  $K_s \eta$  vs.  $K^+ K^- \pi^0$ (f) Signal for  $K_s \omega$  vs.  $K^+ K^- \pi^0$ **Figure 110:**  $CP$  tag vs.  $K^+ K^- \pi^0$  peaking background study plots for MC sample.

## References

- [1] Nicola Cabibbo. Unitary Symmetry and Leptonic Decays. *Phys. Rev. Lett.*, 10:531–533, 1963. [648(1963)].
- [2] Makoto Kobayashi and Toshihide Maskawa. CP Violation in the Renormalizable Theory of Weak Interaction. *Prog. Theor. Phys.*, 49:652–657, 1973.
- [3] Y. Amhis et al. Averages of  $b$ -hadron,  $c$ -hadron, and  $\tau$ -lepton properties as of summer 2014. 2014.
- [4] Michael Gronau and David London. How to determine all the angles of the unitarity triangle from  $B^{(d)0} \rightarrow DK_{(s)}$  and  $B^{(s)0} \rightarrow D^0$ . *Phys. Lett.*, B253:483–488, 1991.
- [5] Michael Gronau and Daniel Wyler. On determining a weak phase from CP asymmetries in charged  $B$  decays. *Phys. Lett.*, B265:172–176, 1991.
- [6] David Atwood, Isard Dunietz, and Amarjit Soni. Enhanced CP violation with  $B \rightarrow KD^0\bar{D}^0$  modes and extraction of the CKM angle  $\gamma$ . *Phys. Rev. Lett.*, 78:3257–3260, 1997.
- [7] David Atwood, Isard Dunietz, and Amarjit Soni. Improved methods for observing CP violation in  $B^\pm \rightarrow KD$  and measuring the CKM phase  $\gamma$ . *Phys. Rev.*, D63:036005, 2001.
- [8] N. Lowrey et al. Determination of the  $D^0 \rightarrow K^-\pi^+\pi^0$  and  $D^0 \rightarrow K^-\pi^+\pi^+\pi^-$  Coherence Factors and Average Strong-Phase Differences Using Quantum-Correlated Measurements. *Phys. Rev.*, D80:031105, 2009.
- [9] Roel Aaij et al. Study of  $B^- \rightarrow DK^-\pi^+\pi^-$  and  $B^- \rightarrow D\pi^-\pi^+\pi^-$  decays and determination of the CKM angle  $\gamma$ . *Phys. Rev.*, D92(11):112005, 2015.
- [10] Anjan Giri, Yuval Grossman, Abner Soffer, and Jure Zupan. Determining  $\gamma$  using  $B^\pm \rightarrow DK^\pm$  with multibody  $D$  decays. *Phys. Rev.*, D68:054018, 2003.
- [11] J. P. Lees et al. Observation of direct CP violation in the measurement of the Cabibbo-Kobayashi-Maskawa angle  $\gamma$  with  $B^\pm \rightarrow D^{(*)}K^{(*)\pm}$  decays. *Phys. Rev.*, D87(5):052015, 2013.
- [12] K. Trabelsi. Study of direct CP in charmed  $B$  decays and measurement of the CKM angle  $\gamma$  at Belle. In *7th Workshop on the CKM Unitarity Triangle (CKM 2012) Cincinnati, Ohio, USA, September 28-October 2, 2012*, 2013.
- [13] The LHCb Collaboration. Measurement of the CKM angle  $\gamma$  from a combination of  $B \rightarrow DK$  analyses. 2016.
- [14] K. A. Olive et al. Review of Particle Physics. *Chin. Phys.*, C38:090001, 2014.
- [15] M. Nayak, J. Libby, S. Malde, C. Thomas, G. Wilkinson, R. A. Briere, P. Naik, T. Gershon, and G. Bonvicini. First determination of the CP content of  $D \rightarrow \pi^+\pi^-\pi^0$  and  $D \rightarrow K^+K^-\pi^0$ . *Phys. Lett.*, B740:1–7, 2015.

- [16] Roel Aaij et al. A study of  $CP$  violation in  $B^\pm \rightarrow Dh^\mp$  ( $h = K, \pi$ ) with the modes  $D \rightarrow K^\mp \pi^\pm \pi^0$ ,  $D \rightarrow \pi^+ \pi^- \pi^0$  and  $D \rightarrow K^+ K^- \pi^0$ . *Phys. Rev.*, D91(11):112014, 2015.
- [17] Mario Gaspero, Brian Meadows, Kalanand Mishra, and Abner Soffer. Isospin analysis of  $D^0$  decay to three pions. *Phys. Rev.*, D78:014015, 2008.
- [18] Bernard Aubert et al. Amplitude analysis of the decay  $D^0 \rightarrow K^- K^+ \pi^0$ . *Phys. Rev.*, D76:011102, 2007.
- [19] C. Cawlfeld et al. Measurement of interfering  $K^{*+} K^-$  and  $K^{*-} K^+$  amplitudes in the decay  $D^0 \rightarrow K^+ K^- \pi^0$ . *Phys. Rev.*, D74:031108, 2006.
- [20] M. Ablikim et al. Design and Construction of the BESIII Detector. *Nucl. Instrum. Meth.*, A614:345–399, 2010.
- [21] M. Ablikim. Measurement of the integrated luminosities of the data taken by BESIII at  $\sqrt{s} = 3.650$  and  $3.773$  GeV. *Chin. Phys.*, C37:123001, 2013.
- [22] M. Ablikim et al. Measurement of the  $e^+ e^- \rightarrow \pi^+ \pi^-$  cross section between 600 and 900 MeV using initial state radiation. *Phys. Lett.*, B753:629–638, 2016.
- [23] Tomasz Skwarnicki. *A study of the radiative CASCADE transitions between the  $\Upsilon'$  and  $\Upsilon$  resonances*. PhD thesis, Cracow, INP, 1986.
- [24] H. Albrecht et al. Search for Hadronic  $b \rightarrow u$  Decays. *Phys. Lett.*, B241:278–282, 1990.
- [25] David Mark Asner et al. Determination of the  $D^0 \rightarrow K^+ \pi^-$  Relative Strong Phase Using Quantum-Correlated Measurements in  $e^+ e^- \rightarrow D^0 \bar{D}^0$  at CLEO. *Phys. Rev.*, D78:012001, 2008.
- [26] Pengfei Duan et al. Charge asymmetry and multiplicities in  $\psi''$  data. Technical report, IHEP.
- [27] Bai-Cian Ke.  $\pi^0$  reconstruction efficiency. Technical report, Carnegie Mellon University.
- [28] S. Malde, C. Thomas, G. Wilkinson, P. Naik, C. Prouve, J. Rademacker, J. Libby, M. Nayak, T. Gershon, and R. A. Briere. First determination of the  $CP$  content of  $D \rightarrow \pi^+ \pi^- \pi^+ \pi^-$  and updated determination of the  $CP$  contents of  $D \rightarrow \pi^+ \pi^- \pi^0$  and  $D \rightarrow K^+ K^- \pi^0$ . *Phys. Lett.*, B747:9–17, 2015.
- [29] Roel Aaij et al. Search for  $CP$  violation in  $D^0 \rightarrow \pi^+ \pi^- \pi^0$  decays with the energy test. *Phys. Lett.*, B740:158–167, 2015.
- [30] Colin Gay.  $B$  mixing. *Ann. Rev. Nucl. Part. Sci.*, 50:577–641, 2000.
- [31] S. Malde, C. Thomas, and G. Wilkinson. Measuring  $CP$  violation and mixing in charm with inclusive self-conjugate multibody decay modes. *Phys. Rev.*, D91(9):094032, 2015.
- [32] Roy A. Briere. Quantum Correlated Charm at Threshold and Inputs to Extractions of  $\gamma$  from  $B$  Decays. 2014.

- [33] D. M. Asner and W. M. Sun. Time-independent measurements of  $D^0 - \bar{D}^0$  mixing and relative strong phases using quantum correlations. *Phys. Rev.*, D73:034024, 2006. [Erratum: *Phys. Rev.* D77,019901(2008)].
- [34] David Atwood and Alexey A. Petrov. Lifetime differences in heavy mesons with time independent measurements. *Phys. Rev.*, D71:054032, 2005.
- [35] Zhi-zhong Xing.  $D^0 - \bar{D}^0$  mixing and CP violation in neutral  $D$  meson decays. *Phys. Rev.*, D55:196–218, 1997.